



HAL
open science

Probabilistic approach for modelling pore structure and reactive transport in porous media due to precipitation and dissolution of solid phases

Qingxiang Xiong

► **To cite this version:**

Qingxiang Xiong. Probabilistic approach for modelling pore structure and reactive transport in porous media due to precipitation and dissolution of solid phases. Civil Engineering. INSA de Rennes, 2021. English. NNT : 2021ISAR0027 . tel-04460413

HAL Id: tel-04460413

<https://theses.hal.science/tel-04460413>

Submitted on 15 Feb 2024

HAL is a multi-disciplinary open access archive for the deposit and dissemination of scientific research documents, whether they are published or not. The documents may come from teaching and research institutions in France or abroad, or from public or private research centers.

L'archive ouverte pluridisciplinaire **HAL**, est destinée au dépôt et à la diffusion de documents scientifiques de niveau recherche, publiés ou non, émanant des établissements d'enseignement et de recherche français ou étrangers, des laboratoires publics ou privés.

THESE DE DOCTORAT DE

L'INSTITUT NATIONAL DES SCIENCES

APPLIQUEES RENNES

ECOLE DOCTORALE N° 602

Sciences pour l'Ingénieur

Spécialité : Génie Civil

Par

Qing Xiang XIONG

Probabilistic approach for modelling pore structure and reactive transport in porous media due to precipitation and dissolution of solid phases

Thèse présentée et soutenue à Rennes, le 23/07/2021

Unité de recherche : LGCGM- INSA RENNES

Thèse N° : 21ISAR 21 / D21 - 21

Rapporteurs avant soutenance:

Naïma BELAYACHI

Abdelkarim AÏT-MOKHTAR

Maître de Conférences – HDR, Université d'Orléans

Professeur des Universités, Université de La Rochelle

Composition du Jury :

Président :

Ouali AMIRI

Professeur des Universités, Université de Nantes

Examineurs :

Ouali AMIRI

Professeur des Universités, Université de Nantes

Farid BENBOUDJEMA

Professeur des universités, ENS Paris-Saclay

Fekri MEFTAH

Professeur des Universités , INSA RENNES

Naïma BELAYACHI

Maître de Conférences – HDR, Université d'Orléans

Abdelkarim AÏT-MOKHTAR

Professeur des Universités, Université de La Rochelle

Dir. de thèse :

Fekri MEFTAH

Professeur des Universités , INSA RENNES

Acknowledgements

The research work reported in this thesis was conducted within the GEOSAX Group and Laboratoire de Génie Civil et Génie Mécanique (LGCGM) at INSA de Rennes, France. This work was supported by the Co-operation Program of CSC- UT INSA.

First, I would like to express my sincere gratitude to my supervisor, Professor Fekri MEFTAH, who impacted and helped me a lot during my PhD research project. Without his help, I could not finish this thesis. His stringent attitude toward work, profound foundation of professional knowledge, and intelligent thinking, inspired me to go further in my research career. He has made me realize that pursuing scientific truth is challenging, but it is also worthwhile.

I also greatly acknowledge China Scholarship Council, who gave me the chance to work abroad by financing three and a half years scholarship. I should also thanks to my country-China, who offered warm consideration to all the Chinese in France during the most difficult time of COVID-19 pandemic.

Moreover, I would like to thank the members of "Comite de suivi individuel", Professor Farid BENBOUDEJEMA and Professor James LEDOUX, for their supervision and valuable advice on my PhD project during three times of mid-term defense.

Fourth, I am very thankful for my "composition du jury" of PhD defense, Professor Farid BENBOUDEJEMA and Professor Ouali AMIRI, for sharing experimental data with me, especially Professor Naïma BELAYACHI and Professor Abdelkarim AÏT-MOKHTAR, who were my "rapporteurs avant soutenance". Thanks for their insightful suggestions on my thesis as well as their presence on the spot of my PhD defense in Rennes.

I am also grateful to all colleagues and friends in Rennes: Noubough SLEIMAN, Nelson ALVARADO, Simon GUIHENEUF, Josue YOKOPI, Jian Hua FAN, Ye TIAN, Hai Yun YAO, Chuan CHEN, BoYuan YANG, Try MENG, Peng Zhi WANG, Li Pin CHEN, Cai HU and Yi WU. Their friendships are my most beautiful memories in France.

Last, I'm definitely indebted to my family. I would like first to give my deep appreciation to my parents and my sister, for their 100% love and unconditional support. I love them. I also thank my lovely niece, Ruo Xi (Dodo). She is an angel in my life, bringing happiness during my tough and lonely moments abroad. Besides, I cannot express my appreciation to my fiance, Jun Kai HUANG. He is my soulmate, giving me unlimited love and encouragement. I love you.

Qing Xiang XIONG

A Rennes, le 23/07/2021

Contents

Introduction	1
1. Literature Review on Characterization of Pore Structure and Transport Properties	4
1.1 Introduction.....	4
1.2 Characterization of pore structure in porous materials	4
1.2.1 Porosity.....	5
1.2.2 Pore size distribution	7
1.2.2.1 Classifications for pore sizes	7
1.2.2.2 Experimental methods for pore size distribution.....	8
1.2.2.3 Probabilistic Methods for Pore Structure.....	11
1.3 Deteriorations in porous materials	12
1.4 Reactive transport in porous materials.....	15
1.4.1 Transport models	15
1.4.2 Reactive transport models	18
1.4.3 General methods for solving reactive transport models.....	20
1.5 Transport properties	21
1.5.1 Experimental investigations on permeability	21
1.5.2 Modelling investigations on permeability	22
1.5.3 Water sorption isotherm	25
1.6 Conclusions.....	26
2. Probabilistic Approach of Pore Structure Evolution Induced by Precipitation and Dissolution.....	28
2.1 Introduction.....	28
2.2 Probabilistic porous network model	31

2.2.1 Probabilistic method for pore size distribution	32
2.2.2 Transformation models for pore size.....	37
2.2.3 Water saturation degree determined by probabilistic model	38
2. 3. Experimental data for initial pore size distribution	39
2. 4. Parametric investigation	40
2.4.1 Pore size distribution implemented by linear transformation	41
2.4.2 Limitations and constraints for non-linear transformation.....	41
2.4.3 Comparisons between method one and method two	43
2.4.3.1 Single transformation of pore size distribution with constant waterfront	43
2.4.3.2 Single transformation of pore size distribution with varied waterfront.....	44
2.4.3.3 Successive transformations of pore size distribution with varied waterfront..	46
2.4.4 Further development on method two.....	47
2.4.4.1 Single transformation of pore size distribution.....	47
2.4.4.2 Successive transformations of pore size distribution.....	50
2. 5 Conclusions.....	53
Appendix 2A. Non-linear transformation models	55
Appendix 2B. Determination for probability density function and parameter ε under single transformation of pore sizes	55
Appendix 2C. Determination for probability density function and parameter ε under successive transformations of pore sizes	58
3. Local-like Hygro-Chemical Reactive Transport Model for Porous Materials Subjected to Precipitation and Dissolution	63
3.1 Introduction.....	63
3.2 Development of chemical box	65
3.2.1 Chemical equilibrium constant.....	66
3.2.2 The law of mass action.....	66
3.2.3 Local reaction for salt precipitation and dissolution	67

3.2.4 Modelling results for chemical reactions	68
3.2.4.1 Validation for one single time of reaction.....	69
3.2.4.2 Comparison of the three iterative methods	69
3.2.4.3 Validation for successive reactions	70
3.3 Development of hygro-chemical transport model	72
3.3.1 Description of porous materials	73
3.3.2 Mass balance	75
3.3.3 Assumptions and solutions	76
3.4 Implementations and results	77
3.4.1 One single drying or wetting process	79
3.4.2 Drying and wetting cycles under different Q_c	85
3.4.2.1 Water saturation degree ranges in $[0.1, 0.9]$, add ions with different Q_c	85
3.4.2.2 Water saturation degree ranges in $[0.1, 0.9]$, add/remove ions with different Q_c	88
3.4.3 Drying and wetting cycles under varying intervals of water saturation degree	91
3.5 Conclusions.....	95
Appendix 3A. Iterative schema for local chemical equilibrium.....	98
Appendix 3B. Solution procedure of transport equations.....	99
4. Modelling of Water Sorption Isotherm and Permeability Based on the Probabilistic Approach of Pore Structure Evolution	101
4.1 Introduction.....	101
4.2 Modelling of water sorption isotherm based on the probabilistic porous network	104
4.2.1 Relation for relative humidity and capillary pressure	105
4.2.2 Relation for capillary pressure and waterfront	109
4.2.3 Water saturation degree based on the probabilistic porous network	113
4.3 Modelling of permeability based on the probabilistic porous network	117
4.3.1 Permeability under constant RH based on successive transformations of pore sizes	

.....	120
4.3.2 Permeability under varying RH based on single transformation of pore sizes	125
4.3.2.1 Validation of the analytical model for permeability	126
4.3.2.2 Evolution of permeability due to salt precipitation and dissolution	129
4.4 Conclusions.....	135
Appendix 4A. Determination of water saturation degree based on the probabilistic pore size distribution model.....	138
Appendix 4B. Permeability based on the probabilistic pore size distribution model.....	139
5. Conclusions and Perspectives	143
5.1 Conclusions.....	143
5.2 Perspectives	144
5.2.1 Development of compound-lognormal pore size distribution.....	144
5.2.2 Extended description of water saturation degree	145
5.2.3 Coupling of pore structure evolution and reactive transports	146
5.2.4 Extending probabilistic approach to diffusivity based single fluid model	147
List of symbols	149
List of figures	151
List of tables	158
Bibliography.....	159
Résumé en français.....	172

Introduction

Building materials such as concrete, stones and bricks are open porous materials that are widely used in building structures. In recent years, the durability of building materials has been attracted much concern since it is essential in ensuring the long and durable service lifetime and good performance of building structures [1]. The durability issues such as freeze-thaw, salt crystallisation, leaching, and chloride-induced corrosion are very common deteriorations in porous materials, which are strongly related to their microstructures [2–6]. Meanwhile, the degradations of porous materials also alter the microstructure of building materials [7,8]. Therefore, it is crucial to gain a comprehensive characterisation of the microstructure in evaluating the durability-related processes in porous materials.

The alteration of microstructure induced by degradation processes results in an evolution of both overall porosity and pore size distribution of the material [9,10]. Thus, degradations such as salt precipitation and dissolution in porous materials are here of interest in this research. Moreover, precipitation and dissolution strongly depend on moisture transport when the porous material is subjected to cyclic drying and wetting. Therefore, it is equally important to describe the water and ionic transport involved in the precipitation and dissolution processes.

With this motivation in mind, the first objective is to develop a probabilistic representation of the evolution for pore size distribution induced by precipitation and dissolution of chemical species in a partially saturated porous material. The second objective is to develop a moisture transport model contains ionic species and chemical reactions to illustrate the service life of the porous materials when subjected to the cyclic drying and wetting process. Finally, extended explorations of this project are conducted in establishing analytical models for the durability-related properties in porous materials, including water sorption isotherm, relative humidity, water saturation degree, and permeability based on the probabilistic pore size distribution model.

To achieve the three aforementioned objectives, this thesis is organised into five main chapters (see in figure 1). A brief outline of each chapter is given as follows.

Chapter 1 is the literature review on the characterisation of pore size distribution regarding experimental measurements and numerical models. Meanwhile, this chapter also introduces fundamentals of transport processes such as water and ionic transport, and their correlations with chemical reactions concerning precipitation and dissolution. Finally, some classical methods in investigating transport properties such as permeability are summarised to end this chapter.

Chapter 2 develops a porous network model to illustrate the evolution of pore size distribution due to the modification of overall porosity and water saturation degree during salt precipitation

and dissolution. This model is based on two probabilistic methods of pore size distribution and three transformation models for the relationship between initial and modified pore sizes (correspondingly before and after salt precipitation and dissolution). According to the comparison results on pore size distribution, the most appropriate model is determined for the following research (filling and emptying ratio) of this thesis. Moreover, successive transformations are also introduced to investigate the heredity of pore size distribution after several transformations. Finally, parametric studies regarding capillary interface (or the so-called waterfront) and opening zone are conducted, aiming at give a quantitative understanding of pore size modifications induced by precipitation/dissolution.

Chapter 3 investigates the water-ionic transport process coupling with chemical reaction of precipitation/dissolution for sodium chloride (NaCl) in porous materials. Firstly, a chemical box dealing with precipitation/dissolution is developed in MATLAB. Secondly, a local-like transport model coupling with chemical reaction is proposed to illustrate the water-ionic transport process in porous materials. Coupling functions between physical transport and chemical box are solved by adopting the operator-splitting method (OSA). By adopting this model, the ionic concentrations, porosity and time required to fill all the pores under long-term exposition are investigated. Meanwhile, a prediction relation between ionic flux and the time of filling the pores with precipitation is obtained by investigating the reactive transport process under cyclic drying and wetting conditions. Finally, brief comments on simulation results are given for further improvement.

Chapter 4 first develops an analytical model of water sorption isotherm by adopting the probabilistic pore size distribution model in Chapter 2, which presents the interactions between water content and relative humidity. Then, according to Young-Laplace equation and Kelvin's equation, the critical pore size for the waterfront under arbitrary relative humidity is determined. After that, by adopting Koichi's model, permeability is described based on the proposed probabilistic pore size distribution model. Meanwhile, the permeability model is validated by comparing it with experimental results provided by Amiri. Finally, the effects of modified porosity and pore size distribution on permeability are investigated by developing an evolution permeability model under precipitation/dissolution conditions.

Finally, the general conclusions and perspectives are given in Chapter 5.

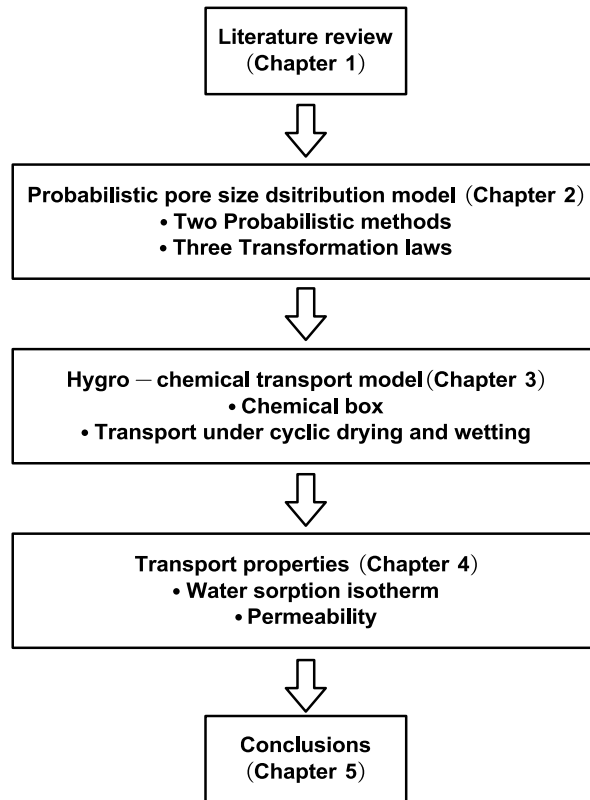


Figure 1 Flowchart of this thesis.

Chapter 1

Literature Review on Characterization of Pore Structure and Transport Properties

1.1 Introduction

Porous materials such as concrete, mortar, stones, and bricks are dominant materials in the building industry for the past several decades throughout the world [11]. With the service duration of buildings increasing, the durability-related problems are remarkable. The maintenance and sustainability of building materials face a great challenge. Therefore, a detailed understanding of the mechanism of deterioration in porous materials is essential for preventing the porous materials from degradation agents and predicting their durability, further saving the cost for maintenance and reparations [2,7]. The first step to this attempt is making a comprehensive overview of the pore structure which is the most fundamental property of porous materials. Thus, in the first part, the characterizations of pore structures regarding experimental measurements and probabilistic models are reviewed in this chapter. Second, some common deteriorations in general that affect the durable service life of building materials are summarised. Since most processes of deterioration are influenced by water-ionic transport in porous materials, thus, currently used models for depicting the transport process and its properties are briefly described in the last part of this chapter.

1.2 Characterization of pore structure in porous materials

The pore structure is inherent to porous materials. All the macroscopic properties (physical, chemical and mechanical properties) of porous materials are influenced, more or less, by the microstructure [12]. The essential characteristics of the pore structure are porosity and the pore size distribution, which are also the primary research target in our work.

Before attempting the definition of porosity and pore size distribution, the object “pore” must be defined. A pore is defined as the pore space bounded by solid surfaces and erected planes, analogously as a room is defined by its walls and the doors, as is shown in figure 1.1 [13].

With the definition of pores, the pore space is the summation volume of the pores that consists of two sorts of pores, the closed pores and the opened pores [14]. The closed pores usually contain air insides, making no difference to the substance exchange but affect notably the

strength of porous materials. The opened pores, connecting by a pore throat, contain fluids, such as air, water, or the mixture of dissolved minerals, influencing both strength and transport properties of porous materials [15]. Moreover, the pore fluids can be transported from one pore to another through the connection path, or it can exchange the fluids from the internal pore to the external pore of porous material.

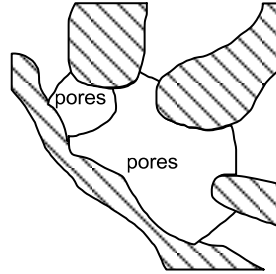


Figure 1. 1 Schematic of pores [13].

1.2.1 Porosity

The porosity is a critical parameter for porous material because many properties such as strength, permeability, and diffusivity, shrinkage, and creep are closely related to porosity [16]. Porosity measures the fraction of pore space to the total volume of materials.

According to the sorts of pores, the porosity can be defined as total porosity and open porosity. Total porosity, containing both interconnected pores and isolated pores, is defined as the ratio of the total porous volume and the bulk volume. It is a dimensionless quantity, usually expressed as a percentage value, and is obtained regardless of pore connections [17]. The total porosity is defined as:

$$\phi = \frac{V_{pore}}{V_{total}} \quad (1.1)$$

Thus, the portion of the bulk volume occupied by solid skeleton and precipitated solid is expressed as:

$$1 - \phi = \frac{V_{solid}}{V_{total}} \quad (1.2)$$

However, as the limitation of experimental techniques, we usually can only test the open pores in most cases. Thus, we introduce another definition - effective porosity, which is the fraction for the volume of opening and interconnecting pores and the bulk volume. The effective porosity is always smaller than the total porosity [18]. Non-interconnected pores cannot contribute to the transport of porous materials; thus, they can be negligible sometimes.

Over the past years, several methods have been developed to describe the porosity, which are summarised as follows:

1. *Direct method.*

According to equation (1.1), we need to know the bulk volume and the pores volume to obtain the porosity. Thus, the direct method obtains the pores volume by following procedures: measuring the bulk volume, crushing the specimen, removing all pores, and then measuring the remained volume of solids [13]. By using this method, we can obtain the total porosity. However, this method destroys the materials, which is a very limited used measurement.

2. Imbibition method.

This is a direct method for effective porosity [13]. In this method, the samples are immersed in the wetting fluids, and fluids are enforced into the connected pores. After immersion, the mass of the saturated sample should be:

$$M_{wet} = M_{dry} + \rho_w V_{pore} \quad (1.3)$$

where M_{dry} is the mass for the dry sample and ρ_w is the water density. Therefore, the pore volume can be obtained as:

$$V_{pore} = \frac{M_{wet} - M_{dry}}{\rho_w} \quad (1.4)$$

If the sample takes a long time to be well immersed with full saturation, the imbibition method should be a reliable porosity measurement [19].

3. MIP method.

The MIP method is a very commonly used technique, which is based on the premise that a non-wetting liquid intrudes capillary pores under pressure according to the well-known Washburn relations [20]:

$$P = \frac{2\gamma \cos \theta}{r} \quad (1.5)$$

where P is the intrude pressure, γ is the surface tension of the liquid, θ is the contact angle of the liquid and r is the intruded pore radius.

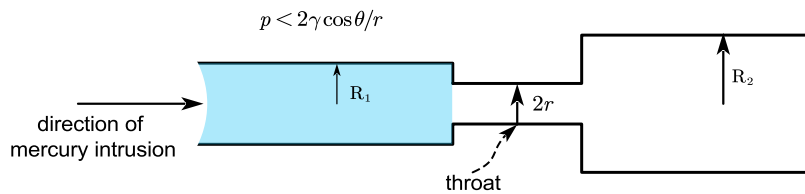


Figure 1. 2 Bottle-ink effect.

The MIP method measures the effective porosity based on the mechanism that a porous sample can be immersed in mercury only for the opened and interconnected pores. However, MIP results are affected by several factors [12,15]. First, the measured results may be affected by ‘bottle-ink’ effects (see figure1.2). [21] Thus, the tested porosity may be less than the realistic porosity, which will be talked about in the next section. The second is that the pores are assumed to be cylindrical, and they are entirely and equally accessible to the outer surface of

a specimen. These assumptions may be far away from reality, leading to the consequence that most pores being reported one or two orders of magnitude smaller than they actually are [22]. Finally, it should be noted that the MIP method cannot provide information on closed pores nor pore connectivity and pore shapes.

4. Non-destructive 3D visualization methods.

More recently developed methods, such as NMR (nuclear magnetic resonance) microscopy and x-ray computed micro-tomography (XRCT) methods, are non-destructive techniques that provide the 3D data of porosity with a quite good accuracy [12].

Such methods can provide morphological information, including pore shapes, spatial distribution, and connectivity that cannot be measured by the MIP method [23,24]. In addition, it provides an accurate measurement of true pore size distribution, which is different from the MIP method that only detects the pore throats. However, it should be concerned that the accuracy of the testing results depends strongly on the resolution of the instruments. For instance, when performing the XRCT method, a small piece of the scanned object is measured to replace the whole object in order to improve the image quality (the resolution and contrast of the image). However, it should be emphasised that the obtained result on the limited size of the sample is not reliable to represent the whole pore structure [24].

To be concluded, among these experimental measurements stated above, the MIP method is a relatively easy and low-cost method that is widely applied when characterizing the pore structures. However, it should be aware that porosity is inadequate to describe the pore structure; even the same porosity will lead to different microstructures of porous materials [14]. Hence, we also need to study the pore size distribution to obtain a complete comprehension of pore structure.

1.2.2 Pore size distribution

Pore size distribution is another essential property of porous materials that influences significantly the durability related properties of porous materials. The pore sizes are randomly distributed with radius covers several orders of magnitude from nanometres to centimetres. Many reports have been devoted to make a general classification for the complex pore sizes. However, since the diversity of different porous materials, the classification of pores may be different [15].

1.2.2.1 Classifications for pore sizes

In 1972, The IUPAC [25] has proposed a coarse classification of pore sizes for concrete materials, as is shown in following:

- Micro-pores with sizes less than 2nm
- Meso-pores with sizes from 2nm to 50nm
- Macro-pores with sizes larger than 50 nm.

In 1981, Mindess et al. [26] have suggested an upgraded classification of pore sizes for cement pastes by dividing the pores as:

- Interlayer pores with sizes less than 0.5nm
- Micro-pores with sizes from 0.5nm to 2.5nm
- Gel pores with sizes from 2.5nm to 10nm
- Small capillary pores with sizes from 10nm to 50nm
- Large capillary pores with sizes from 50nm to 10 μ m.

In 2004, Jennings [27] has given a new category of pore sizes for cement pastes as following:

- Interlayer pores with sizes less than 0.5nm
- Small gel pores with sizes from 1.2nm to 2nm
- Large gel pores with sizes from 2nm to 5nm
- Capillary pores with sizes larger than 75nm.

In 2014, Gong et al. [28] have proposed a classification of pore sizes for the cement pastes as following:

- Micro-pores with sizes from 1nm to 100 nm
- Meso-pores with sizes from 100nm to 10 μ m
- Macro-pores with sizes from 10 μ m to 1cm.

It can be observed from above that the borderlines between the different classifications of pore sizes are not strict. It depends on the experimental techniques used to measure the pore size for different materials. However, it should be noted that although the classification of pore sizes exists differently, the spectrum of the pore sizes is continuous.

In this research, the pore size classification will be defined as follows (see figure 1.3):

- Gel pores have sizes ranging from 0.25nm to 5nm
- Capillary pores have sizes ranging from 2.5nm to 5 μ m
- Air voids have sizes larger than 5 μ m.

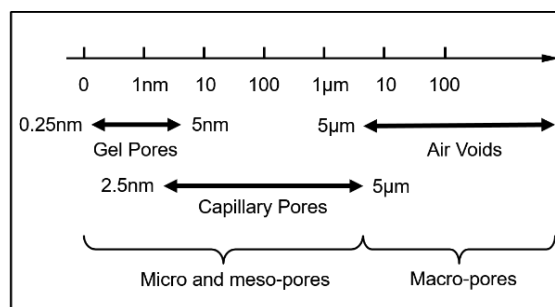


Figure 1. 3 Classification of pore sizes in this research.

1.2.2.2 Experimental methods for pore size distribution

Being different from explicit observation for porosity, accurate depiction of pore size distribution has been challenged [15,17,21,22]. It is essential to recognize that a variety of

techniques have been adopted to characterise pore size distribution, among them the most commonly used techniques are summarised as follows:

1. *Water/gas condensation.*

This method is based on the principle that two materials are coming into contact, one in flow state and the other in solid state [14]. Assuming that pores are in cylindrical shapes, the pore size distribution can be obtained according to Kelvin's equation [29]:

$$d = \frac{-4\gamma M \cos \theta}{\rho RT \ln(P/P_0)} \quad (1.6)$$

where d is the diameter of detected pore size, γ is the surface tension of the condensate, M is the molecular weight of the condensate, θ is the contact angle (which is usually assumed as zero), ρ is the density of the condensate, R is the gas constant, T is the temperature and P/P_0 is the relative vapor pressure at which capillary condensation occurs.

This method provides data for open porosity and pore size distribution for the small pores. As illustrated by diamond [30], the condensation method detects a narrower range of pores (with sizes yield from 5nm to 10nm) than the MIP method with a coarser size distribution. It reveals that the condensation method seems to be the best choice to complete the wide range of pore sizes when small pores cannot be measured by other methods. However, it should be emphasized that the pore size distribution obtained by the condensation method for the same samples may differ because of different condensate (such as water, nitrogen, Ethanol).

2. *Mercury intrusion porosimetry.*

This technique is the most successfully used method for detecting the pore size distribution for a long time [22,22,30–32]. The mechanism of the MIP method has been introduced in equation (1.6). The forced pressure is inversely proportional to the pore radius. This is a percolation process and requires an interconnected network of pore structure. Thus, the MIP method measures the open and connected pore size distribution rather than the true distribution of pore volume. Moreover, accounting for the “bottle-ink” effect, the MIP method overestimates the fine pores and underestimates the large pores, especially for large capillary pores and air voids. Another concern of the MIP method is that the specimen needs to be dried prior to testing, which alters the pore structure during the drying process [33]. Third, the high pressure applied by the MIP method will damage the microstructure [34]. Despite these drawbacks, the MIP method is still a reliable and quick measurement covering a quite wide range of pore sizes [26].

3. *Direct method with microscopy.*

Microscopes can be used to directly observe the pore structure by giving an image of the exact position of the pore. It is the only method that can relate porosity with pathology. Besides, it can also measure a wide range of pore sizes. Several microscopies can be adopted to measure the pore size: stereo binocular microscope, petrographic microscope, and scanning electron microscope [14]. Among them, scanning electron microscope (SEM) is the most frequently used microscopy tool. This method is different and convenient because it can be applied on

both polished and rough samples. However, the sample analysed by microscopy should be small to reach the satisfied resolution, which will influence the accuracy of the tested results.

4. Nuclear magnetic resonance.

The significant characteristic of this method is non-invasive and non-destructive [35]. It is the only technique to study the pore structure without any alteration or damage induced by pre-drying because it uses water as the probe [34,36,37]. Adopting this method can provide more details in characterizations of porous materials, for instance, the density, the composition ratios, the porosity, and the pore size distribution [34]. It is a novel, quick measurements methods that can rapidly improve the characterisation of porous materials.

5. X-ray computed micro-tomography.

It is a three-dimensional imaging technique, and there is neither resorting to any assumption of regular pore geometry in the interpretation of results nor invasive or pre-drying manner during the experimental procedure [38]. Adopting this method can examine the three-dimensional pore structure of the material directly by obtaining more features, such as connectivity and tortuosity [39]. However, the X-ray imaging system is susceptible to resolution. Moreover, there is a limitation of the overall sample size; the limited sample sizes involved in testing are insufficient to represent the pore structures of the whole material [38].

By giving a glimpse of the experimental methods, it can be concluded that it is quite difficult to characterise the pore structure by a certain measurement method accurately. The reasons are as follows:

- The range of pore sizes in cement-based material is quite broad, containing several orders of magnitude; for instance, the pore sizes can range from 1nm to 1cm for concrete materials. On the contrary, the detected range of a certain experimental technique is limit. For instance, the adsorption method is suitable for microspores. The MIP method is good at large microspores and mesoporous. Image analysis is often used for macrospores. Moreover, these experimental methods have inherent drawbacks that may affect the accuracy of the tested results.
- Many of the techniques used to determine the pore structure parameters require pre-treatment of the specimen, such as pre-drying. It has been robustly proved that the drying procedure alters the microstructure of porous material by declining the capillary interface in interlayer pores and the gel pores [40]. However, the capillary interface is the object of our research; removing the water will disturb the in-situ profile of the microstructure, which contradicts the target of our research.
- In addition to the pre-treatment conditions, some experiments will disturb or even destroy the specimen during the implementation. For instance, the MIP method may need high pressure to force the mercury into the small pores. However, the partition of pores may too fragile that damaged by the pressure.

Since the pore structure is heterogeneous and anomalous morphology in pore sizes, it is hard to describe it in full range by a certain experimental method. Therefore, many researchers have resorted to probabilistic models in the assessment of pore size distribution. In the next section,

we will review some probabilistic methods commonly used in characterizing pore size distribution in porous materials.

1.2.2.3 Probabilistic Methods for Pore Structure

The earliest fitting results for the pore size distribution and the probabilistic model has been presented by Hatch et al. [41]. It has been indicated that the size-frequency distribution curve obeys a lognormal distribution. As shown in figure 1.4, the median size is $4.5\mu\text{m}$ for both samples, sample D has a uniform and small pore size distribution, and sample A3 shows irregular and larger pore size distribution. From this example, it can be found that porous materials having the same median pore size (or the so-called average pore size) may have significantly different pore size distribution. Moreover, although the most straightforward approach in analysis porosity data is an average pore size, this approach may fail to quantitatively describe the influence of pore size distribution in terms of different pore size classifications. Thus, a general form of function that is used in describe the pore size distribution will also be needed in this research, among them, a statistical representation of pore size distribution model should be a good choice both in mathematical implementations and as well as standpoint of evolution of pore structures.

Several probability distribution laws can be used to describe the pore size distribution in porous materials, including Raleigh-Ritz (R-R) distribution, Weibull distribution, normal distribution, and lognormal distribution [42]. Hou et al. [43] adopted these probabilistic distribution laws to describe the pore size distribution for cementitious materials. After comparing the fitting results with the simulated results obtained by these four probabilistic models, the lognormal distribution is proved to be the best with the highest correlation coefficients to approximate the pore size distribution for cementitious material.

Many reports have devoted in adopting lognormal distribution to describe the pore size distribution of porous materials. Diamond et al. [44] proposed a generalized lognormal model to describe the pore size distribution for cement pastes with different water-cement ratios and curing time. The results revealed that the intruded pores obeyed a single lognormal distribution, and no evidence for the existence of a bimodal distribution curve was found. In 1989, Shi et al. [45] created a mixture model of two lognormal distributions to describe the evolution of pore size distribution induced by the cement hydration process. This work showed the possibility of describing the evolution of pore size distribution due to the curing time for cementitious materials. It can also be used to predict the pore sizes of cementitious materials at any age. In 1991, Shi et al. [46] even proposed a mixture model of three lognormal distributions to fit pore distribution over the range of sizes extending four orders of magnitude from 1nm to $10\mu\text{m}$. These three sub-distribution were associated with coarse pores, capillary pores, and gel pores, respectively. In 1993, Holly et al. [47] studied the permeability of cement paste relating to the pore size distribution by using unimodal and bimodal lognormal distributions (one sub-distribution represented the gel pores and the other sub-distribution represented the capillary pores) of pore sizes. The results implied that the cement pastes with the same average pore size and porosity but different pore size distributions can lead to different permeability. In 2013, Chen et al. [48] compared the existing models of the pore size

distribution for cement-based materials with the test results by the MIP method. It was turned out that among the existed five models, the model of mixture lognormal distributions proposed by Shi et Brown [46] showed the best fitting agreement with experimental results. In 2019, Jiang et al. [49] adopted a mixture model of three lognormal distributions for the pore sizes: gel pores, small capillary pores, and large capillary pores in cementitious materials. By adopting this method, the water vapour sorption hysteresis was simulated and evaluated.

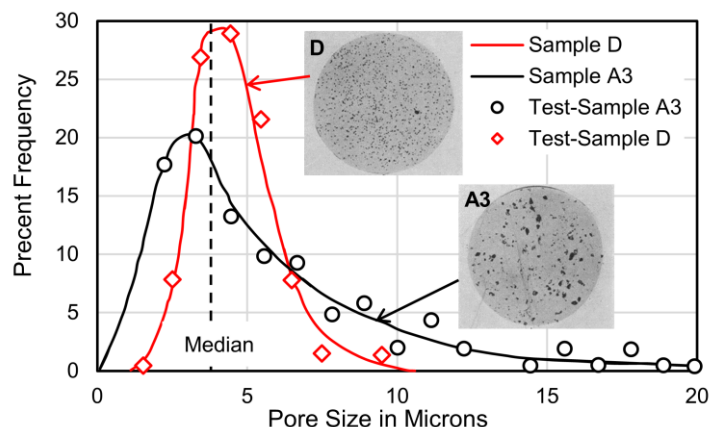


Figure 1. 4 Fitting results for the size-frequency distribution of sample A3 and D. [41]

In this research, the lognormal distribution is adopting to describe the initial pore size distribution before salt precipitation and dissolution. The lognormal distribution has the physical basis that it describes the multiplicative process. For instance, cement hydration may be regarded as a subdivision of void space during which hydration products divide the large voids between particles into small pores [46]. Moreover, the lognormal distribution has a distinct advantage: it defines only positive pore radii ranging from 0 to $+\infty$, in contrast to the standard normal (Gaussian) distribution that contains negative values [50].

1.3 Deteriorations in porous materials

Deteriorations in porous materials is a wide-range topic that refers to many kinds of physical and chemical processes. This section will summarise several deterioration factors that are very common inducements as the durability related problems.

1. Carbonation of concrete.

Carbonation is a neutralizing process, during which the chemical reaction of $\text{Ca}(\text{OH})_2$ in cement hydration products with CO_2 forms CaCO_3 and water [51]. With the intrusion of CO_2 , the PH will decrease, which perturbs the alkaline environment and destroy the passivity of rebar. Consequently, corrosion will happen to the embedded reinforcement bars. However, according to the research in [52], carbonation also affects the durability of plain concrete. The formation of CaCO_3 changes the permeability of concrete due to the alterations in porosity (the volume of hydrates increases and the porosity decreases). Meanwhile, the carbonation rate depends on the porosity and moisture content of the concrete [51–53]. Therefore, carbonation alters the pore structure and further affects the transport properties such as

permeability and diffusivity. Thus, to a large degree, it can be said that carbonation is a closely related pathogen agent to the durability of porous material.

2. Calcium leaching.

Calcium leaching is another common corrosion factor that involves the transport of species out of the materials. Calcium leaching is a diffusion-dissolution-driven process that requires a high water content to support the soluble constituent dissolve in the porous solution of the matrix [54–56]. Furthermore, the concentration gradients between the pore solution and the external environment cause the diffusion of calcium ions from the pore solution to the surrounding water [57]. As a result, the dissolution of solid components (C-S-H) will weaken the structure of porous materials through the porosity increase and mass loss induced by calcium leaching, as is shown in figure 1.5. Therefore, it reveals that leaching affects the durability of porous materials by altering the pore structure.

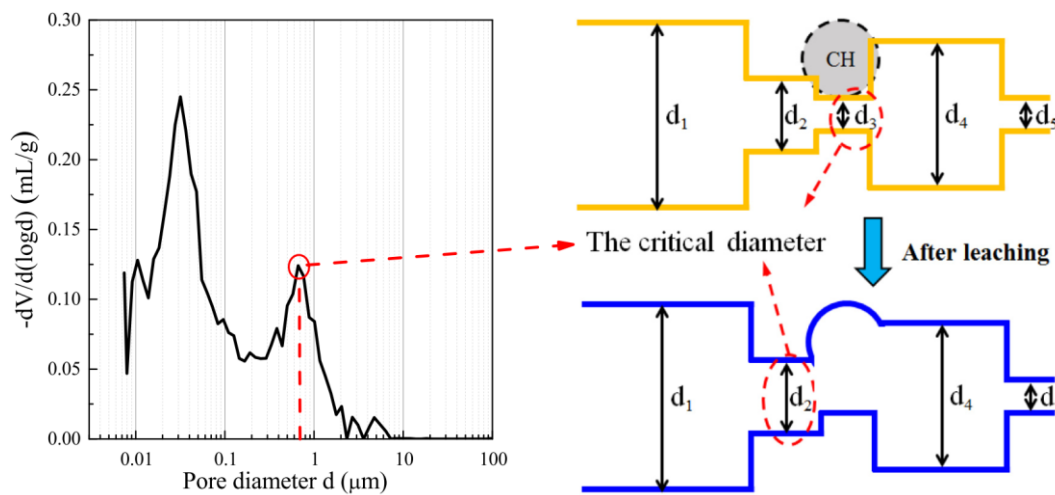


Figure 1. 5 Schematic for the pore structure altered by calcium leaching.[57]

3. Freeze-thaw damage.

Frost damage has a strong link with porosity and pore size distribution. Large pore size is responsible for frost damage within porous material because large pores significantly affect the freeze-thaw procedure than small pores [58]. On the one hand, the freeze-thaw damage alters the pore structure by generating new pore spaces with uniform cracks induced by ice. As a consequence, the transport properties such as water absorption and electrical conductivity increase two to three times with freeze and thaw damage [59]. On the other hand, the frosted-induced cracks allow additional water to fill the cracks, and more ice will be formed in the subsequent cycles, which induces a more significant cracking [57]. It can be found that freeze-thaw cycles influence the durability of concrete by the alteration of pore structure.

4. Salt crystallisation.

Salt crystallisation is recognized as one of the most notorious deterioration factors responsible for the degradation of porous materials [60]. As water evaporates, saline water from environment intrudes into porous materials through the capillary suction or diffusion effects (see figure1.6). The saline solution becomes supersaturated when the concentration of pore solution is larger than the threshold value. Consequently, salt precipitates on the surface of

porous materials (efflorescence), influencing the appearance of porous materials [1,2,5]. Even worse, crystallisation occurs within pore space (subflorescence) and generates crystallization pressure on pore walls. Once crystallisation pressure exceeds the tensile stress of porous material, cracks occur on pore walls, which is the most destructive for porous materials [61–63].

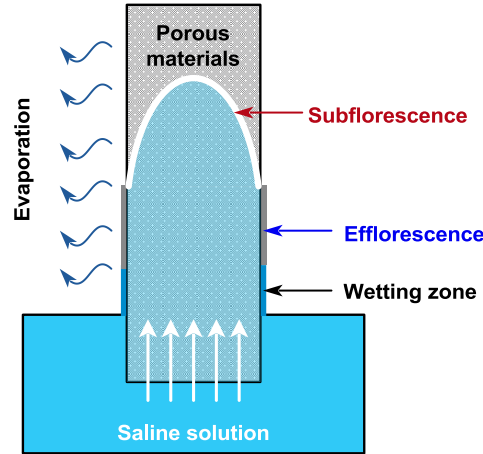


Figure 1. 6 Schematic for salt precipitation inside porous materials (subflorescence) and on the surface of porous materials (efflorescence).

Crystallization pressure can be determined by the equation proposed by Correns (see equation (1.7)). When the crystallization pressure is out of the range of the stress threshold of the solid skeleton, the pressure releases by cracking of pore structure. When porous materials undergo repeated salt precipitation, cracks propagate, and the degradation process is accelerated.

$$P = \frac{RT}{V_{salt}} \ln \left(\frac{C_{salt}}{C_{sat}} \right) \quad (1.7)$$

where R is the ideal gas constant; T is the absolute temperature; V_{salt} is the molar volume of salt crystallisation, C_{salt} and C_{sat} are the actual and saturated concentrations of the salt solution, respectively.

On the contrary, when porous materials are rewetted again, water adsorbs on the surface of the pore wall; thus, saline concentration decreases. Consequently, crystallisation dissolves into the unsaturated solution again. Repeated precipitation/dissolution cycles affect the durability of porous materials by changing the pore structure and transport properties of materials [7,64]. It should be emphasised that salt precipitation and dissolution and the involved transport manner are two main research objectives of this thesis.

It can be concluded that the deteriorations stated above, including carbonation, calcium leaching, freezing-thaw cycles, and salt precipitation and dissolution, strongly affect the geometrical structure of porous materials. However, characteristics of pore structures are not sufficient to provide an overall criterion for the durability of porous materials. Fluids transport processes are of equal importance. For instance, the more permeable the material, the more the aggressive species can penetrate and generate potential damages [33]. Thus, porous structure and transport properties are two essential factors in evaluating the durability of

porous materials.

1.4 Reactive transport in porous materials

When porous materials such as cement-based materials are exposed to aggressive environment, water and ions transport through the materials by capillary suction. Such processes may cause deteriorations, including carbonation and chloride penetration, which significantly influence the service life of materials. Thus, it is of obvious importance with respect to specific durability considerations including the transport of water and ions through porous materials. In general, water and ions transport is a combination of physical and chemical processes, which always involves chemical reaction and transport of chemical species. Moreover, transport varies with the moisture saturation of porous materials, therefore, it is difficult to describe these processes precisely, although a number of reasonable models has been proposed [49,64–71].

In this research, water and ionic transport accompanied by salt precipitation and dissolution are numerically investigated. First, common models for water/ionic transport and chemical reactions are investigated in this section, respectively.

1.4.1 Transport models

Fluid transport is a vital factor in estimating the durability when porous materials have a risk of being damaged by sulphate intrusion, salt deterioration, frost destroy and other problems that affect the durability of materials [72]. Many models [65–67,73,74] have been developed to deal with transport within porous materials in the past. Here, we recall several modelling approaches describing transport problems in porous materials.

1. Macroscopic description of flow based on Darcy's law.

Darcy's law is widely used for fluids transport (limited to slow, viscous flow) in porous materials. Darcy's law gives a simple relationship between the instantaneous discharge rate through a porous medium, the viscosity of the fluid, and the pressure drop over a given distance [13]:

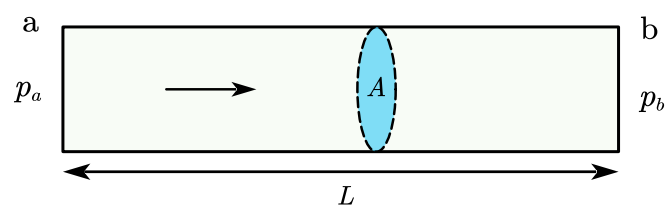


Figure 1. 7 Simple Darcy flow through a homogeneous material induced by pressure gradient.

$$Q = \frac{-K_0 A (p_b - p_a)}{\eta L} \quad (1.8)$$

where Q is the total discharge, K_0 is the inherent permeability of the material, A is the

cross-sectional area of the flow, $p_b - p_a$ is the total pressure drop, η is the viscosity and L is the length over which pressure drop is occurring.

2. Transport models for pure water

The general water transport model incorporates the coupled movement of liquid water, water vapour, and dry air at the macroscopic scale. The porous materials can be represented by a set of differential equations in time and space with the mass balance of liquid water (l), water vapour (v), and dry air (a) [74]:

$$\frac{\partial(\rho_l \phi S_l)}{\partial t} = - \text{div} Q_l - \mu \quad (1.9)$$

and

$$\frac{\partial[\rho_v \phi (1 - S_l)]}{\partial t} = - \text{div} Q_v + \mu \quad (1.10)$$

and

$$\frac{\partial[\rho_a \phi (1 - S_l)]}{\partial t} = - \text{div} Q_a \quad (1.11)$$

where ρ_i is the mass density of each component ($i = l, v, a$), and S_l is the water saturation degree, μ is the rate of liquid water mass changing into vapour per unit volume of porous material, and Q_i is the flux of component i .

According to the generalized Darcy's law, the flux of liquid water can be expressed as:

$$Q_l = - \rho_l \frac{K_0}{\eta_l} k_{rl}(S_l) \nabla p_l \quad (1.12)$$

where K_0 is the intrinsic permeability of the porous material, p_l is the liquid water pressure, η_l is the dynamic viscosity of liquid water and k_{rl} is the relative permeability of the liquid water.

The flux of water vapour and dry air can be expressed as [72,74]:

$$Q_i = - \rho_i \frac{K}{\eta_g} k_{rg}(S_l) \nabla p_g - \frac{M_i p_{atm}}{RT} f(\phi, S_l) D_{va} \nabla \left(\frac{p_i}{p_g} \right) \quad (1.13)$$

where $i = v, a$, η_g is the dynamic viscosity of gaseous phase and k_{rg} is the relative permeability of the gaseous phase, R is the ideal gas constant, T is the absolute temperature, M_i is the molar mass of component i , $f(\phi, S_l)$ is the resistance factor of gas diffusion, and D_{va} is the free water vapour diffusion coefficient in the air.

The capillary pressure p_c is defined as the difference between the gas pressure and the liquid water pressure:

$$p_c = p_g - p_t \quad (1.14)$$

This model can be used in numerical simulation for transport involving dry air, water vapour, and pure water in porous materials. The presence of dissolved ions are not considered in this model.

3. Transport models for saline solution

Samson et al. [75] proposed a solid, liquid, and gaseous transport model by adopting the homogenization technique. This model considers the interactions between ions and ions or the ions and solvent in the porous solution, different from the pure water transport model stated above.

The application of the mass conservation equation for ionic species diffusion in the liquid phase is given as:

$$\frac{\partial(c_j)}{\partial t} + \text{div}(J_j) = 0 \quad (1.15)$$

where c_j is the concentration of the j th ionic species in porous solution and J_j is the flux of the same species in the liquid phase.

According to the extended Nernst-Planck equation, the ionic diffusion term can be described as:

$$J_j = -D_j^\mu \nabla(c_j) - \frac{D_j^\mu z_j F}{RT} c_j \nabla(\Psi) - D_j^\mu c_j \nabla(\ln \gamma_j) \quad (1.16)$$

where D_j^μ is the diffusion coefficient of the j th ionic species, F is the Faraday constant (C/mol), z_j is the valence of the j th ionic species, γ_j is the chemical activity coefficient of the j th ionic species in the porous solution, which can be determined by various mathematical equations [71], and Ψ is the diffusion potential set up by the drifting ions.

The local potential can be calculated based on the Poisson equation:

$$\nabla^2 \Psi - \frac{\rho}{\varepsilon} = 0 \quad (1.17)$$

where ρ represents the electrical charge density and ε is the dielectric constant of the medium. The electrical charge density can be derived as:

$$\rho = F \sum_{j=1}^N z_j c_j \quad (1.18)$$

For dilute pore solution, the effect of chemical activity can be neglected, thus the extended Nernst-Planck equation can be expressed as:

$$J_j = -D_j^\mu \nabla(c_j) - \frac{D_j^\mu z_j F}{RT} c_j \nabla(\Psi) \quad (1.19)$$

This model is a straightforward application for the Nernst-Planck equation, allowing one to calculate the concentration and potential profiles for very complex transport cases based on the averaging of the conservation law and constitutive equation at the microscopic scale [75]. This one-dimensional model can also be extended to two-dimensional cases.

1.4.2 Reactive transport models

The investigation of reactive transport (water and ionic transport coupled with chemical reactions) is essential because when porous materials are exposed to an aggressive environment, the transport process will facilitate the ingress of contaminants in porous materials. In natural conditions, ionic transport is often accompanied by chemical reactions [71,76]. Thus, reactive transport has been widely regarded as a crucial topic related to the durability of porous materials [77]. Here we introduced several reactive transport models.

1. Samson's model.

Samson's model [68] follows a multi-ionic approach that considers the ionic movement and chemical reactions separately. The ionic transport is described by the extended Nernst-Planck model which has been presented above.

$$\frac{\partial(c_j)}{\partial t} - \text{div}(D_j^\mu \nabla(c_j) + \frac{D_j^\mu z_j F}{RT} c_j \nabla(\Psi) + D_j^\mu c_j \nabla(\ln \gamma_j)) = 0 \quad (1.20)$$

After solving the transport equations, the chemical equilibrium between the ionic concentrations and the solid phases of the hydrated cement paste is locally maintained. The chemical reactions under the local equilibrium assumption is given as:

$$K_m = \prod_{j=1}^N c_j^{v_m} \gamma_j^{v_m} \quad \text{with} \quad m = 1, \dots, M \quad (1.21)$$

where M is the number of solid phases, N is the number of ions, K_m is the equilibrium constant of the solid m , c_j is the concentration of the j th ionic species, γ_j is the chemical activity coefficient, and v_m is the stoichiometric coefficient of the j th ionic species in the m th chemical reaction.

2. Reeves's model.

Reeves's model [78] studies multicomponent mass transport with equilibrium chemical reactions. The transport equations of the N_c components and the N_x complexes are expressed as:

$$\frac{\partial(\phi c_j)}{\partial t} + \text{div}(c_j \tilde{q}) = r_j^c \quad j = 1, \dots, N_c \quad (1.22)$$

and

$$\frac{\partial(\phi x_i)}{\partial t} + \text{div}(x_i \vec{q}) = r_i^x \quad i = 1, \dots, N_x \quad (1.23)$$

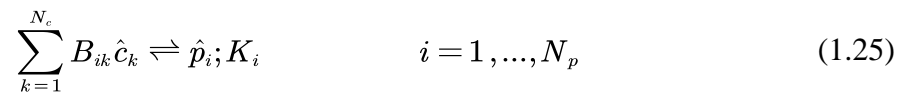
where c_j is the concentration of the j th component, x_i is the concentration of the i th complex, \vec{q} is the species discharge, r_j^c is the accumulation rate of the moles of the j th component, r_i^x is the accumulation rate of moles of the i th complex due to precipitation and dissolution, ϕ is the porosity of porous materials.

The chemical constituents may exist as immobile precipitates. The continuity equation for the immobile species N_p implies:

$$\frac{\partial(\phi p_i)}{\partial t} = r_i^p \quad i = 1, \dots, N_p \quad (1.24)$$

where p_i is the concentration of the i th precipitate, r_i^p is the accumulation rate of moles of the i th precipitate.

By assuming that dissolution of solids occurs in reaction with the components as products, chemical reactions can be expressed as:



where \hat{c}_k is the chemical formula for the k th component, B_{ik} is the stoichiometric coefficient for the k th component in the i th chemical reaction, \hat{p}_i is the chemical formula for the i th precipitate, K_i is the equilibrium constant for the i th chemical reaction.

According to the law of mass action, the chemical reactions under the local equilibrium assumption is given as:

$$K_i = \prod_{k=1}^{N_c} c_k^{B_{ik}} \quad \text{with} \quad i = 1, \dots, N_p \quad (1.26)$$

3. Miller's model.

Miller's model [79] assumes a chemical equation in which the formation of the complex $B_i^{n_{ci}}$

in the porous solution phase from a basis set of species $A_j^{n_j}$:

$$K_i = \gamma_{ci} m_{ci} \left(\prod_{j=1}^{N_s} (\gamma_j m_j)^{a_{ij}} \right)^{-1} \quad (1.27)$$

where m_{ci} is the molar concentration of the complex $B_i^{n_{ci}}$, γ_j is the activity coefficient of

the j th ionic species and m_j is the molar concentration of the j th ionic species, a_{ij} is the stoichiometric coefficient of the j th ionic species in the i th reaction.

The total concentration of each basic species present in the porous solution is given as:

$$c_j = m_j + \sum_{i=1}^{N_c} a_{ij} m_c \quad (1.28)$$

Based on the mass balance of the chemical species for the porous fluids, the one-dimensional transport c_j is written as:

$$\frac{\partial c_j}{\partial t} - D \frac{\partial^2 c_j}{\partial x^2} + v \frac{\partial c_j}{\partial x} = 0 \quad (1.29)$$

where D is the diffusion coefficient of the j th ionic species, v is the actual fluid velocity.

1.4.3 General methods for solving reactive transport models

According to the models above, it can be concluded that the chemical reactions are expressed as a set of non-linear algebraic equations based on the law of mass action (with the assumption of a local equilibrium state). The ionic transport governing equations, describing the mass conservation equations of ionic species, are a set of partial differential equations. There are three general approaches for solving the coupled system of chemical reactions and ionic transport. The first is the coupled method in which algebraic and partial differential equations are solved together (which is the abbreviation of DEA). The second one is the one-step method that directly substitutes the chemical equation into the transport equations (which is the abbreviation of DSA). The third method is the so-called two-step method that split algebraic equations and partial differential equations and solve these two items, respectively (which is the abbreviation of OSA). The schematic of the methods for solving the reactive transport equations can be found in figure 1.8.

Yeh et al. [77] have suggested that DSA and DEA are appropriate for one-dimensional investigation. OSA model required the fewest constraints on computer resources in terms of the central processing unit (CPU) memory and CPU time, which are suitable for two- and three-dimensional problems. Walter et al. [80] developed a numerical model for reactive transport based on the OSA, and the computational results showed that for the reactive transport with the assumption of local equilibrium, the sequential non-iterative approach (SNIA) is efficient enough to simulate the problem. Xu's research [81] showed that DSA is high accuracy and quadratic rate of convergence. However, it has high requirements of computing time and memory. It has also been pointed out that for chemical reactions with entirely local equilibrium, especially for mineral dissolution/precipitation problems, the SNIA is more efficient than the sequential iterative approach (SIA), which requires about half the CPU time of SIA. Correspondingly, the numerical solutions obtained by SNIA are less accurate than SIA (which contain more numerical dispersion). Carayrou et al. [82] reviewed the OSA for numerical modelling of reactive transport by developing analytical solutions of

the mass balance in porous materials. The results reveal that the estimated errors do not depend on the technique used to solve each operator but on the splitting method itself. In addition, the lattice Boltzmann method [83,84] is also a powerful technique for solving reactive transport problems.

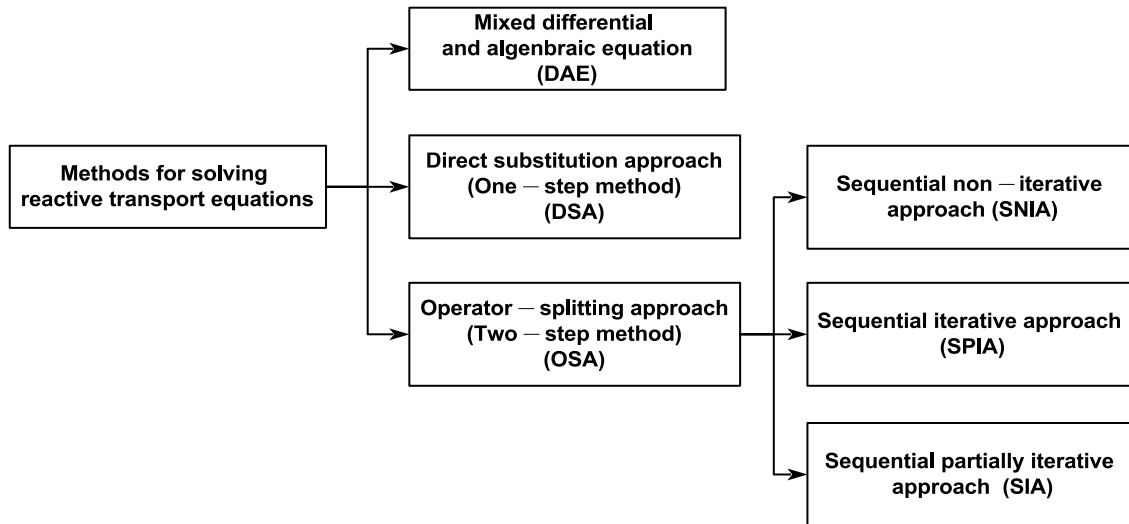


Figure 1. 8 Schematic of the methods for solving the reactive transport equations.

In our research regarding the relative transport model in chapter 3, OSA is adopted to solve the water-ionic transport coupling with chemical reactions equation. First, the ionic concentration and water saturation degree involving the transport process are derived. After that, the concentration of the pore solution is calibrated by chemical reactions. If the equilibrium is perturbed, precipitation/dissolution occurs to modify the concentration. Then the modified concentration will be the inputs of the next transport process. Such an implementation is repeated until the convergence condition is attained.

1. 5 Transport properties

Transport properties are crucial indications for characterizing the migration and penetration of water and other chemical fluxes through porous materials, which are fundamental properties closely related to the microstructure of porous materials. For concrete materials, it is well recognized that both total porosity and its distributions determine the permeability, and only pores with radius greater than a specific value contribute significantly to permeability [47]. To a large degree, developing a good permeability model strongly depends on the representative microstructure of porous materials that gives realistic pore size distribution [85,86].

1.5.1 Experimental investigations on permeability

The experimental methods measuring the permeability of porous materials can be divided into two sorts. The first is the direct method, which monitors the steady flow through saturated specimens under a hydrostatic pressure gradient [42]. Another method is the indirect method, which is very commonly used. This method is the combination of experiments and analytical

modelling methods, in which permeability is estimated through the theoretical analysis like the Katz-Thompson model, and pore characteristics are derived from the experimental methods, including MIP, SEM, and NMR techniques [87].

However, experimental investigation on permeability has unavoidable disadvantages. First, as the commonly used fluids in permeability tests, the penetrated water may lead to dissolution of hydrated cement phases, causing the redistribution of the soluble phases. Consequently, the pore structure and, thus, the permeability can be affected [85,88]. Second, the pre-treatment of specimens strongly influences permeability. For instance, drying process may cause micro-cracks in the samples, and as a result, the permeability is altered [89]. The third disadvantage, which is ubiquitous to essentially all permeability measurements, is that specimens having a rather low-permeability material are saturated only with great difficulty. [86]. All of these influencing factors make permeability measurements difficult.

1.5.2 Modelling investigations on permeability

Many modelling approaches have been developed to predict the permeability of porous materials, which can be classified as empirical modelling methods, analytical modelling methods, network modelling methods, probabilistic modelling methods and computational modelling methods. In this section, several commonly used methods for description of permeability modelling will be introduced.

1. Mehta - Manmohan model.

This is an empirical model that considers porous material microstructure as the basis of development. By assuming simple Hagen-Poiseuille flow in the capillaries, we have [90]:

$$K_0 = \exp(3.8V_1 + 0.2V_2 + 0.56 \times 10^{-6}TD + 8.09MTP - 2.53) \quad (1.30)$$

Where K_0 is the intrinsic permeability of the material, V_1 and V_2 are pore volumes in the >132nm and 29nm-132nm range, respectively. TD is the threshold diameter, and MTP is the total pore volume divided by the degree of hydration.

2. Carman - Kozeny model.

This model is based on Poiseuille's law, and the intrinsic permeability can be given as [91,92]:

$$K_0 = - \frac{\phi(V/S_{pore})^2}{2\lambda} \quad (1.31)$$

where V is the pore volume, S_{pore} is the internal surface area of pore space and λ is the tortuosity of the conducting channels.

3. Katz -Thompson model.

Another commonly used analytical model for predicting permeability is the Katz-Thompson model, in which the intrinsic permeability is expressed as [93]:

$$K_0 = \frac{1}{226} \frac{\sigma}{\sigma_0} l_c^2 \quad (1.32)$$

where l_c is the representative length of the pore, σ is the electric conductivity of the saturated porous material and σ_0 is the conductivity of the solution in the pore.

However, these two models do not consider the pore size distribution of porous materials, which may induce a noticeable difference between modelling and experimental results. Thus, improved models for permeability are reviewed which considers the pore structure by adopting the probabilistic porous network model.

4. Millington's model.

This model is developed by Millington and Quirk in 1961[94]. By considering the porosity and pore size distribution, the permeability for porous materials can be expressed as:

$$K_0 = \frac{1}{8} \frac{\phi^{4/3}}{\phi^2} 2 \int_0^\phi d(\phi - \phi_r) r^2 (\phi - \phi_r) \quad (1.33)$$

where ϕ is the overall porosity of the porous material, r is the equivalent radius of the pores, ϕ_r is the partial porosity for the pores with radius $< r$. Permeability calculated by this model depends on several factors: the isotropy of pore distribution and the random distribution of pore sizes in porous materials.

5. Mokhtar's model

This is a network model, in which the pore sizes are considered as regular shapes that combine with the simple geometrical rules and obey basic statistical laws. The permeability is deduced from computer simulations based on the porous network. Mokhtar et al. [95] proposed a permeability model based on a two-dimensional network of tubes with the lognormal pore size distribution, which is expressed as:

$$K_0 = \sum_{j=1}^N e^{6\xi_j^2} \frac{\varepsilon_{pj} R_{pmj}^2}{8} \quad (1.34)$$

where N is the number of "peaks" for pore size distribution, ε_{pj} is defined as the elementary porosity for each sub-distribution of pore sizes. For each peak j , the following parameters can be defined:

$$\xi_j = \frac{\varepsilon_{pj}}{\alpha_j \sqrt{2\pi}} \quad (1.35)$$

and

$$R_{pmj} = \frac{R_{pmaxj}}{e^{2\xi_j^2}} \quad (1.36)$$

where α , R_{pmax} are experimental parameters of pore size distribution from the MIP test.

This model shows the effects of pore size distribution on permeability. Moreover, it can be observed that by adopting a multi-distribution of pore size, this model present an analytical manner for permeability calculation on the basis of all types of pores.

6. Amiri's model.

Another network model is proposed by Amiri et al. [89], in which a permeability model based on the tri-dimensional cubic porous network is developed. Amiri's model considers the pore size distribution, the tortuosity, critical pore radius, and constrictivity. The analytical expression is given as:

$$K_0 = \frac{\delta \varepsilon_p}{24\tau^2} R_n^2 \quad (1.37)$$

where ε_p is the porosity, τ is the tortuosity, δ is the constrictivity factor and R_n is the critical pore radius for each sub-distribution of pore size. For Amiri's research in [89], there are three categories of pores: macro-pores ($R > 50\text{nm}$), meso-pores ($3\text{nm} < R < 50\text{nm}$) and micro-pores ($R \leq 3\text{nm}$).

7. Koichi's model.

Koichi [42] gave a probabilistic model for permeability. First, a steady-state laminar flow is assumed and pores are considered as a bundle of straight capillary tubes, thus, the total flow through the porous material can be expressed as:

$$Q = - \left(\frac{1}{8\eta} \int_0^\infty r^2 \Omega_A dr \right) \frac{dP}{dx} \quad (1.38)$$

where η is the fluid viscosity, Ω_A is the average aerial distribution function of pores exposed on any arbitrary face cut perpendicular to the flow, such that the total aerial porosity ϕ_A is equal to the term $\int \Omega_A dr$, dP/dx is the fluid pressure gradient.

Based on equation (1.38), the modified expression for total flow through the porous material can be extended as follows:

$$Q = - \left(\frac{1}{8\eta} \int_0^\infty \int_0^\infty K r_{eq}^2 dA_a dA_b \right) \frac{dP}{dx} \quad (1.39)$$

where K is a parameter depends on the geometrical characteristics of the porous material, dA_a and dA_b are aerial porosity of the pores with radius r_a and r_b .

After simplifying equation (1.39) and combining it with Dacy's law, the intrinsic permeability can be expressed as:

$$K_0 = \frac{1}{8} \left(\int_0^\infty r dA \right)^2 \approx \frac{\phi^2}{50} \left(\int_0^\infty r dV \right)^2 \quad (1.40)$$

where $dV = ndA/\phi$ is the incremental normalized volumetric porosity. It can be found that in this model, the permeability is only related to the porosity and pore size distribution of porous material. The pore size distribution can usually statistically represent by the probabilistic model, such as Rayleigh-Ritz distribution in [6,42,96].

Moreover, there are some computational modelling approaches for permeability, which are based on the 3D representation for the microstructure of porous materials, such as the CEMHYD3D model and HYMOSTRUC3D model [87], in which the connectivity of the transport path is considered explicitly. By varying different geometric aspects of the network and evaluating the corresponding effects on the water flow, the relation between pore structure and transport properties can be build up. It should be emphasized that the permeability model developed in this research is on Koichi's model, which will be introduced in chapter 4.

1.5.3 Water sorption isotherm

When porous materials are exposed to the vapour of wetting fluid, water molecules will adsorb or desorb in the pore space due to the varying relative humidity. The van der Waals forces are the main factors acting the interactions between the liquid water and vapour [97]. The smaller the capillary pore size, the higher the van der Waals interactions between water molecules and pore walls. Therefore, the adsorbed water first fills the smaller capillary pores at the given relative humidity. As the relative humidity increases, the water absorbs in the larger capillary pores. Thus, according to the Young-Laplace equation and Kelvin's equation, the water adsorption process is inversely proportional to the capillary pore size, and capillary pressure is also inversely proportional to the capillary pore size.

Water sorption isotherm can be adopted to describe the pore size distribution in porous materials [98]. As shown in figure 1.9, when the relative humidity is low, water condenses in smaller pores. The larger pores are gradually filled as the relative humidity increases. When the relative humidity reaches the maximum value (as one), the maximum pore size is filled with water at the end of the water adoption process. Thus, the water saturation degree is equal to one. Each relative humidity value can correspond to the pore size determined by the capillary pressure during the adsorption process according to the Young-Laplace equation and Kelvin's equation. If the porous material is totally dried before the water adsorption process, thus the total volume of adsorbed water in the porous material should be the total volume of pores that can be invaded. In this way, the cumulative pore volume of porous material can be derived from the water sorption isotherm with the relative humidity varying from zero to one.

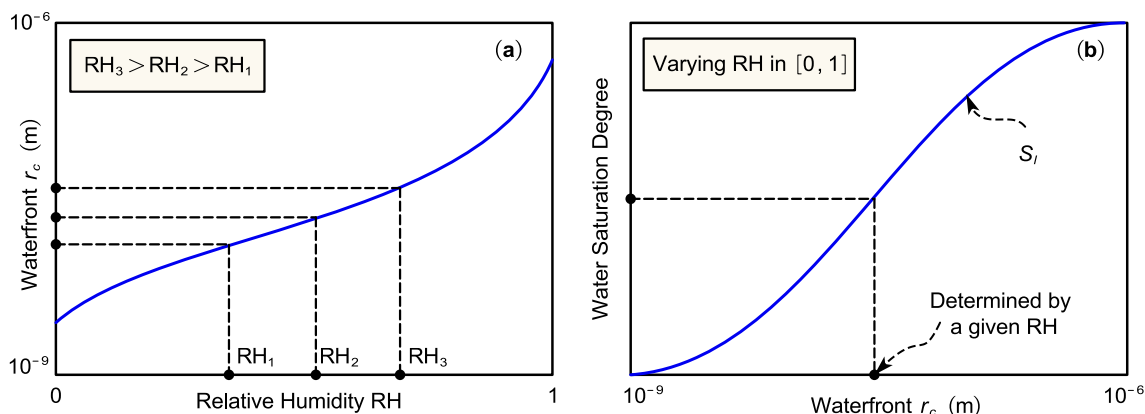


Figure 1. 9 Schematic for the water sorption isotherm.

In our research, the pore size distribution can be represented by the probability density function $P(r)$. Based on the water sorption isotherm, if we integrate the probability density function over the range from zero to the pore radius r_c determined by the relative humidity, thus we can obtain the corresponding water saturation degree as:

$$S_l = \int_0^{r_c} P(r) dr \quad (1.41)$$

1. 6 Conclusions

In this chapter, two fundamental indications for characterizing the pore structures are introduced, including the porosity and the pore size distribution. Meanwhile, several experimental methods for characterising pore structures are reviewed and compared. To be concluded, it is hard to describe in full detail by certain experimental methods because the pore structure is heterogeneous and anomalous in morphology. Thus, several probabilistic models are introduced in describing pore size distribution. It is proved that probabilistic method should be the best choice when experimental measurements of pore sizes are challenged. Finally, the lognormal distribution is determined to evaluate the initial pore size distribution in this research.

Second, several common deterioration factors that may affect pore structures in porous materials are reviewed. It is found that those deteriorations also affect the durability of porous materials by altering the transport processes in porous materials. Moreover, the transport properties, such as permeability, are of equal importance in evaluating the durability of porous materials.

We also give a glimpse of transport models that describe the movement of pure water and saline solution separately. Moreover, reactive transport models consisting of water-ionic transports and chemical reactions are reviewed. It is essential because ionic transport often accompanies chemical reactions for porous materials in natural conditions. Reactive transports

have a strong link with the durability of the porous material. Thus, developing a reactive transport model is one of the main objectives of our following research. Finally, some computational methods for solving the reactive transport models are introduced and compared. It is concluded that the operator-splitting method is the most efficient with the least time-consuming, which will be adopted to solve our reactive transport model in this research.

Finally, methods for evaluating permeability in porous materials are summarised from the experimental and numerical modelling perspectives. It is found that experimental methods have limitations that are not sufficient to capture the evolution of transport properties during reactive transport processes. Therefore, it is essential to develop an analytical model to estimate the permeability of porous materials. This will potentially contribute to the assessment of the durability of porous materials.

Chapter 2

Probabilistic Approach of Pore Structure Evolution Induced by Precipitation and Dissolution

2.1 Introduction

Pore structure of a construction material is an intrinsic property which is closely related to durability and service life of building structures. Salt precipitation and dissolution are notorious deteriorating factors of construction materials, particularly the materials with highly interconnected pores which facilitate transport of moisture and aggressive chemical species [6,99]. Salt precipitation and dissolution critically alter microstructure of porous materials [100,101]. Nucleation and propagation of salt in pore space during salt precipitation generate pressure on the pore wall, which produces fractures on or through the pores [102]. Subsequent salt dissolution increases porosity and accelerates penetration of fluid through the pores, which ultimately reduces durability of construction materials [15,103]. As suggested by George et al. [104] and Coussy et al. [5], salt precipitation and dissolution are generally unavoidable. Thus, understanding the mechanisms by which salt deteriorates construction materials is the key to ascertain durability of these materials. Evaluating modifications on pore structure due to salt precipitation and dissolution is the first step towards attaining such understanding.

Porosity is an overall measure of pore structure, which gives ratio of pore volume to total volume of a porous material. However, porosity does not give any information about pore structure: pore size, shape or distribution [16]. Two porous materials with similar porosity may have entirely different pore structures [53]. Thus, pore size distribution (PSD) needs to be considered when investigating phenomena that modify the pore structure [3].

Salt precipitation and dissolution are strongly affected by water content of porous material [4]. At macroscopic scale, precipitated salt can be observed at the vicinity of drying front (i.e., boundary between saturated and non-saturated zones) inside porous material when specimen subjected to up-taking and drying cycles of saline solution [10]. Even if no explicit experimental evidence exists to the authors' knowledge, the same schema can be adopted at pore scale. Indeed, a given degree of water saturation corresponds to the location of water front at a pore size that coincides with the radius of water capillary meniscus [6]. Therefore, one

may extrapolate that salt precipitation and dissolution occur at the vicinity of waterfront within pore structure [3]. On the basis of this inference, precipitation and dissolution mainly affect pores at close proximity to waterfront. Thus, modifications of pore size may predominantly restrict to a certain pore population with size close to the radius of capillary meniscus. In this case, overall porosity is not sufficient to describe elaborated modifications occurring near the waterfront at pore scale. Thus, detailed evolution of pore size distribution needs to be considered together with overall porosity and water saturation degree.

From experimental point of view, there are several experimental methods dedicated to characterizing both overall porosity and pore size distribution (see Table 2.1) [21,30,38]. However, sample pre-treatments such as sample drying are generally required prior to analysis of pore size distribution when adopting experimental methods [17], which may alter water profile of pore structure. Moreover, some experimental methods are destructive that may damage pore structure of the investigated material [105]. Thus, experimental methods face the dilemma that how to characterise pore size distribution and at the same time allow water-dependent evolution of pore size distribution within porous material. Indeed, no convincing and experimentally verified answer yet exists on quantitative measurement of pore size distribution in the course of salt precipitation and dissolution. For instance, some consider only the behaviour of crystallization relevant to solution properties [8], while others still focus on the study of weight loss and degradation of visual appearance due to salt precipitation [7]. Such studies may generate results that cannot readily be compared with our lack of knowledge concerning quantitative measurement of pore size distribution in the course of salt precipitation and dissolution. Moreover, experimental methods are indeed out of the scope of this research. This research is aiming at proposes a modelling approach in order to describe elaborated evolution of pore size distribution of porous material when subjected to salt precipitation and dissolution.

Table 2. 1 Peculiarities for several common methods for PSD measurement.

Methods	Advantage	Disadvantage
MIP	Easy, fast, provide the PSD nearly covering the whole range of pore sizes.	Pre-drying of the sample, limitation of bottle-ink effect, assumption of cylindrical pore shape, high pressure that may damage the sample.
Nitrogen/water sorption method	Determine the surface and PSD.	Pre-drying of the sample, a quite narrow detected range pore sizes.
SEM	Direct observation without disturbing the sample.	Absence of depiction for tortuosity and connectivity of porous structure, limitation of image resolution.
Nuclear magnetic resonance method	No need for pre-drying, non-destruction for the sample.	Results may be unreliable because of the limited sample's dimension.

Pore size distribution is a complex property that encompasses pore size with several orders of magnitude. Figure 2.1 illustrates a commonly used classification of pores in cement-based material according to the pore radius: gel pores (0.25nm - 5nm), capillary pores (2.5nm - 5µm), and air voids (> 5µm) [28]. Gel pores are generally detected by nitrogen or water

adsorption method. Capillary pores and air voids are evaluated by mercury intrusion porosimetry and image analysis, respectively.

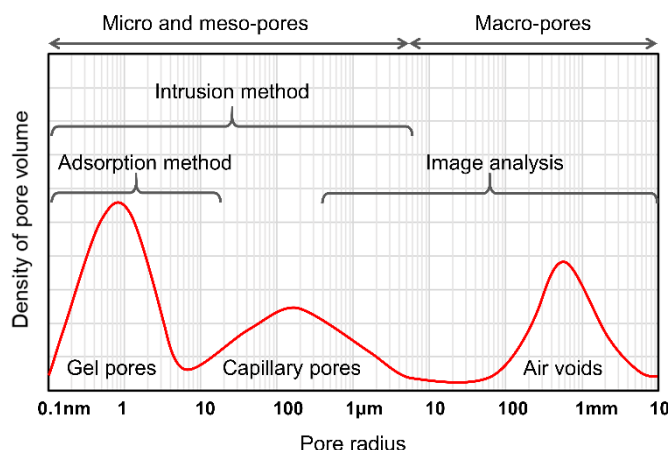


Figure 2. 1 Classification of pore sizes in cement-based material.

In spite of heterogeneities in pore size, pore size distribution obeys a statistical behaviour [106], which indicates that shape of pore size vs. pore size-frequency curve follows a probabilistic model, such as Raleigh-Ritz (R-R) distribution [107], Weibull distribution [108], normal distribution [108], or lognormal distribution [46]. Among these models, lognormal distribution has been reported to yield the most accurate estimation on pore size distribution of cementitious materials [43,48].

The earliest work on fitting lognormal distribution into experimental pore size distribution was presented by Hatch et al. [41] and Austin [109]. In 1971, Diamond et al. [44] developed a generalized lognormal distribution to characterise pore size distribution of cement mortars. In 1991, Shi et al. [46] proposed a multimodal lognormal distribution model to simulate pore size distribution of cement mortars. In 1992, Holly et al. [47] established a porous network model based on multi-lognormal distribution to describe effect of alterations in microstructure on permeability of cement mortars. In 2013, Chen et al. [48] demonstrated that compound lognormal distribution was the most effective among selected statistical models to characterise porous structure. Recently, Jiang et al. [49] adopted a triple-compounded lognormal distribution to predict hysteresis of water vapour sorption in cement-based materials. These literature reports support that lognormal distribution, which is applicable exclusively for positive pore radius, is powerful to model pore size distribution of cement-based materials [50]. Therefore, in this study, we adopted lognormal distribution to describe initial pore size distribution prior to salt precipitation and dissolution.

Based on a premise that initial pore size distribution follows lognormal distribution, this research aims to develop two probabilistic methods to describe modified pore size distribution concerning waterfront induced by salt precipitation and dissolution. The probabilistic methods are achieved by accomplishing the transformation models between pore radius before and after salt precipitation and dissolution. Then two methods are compared by investigating the modified pore size distribution according to the varied porosity. The most appropriate method is determined regarding the performance and physical basis. Finally, successive transformations of pore size distribution and filling or emptying ratio due to the long-term salt

precipitation and dissolution are investigated by adopting the most appropriate method.

This chapter is organised as follows. Section 2.2 introduces two probabilistic approaches for pore size distribution and three transformation models for pore radius. Initial pore size distribution derived by MIP test and subsequent simulation of the experimental data by lognormal distribution are given in Section 2.3. Section 2.4 deals with parametric investigations for evolutions of pore size distribution. Comparisons among probabilistic methods and transformation models are also available in this section. Some conclusions and discussions are given in the last section.

2.2 Probabilistic porous network model

Porous material is regarded as a heterogeneous, multi-phase material (figure 2.2). Solid phase is composed of solid matrix and precipitated salt. Liquid phase is constituted of saline solution with water as the solvent and ionic species as the solute. Meanwhile, dry air and water vapour make up the gaseous phase. In most porous materials, especially cement-based materials, gel pores filled with water constitute a small proportion of pore population [47]. Large pores exist as isolated cavities, and contribute little to fluid transport and chemical reactions [4,110]. While interconnected capillary pores partially filled with water determine permeability and transport property of porous materials [47]. Capillary interface (i.e., water front) which is often located at capillary pores, separates the liquid from gaseous phase. As suggested by Yokoyama et al. [111], quantity of pores exceeding 100 nm in diameter strongly affects the water absorbency, while number of pores smaller than 10 nm in diameter governs moisture content of a porous material, which verifies our hypothesis that liquid-gas interface is located at capillary pores. The capillary pores dominate the water saturation degree in our proposed model.

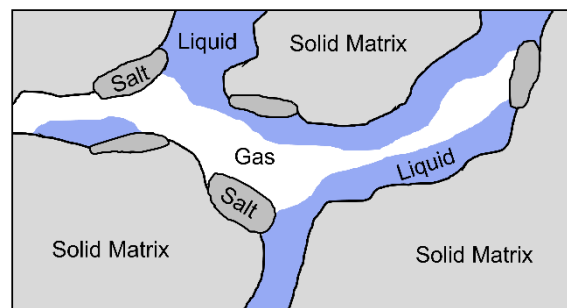


Figure 2. 2 Phases of a porous material.

Salt precipitation and dissolution are one of the most important deteriorating factors of pore structure [112]. Precipitation and dissolution are complex phenomena that involve physical and chemical processes [113,114]. During exposure of porous materials to an aggressive (i.e., high salt concentration) environment (i.e., relative humidity or temperature), soluble salt continuously penetrates the materials by capillary suction[5]. Due to changes in environmental conditions, water evaporates, which increases the concentration of salt near the capillary interface [3,7]. When the concentration exceeds the supersaturation threshold concentration

for precipitation, salt precipitates out of saline solution, nucleates, and grows on surface of pore wall near the waterfront (or the so-called capillary interface) [10,104]. Further changes in environmental condition induce condensation of water vapour inside pores, which dissolves precipitated salt and decreases salt concentration [5]. Salt precipitation and dissolution are a reversible process that repeated occurrence influences integrity of pore structure as stated previously. Therefore, it is essential to make a correlation between microstructure, precipitation and dissolution processes as well as environment conditions.

The primary step of achieving this objective is to develop a model in describing the water-dependent evolution of pore size distribution in the course of salt precipitation and dissolution. However, it should be noted that this research substantially focuses on the morphological development of pore structure itself, the reactive skeleton of porous materials are not involved in this research.

2.2.1 Probabilistic method for pore size distribution

As suggested by Shi et al. [46], initial pore size distribution of porous material is presented as a lognormal probability density function (PDF):

$$P_0(r_0) = \frac{1}{\sigma_r \sqrt{2\pi} r_0} \exp\left[-\frac{(\ln(r_0) - \mu_r)^2}{2\sigma_r^2}\right] \quad (2.1)$$

Correspondingly, the cumulative distribution function (CDF) is given by:

$$F(r_0) = \frac{1}{2} + \frac{1}{2} \operatorname{erf}\left[\frac{\ln(r_0) - \mu_r}{\sqrt{2}\sigma_r}\right] \quad (2.2)$$

where r_0 is initial pore radius, μ_r is location parameter and σ_r is shape parameter.

The PDF must satisfy normalization conditions of probability theory:

$$\left\{ \begin{array}{l} P_0(r_0) \geq 0 \\ \int_0^{\infty} P_0(u) du = 1 \end{array} \right. \quad (2.3)$$

The parameters of function $P_0(r_0)$ are determined by MIP analysis. According to Washburn equation [20], larger pores are filled initially, followed by smaller pores at increasing pressures. Minimum pore radius is determined by maximum pressure imposed on porous materials: the higher is the imposed pressure, the smaller is the detected pore size, and the greater is the cumulated pore volume [115]. Function $1 - F(r_0)$ represents cumulative fraction of pore volume which is occupied by pores with pore radius greater than r_0 .

Initial pore volume fraction of pores with radius ranges from zero to r_0 is expressed with the following function:

$$\phi_0(r_0) = \int_0^{r_0} \phi_0 P_0(u) du \quad (2.4)$$

where ϕ_0 is initial porosity of a representative porous medium. The porosity is defined as a ratio of total pore volume V_p to bulk volume V :

$$\phi_0 = \frac{V_p}{V} \quad (2.5)$$

In this study, the pores are assumed cylindrical and interconnected. Hence, initial volume of pore with r_0 radius is calculated by:

$$v_p^0 = \pi r_0^2 L \quad (2.6)$$

where L is pore length, and L keeps constant because salt precipitation and dissolution affect pore radius rather than pore length.

Due to salt precipitation and dissolution, pore radius changes and we assume that initial pore radius r_0 undergoes erosion on a distance of $\varepsilon(r_0, r_c)$, as shown in figure 2.3 [102]. Accordingly, the relationship between initial pore radius and modified pore radius is represented by transformation function T :

$$T \rightarrow r_1 = f(r_0, r_c) = r_0 + \varepsilon(r_0, r_c) \quad (2.7)$$

where r_1 is modified pore radius after salt precipitation and dissolution, r_c is the pore radius for the capillary interface (or waterfront), $\varepsilon(r_0, r_c)$ is the eroded size of pore, when salt precipitation occurs, $\varepsilon(r_0, r_c) < 0$; when salt dissolution occurs, $\varepsilon(r_0, r_c) > 0$. Function $f(r_0, r_c)$ represents the transformation model of pore radius, which will be illustrated in Subsection 2.2.2.

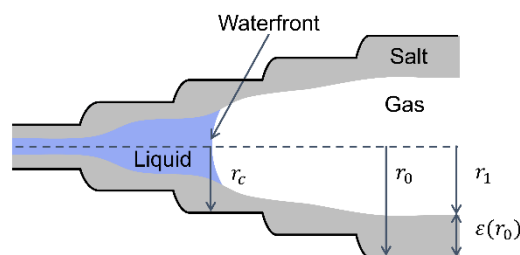


Figure 2. 3 Modification of pore radius due to salt precipitation and dissolution. r_0 = initial pore radius, r_1 = modified pore radius after salt precipitation and dissolution, r_c = capillary pore radius at which waterfront is located, $\varepsilon(r_0, r_c)$ = eroded size of pore.

Under proposed transformation model of pore size, filling and emptying ratio (τ) induced by salt precipitation and dissolution can be expressed as:

$$\tau = \left| \frac{\varepsilon(r_0, r_c)}{r_0} \right| \quad (2.8)$$

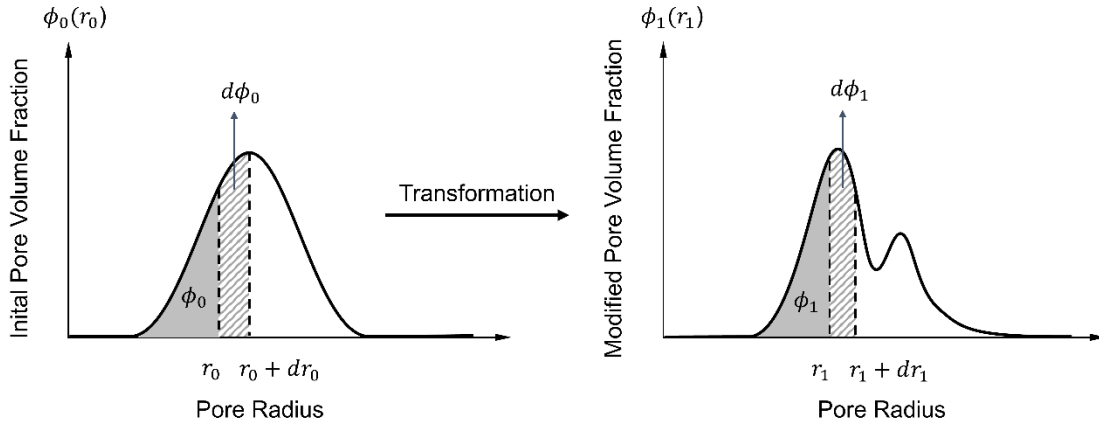


Figure 2. 4 Initial and modified pore volume fractions with the consideration of transformation effects.

Correspondingly, when salt precipitation and dissolution transform porosity from ϕ_0 to ϕ_1 , the pore with radius of r_0 belonging to initial probability density function P_0 becomes the pore with radius of r_1 belonging to modified probability density function P_1 (figure 2.4). Therefore, pore volume fraction of modified pores with radius ranges from zero to r_1 is expressed as:

$$\phi_1(r_1) = \int_0^{r_1} \phi_1 P_1(u) du \quad (2.9)$$

Meanwhile, modified volume of pore with r_1 radius is defined by:

$$v_P^1 = \pi r_1^2 L \quad (2.10)$$

As mentioned previously, the initial probability function P_0 can be expressed by lognormal distribution, the modified probability density function P_1 will be derived herein by proposing two probabilistic methods to describe the transformation of pore size distribution induced by porosity change.

1. Method one.

This method is directly deduced by the change of random variable technique. As stated above, the initial pore sizes are random variables that obey the probability density function $P_0(r_0)$, and $r_1 = f(r_0, r_c)$ is a transformation function. Thus, as shown in figure 2.5, the probability for an infinitesimal increment of r_0 corresponds to the probability for an infinitesimal increment of r_1 should be in identical relation:

$$p(r_1 < R_1 < r_1 + dr_1) = p(r_0 < R_0 < r_0 + dr_0) \quad (2.11)$$

In terms of the probability density, we can write this equality into the form:

$$P_1(r_1)dr_1 = P_0(r_0)dr_0 \quad (2.12)$$

Thus, we can get the following expression for the modified probability density function P_1 :

$$P_1(r_1) = \left| \left(\frac{df(r_0, r_c)}{dr_0} \right)^{-1} \right| P_0(r_0) \quad (2.13)$$

Note that the transformation function $f(r_0, r_c)$ in equation (2.13) is monotonic. Consider a more general case that transformation function $r_1 = f(r_0, r_c)$ is non-monotonic and several values of the argument r_0 correspond to the same value r_1 of the function, in this case, the probability density function of r_1 is thus given by:

$$P_1(r_1) = \sum_k \left| \left(\frac{df(r_{0,k}, r_c)}{dr_{0,k}} \right)^{-1} \right| P_0(r_{0,k}) \quad (2.14)$$

Where $r_{0,k}$ are roots of transformation function $f(r_0, r_c)$, and k is the number of roots. Equation (2.14) indicates that method one can be used in non-monotonic case as long as the support of r_0 is divided into several intervals, during which the corresponding transformation functions are monotonic.

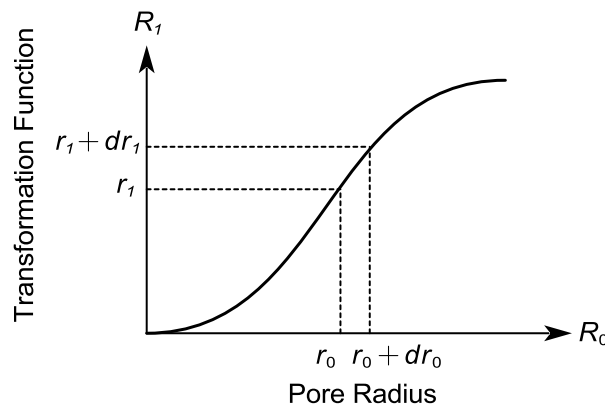


Figure 2. 5 Classical transformation technique of the random variable r_0 .

Meanwhile, equation (2.13) can also be derived from the physical perspective of pore size modification. Based on the assumption that the ratio of variation for porosity is equal to the ratio of corresponding global porosity before and after salt precipitation and dissolution:

$$\frac{d\phi_0}{d\phi_1} = \frac{\phi_0}{\phi_1} \quad (2.15)$$

Substituting equation (2.4) and equation (2.9) into equation (2.15), we can obtain the modified probability density function P_1 as follows:

$$P_1(r_1) = \left| \left(\frac{df(r_0, r_c)}{dr_0} \right)^{-1} \right| P_0(r_0) \quad (2.16)$$

It can be observed that method one shows good consistency in modified probability density

function P_1 obtained from both the mathematical and physical perspectives.

2. Method two.

This method can be derived by assuming that ratio of porosity before and after salt precipitation and dissolution is equal to ratio of volume for pores with radius r_0 and r_1 :

$$\frac{d\phi_1}{d\phi_0} = \frac{dv_P^1}{dv_P^0} = \frac{r_1 dr_1}{r_0 dr_0} \quad (2.17)$$

Thus, modified probability density function after salt precipitation and dissolution is derived by substituting equation (2.4) and equation (2.9) into equation (2.17):

$$P_1(r_1) = \frac{\phi_0}{\phi_1} \frac{f(r_0, r_c)}{r_0} P_0(r_0) \quad (2.18)$$

With the modified probability density function, the pore volume fraction after modification can be obtained by substituting equation (2.18) to equation (2.9):

$$\phi_1 = \int_0^{\infty} \phi_0 \frac{f(u, r_c)}{u} \left(\frac{df(u, r_c)}{du} \right) P_0(u) du \quad (2.19)$$

It should also be noted that by adopting these two probabilistic methods, successive probability density function $P_{n+1}(r_n, r_c)$ can also be derived after several times of transformations for pore radius (n is the transformation number), of which the details on the successive transformations are provided in Appendix 2C. The successive probability density function can be used to interpret the cumulative effects of pore erosion, denoting as $\varepsilon_{n+1}(r_n, r_c)$.

Accordingly, the transformation function for pore radius after successive modifications can be expressed as:

$$T_{n+1} \rightarrow r_{n+1} = f_{n+1}(r_n) = r_n + \varepsilon_{n+1}(r_n) = r_0 + \underbrace{\varepsilon_{n+1} \circ \varepsilon_n \circ \varepsilon_{n-1} \circ \dots \circ \varepsilon_1}_{\text{cumulative effects of pore size erosion}}(r_0, r_c) \quad (2.20)$$

It can be found that the term of cumulative effects $\varepsilon_{n+1}(r_n, r_c)$ shows the heredity (or the so-called memory effects) of pore size transformation, that is, the modified pore size can be traced back to its parent, the initial pore size. Note that for successive transformations, the pore radius for waterfront r_c can be considered into two cases: capillary interface keeps constant during pore size modification, and capillary interface varies with the pore size modification.

Heretofore, we have developed the probabilistic methods describing probability density functions for initial pore radius and modified pore radius after salt precipitation and dissolution. The next section defines transformation models for equation (2.7).

2.2.2 Transformation models for pore size

1. Linear transformation model.

This model assumes that incremental function $\varepsilon(r_0, r_c)$ is proportional to initial pore radius, which indicates that salt precipitation and dissolution modify entire range of pore sizes. The incremental function $\varepsilon(r_0, r_c)$ is defined as:

$$\varepsilon(r_0, r_c) = \varepsilon_L \cdot r_0 \quad 0 \leq r_0 \leq \infty \quad (2.21)$$

Accordingly, linear transformation for pore radius is expressed as:

$$T_L \rightarrow r_1 = f(r_0, r_c) = r_0 + \varepsilon_L r_0 \quad (2.22)$$

where ε_L is a constant which denotes the magnitude of variation in pore radius, and it is obtained by substituting equation (2.22) into equation (2.19):

$$\varepsilon_L = \sqrt{\frac{\phi_1}{\phi_0}} - 1 \quad (2.23)$$

Under linear transformation model, magnitude of pore size variation ε_L is influenced only by overall porosity, at which pores are uniformly filled/emptied on the whole range. Moreover, it should be noted that waterfront is not taken into account in linear transformation model; that is, pore size modification implemented by this model is water-independent.

2. Non-linear transformation models.

Non-linear transformation models account for location of waterfront. In non-linear transformation models, saline solution partially fills pore space and forms waterfront, which separates saturated pores from the unsaturated pore counterparts. Assuming that waterfront is located in pores with radius r_c , opening zone towards the waterfront is denoted as β , the incremental function $\varepsilon(r_0, r_c)$ is given by:

$$\varepsilon(r_0, r_c) = \varepsilon \cdot S(r_0, r_c) \quad (2.24)$$

where $S(r_0, r_c)$ is a sigmoidal function ($0 \leq S(r_0, r_c) \leq 1$), which can be defined by two transformation models: monotonic and non-monotonic transformation models.

(1) Monotonic transformation model (MT).

Figure 2.6(a) shows that in monotonic transformation model, function $S_{MT}(r_0, r_c)$ assumes an S-shape. Modification on pore size distribution affects pore which radius is larger than $r_c - \beta$. More precisely, modification gradually increases in pores which radius is between $r_c - \beta$ and $r_c + \beta$. At pores with radius greater than $r_c + \beta$, the modification is regarded as homogeneous increment constant ε_{MT} . Thus monotonic transformation model is expressed as:

$$T_{MT} \rightarrow r_1 = f(r_0, r_c) = r_0 + \varepsilon_{MT} S_{MT}(r_0, r_c) \quad (2.25)$$

Details on function $S_{MT}(r_0, r_c)$ and erosion parameter ε_{MT} are provided in Appendix 2A and 2B, respectively.

(2) Non-monotonic transformation model (NMT).

Figure 2.6(b) illustrates non-monotonic transformation model whereby $S_{NMT}(r_0, r_c)$ is symmetrical S-shape function. Non-monotonic transformation restricts occurrence of salt precipitation and dissolution near waterfront in pores with radius between $r_c - \beta$ and $r_c + \beta$. Within the range of $[r_c - \beta, r_c + \beta]$, modification on the pore radius increases from zero to maximum value, and reverts to zero. Pores located far from waterfront are barely affected by salt precipitation and dissolution such that modifications on these pores are disregarded. Therefore, non-monotonic transformation model is expressed as:

$$T_{NMT} \rightarrow r_1 = f(r_0, r_c) = r_0 + \varepsilon_{NMT} S_{NMT}(r_0, r_c) \quad (2.26)$$

Details on transformation function S_{NMT} and parameter ε_{NMT} are available in Appendix 2A and 2B, respectively.

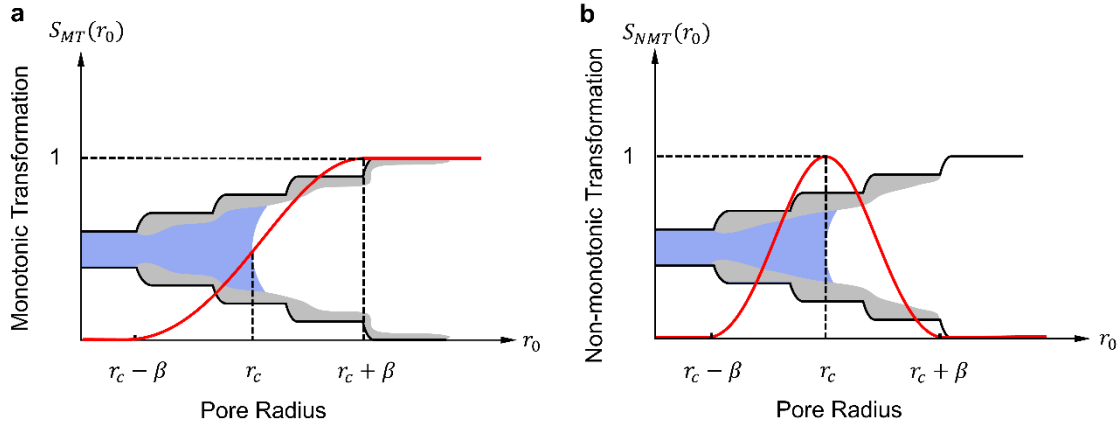


Figure 2. 6 Non-linear transformation models. (a) Monotonic transformation model. (b) Non-monotonic transformation model.

It can be observed from figure 2.6 that monotonic transformation model shows a diffused modification of pore size, while non-monotonic transformation shows a highly localised modification in the vicinity of waterfront. Non-linear transformation models show the transformation effects between initial and modified pore radius which are related to waterfront.

2.2.3 Water saturation degree determined by probabilistic model

As shown in figure 2.7, water condensation occurs in pores with radius smaller than r_c , therefore, water saturation degree S_l is derived by integrating volume of pores with radius smaller than r_c [6]:

$$S_l = \int_0^{r_c} P_i(u) du \quad (2.27)$$

where P_i represents probabilistic density function before or after salt precipitation and dissolution by adopting probabilistic method one or method two, i is the transformation number. Equation (2.27) shows a direct relationship between water saturation degree and waterfront. Based on figure 2.7, it is apparent that water saturation degree increases as waterfront moves to larger pores.

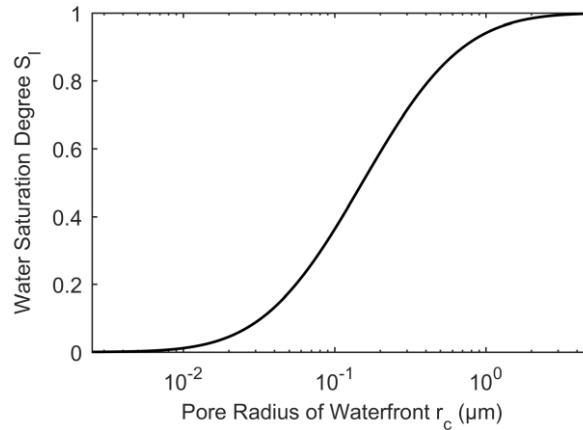


Figure 2. 7 Relationship between water saturation degree and pore radius of waterfront.

2. 3. Experimental data for initial pore size distribution

Initial pore size distribution incorporated in models described in Section 2.2 is derived from experimental data of incremental pore volume distribution of masonry cement measured by MIP analysis.

Table 2. 2 Analysed properties of masonry cement and fitting values for parameters of lognormal distribution model.

Matrix properties	Masonry cement
Porosity ϕ_0	0.2029
Cumulative pore volume $V_p(\text{mL/g})$	0.0971
Specimen's diameter (mm)	35
Specimen's thickness (mm)	11.10
Minimum radius (μm)	0.0015
Maximum radius (μm)	160.2297
Simulated σ_r	1.2
Simulated μ_r	-1.8788
Initial pore size distribution	See figure 2.10

Figure 2.8 shows that pores with radius between 0.01 to $1\mu\text{m}$ constitute the major proportion of pores present in the sample. Moreover, it suggests that the simulated cumulative volume fraction by lognormal distribution agrees with experimental pore volume distribution data. By fitting experimental cumulative volume fraction curve to lognormal distribution, values of

fitted parameters σ_r and μ_r (Table 2.2) are obtained for deriving probability density function of initial pore distribution (figure 2. 9).

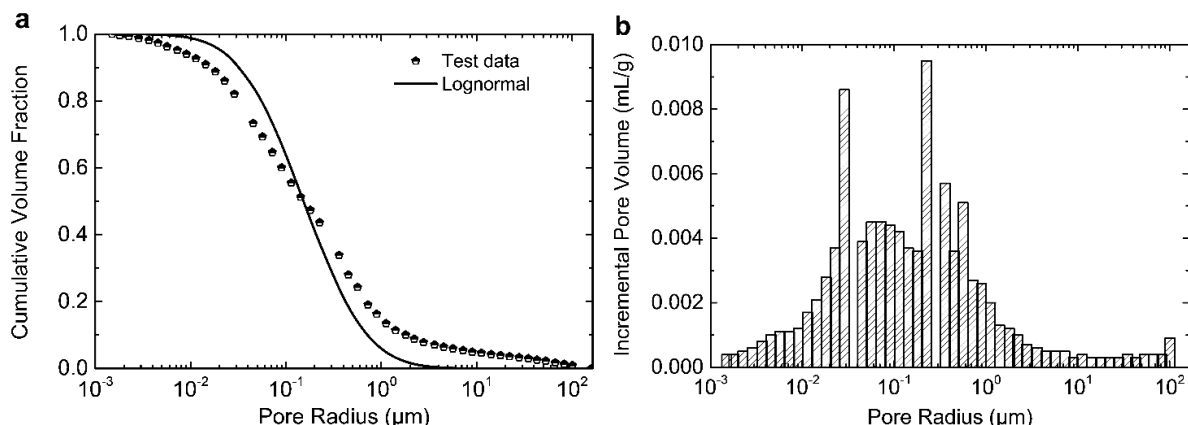


Figure 2. 8 Pore size distribution of masonry cement. (a) Experimental and simulated cumulative volume fraction. (b) Incremental pore volume distribution.

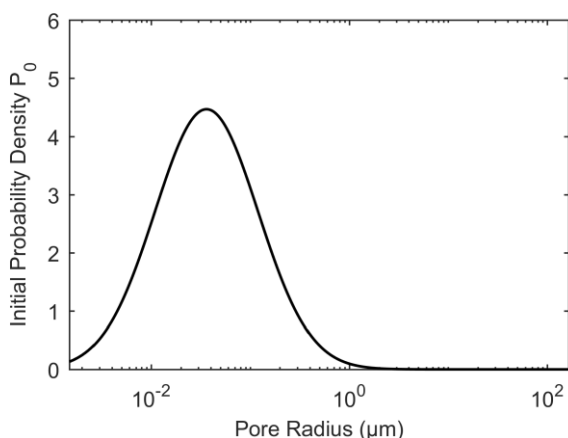


Figure 2. 9 Profile for probability density curve of initial pore size distribution fitted by lognormal distribution.

2. 4. Parametric investigation

Figure 2.9 shows that the size of pores in masonry cement ranges from $0.0015\mu\text{m}$ to $160.2\mu\text{m}$. As previously mentioned, the size of capillary pores ranges from $0.0025\mu\text{m}$ to $5\mu\text{m}$ (see in figure 2.1), which allows waterfront r_c moves within the pores with radius in the range of $[0.0025\mu\text{m}, 5\mu\text{m}]$. Correspondingly, the opening zone β should be satisfied that $r_c - \beta \geq r_{min}$ and $r_c + \beta \leq r_{max}$. In addition, it should be emphasized that the presented transformation models cannot yield negative pore radius value. Negative pore radius value indicates that pores are completely filled by excess amount of precipitated salt which may eventually induce fractures within porous material [65,116,117], which is equally of importance, while out of range of our research.

2.4.1 Pore size distribution implemented by linear transformation

During salt precipitation and dissolution, pore size undergoes series of transformation in porosity that $\phi_0 \rightarrow \phi_1 \rightarrow \dots \rightarrow \phi_i \rightarrow \phi_{n+1}$.

Figure 2.10 a-b show linear transformation from initial pore size distribution. Salt precipitation induces a reduction in porosity from 0.20 to 0.05, which shifts initial probability density and cumulative volume fraction curve towards lower range of pore radius, and increases the probability density. This indicates that salt precipitation generates smaller pores and reduces larger pores. In contrast, an increase in porosity from 0.2 to 0.9 induced by salt dissolution shifts initial probability density and cumulative volume fraction curve towards higher range of pore radius, and increases the width of probability density curve, hence promoting formation of larger pores. In addition, probability density decreases with the increase in porosity. Linear transformation model considers modifications on every pore size, of which a higher alteration from initial porosity produces a more significant change in pore radius.

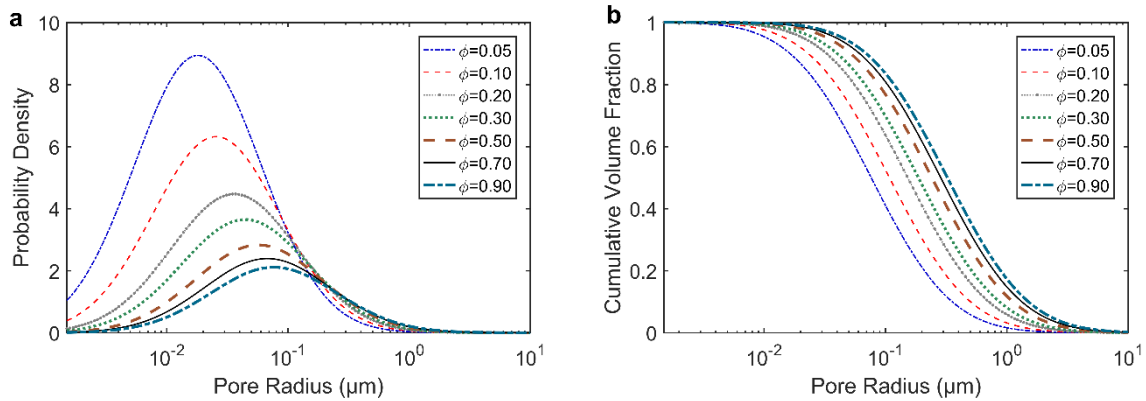


Figure 2. 10 Linear transformation model of pore size distribution. (a) Probability density curve. (b) Cumulative volume fraction curve.

Although linear transformation model provides simplified understanding and good representation of salt precipitation and dissolution, this model is not an accurate representation of actual condition because it does not consider the dependence of salt precipitation and dissolution on waterfront.

2.4.2 Limitations and constraints for non-linear transformation

In contrast to linear transformation model, which simultaneously affects all pore sizes, non-linear transformation models aim to represent a water-dependent transformation of pore size. The non-linear transformation models involve single transformation and successive transformations of pore size distribution. This section illustrates the non-linear transformation models respectively by monotonic (diffused) and non-monotonic (highly localised) cases with method one and method two.

As expressed in Appendix 2A, for monotonic transformation model, function $S_{MT}(r_0)$ must be monotonic to ensure the transformation relationship is one-to-one correspondence

(bijective). Note that when salt dissolution occurs, porosity increases and $\varepsilon > 0$, the transformation function $f(r_0, r_c)$ is strictly increasing unconditionally. Conversely, when salt precipitation occurs, porosity decreases and $\varepsilon < 0$, the following relation should be satisfied to ensure the transformation function is monotonic:

$$\frac{df(r_0, r_c)}{dr_0} > 0 \quad \text{and} \quad \varepsilon < 0 \quad (2.28)$$

Thus, erosion parameter ε should satisfy:

$$0 > \varepsilon > \varepsilon_{\min} = -\frac{4}{3}\beta \quad (2.29)$$

where ε_{\min} is the minimum magnitude of decreased pore radius when salt precipitation occurs.

Moreover, as described in Appendix 2B, this constraint is also reflected in the porosity, i.e., the minimum porosity it can reach during salt precipitation can be expressed as a function of ϕ_{\min} :

$$\text{Method one: } \phi_{\min} = \phi_0 (\varepsilon_{\min} U_1 + 1)^2 < \phi_1 < \phi_0 \quad (2.30)$$

$$\text{Method two: } \phi_{\min} = \phi_0 (\varepsilon_{\min}^2 I_2 + \varepsilon_{\min} I_1 + 1)^2 < \phi_1 < \phi_0 \quad (2.31)$$

where U_1 , I_1 and I_2 are definite integrals that are given in Appendix 2B.

As illustrated above, the waterfront may occur in capillary pores with sizes ranging from $0.0025\mu\text{m}$ to $5\mu\text{m}$. When the waterfront locates in smaller pores, the precipitation/dissolution occurs in a narrow zone because of the limited pore space, making a slight contribution to porosity. While when the waterfront locates in larger pores, the opening zone becomes broader, which indicates the precipitation is related to pores with a wide range of sizes. Consequently, the porosity is altered significantly. Reflecting in equations (2.30) and (2.31), when the absolute value of ε_{\min} is small, the variation of porosity is slight; conversely, when the absolute value of ε_{\min} is large, the variation of porosity is significant.

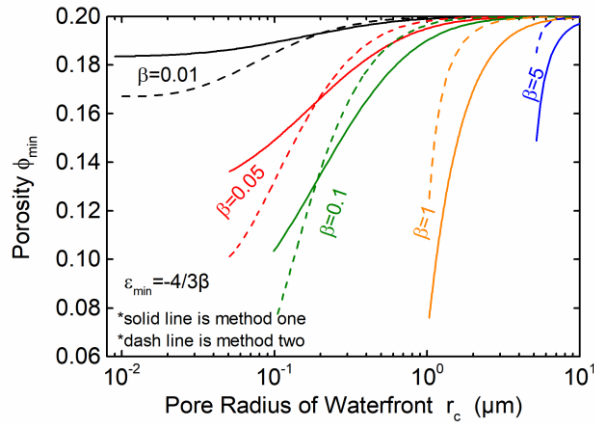


Figure 2. 11 Relationship between porosity ϕ_{\min} and waterfront r_c under different opening zone β for monotonic transformation model.

Figure 2.11 shows the relationship between porosity ϕ_{min} and pore radius of waterfront r_c when adopting monotonic transformation model. Different cases of β are considered here, including $0.01\mu\text{m}$, $0.05\mu\text{m}$, $0.1\mu\text{m}$, $1\mu\text{m}$, and $5\mu\text{m}$. It should be noted that for a given pore size of waterfront r_c , there must be a unique value of ϕ_{min} in both method one and method two. It is observed in figure 2.11 method two can describe a broader range of decreased porosity than method one. For instance, when β is valued at $0.1\mu\text{m}$, method two can describe a decreased porosity as low as 0.08 while method one describes the ϕ_{min} reaching 0.1. Thus method two has better compatibility in describing the pore filling process than method one.

For non-monotonic transformation model, there are no constraints for porosity. All we need to pay attention to is that the parameter ε cannot make the modified pore radius negative. Negative pore radius means pore is filled; when the quantity of precipitation exceeds the volume of the confined pore, cracking occurs to pore structure [5].

2.4.3 Comparisons between method one and method two

2.4.3.1 Single transformation of pore size distribution with constant waterfront

This part compares method one with method two by modelling the pore size distribution after one single transformation due to salt precipitation and dissolution. By adopting non-linear transformation models, the modifications of pore sizes (due to precipitation and dissolution) mainly occur near the capillary interface. It indicates that the pore sizes affected by the homogeneous effect play important roles compared to the linear transformation.

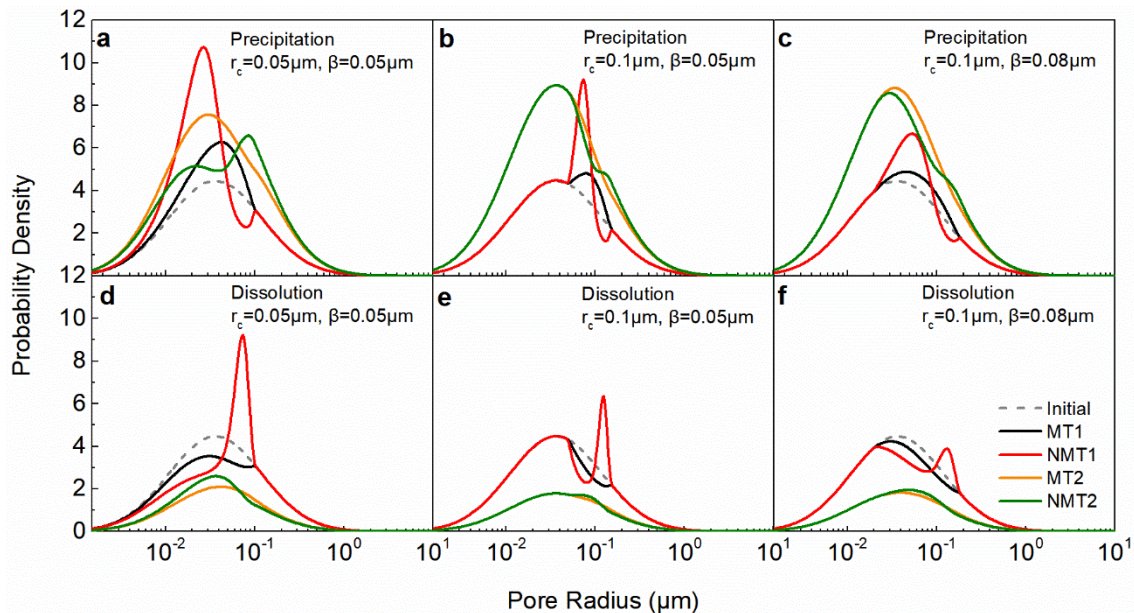


Figure 2. 12 Pore size distribution after single occurrence of salt precipitation/dissolution. Precipitation case: porosity decreases from 0.2 to 0.1; Dissolution case: porosity increases from 0.2 to 0.5. MT1 denotes monotonic transformation-method one; NMT1 denotes non-monotonic transformation- method one; MT2 denotes monotonic transformation-method two; NMT2 denotes non-monotonic transformation- method two.

Figure 2.12 shows the modified pore size distributions implemented by method one and method two when the porous material undergoes one single occurrence of salt precipitation and dissolution. When salt precipitation occurs, parameter ε is assumed as $-0.02\mu\text{m}$ for both method one and method two; whereas, when salt dissolution occurs, parameter ε is assumed as $0.02\mu\text{m}$ for both method one and method two. It can be found that for method one, significant modifications of pore sizes occur near the waterfront and the modifications transfer with the waterfront moves to large pores; while for method two, modifications of pore sizes occur in a quite wide range pore of sizes. While when the waterfront keeps constant and the opening zone becomes broader, the modification ranges for both method one and method two become more expansive, while the peak value of probability density decreases.

By comparing method one with method two, it can be found that method one shows a highly localised modification of the pore sizes near the waterfront, which is significantly affected by the waterfront and the opening zone. On the contrary, method two presents a diffusive modification of pore sizes for all pores, which is mainly determined by porosity and the waterfront. In reality, when porous materials undergo saline deteriorations, modifications of pore size distribution are inclined to appear in an extensive range of pore sizes near the waterfront rather than a localized modification in a narrow range of pore sizes [6]. Therefore, method two is more appropriate to describe the modification of pore size distribution due to the salt precipitation and dissolution than method one.

2.4.3.2 Single transformation of pore size distribution with varied waterfront

The section deals with the modified pore size distribution implemented by both method one and method two regarding the varied waterfront. The main objective of this section is to investigate how the pore size distribution evolved with moved waterfront. This phenomenon does happen in reality. For instance, when the relative humidity changes, the waterfront (or capillary interface) in porous materials also alters [86].

Table 2. 3 Parameters for modified pore size distribution determined by both method one and method two regarding monotonic and non-monotonic transformation models.

β	S_l	ϕ_0	r_c [μm]	ε			
				MT1	NMT1	MT2	NMT2
0.1	0.400	0.200	0.1127	0.0000	0.0000	0.0000	0.0000
0.1	0.410	0.195	0.1163	-0.0065	-0.0137	-0.0045	-0.0052
0.1	0.421	0.190	0.1200	-0.0133	-0.0284	-0.0094	-0.0111
0.1	0.432	0.185	0.1244	-0.0205	-0.0440	-0.0148	-0.0179
0.1	0.444	0.180	0.1290	-0.0281	-0.0609	-0.0208	-0.0259
0.1	0.457	0.175	0.1342	-0.0362	-0.0794	-0.0275	-0.0355
0.1	0.470	0.170	0.1396	-0.0448	-0.0994	-0.0350	-0.0469
0.1	0.485	0.165	0.1460	-0.0543	-0.1220	-0.0436	-0.0613
0.1	0.500	0.160	0.1530	-0.0644	-0.1468	-0.0535	-0.0795

To this end, this section conducts salt precipitation process with overall porosity decreasing

from 0.2 to 0.16. Correspondingly, two probabilistic methods and two non-linear transformation models are adopted to implement the modified pore size distribution after one single time of salt precipitation. In this case, the opening zone β is fixed at $0.1\mu\text{m}$ (see in Table 2.3). The parameter ε versus porosity determined by both method one and method two regarding monotonic and non-monotonic transformation models is showed in figure 2.13.

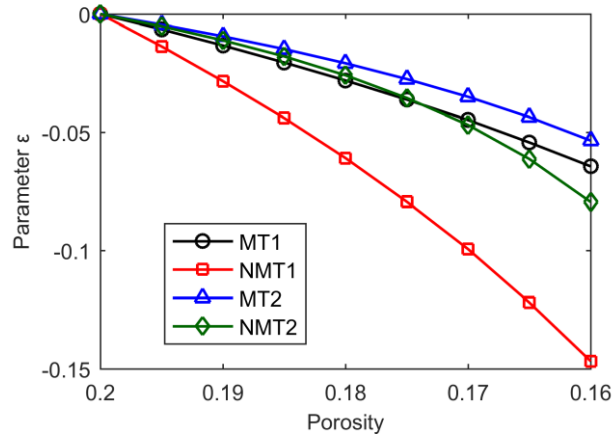
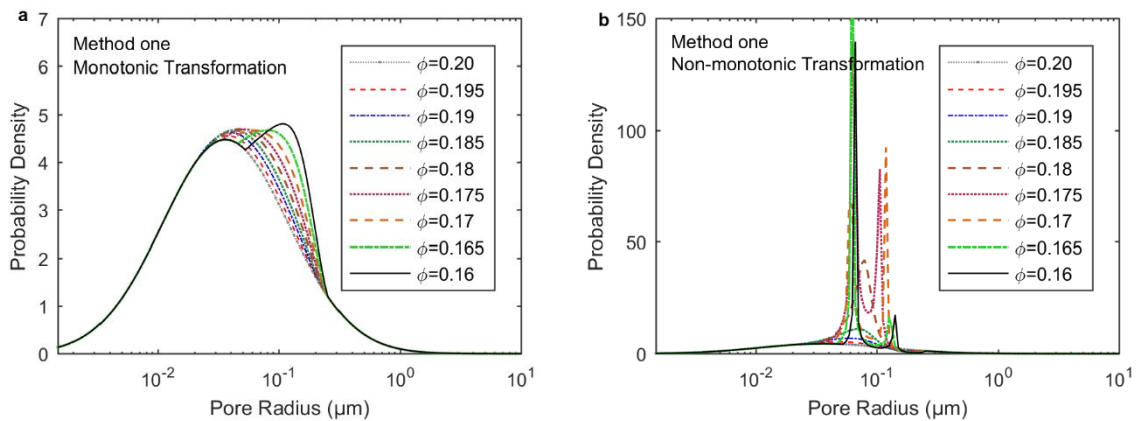


Figure 2. 13 Parameter ε against porosity.

It can be observed in figure 2.14a-b that method one shows a local modification of the pore size distribution. Meanwhile, for method one implemented by monotonic transformation model, the modification of pore size distribution becomes more and more significant as the evolution of water saturation degree and porosity. The peak value of probability density increases when the waterfront moves to large pores. For method one implemented by non-monotonic case, significant modifications occur near the waterfront, and the modified pore size distribution curve evolves into bimodal. It should be noted that as the porosity dramatically increases, the probability density even goes to infinity, far from the pore size distribution in reality. This can be explained by the reason that non-monotonic transformation model may exist singularities when the reduced porosity exceeds the limit values indicated in equation (2.30) during the salt precipitation case. Consequently, the numerical computations will be intricate and difficult when singularities occur in non-monotonic transformation model. Thus, method two is proposed to overcome this drawback.



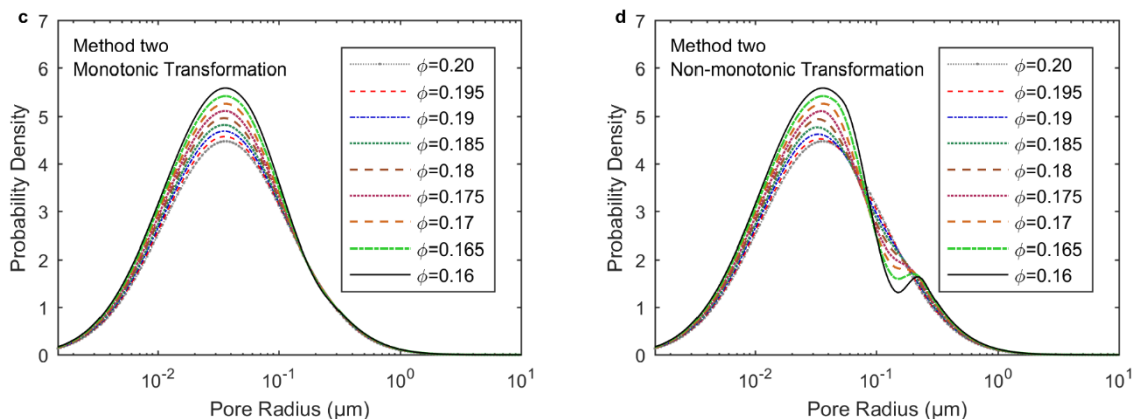


Figure 2. 14 Pore size distribution after single occurrence of salt precipitation by both method one and method two. The initial porosity of 0.20 decreases to 0.16 which corresponds to increments in water saturation degree from 0.40 to 0.50.

For method two (see in figure 2. 14c-d), the modification of pore sizes is very different compared with method one. The peak value of probability density increases as the porosity decreases for both monotonic and non-monotonic transformation models. It is interesting that precipitation fills pores near the waterfront, which divides the large capillary pores into smaller capillary pores. Thus, the unimodal pore size distribution develops into bimodal distribution. Such a phenomenon has also been introduced in [46]. As was illustrated by Shi et al. [46], with the process of hydration, hydration products divided the large pores into small pores, leading the pore size distribution to three sub-distributions, the first sub-distribution was associated with coarse pores, the second sub-distribution includes capillary pores and the third-distribution is related to fine pores.

To be concluded, method one shows a sharp and highly localized modification in a narrow range of pore sizes. Moreover, method one may lead to singularities when adopting non-monotonic transformation model to describe the process of salt precipitation. In contrast, method two gives a uniform and regular modification in the broad range of pore sizes, which is close to natural phenomenon. Meanwhile, to avoid the difficulties induced by singularities in numerical computation, method two is recommended in the following research.

2.4.3.3 Successive transformations of pore size distribution with varied waterfront

In this section, pore size distribution is implemented by both method one and method two regarding the varied waterfront with the consideration of successive transformations.

As the evolutions of the waterfront r_c and opening zone β , significant modifications take place near the waterfront for method one. While for method two, the modification occurs in a broader range of pore sizes. Two different configurations are considered both for method one and method two. If β keeps constant (see in figure 2.15a and c), the moved waterfront brings successive jagged modifications of pore radius near the capillary interface. Consequently, the pore size distribution presents multi-modal, and the number of modes is precisely equal to the number of pore size transformations due to salt precipitation/dissolution. If β evolves

simultaneously with the waterfront (see in figure 2. 15b and d), the modification of pore radius implemented by method one becomes more and more slight, while that implemented by method two deviate significantly from initial pores.

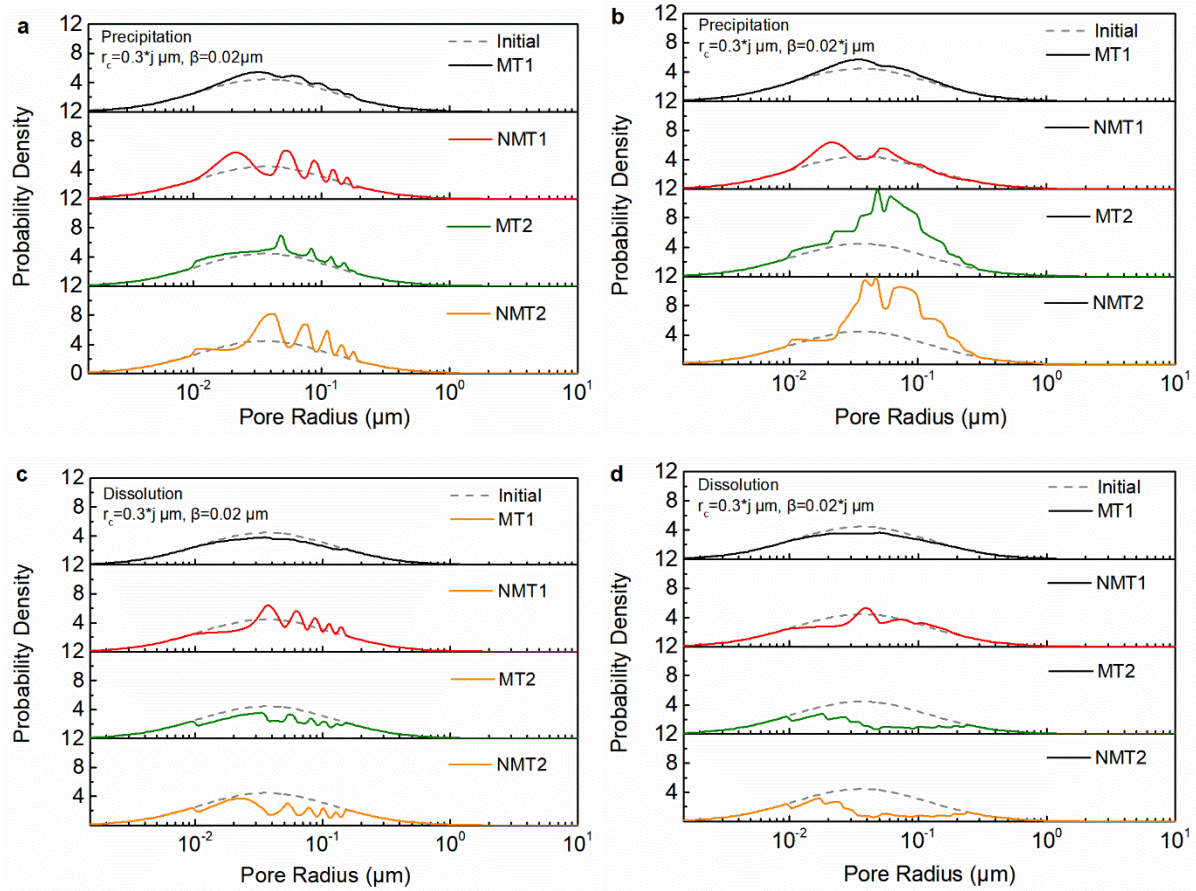


Figure 2. 15 Pore size distribution with varied waterfront after successive occurrences of salt precipitation and dissolution, respectively. (j is transformation times and valued at 5 in this implementation. When precipitation occurs, porosity decreases from 0.2 to 0.15; when dissolution occurs, porosity increases from 0.2 to 0.3).

It can be concluded that as the opening zone of waterfront becomes broader, the probability density profile presented by monotonic and non-monotonic transformation models are similar, and modifications of pore size presented are more and more slight. This is because of the reason that large value of opening zone may cause the same quantity of salt precipitation/dissolution (determined by porosity decrease/increase) to distribute evenly in a wide range, consequently, modifications of pore size are not so considerable.

2.4.4 Further development on method two

2.4.4.1 Single transformation of pore size distribution

We consider a generalized situation at which drying of a porous material shifts waterfront towards smaller pores. Salt precipitation and dissolution are stabilised in pore space close to

waterfront and modify pores around the waterfront. On the other hand, when a porous material is wetted, waterfront moves towards larger pores and the precipitated salt near the waterfront is re-dissolved in saline solution. The water-dependent transformation models predict evolution of pore size distribution due to salt precipitation and dissolution.

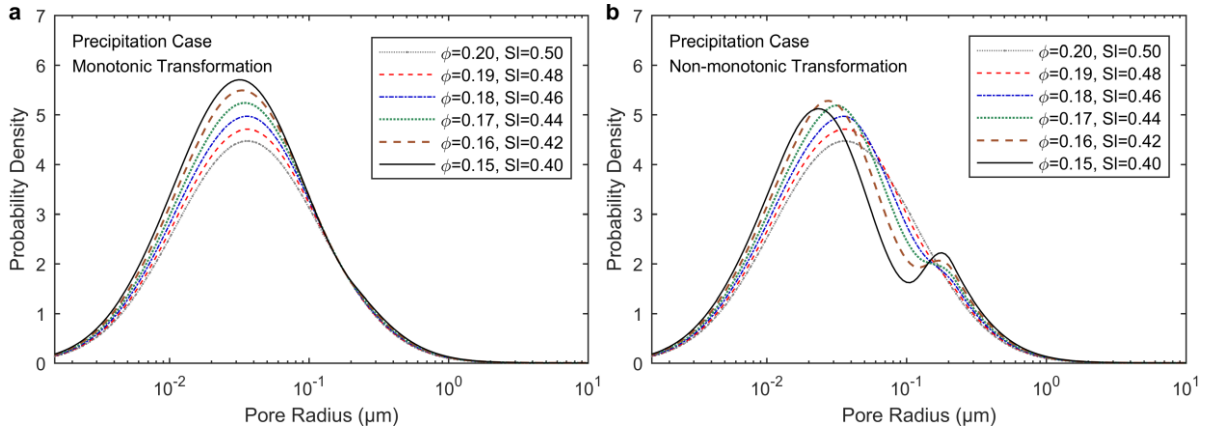


Figure 2. 16 Pore size distribution after single occurrence of salt precipitation by method two. The initial porosity of 0.20 decreases to five degrees of porosity (0.19, 0.18, 0.17, 0.16, and 0.15) which corresponds to reductions in water saturation degree from 0.50 to five degrees (0.48, 0.46, 0.44, 0.42, 0.40).

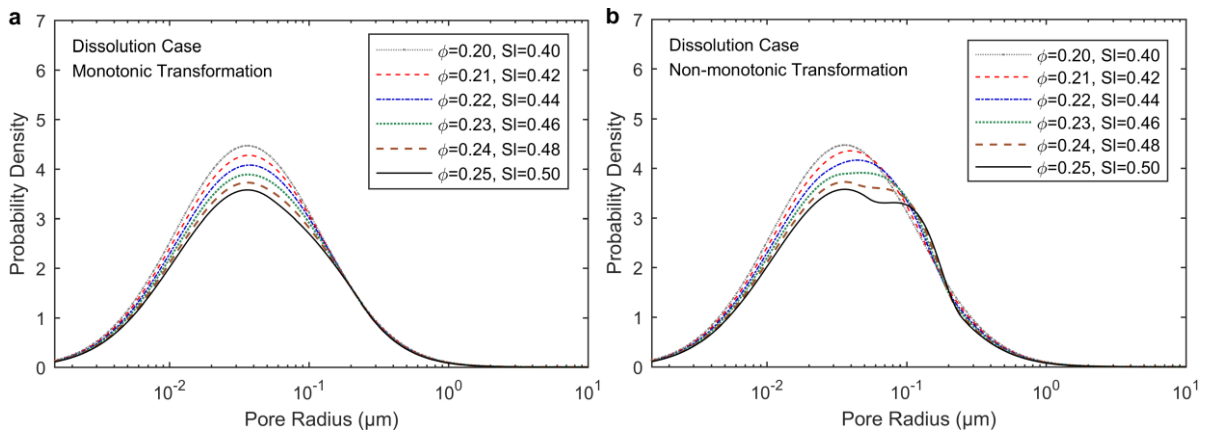


Figure 2. 17 Pore size distribution after single occurrence of salt dissolution by method two. The initial porosity of 0.20 increases to five degrees of porosity (0.21, 0.22, 0.23, 0.24, and 0.25) which corresponds to increases in water saturation degree from 0.40 to five degrees (0.42, 0.44, 0.46, 0.48, 0.50).

Figure 2.16 and 2.17 illustrate monotonic and non-monotonic transformation of pore size distribution due to single occurrence of salt precipitation and dissolution by method two. The location of waterfront is deduced at given porosity and water saturation degree based on equation (2.27). Salt precipitation promotes decreasing porosity, which shifts waterfront towards lower range of pore radius. Simultaneously, probability density increases and number of small pores increases for both monotonic and non-monotonic transformation. In contrast, due to salt dissolution, waterfront moves towards larger pores as a consequence of increasing porosity and water saturation degree. Probability density decreases and amount of larger pores

increases for both monotonic and non-monotonic transformation. The modifications on porosity also alter pore volume fraction (determined by equation (2.9)), as illustrated in figure 2.18, the area denotes the integration of pore volume fraction (or overall porosity). The more significant is the deviation from initial porosity, the larger is the filled/emptied area being created, particularly under non-monotonic transformation.

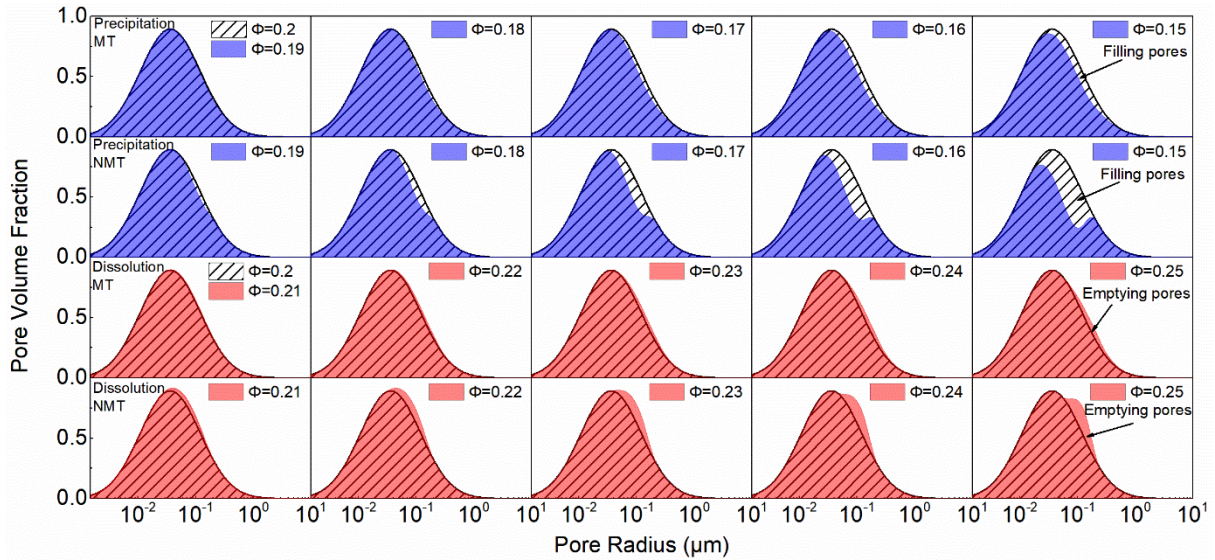


Figure 2. 18 Evolution of pore volume fraction due to salt precipitation and dissolution by method two.

Figure 2.19 suggests that non-monotonic transformation generates higher filling/emptying ratio than monotonic transformation at similar water saturation degree and porosity during salt precipitation and dissolution. Due to salt precipitation (figure 2.19a), non-monotonic transformation generates a filling ratio of 61.6% when porosity decreases from 0.20 to 0.15. Comparatively, monotonic transformation produces a filling ratio of 24.9%. Similarly, due to salt dissolution (figure 2.19b), emptying ratio implemented by non-monotonic transformation is higher than that resulted from monotonic transformation counterpart (45.6% vs. 23% at 0.25 porosity). Non-monotonic transformation model simulates pore filling/emptying accounting for highly localised (i.e., at vicinity of waterfront) occurrence of salt precipitation and dissolution, which provides a more favourable representation of actual pore clog due to salt precipitation.

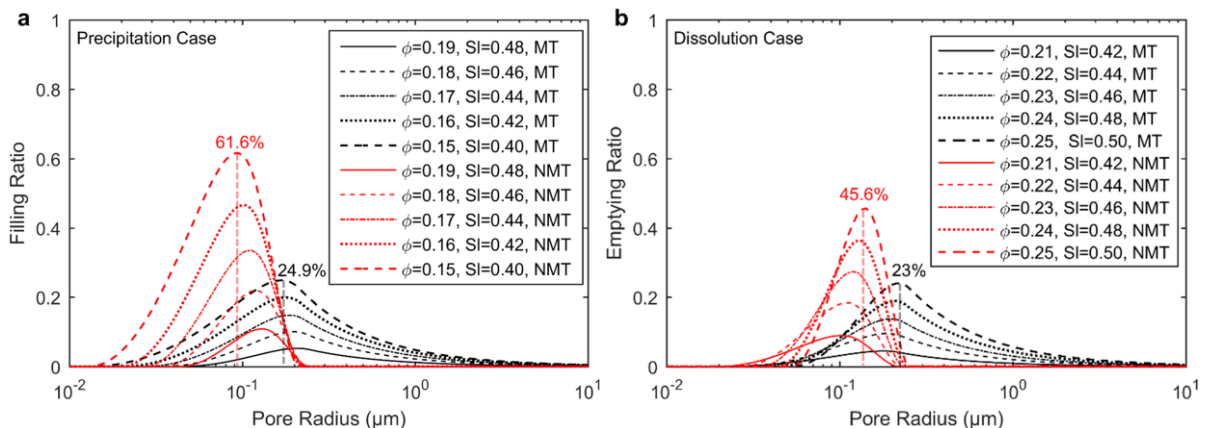


Figure 2. 19 Filling and emptying ratios after single (a) salt precipitation and (b) salt dissolution by method two.

Non-linear transformation models indicate that the pores affected by the homogeneous effect make a substantial contribution. Non-linear transformation of pore size distribution considers localisation of salt precipitation and dissolution at vicinity of waterfront, and indicates higher filling/emptying ratio than linear transformation counterpart which generates a uniform distribution of salt precipitation and dissolution. Due to salt precipitation and dissolution, non-monotonic transformation model modifies pore size distribution from unimodal to bimodal for large deviation in porosity because pore filling/emptying introduces a new peak in probability density function curve, which consequently alters pore population structure (i.e., proportion of small and large pores). Modifications on pore size distribution from unimodal to bimodal and multi-modal have been systematically introduced by Shi et al. [46] and Holly et al. [47]. In conclusion, non-linear transformation models more accurately represent the actual salt precipitation and dissolution which occur at close proximity to waterfront.

2.4.4.2 Successive transformations of pore size distribution

Under successive transformations, modifications on pore size distribution are generated by several occurrences of salt precipitation and dissolution (please refer to Appendix 2C for expressions of successive transformations). The modifications on pore size distribution are cumulative, of which existing pore size distribution is determined by preceding pore size distribution. Two examples were considered (Table 2.4): salt precipitation which decreases porosity from 0.20 to 0.15 after 30 successive transformations, and salt dissolution which increases porosity from 0.20 to 0.25 after 30 successive transformations.

Table 2. 4 Values of parameters for successive transformations of pore size distribution by method two.

Chemical Reactions	Water Saturation Degree	Opening Zone β (μm)	Porosity
Salt precipitation	0.4	0.1	0.20→0.15
	0.5		
Salt dissolution	0.4	0.1	0.20→0.25
	0.5		

1. Parameter ε versus porosity.

Constant ε denotes a magnitude of change in pore radius. Detailed definition on ε in successive transformations is available in Appendix 2C. When ε is less than zero, salt precipitation occurs. On the other hand, when ε is greater than zero, precipitated salt is re-dissolved. The higher is the value of $|\varepsilon|$, the more significant is the modification on pore radius.

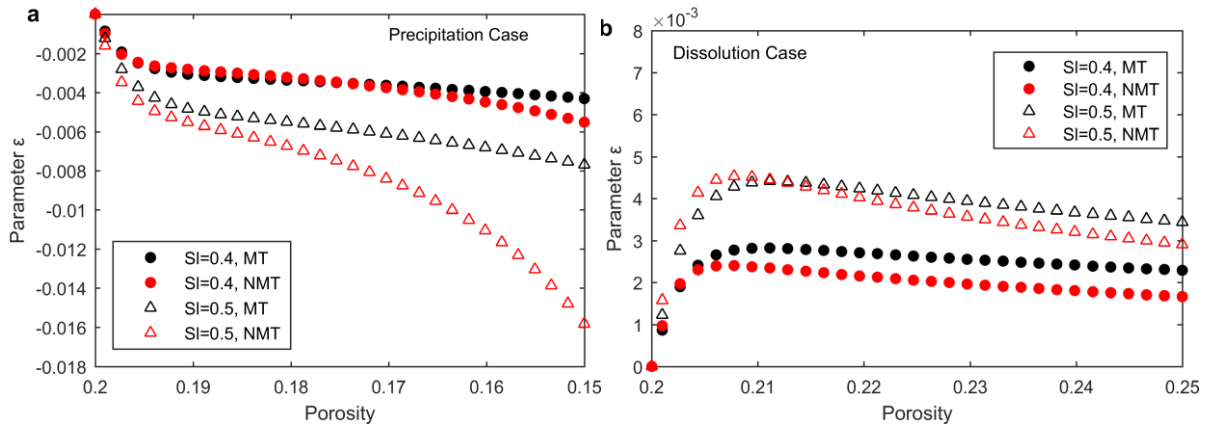


Figure 2. 20 Parameter ϵ against porosity for successive transformations of (a) salt precipitation and (b) salt dissolution by method two.

During salt precipitation (figure 2.20a), decrease in porosity reduces the value of ϵ . On the other hand, during salt dissolution (figure 2.20b), increase in porosity initially increases value of ϵ significantly. However, the value of ϵ progressively decreases before stabilizes. During salt precipitation at water saturation degree of 0.4, waterfront is located in small capillary pores, and there is small difference in value of ϵ for monotonic and non-monotonic transformation models. Increase in water saturation degree to 0.5 shifts waterfront to larger pores. Value of ϵ derived from non-monotonic transformation differs greatly from that derived from monotonic transformation. These results reveal that modification on pore radius is affected by water saturation degree. However, it should be pointed out that the values of ϵ calculated by proposed models are applicable to porosity which generates positive pore radius. Negative pore radius indicates completely filled pores, which produces localised damage near waterfront.

2. Historical evolution of pore size distribution.

This section compares modifications of pore size distribution due to single transformation (where porosity increases/decreases in one-step) and 30 successive transformations (where porosity gradually increases/decreases by several steps) induced by salt precipitation and dissolution.

The comparisons between single transformation and successive transformations are shown in figure 2.21a-d. Under monotonic transformation, it is not surprising that there is no significant difference in modification on pore size distribution due to single transformation and successive transformations. Similarly, water saturation degree does not have noticeable influence on pore size distribution. Under non-monotonic transformation, single transformation generates bimodal distribution. On the other hand, successive transformations display a prominent increase in probability density near waterfront. Consequently, filling/emptying ratio generated from successive transformations is higher than that generated from single transformation for both monotonic and non-monotonic transformation, except for salt dissolution under non-monotonic transformation. Overall, these findings suggest that cumulative modifications on pore size due to successive salt precipitation should not be overlooked.

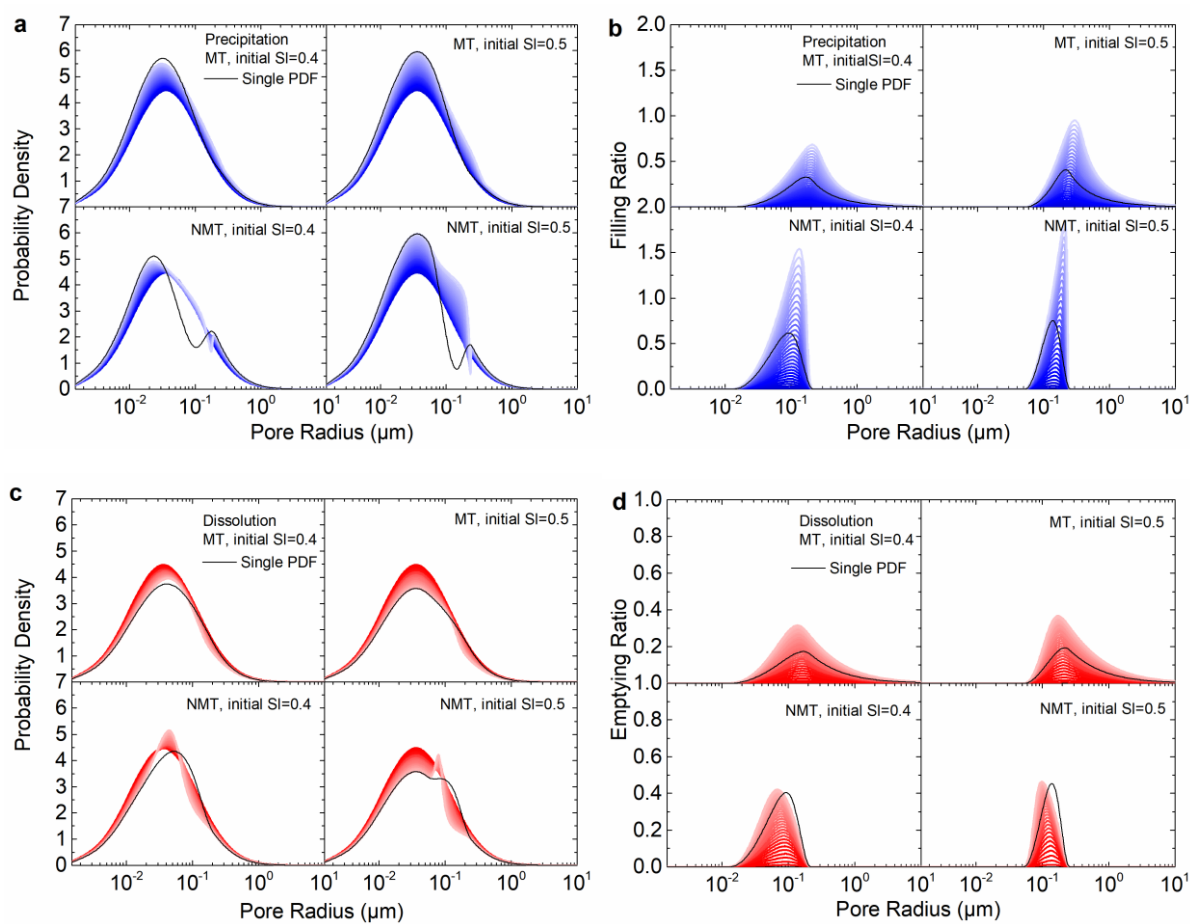


Figure 2. 21 Effect of single and successive transformations on pore size distribution (a and c) and filling/emptying ratio (b and d) by method two. Gradient colour represents successive modifications in the pore size distribution and filling/emptying ratio. As the colour is getting lighter, the porosity deviates more and more significantly from the initial one.

Successive transformation model illustrates evolution of pore size distribution due to long-term exposure of porous material to saline solution. Salt precipitation and dissolution do not alter range of pore size, but change the proportion of small and large pores. Successive transformation model illustrates modifications on pore size distribution due to actual non-homogeneous salt precipitation and dissolution, which predominantly occur at close vicinity of waterfront and influenced by porosity and water saturation degree.

3. Evolution of water saturation degree due to successive transformations.

Under successive transformations, although waterfront is supposed to be in equilibrium, water saturation degree is affected by cumulative effects of successive transformations due to salt precipitation and dissolution. As shown in figure 2.22, due to salt precipitation (figure 2.22a), water saturation degree derived from successive monotonic transformation progressively increases, while water saturation degree derived from successive non-monotonic transformations decreases with decreasing porosity. On the other hand, due to salt dissolution (figure 2.22b), water saturation degree derived from successive monotonic transformation reduces slightly while successive non-monotonic transformation gradually increases water saturation degree with increasing porosity.

It is worth noting that this research assumes that liquid-vapour interface (i.e., waterfront) remains in equilibrium state in spite of the variations in porosity. Nevertheless, salt precipitation and dissolution are complex phenomena involving mass transfers and chemical reactions. Formation of salt crystals generally accompanies alterations in environmental conditions (salt concentration, pressure, relative humidity, and atmospheric temperature) [118,119]. Changes in these environmental factors easily disturb the equilibrium state at waterfront [120]. Hence, dynamic effects in environmental factors should be accounted for to consistently estimate water saturation degree at different porosity in future.

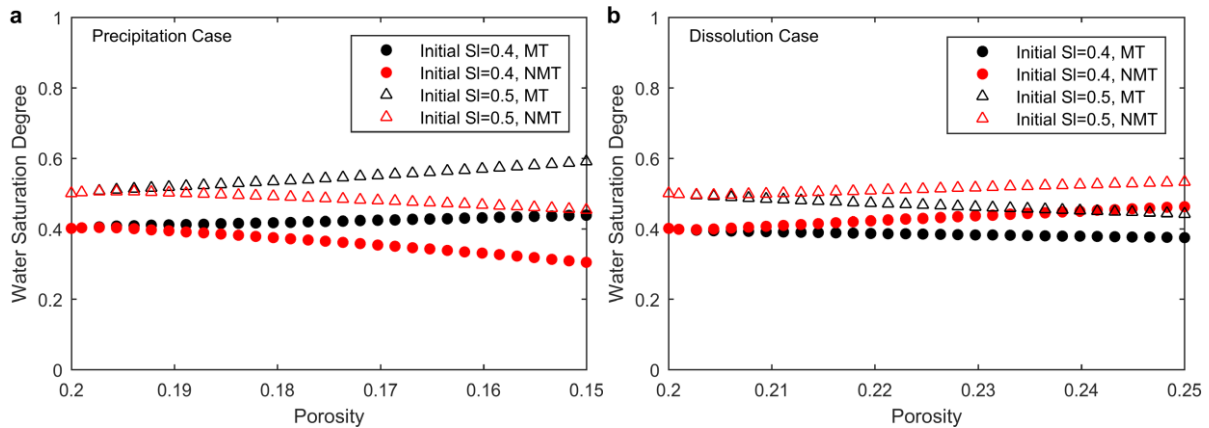


Figure 2. 22 Evolution of water saturation degree due to successive transformations. (a) Water saturation degree varies with decreased porosity during salt precipitation process. (b) Water saturation degree varies with increased porosity during salt dissolution process.

2. 5 Conclusions

This chapter studies the water-dependent evolution of pore size distribution induced by salt precipitation (pore filling) and dissolution (pore emptying), two probabilistic methods are established regarding the probability density functions for initial and modified pore-size distributions. These two methods are achieved by accomplishing the transformation models that determine a magnitude of change in pore radius, namely the parameter ε . One linear transformation model and two non-linear transformation models are constructed as a bridge connecting the initial pore radius and modified pore radius during salt precipitation and dissolution.

Comparisons between method one and method two reveal that method one presented a highly localized modification of the pore size distribution near the waterfront, which is significantly affected by the waterfront and opening zone. On the contrary, method two presents a wide range of modifications for all the pores, which is determined by the porosity and water saturation degree. Moreover, method one leads to singularities when the transformation model is non-monotonic, which may cause difficulties in computational work. Consequently, the modification of pore size distribution implemented by method two is more appropriate to describe the modification of pore size distribution induced by the salt precipitation and dissolution than method one.

Linear transformation model does not adequately characterise modifications on pore size distribution due to salt precipitation and dissolution. In comparison, non-linear transformation models (monotonic transformation model and non-monotonic transformation model) allow estimation on water-dependent modifications of pore sizes. Monotonic transformation model permits the modifications to occur in all unsaturated pores. While non-monotonic transformation model restricts the modifications to pores at close proximity to waterfront. Furthermore, non-monotonic transformation induces bimodal pore size distribution and a higher filling/emptying ratio than the monotonic transformation counterpart, suggesting that non-monotonic transformation model more favourably represents pore clog due to salt precipitation and dissolution.

Successive transformations of pore size distribution are developed to describe the evolution of pore size distribution due to long-term exposure of porous materials to saline solution. The results suggest that the cumulative effects (heredity) of successive transformations on pore size distribution is of equal importance and should not be disregarded.

The proposed probabilistic model provides a reasonable interpretation of physical parameters and water-dependent evolution of pore size distribution. However, it is still not capable of accurately quantifying pore structure development in the course of salt precipitation and dissolution. The author intend to study the proposed model by considering unstable waterfront and the environmental conditions that influence the waterfront. Most importantly, the model presented in this research is purely theoretical. Relating the properties of the probabilistic pore size distribution model to the physical and mechanical properties of porous materials warrants further investigation. Moreover, although no appropriate experiments are available to validate the proposed model at present, it is necessary to make efforts to find out feasible experimental methods to validate the modelling results and further understand the mechanisms suggested by the proposed model.

Appendix 2A. Non-linear transformation models

The S-shape function S_{MT} for monotonic transformation model is expressed as:

$$S_{MT} = \begin{cases} 0 & r_c \leq r_0 \leq r_c - \beta \\ H(r_0, r_c) = \frac{3}{4} \left(\frac{r_0 - r_c}{\beta} - \frac{(r_0 - r_c)^3}{3\beta^3} \right) + \frac{1}{2} & r_c - \beta < r_0 \leq r_c + \beta \\ 1 & r_c + \beta < r_0 < \infty \end{cases} \quad (2A.1)$$

The symmetric S-shape function S_{NMT} for non-monotonic transformation model is given by:

$$S_{NMT} = \begin{cases} 0 & 0 \leq r_0 \leq r_c - \beta \\ G(r_0, r_c) = \frac{3}{4} \left(\frac{2r_0 + \beta - 2r_c}{\beta} - \frac{(2r_0 + \beta - 2r_c)^3}{3\beta^3} \right) + \frac{1}{2} & r_c - \beta < r_0 \leq r_c \\ K(r_0, r_c) = -\frac{3}{4} \left(\frac{2r_0 - \beta - 2r_c}{\beta} - \frac{(2r_0 - \beta - 2r_c)^3}{3\beta^3} \right) + \frac{1}{2} & r_c < r_0 \leq r_c + \beta \\ 0 & r_c + \beta < r_0 < \infty \end{cases} \quad (2A.2)$$

Appendix 2B. Determination for probability density function and parameter ε under single transformation of pore sizes

Method one. For single transformation, the modified pore size distribution is given as:

$$P_1(r_1) = \left| \left(\frac{df_1(r_0, r_c)}{dr_0} \right)^{-1} \right| P_0(r_0) \quad (2B.3)$$

According to the definition of porosity, we have the relationship as follows:

$$\frac{\phi_1}{\phi_2} = \frac{v_1^p}{v_0^p} = \frac{\bar{r}_1^2}{\bar{r}_0^2} \quad (2B.4)$$

where v_0^p and v_1^p are the pore volume before and after modification (induced by salt precipitation or dissolution), respectively, \bar{r}_0 and \bar{r}_1 are the average (representative) pore radius before and after modification, which are given respectively as:

$$\bar{r}_0 = \int_0^{\infty} r_0 P_0(r_0) dr_0 = e^{\mu_r + \frac{\sigma_r^2}{2}} \quad (2B.5)$$

and

$$\bar{r}_1 = \int_0^{\infty} r_1 P_1(r_0) dr_0 \quad (2B.6)$$

After integrating equation (2B.6) in the range from zero to infinity, \bar{r}_1 can be rewritten as follows:

$$\bar{r}_1 = \bar{r}_0(1 + \varepsilon U_1) \quad (2B.7)$$

By substituting equation (2B.4) into equation (2B.7), the parameter ε is expressed as:

$$\varepsilon = \frac{\sqrt{\frac{\phi_1}{\phi_2}} - 1}{U_1} \quad (2B.8)$$

where U_1 is the definite integration that should be deduced based on the linear transformation and non-linear transformation models (monotonic and non-monotonic transformation).

- ❖ For linear transformation model, the definite integration U_1^L is deduced as one, thus parameter ε can be deduced as:

$$\varepsilon_L = \sqrt{\frac{\phi_0}{\phi_1}} - 1 \quad (2B.9)$$

- ❖ For non-linear transformation models, the definite integration U_1 should be considered respectively based on the monotonic and non-monotonic transformation models.

- By adopting monotonic transformation model, the definite integration U_1 is given as follows:

$$U_1^{MT} = \frac{1}{\bar{r}_0} \left(\int_{r_c - \beta}^{r_c + \beta} H(r_0, r_c) P_0(r_0) dr_0 + \int_{r_c + \beta}^{\infty} P_0(r_0) dr_0 \right) \quad (2B.10)$$

- By adopting non-monotonic transformation model, the definite integration U_1 becomes:

$$U_1^{NMT} = \frac{1}{\bar{r}_0} \left(\int_{r_c - \beta}^{r_c} G(r_0, r_c) P_0(r_0) dr_0 + \int_{r_c}^{r_c + \beta} K(r_0) P_0(r_0) dr_0 \right) \quad (2B.11)$$

With the definite integrations U_1^{MT} and U_1^{NMT} under two different non-linear transformation models, parameter ε_{MT} and ε_{NMT} can be obtained according to equation (2B.8), which completes the transformation relation between the pore radius before and after salt precipitation/dissolution.

Method two. The modified pore size distribution after single transformation is deduced as:

$$P_1(r_1) = \frac{\phi_0}{\phi_1} \frac{f(r_0, r_c)}{r_0} P_0(r_0) \quad (2B.12)$$

By substituting equation (2B.12) into modified porosity fraction function, we have:

$$\phi_1 = \int_0^{\infty} \phi_0 \frac{f(u, r_c)}{u} \left(\frac{df(u, r_c)}{du} \right) P_0(u) du \quad (2B.13)$$

Equation (2B.13) can be rewritten as follows after definite integration:

$$\phi_1 = \phi_0(1 + \varepsilon I_1 + \varepsilon^2 I_2) \quad (2B.14)$$

Solving equation (2B.14) could obtain the expression of parameter ε :

$$\varepsilon = \frac{-I_1 \pm \sqrt{I_1^2 - 4I_2(1 - \frac{\phi_1}{\phi_0})}}{2I_2} \quad (2B.15)$$

where I_1 , I_2 are definite integrals which are determined respectively according to linear and non-linear (monotonic and non-monotonic) transformation models.

❖ For linear transformation model, the modified pore size distribution is given as:

$$P_1(r_1) = \frac{\phi_0}{\phi_1} (1 + \varepsilon_L) P_0(r_0) \quad (2B.16)$$

Then the porosity fraction function yields:

$$\phi_1(r_0) = \phi_0(1 + \varepsilon_L)^2 \int_0^{\infty} P_0(u) du \quad (2B.17)$$

As to the fact that $\int_0^{\infty} P_0(u) du = 1$, thusly, equation (2B.17) can be solved to determine the parameter ε_L for linear transformation model:

$$\varepsilon_L = \sqrt{\frac{\phi_0}{\phi_1}} - 1 \quad (2B.18)$$

❖ For non-linear transformation models, the definite integrations I_1 and I_2 are determined respectively according to monotonic and non-monotonic transformation models.

- By adopting monotonic transformation model, we have:

$$I_1^{MT} = \int_{r_c - \beta}^{r_c + \beta} \left(\frac{H(r_0, r_c)}{r_0} + \frac{dH(r_0, r_c)}{dr_0} \right) P_0(r_0) dr_0 + \int_{r_c + \beta}^{\infty} \frac{1}{r_0} P_0(r_0) dr_0 \quad (2B.19)$$

$$I_2^{MT} = \int_{r_c - \beta}^{r_c + \beta} \left(\frac{H(r_0, r_c)}{r_0} \cdot \frac{dH(r_0, r_c)}{dr_0} \right) P_0(r_0) dr_0 \quad (2B.20)$$

- By adopting non-monotonic transformation model, I_1 and I_2 are defined as:

$$\begin{aligned}
I_1^{NMT} &= \int_{r_c - \beta}^{r_c} \left(\frac{G(r_0, r_c)}{r_0} + \frac{dG(r_0, r_c)}{dr_0} \right) P_0(r_0) dr_0 \\
&+ \int_{r_c}^{r_c + \beta} \left(\frac{K(r_0, r_c)}{r_0} + \frac{dK(r_0, r_c)}{dr_0} \right) P_0(r_0) dr_0
\end{aligned} \tag{2B.21}$$

$$\begin{aligned}
I_2^{NMT} &= \int_{r_c - \beta}^{r_c} \left(\frac{G(r_0, r_c)}{r_0} \cdot \frac{dG(r_0, r_c)}{dr_0} \right) P_0(r_0) dr_0 \\
&+ \int_{r_c}^{r_c + \beta} \left(\frac{K(r_0, r_c)}{r_0} \cdot \frac{dK(r_0, r_c)}{dr_0} \right) P_0(r_0) dr_0
\end{aligned} \tag{2B.22}$$

By considering the definite integration I_1 and I_2 under two different non-linear transformation models, parameter ε_{MT} and ε_{NMT} can be obtained according to equation (2B.15), which completes the transformation relation between the pore radius before and after modifications.

Appendix 2C. Determination for probability density function and parameter ε under successive transformations of pore sizes

We can also deduce the pore size distribution after n times of successive transformation by adopting successive monotonic transformation and non-monotonic transformation models under both method one and method two.

The transformation function r_{n+1} denotes the modified pore radius after n times of transformation, defining as:

$$r_{n+1} = f_{n+1}(r_n) = r_{n+1} + \varepsilon_{n+1}(r_n) = r_0 + \underbrace{\varepsilon_{n+1} \circ \varepsilon_n \circ \varepsilon_{n-1} \circ \dots \circ \varepsilon_1}_{\text{cumulative effects of pore size erosion}}(r_0, r_c) \tag{2C.23}$$

Method one. By adopting the monotonic transformation model, the probability density function can be written as:

$$P_{n+1}(r_n) = \begin{cases} P_0(r_n) & 0 \leq r_n \leq r_c - \beta \\ \prod_{i=0}^n (1 + \varepsilon_{i+1} \cdot dH(r_n, r_c))^{-1} P_0(r_n) & r_c - \beta < r_n \leq r_c + \beta \\ P_0(r_n) & r_c + \beta < r_n < \infty \end{cases} \tag{2C.24}$$

By adopting the non-monotonic transformation model, the probability density function is given by:

$$P_{n+1} = \begin{cases} P_0(r_n) & 0 \leq r_n \leq r_c - \beta \\ \prod_{i=0}^n (1 + \varepsilon_{i+1} \cdot dG(r_n, r_c))^{-1} P_0(r_n) & r_c - \beta < r_n \leq r_c \\ \prod_{i=0}^n (1 + \varepsilon_{i+1} \cdot dK(r_n, r_c))^{-1} P_0(r_n) & r_c < r_n \leq r_c + \beta \\ P_0(r_n) & r_c + \beta < r_n < \infty \end{cases} \quad (2C.25)$$

The average pore radii after n times of modification due to pore filling or emptying can be denoted as:

$$\bar{r}_{n+1} = \int_0^{\infty} f_{n+1}(r_n, r_c) P_n(r_n) dr_n \quad (2C.26)$$

After integration for equation (2C.26), it can be reorganized as:

$$\bar{r}_{n+1} = \bar{r}_0 (Z_1 + \varepsilon_{n+1} Z_2) \quad (2C.27)$$

Hence parameter ε_{n+1} is deduced as:

$$\varepsilon_{n+1} = \frac{\sqrt{\frac{\phi_{n+1}}{\phi_0}} - Z_1}{Z_2} \quad (2C.28)$$

where Z_1 and Z_2 are definite integrations that should be deduced by monotonic and non-monotonic transformation models.

- For monotonic transformation model, Z_1 and Z_2 are described as:

$$Z_1^{MT} = \frac{1}{\bar{r}_0} \left(\begin{aligned} & \int_0^{r_c - \beta} r_n P_0(r_n) dr_n \\ & + \int_{r_c - \beta}^{r_c + \beta} r_n \prod_{i=0}^n (1 + \varepsilon_{i+1} \cdot dH(r_n, r_c))^{-1} P_0(r_n) dr_n \\ & + \int_{r_c + \beta}^{\infty} r_n P_0(r_n) dr_n \end{aligned} \right) \quad (2C.29)$$

$$Z_2^{MT} = \frac{1}{\bar{r}_0} \left(\begin{aligned} & \int_{r_c - \beta}^{r_c + \beta} H(r_n) \prod_{i=0}^n (1 + \varepsilon_i \cdot dH(r_n, r_c))^{-1} P_0(r_n) dr_n \\ & + \int_{r_c + \beta}^{\infty} r_n P_0(r_n) dr_n \end{aligned} \right) \quad (2C.30)$$

- For non-monotonic transformation model, we have:

$$Z_1^{NMT} = \frac{1}{\bar{r}_0} \left(\begin{aligned} & \int_0^{r_c - \beta} r_n P_0(r_n) dr_n \\ & + \int_{r_c - \beta}^{r_c} r_n \prod_{i=0}^n (1 + \varepsilon_{i+1} \cdot dG(r_n, r_c))^{-1} P_0(r_n) dr_n \\ & + \int_{r_c}^{r_c + \beta} r_n \prod_{i=0}^n (1 + \varepsilon_{i+1} \cdot dK(r_n, r_c))^{-1} P_0(r_n) dr_n \\ & + \int_{r_c + \beta}^{\infty} r_n P_0(r_n) dr_n \end{aligned} \right) \quad (2C.31)$$

$$Z_1^{NMT} = \frac{1}{\bar{r}_0} \left(\begin{aligned} & \int_{r_c - \beta}^{r_c} G(r_n, r_c) \prod_{i=0}^n (1 + \varepsilon_{i+1} \cdot dG(r_n, r_c))^{-1} P_0(r_n) dr_n \\ & + \int_{r_c}^{r_c + \beta} K(r_n, r_c) \prod_{i=0}^n (1 + \varepsilon_{i+1} \cdot dK(r_n, r_c))^{-1} P_0(r_n) dr_n \end{aligned} \right) \quad (2C.32)$$

Method two. By adopting the monotonic transformation model, the probability density function can be written as follows:

$$P_{n+1}(r_n) = \frac{\phi_0}{\phi_{n+1}} \begin{cases} P_0(r_n) & 0 \leq r_n \leq r_c - \beta \\ \frac{\prod_{i=0}^n (r_n + \varepsilon_{i+1} \cdot H(r_n, r_c))}{(r_n)^{n+1}} P_0(r_n) & r_c - \beta < r_n \leq r_c + \beta \\ \frac{\prod_{i=0}^n (r_n + \varepsilon_{i+1})}{(r_n)^{n+1}} P_0(r_n) & r_c + \beta < r_n < \infty \end{cases} \quad (2C.33)$$

The pore size distribution implemented by the non-monotonic transformation model is given by:

$$P_{n+1} = \frac{\phi_0}{\phi_{n+1}} \begin{cases} P_0(r_n) & 0 \leq r_n \leq r_c - \beta \\ \frac{\prod_{i=0}^n (r_n + \varepsilon_{i+1} \cdot G(r_n, r_c))}{(r_n)^{n+1}} P_0(r_n) & r_c - \beta < r_n \leq r_c \\ \frac{\prod_{i=0}^n (r_n + \varepsilon_{i+1} \cdot K(r_n, r_c))}{(r_n)^{n+1}} P_0(r_n) & r_c < r_n \leq r_c + \beta \\ P_0(r_n) & r_c + \beta < r_n < \infty \end{cases} \quad (2C.34)$$

The global porosity fraction function $\phi_{n+1}(r_n)$ after successive transformations (n times) is defined as:

$$\phi_{n+1}(r_n) = \int_0^{\infty} \phi_{n+1} P_{n+1}(r_n) \left(\frac{df_{n+1}(r_n, r_c)}{dr_n} \right) dr_n \quad (2C.35)$$

It can be reorganized as following by doing integrations:

$$\phi_{n+1} = \phi_0 (J_1 + \varepsilon_{n+1} J_2 + \varepsilon_{n+1}^2 J_3) \quad (2C.36)$$

Thus parameter ε_{n+1} can be calculated as follows:

$$\varepsilon_{n+1} = \frac{-J_2 \pm \sqrt{J_2^2 - 4J_3(J_1 - \frac{\phi_{n+1}}{\phi_0})}}{2J_3} \quad (2C.37)$$

in which J_1 , J_2 and J_3 are definite integrations, which are calculated according to monotonic transformation model and non-monotonic transformation model, respectively:

- For monotonic transformation model, we have:

$$J_1^{MT} = \int_0^{r_c - \beta} P_0(r_n) dr_n + \int_{r_c - \beta}^{r_c + \beta} \frac{\prod_{i=0}^n (r_n + \varepsilon_i \cdot H(r_n, r_c))}{(r_n)^{n+1}} P_0(r_n) dr_n \quad (2C.38)$$

$$+ \int_{r_c + \beta}^{\infty} \frac{\prod_{i=0}^n (r_n + \varepsilon_i)}{(r_n)^{n+1}} P_0(r_n) dr_n$$

$$J_2^{MT} = \int_{r_c - \beta}^{r_c + \beta} \left(\frac{H(r_n)}{r_n} + \frac{dH(r_n)}{dr_n} \right) \frac{\prod_{i=0}^n (r_n + \varepsilon_i \cdot H(r_n, r_c))}{(r_n)^{n+1}} P_0(r_n) dr_n \quad (2C.39)$$

$$+ \int_{r_c + \beta}^{\infty} \left(\frac{1}{r_n} \right) \frac{\prod_{i=0}^n (r_n + \varepsilon_i)}{(r_n)^{n+1}} P_0(r_n) dr_n$$

$$J_3^{MT} = \int_{r_c - \beta}^{r_c + \beta} \left(\frac{H(r_n, r_c)}{r_n} \cdot \frac{dH(r_n, r_c)}{dr_n} \right) \frac{\prod_{i=0}^n (r_n + \varepsilon_i \cdot H(r_n, r_c))}{(r_n)^{n+1}} P_0(r_n) dr_n \quad (2C.40)$$

- For non-monotonic transformation model, we have:

$$J_1^{NMT} = \int_0^{r_c - \beta} P_0(r_n) dr_n + \int_{r_c - \beta}^{r_c} \frac{\prod_{i=0}^n (r_n + \varepsilon_i \cdot G(r_n, r_c))}{(r_n)^{n+1}} P_0(r_n) dr_n \quad (2C.41)$$

$$+ \int_{r_c}^{r_c + \beta} \frac{\prod_{i=0}^n (r_n + \varepsilon_i \cdot K(r_n, r_c))}{(r_n)^{n+1}} P_0(r_n) dr_n + \int_{r_c + \beta}^{\infty} P_0(r_n) dr_n$$

$$J_2^{NMT} = \int_{r_c - \beta}^{r_c} \left(\frac{G(r_n, r_c)}{r_n} + \frac{dG(r_n, r_c)}{dr_n} \right) \frac{\prod_{i=0}^n (r_n + \varepsilon_i \cdot G(r_n, r_c))}{(r_n)^{n+1}} P_0(r_n) dr_n \quad (2C.42)$$

$$+ \int_{r_c}^{r_c + \beta} \left(\frac{K(r_n, r_c)}{r_n} + \frac{dK(r_n, r_c)}{dr_n} \right) \frac{\prod_{i=0}^n (r_n + \varepsilon_i \cdot K(r_n, r_c))}{(r_n)^{n+1}} P_0(r_n) dr_n$$

$$J_3^{NMT} = \int_{r_c - \beta}^{r_c} \left(\frac{G(r_n, r_c)}{r_n} \cdot \frac{dG(r_n, r_c)}{dr_n} \right) \frac{\prod_{i=0}^n (r_n + \varepsilon_i \cdot G(r_n, r_c))}{(r_n)^{n+1}} P_0(r_n) dr_n \quad (2C.43)$$

$$+ \int_{r_c}^{r_c + \beta} \left(\frac{K(r_n, r_c)}{r_n} \cdot \frac{dK(r_n, r_c)}{dr_n} \right) \frac{\prod_{i=0}^n (r_n + \varepsilon_i \cdot K(r_n, r_c))}{(r_n)^{n+1}} P_0(r_n) dr_n$$

Chapter 3

Local-like Hygro-Chemical Reactive Transport Model for Porous Materials Subjected to Precipitation and Dissolution

3.1 Introduction

The water and ionic transport process is a critical issue because it is closely related to the durability of materials, especially for the porous material with functional connectivity [66]. When porous materials are exposed to an aggressive environment during their service life, water in porous materials may be from rain, condensation, capillary suction from groundwater or the environment. Most processes of deteriorations, including carbonation, chloride penetration, salt crystallisation, are influenced by water in porous materials [6]. Among them, salt precipitation and dissolution is one of the most notorious deteriorations for porous materials [4]. Due to the drying and wetting process, the water content in porous materials is changed, consequently concentration of pore solution is affected. During the drying process, salt precipitates on the outer surface (efflorescence) and inner space (sub-florescence) of porous materials [3]. As shown in figure 3.1, the inner salt precipitation can damage the porous structure due to the crystallisation pressure when the volume of precipitated salt is beyond the confined space of porous material. On the contrary, when the porous material is subjected to the wetting process, the salt concentration decreases, salt dissolves in the solution again, which enlarges the pore space and improves the connectivity of pore volume, finally affecting the transport properties of porous materials. Consequently, deteriorations in porous materials are accelerated and serve damages follow.

Moreover, most porous materials in-service experience substantial drying and wetting cycles [121], thus, porous materials are rarely in a constant state of water saturation degree. When structures are in the equilibrium state (i.e., constantly submerged or low water content), the progress of degradation-related actions is much limited [122]. Therefore, it is essential to consider cyclic drying and wetting conditions in numerical simulation of water-dependent activities, which is the root cause of the deterioration in porous materials. A first attempt to quantify such deteriorations in porous materials is to develop a moisture transport model contains ionic species and chemical reactions to illustrate the service life of the porous

materials when subjected to cyclic drying and wetting.

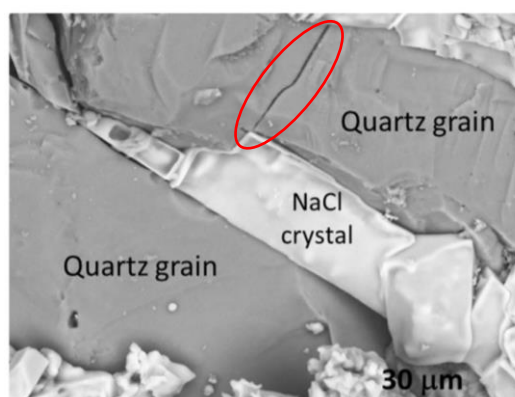


Figure 3. 1 SEM image of salt (NaCl) precipitation in the pore space of sand stone after evaporation of water in the pore solution. The micro cracks marked in the red circles could be due to salt precipitation in the pore space [123].

Within the past decades, the numerical simulation of moisture transport has been widely investigated by many models. For example, Castellazzi et al. [4] presented a coupled multiphase transport model with the presence of salts. Huang et al. [6] developed a numerical model for predicting moisture transport by introducing a wetting front based on the pore size distribution. However, much research ignored the fact that the ionic contained transport generally companies with the chemical reaction referring salts that can either be in liquid or solid phase. The presence of salts profoundly influences the transport properties of porous materials, as has been previously mentioned. Therefore, the chemical reaction concerning salt precipitation and dissolution should also be taken into account in the water and ionic transport model.

Even though some reactive transport models have been devised to provide this capability, equations for the description of models are combinations of partial equations and algebraic equations that are both time and position, which make the computing program very time-consuming and requiring high capability of computational equipment [65,77,80]. Another aspect of the transport and chemical reactions occurs in pores with a smaller size than micrometres; it becomes challenging to observe and measure this process by proper experiments [122]. As to the author's knowledge, very few studies have examined this. Thus, in this chapter, we proposed a local-like hygro-chemical transport model on the specific problem of salt precipitation and dissolution due to the wetting and drying cycles.

The local-like model is considered from a material perspective view, i.e., water and ionic transport equations are described as a function of time only. Since the development of transport models that govern the partitioning of chemical species between aqueous and solid phases is fundamental to understanding processes such as salt precipitation/dissolution, our local-like model provides the ability to govern water and chemical species involving in this process. This model opens a sight on pore-scale inner porous material. It makes the water content and ionic concentration becoming controllable. It seems that for the given porous materials, we have two micro-pipes reaching the inner pore space: one pipe supplies the water and the other pipe supplies the ionic species. By controlling the water and ionic supply through two pipes, we

can model: the concentration profile of ionic species and water saturation degree; how the salt precipitation and dissolution evolve; how the pore space is filled by salt precipitation.

With this motivation, we first consider a representative porous volume for porous materials. Then multiphase equations concerning water, ions and salt are developed based on mass conservation as a set of partial differential equations. Meanwhile, chemical reactions (under the assumption of equilibrium) are developed based on the law of mass action as a set of nonlinear algebraic equations. After that, the operator splitting method (OSA) is adopted to solve the coupled reactive-transport equations.

This chapter is organized as follows. In the first section, a chemical box is developed in MATLAB to deal with local salt precipitation and dissolution reactions. Several cases are implemented to validate the chemical box. In the second section, a local-like transport model is developed and coupled with reactions of precipitation and dissolution. Firstly, several simple cases of hygro-chemical transport under the single time of wetting or drying are investigated. Then long-term transport due to cyclic wetting and drying are investigated by considering varying ionic flux terms and different intervals of water saturation degree. Finally, brief conclusions are presented in the last part of this chapter.

3.2 Development of chemical box

In this section, a chemical box is developed to illustrate salt precipitation and dissolution within porous media. To this end, an appropriate chemical formulation should be built up that could transfer the chemical problems into mathematical equations. Before doing that, it is essential to classify chemical reactions, as suggested by Jacob Rubin [76] in Table 3.1. It can be observed that for level A, the group of “sufficiently fast” and reversible reactions implied that the rate of chemical reactions is large in comparison with other processes that change the solute concentration. Adopting this assumption can permit chemical equilibrium to exist at every point of the pore solution. On the contrary, for an “insufficiently fast” reaction, it is impossible to reach equilibrium anywhere in our system. For lever B, homogeneous reactions suggest that reactions occur within a single phase, while heterogeneous reactions involve at least two phases. For level C, surface reactions are some like adsorption and ion exchange reactions, while classical reactions contain precipitation, dissolution, oxidation-reduction or complex formation.

Table 3. 1 Classification of chemical reactions in salt solution [76].

Chemical Reactions						
Level A	‘Sufficiently fast’ and reversible reactions			‘Insufficiently fast’ and/or irreversible reactions		
Level B	Homogeneous		Heterogeneous		Homogeneous	
Level C		Surface	Classical		Surface	Classical
Class	I	II	III	IV	V	VI

Based on this classification, the type of ‘sufficient fast’ and reversible reactions is considered

in our work, which is based on the assumption that the local equilibrium can be preserved everywhere of the pore solution in this system. This hypothesis is usually valid when describing transport problems in porous fluids, in which the rate of the chemical reaction is much faster than the rate of transport [124]. Meanwhile, the heterogeneous reaction is considered because the precipitation/dissolution reaction involves at least two phases (liquid and solid phases).

3.2.1 Chemical equilibrium constant

The chemical equilibrium constant, an important parameter in describing chemical reactions in equilibria, is reviewed in this section. A reversible chemical reaction can be described by the general chemical equation:



As pore solution is considered to be locally equilibrium after the chemical reactions, thus, the equilibrium constant K_{eq} can be defined as [125]:

$$K_{eq} = \frac{[C]^c [D]^d}{[A]^a [B]^b} \left(\frac{\gamma_C^c \gamma_D^d}{\gamma_A^a \gamma_B^b} \right) \quad (3.2)$$

where $[A]$, $[B]$, $[C]$ and $[D]$ are the concentrations of chemical species and γ_a , γ_b , γ_c and γ_d are the specified ion activity coefficients referring to each chemical species, which indicate how far the solution deviate from the ideal one. For dilute solution (or ideal solution), the ionic activity coefficient approaches one. When the concentration of the solution increases, the activity coefficient becomes significantly different from one, and the pore solution is called a non-ideal solution [75,126]. In this research, the pore solution is considered as ideal solution and the chemical activity coefficient can be regardless.

3.2.2 The law of mass action

Suppose a subset of N_x aqueous species (or ionic species) and a subset of M_p precipitated species (or secondary species) in the related system of precipitation and dissolution. The number of precipitated species is exactly equal to the number of reactions. Chemical reactions can be represented as linear combinations of ionic species such as:

$$\sum_{j=1}^{N_x} a_{ij} x_{ij} \rightleftharpoons p_i \quad (3.3)$$

where a_{ij} is the stoichiometric coefficient of the j th ionic species in the i th precipitated species; x_j is the j th aqueous component with $j = \overline{1, N_x}$; p_i is the i th precipitated species

with $i = \overline{1, M_p}$.

Since the solution is in equilibrium, by adopting the law of mass action [127], precipitation and dissolution of solid-phase are the chemical reactions that are described by a set of nonlinear algebraic equations under local equilibrium condition:

$$K_{eq}^i \prod_{j=1}^{N_s} (c_j^{eq})^{a_{ij}} - 1 = 0 \quad (3.4)$$

where c_j^{eq} is the concentration of the j th aqueous species in the equilibrium state, and K_{eq} is the equilibrium constant of the i th precipitated species, which can be further expressed as:

$$K_{eq}^i = K_{con} \prod_{j=1}^{N_s} (\gamma_j)^{a_{ij}} \quad (3.5)$$

where K_{con} is the conditional equilibrium constant for the ideal solution, and γ_j is the chemical activity coefficient of the j th aqueous component species. It should be noted that $K_{eq}^i = K_{con}$ for the dilute or ideal solution.

Furthermore, equation (3.4) can be extended to equation (3.6) by giving more details:

$$K_{eq}^i \prod_{j=1}^{N_s} \left(c_j^0 - \prod_{k=1}^{M_p} a_{kj} \Delta c_{s-l,k} \right)^{a_{ij}} - 1 = 0 \quad (3.6)$$

where c_j^0 is the initial concentration of the j th aqueous component species (obtained from field measurements) and $\Delta c_{s-l,k}$ is the increased concentration (which is relative to the liquid in the porous medium) of the i th precipitated species p_i , which needs to be obtained by solving equation (3.6).

3.2.3 Local reaction for salt precipitation and dissolution

Equation (3.6) is a set of non-linear equations that can be solved by the Newton-Rapson method. In addition, modified Newton-Raphson method and Boyden method are also adopted in the case of Newton-Rapson method cannot attain the convergence. Figure 3.2 presents the schematic of the chemical box realized by MATLAB code. In this chemical box, the inputs such as initial ionic concentration, initial salt concentration, the equilibrium constant, and the essential information for the chemical equations are given as the first step. Then the criterion of chemical equilibrium based on the law of mass action is implemented to discriminate the salt precipitation and dissolution, as shown in equation (3.7). After that, the three iterative methods are integrated to solve the non-linear algebraic equations. Finally, we get the incremental concentrations for precipitations and ionic species after chemical reactions (that is, saline solution restores equilibrium state again).

$$f_i = K_{eq}^i \prod_{j=1}^{N_s} (c_j^0)^{a_{ij}} - 1 \quad (3.7)$$

It can be found that for a given pore solution, if the equilibrium constant is known, the ionic concentration in equilibrium state can be expressed as follows:

$$\prod_{j=1}^{N_x} (c_j^{eq})^{a_{ij}} = \frac{1}{K_{eq}^i} \quad (3.8)$$

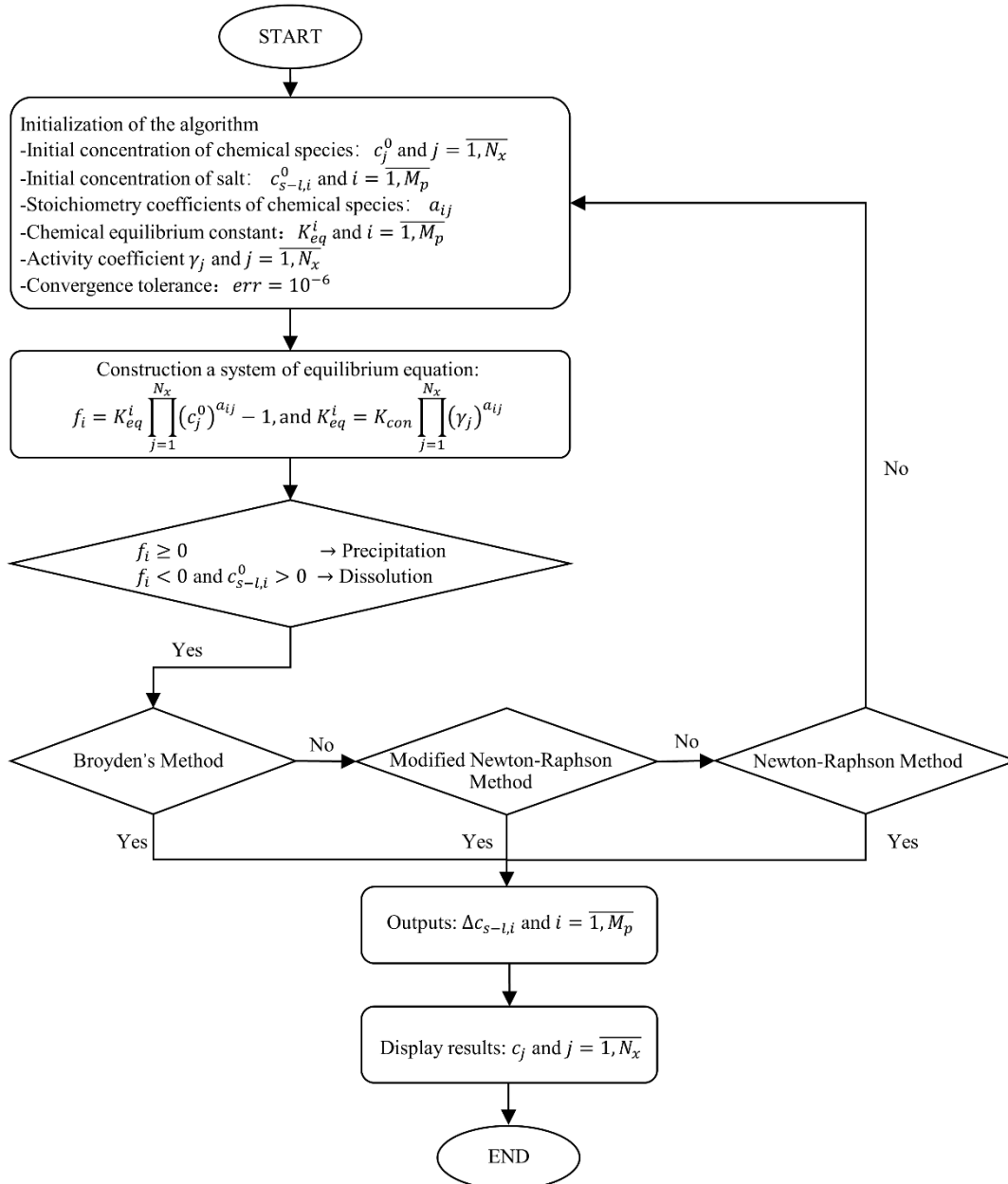


Figure 3. 2 Schematic for chemical box implemented by MATLAB.

3.2.4 Modelling results for chemical reactions

This section validates the chemical box by implementing salt precipitation for one single time of reaction. Meanwhile, the implemented results obtained by MATLAB are compared with the results of COMSOL. After that, successive chemical reactions regarding precipitation and

dissolution are investigated. Note that ionic activity coefficients of involved species are considered as one in this section.

3.2.4.1 Validation for one single time of reaction

For one chemical reaction regarding two ionic species and one precipitated species, we investigate two kinds of solutions with a different equilibrium constant, as shown in figure 3.3.

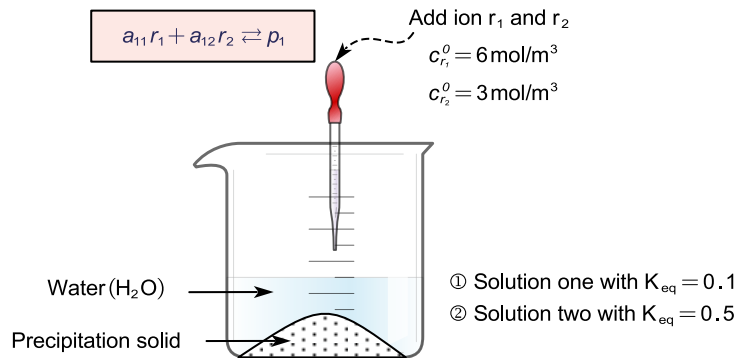


Figure 3. 3 Schematic for one chemical reaction with two different equilibrium constant.

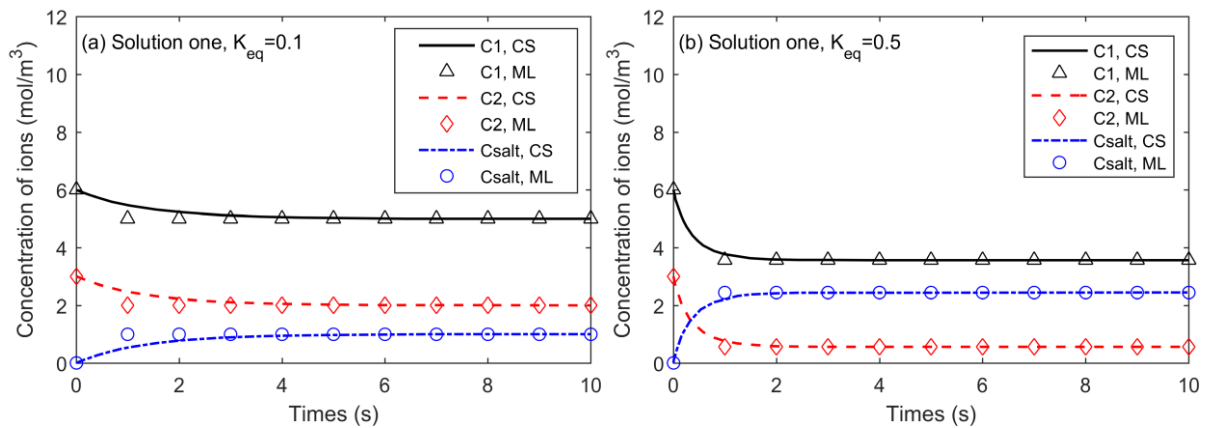


Figure 3. 4 One precipitation reaction under different chemical equilibrium constant.

Figure 3.4 shows the simulation results for concentration profiles of each component when the equilibrium constant is equal to 0.1. It is observed that during the process of salt precipitation, the ionic concentration is decreasing and the salt concentration is increasing. A comparison between figure 3.4 (a) and (b) reveals that the chemical equilibrium constant plays a significant role in the chemical reactions. As the equilibrium constant increases, the chemical reaction goes practically to completion, and the reactant is essentially exhausted. In reality, reaction parameters like temperature, solvent, and ionic strength also influence the equilibrium constant [128]. Moreover, it can also be found that the simulating results by MATLAB are in good agreement with the results by COMSOL.

3.2.4.2 Comparison of the three iterative methods

The efficiency of the three iterative methods, including Newton Raphson method, modified

Newton Raphson method and Broyden's method, is compared in this part by investigating one reaction and two chemical reactions with the same stoichiometric coefficient while different equilibrium constants.

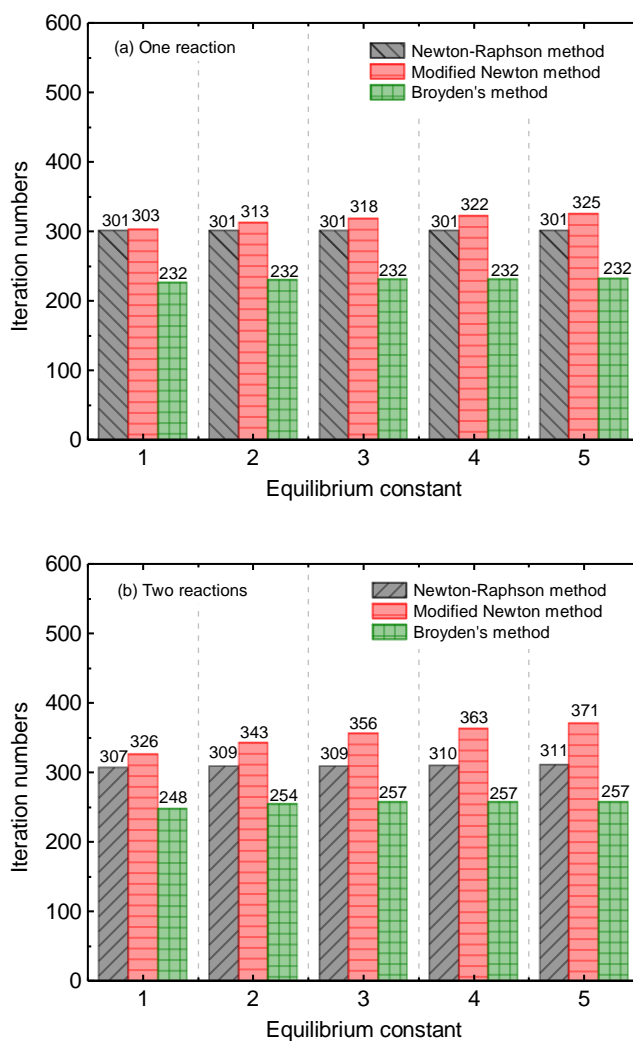


Figure 3. 5 Iterative numbers of each method under different chemical reaction cases.

As the chemical reaction becomes complex in the presented system, the iterative numbers for the three methods are increasing. Moreover, as the equilibrium constant increases, the iterative numbers of the three methods are also increasing. For instance, figure 3.5 (a) shows that for one chemical reaction with the equilibrium constant of 5, the iterative numbers for the Newton Raphson method, modified Newton Raphson method, and Broyden's method are 301, 325, 232, respectively. It indicates that Broyden's method is the most efficient with the fastest convergence rate. On the contrary, modified Newton's method is the most time-consuming. Similar results are also observed for the case of two chemical reactions. Therefore, Broyden's method is the prior choice for the chemical box.

3.2.4.3 Validation for successive reactions

This section deals with the salt precipitation and dissolution after successive times of chemical

reactions. According to the research by Akhlaghi [129], the equilibrium constant of NaCl at room temperature is regarded as 37.68. Therefore, according to equation (3.8), the equilibrium concentration for Na^+ and Cl^- after chemical reaction should be calculated as 0.1629mol/m^3 .

As shown in figure 3.6, the initial ionic concentrations for Na^+ and Cl^- are supposed to be 0.1696mol/m^3 , which are larger than the equilibrium concentrations (0.1629mol/m^3). Thus, the solution is not in equilibrium, and salt precipitation occurs to restore the equilibrium. Supposing that keep adding Na^+ and Cl^- into the solution with the rate of 0.001mol/m^3 . In that case, the equilibrium state is broken, and salt continues precipitating to restore the equilibrium state, as shown in figure 3.7a. It can be found that after several times of salt precipitation, the salt concentration for the ideal solution increases from 0 to 7mol/m^3 .

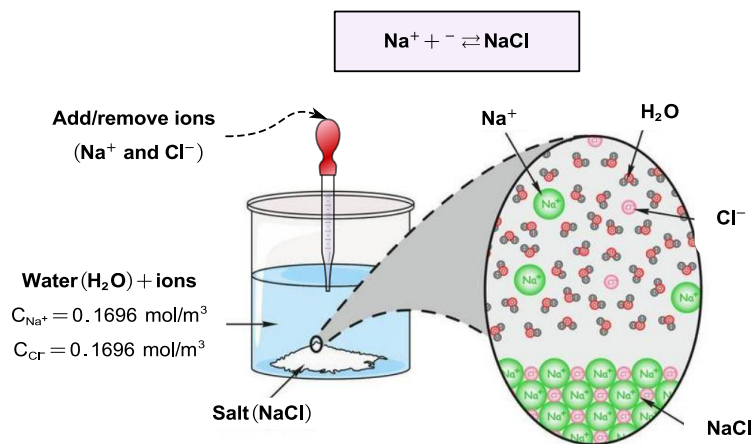


Figure 3. 6 Sodium chloride (NaCl) precipitation and dissolution in pore solution.

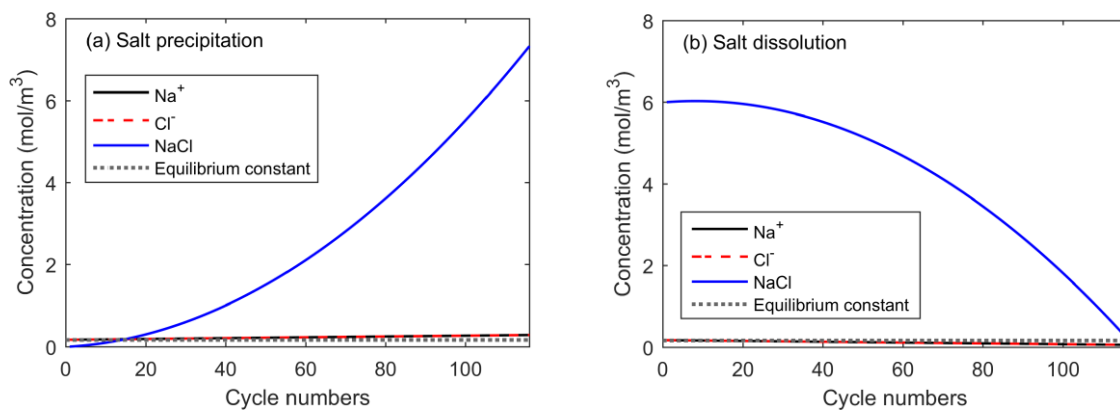


Figure 3. 7 Concentrations for each compositions after successive (a) salt precipitation and (b) salt dissolution.

Figure 3.7b shows the salt dissolution case. It can be found that there are 6mol/m^3 NaCl in the system and the initial ionic concentrations for Na^+ and Cl^- are 0.1696mol/m^3 in the initial state. Similarly, initial concentrations are larger than the equilibrium concentrations and salt precipitation occurs to restore the equilibrium. After that, the solution is in the equilibrium state. Supposing that Na^+ and Cl^- are keeping removed from the solution with the rate of

0.001mol/m^3 . As a result, salt keeps dissolving into the solution in order to restore the equilibrium of ionic concentration until ions are exhausted. These two cases reveal that our chemical box works well with precipitation and dissolution reactions.

To be concluded, this section develops a chemical box concerning salt precipitation and dissolution, which is based on the law of mass action. Three iterative methods are implemented by MATLAB code to solve the mathematical equations. One reaction is investigated, and the modelling results are in good agreement with that by COMSOL. The modelling results also reveal that the equilibrium constant dominates the chemical reactions. A larger equilibrium constant impels the chemical reactions going to completion. Moreover, comparisons between the three iterative methods prove that Boyden's method is the most efficient, which is the prior choice to solving the non-linear algebraic equations of chemical reactions. Finally, it reveals that the proposed chemical box can describe well the local chemical reactions for salt precipitation and dissolution.

3.3 Development of hygro-chemical transport model

As previously mentioned, most porous materials in-service experience substantial drying-wetting cycles [122]. Hygro conditions strongly influence salt precipitation and dissolution. Drying leads to removal of water from pores, and consequent salt precipitation, even micro-cracking. The porous materials regain water on wetting, precipitated salt dissolved into the pore solution again, which alter the pore structure, as shown in figure 3.9. Thus, water and ionic transport models coupling with salt precipitation and dissolution are essential to describe this complex phenomenon.

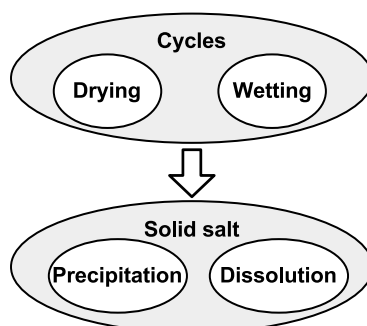


Figure 3. 8 Drying and wetting cycles with salt precipitation and dissolution.

This section intends to describe the water-ionic transport coupling with salt precipitation and dissolution under drying and wetting cycles in porous materials. Within this motivation, the key objectives of this paper are as follows. (1) To propose a pore-scale model to determine the water-ions transport and the salt precipitation and dissolution in porous materials when subjected to drying-wetting cycles. (2) To enhance the physical understanding of the mechanism governing water and ions transport in porous materials. (3) To evaluate the effects of salt precipitation and dissolution on the porosity numerically.

For the local-like hygro-chemical transport equations, the water and ionic transport are time-dependent only, which are controlled by two parameters (water flux term Q_w , and ionic flux

term Q_c). The pore solution is in equilibrium state, and water and ionic transport perturbs the equilibrium state by adding or removing water and ions in the pore solution. Subsequently, salt precipitation or dissolution appears to restore the equilibrium [130]. Before realising this process, some fundamental definitions on multi-components in porous materials are first to be clarified.

3.3.1 Description of porous materials

Making reference to the representative porous volume of porous materials in figure 3.9, porous materials are regarded as heterogeneous, multi-phase materials. All the components involved in chemical reactions are described in molarity and molality in this research. The total volume of the porous material is denoted as Ω . The solid phase incorporates the solid skeleton with the constant volume is denoted as Ω_s^0 , and the volume of precipitated salt is given by $\Omega_{salt} = \sum_i \Omega_i$ and $i = 1, 2, \dots, M_p$ is the number of the salt in porous materials.

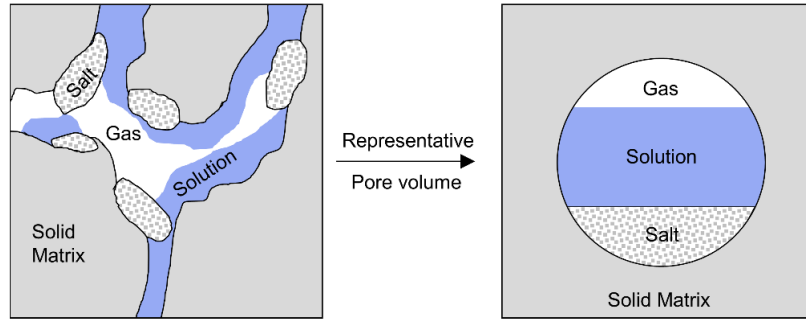


Figure 3.9 Description of representative porous materials.

The volume of the solid phase Ω_s can be represented as:

$$\Omega_s = \Omega_s^0 + \sum_{i=1}^{M_p} \Omega_i \quad (3.9)$$

The liquid phase is represented by Ω_l , which is made of pure water Ω_w and dissolved ions $\sum_j \Omega_j$, and $j = 1, 2, \dots, N_x$ is the number of the ions in the solution. Thus, the volume of liquid solution can be expressed as:

$$\Omega_l = \Omega_w + \sum_{j=1}^{N_x} \Omega_j \quad (3.10)$$

The volume of gaseous phase Ω_g incorporates the volume of dry air Ω_a and the volume of water vapour Ω_v , which is expressed as:

$$\Omega_g = \Omega_a + \Omega_v \quad (3.11)$$

As mentioned in Marsily's research [131], for unsaturated porous materials (salt dissolved aqueous), using the mobile air phase approach does not significantly differ from the immobile approach, except for very special cases. Thus, the gaseous phase, occupying a portion of the

porous space, is neglected in our research.

The porosity is defined as:

$$\phi = \frac{\Omega - \Omega_s}{\Omega} = \frac{1}{\Omega} \left(\Omega - \Omega_s^0 - \sum_{i=1}^{M_p} \Omega_i \right) = \phi_0 - \sum_{i=1}^{M_p} \frac{\Omega_i}{\Omega} \quad (3.12)$$

The water saturation degree for pore solution is given by the fraction of the solution volume and the pore volume, which is expressed as:

$$S_l = \frac{\Omega_l}{\Omega - \Omega_s} = \frac{\Omega_l}{\phi \Omega} \quad (3.13)$$

The amount of the i th salt species in moles relative to porous material is expressed as:

$$s_i = \frac{n_i}{\Omega} \quad (3.14)$$

The mass of the i th salt species relative to porous material is given as:

$$m_i = \frac{n_i M_i}{\Omega} \quad (3.15)$$

where M_i is the molar mass of the i th salt species (kg/mol).

Thus, the total mass of salt relative to porous material is expressed as:

$$m_{salt} = \sum_{i=1}^{M_p} m_i \quad (3.16)$$

By considering equation (3.12), the expression of the porosity can be derived based on the amount of salt:

$$\phi = \phi_0 + \sum_{i=1}^{M_p} \frac{\omega_i (n_i^0 - n_i)}{\Omega} \quad (3.17)$$

where ω_i is the molar volume for the i th salt.

The mass of the solution (combination of water and ionic species) relative to the porous material is given as:

$$m_l = \frac{\bar{m}_l}{\Omega} = \rho_l S_l \phi \quad (3.18)$$

where ρ_l is the density of the solution.

The concentration of the j th ionic species in the solution is expressed as the amount of j th ionic species in moles relative to pore solution, which is read as:

$$c_j = \frac{n_j}{\Omega_l} = \frac{\bar{m}_j}{M_j \Omega_l} \quad (3.19)$$

The volume of the solution Ω_l can be expressed as the composition of water volume and ionic volume:

$$\Omega_l = \Omega_w + \sum_{j=1}^{N_x} n_j \omega_j = \Omega_w + \sum_{j=1}^{N_x} c_j \Omega_l \omega_j \quad (3.20)$$

Base on equation (3.20), the volume of the pure water can be deduced as:

$$\Omega_w = \left(1 - \sum_{j=1}^{N_x} c_j \omega_j\right) \Omega_l \quad (3.21)$$

Thus, the mass of pure water relative to porous material is thus given as:

$$m_w = \frac{\bar{m}_w}{\Omega} = \rho_w \frac{\Omega_w}{\Omega} = \rho_w \left(1 - \sum_{j=1}^{N_x} c_j \omega_j\right) \phi S_l \quad (3.22)$$

where ρ_w is the water density (kg/m³).

The ionic mass relative to porous material is thus given as:

$$m_j = \frac{\bar{m}_j}{\Omega} = \frac{c_j M_j \Omega_l}{\Omega} = \phi S_l c_j M_j \quad (3.23)$$

3.3.2 Mass balance

Based on the representative porous volume in figure 3.9, water and ions are added into or removed from the porous materials; the conservation of the aqueous solution is given as two parts: the conservation of pure water and conservation of ions.

The conservation equation of the pure water is expressed as:

$$\frac{\partial m_w}{\partial t} + \text{div}(m_w v_{w-l}) + \text{div}(m_w v_{l-s}) = -\dot{m}_v \quad (3.24)$$

where \dot{m}_v is the mass of water that transferred into vapor, v_{w-l} is the velocity of water flow relative to the pore solution, v_{l-s} is the velocity of pore solution relative to the porous material, which can be determined by Darcy's law for multi-phase flow.

Moreover, the mass conservation of the ionic species is expressed as:

$$\frac{\partial m_j}{\partial t} + \text{div}(m_j v_{j-l}) + \text{div}(m_j v_{l-s}) = -\dot{m}_{i-j} \quad (3.25)$$

where \dot{m}_{i-j} is the variation of ionic mass relative to the precipitated or dissolved salt after water-ionic transport and $\dot{m}_{salt} = \sum_{i,j} \dot{m}_{i-j}$, and v_{j-l} is the velocity of ionic species relative to the pore solution, which can be determined by Darcy's law for multi-phase flow.

3.3.3 Assumptions and solutions

In the proposed local-like transport model, the water flux term and ionic flux term are time-dependent only, which can be regarded as constant inputs, as is shown in figure 3.10. The evaporation term is supposed to be zero, and the water flux term is shown as:

$$Q_w = \text{div}(m_w v_{w-l}) + \text{div}(m_w v_{l-s}) = \text{cte} \quad \text{and} \quad \dot{m}_{vap} = 0 \quad (3.26)$$

Thus, the water conservation equation can be simplified as:

$$\frac{\partial m_w}{\partial t} + Q_w = 0 \quad (3.27)$$

Meanwhile, in our local-like model, the precipitation salt in the initial state ($t=0$) is assumed as zero, the ionic flux term is considered as constant and denoting by Q_c :

$$Q_c = \text{div}(m_j v_{j-l}) + \text{div}(m_j v_{l-s}) \quad (3.28)$$

Therefore, the mass balance of the dissolved ions can be expressed as:

$$\frac{\partial m_j}{\partial t} + Q_c = -\dot{m}_{i-j} \quad (3.29)$$

It should be noted that the porosity is determined by salt precipitation and dissolution reaction. When $t > 0$, chemical reaction occurs, and \dot{m}_{i-j} is not zero, the corresponding variation of ionic mass relative to precipitated or dissolved salt should be taken into account in equation (3.29). More details for solving transport equations can be found in Appendix 3B.

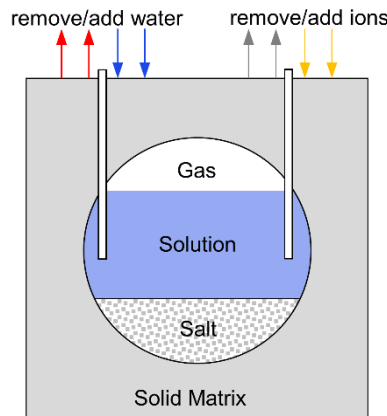


Figure 3. 10 Hygro-chemical transport within the representative porous volume.

To investigate the coupling effects between water-ionic transport and salt precipitation/dissolution, the operator-splitting method (OSA) is adopted to solve the non-

linear algebraic equations for chemical reactions and partial differential equations for transport processes, the schematic of the solving procedure can be found in figure 3.11.

As shown in figure 3.11, the first step is the parametric initializations. The second step deals with the transport process, which alters the water saturation degree by direct water supply Q_w , and alters the ionic concentration by the interaction of Q_w and Q_c (ions supply). For the third step, ionic concentrations are calibrated by salt precipitation and dissolution reactions. After that, the calibrated concentrations are regarded as the inputs of the subsequent transport process. Repeat step two and step three until the water saturation degree reaches the limitation.

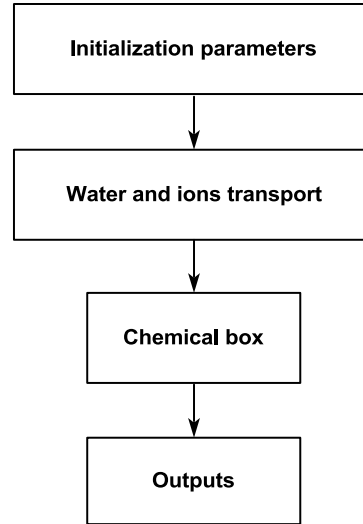


Figure 3. 11 Basic framework of two-step method for the proposed hygro-chemical transport model.

In this research, the hygro-chemical transport model is solved in MATLAB implementation by introducing a time step Δt for each time of iteration, which can be organised as such a logical process:

$$\left\{ \begin{array}{l} B^{(t+\Delta t)} = -\left((Q_c + \Delta m_i^t) \sum_j^{N_x} \frac{\omega_j}{M_j} + \frac{Q_w}{\rho_w}\right) \Delta t + B^t \\ c_j^{(t+\Delta t)} = \left(-\frac{Q_c + \Delta m_i^t}{M_j} \Delta t + c_j^t B^t\right) \frac{1}{B^{(t+\Delta t)}} \\ K_{eq}^i \prod_{j=1}^{N_x} (c_j^t - \sum_{k=1}^{M_p} a_{kj} \Delta c_{s-l,k}^{(t+\Delta t)})^{a_{ij}} - 1 = 0 \\ \phi = \phi_0 + \sum_{i=1}^{M_p} \frac{\omega_i (n_i^0 - n_i^{(t+\Delta t)})}{\Omega} \end{array} \right. \quad (3.30)$$

3.4 Implementations and results

As previously mentioned that the precipitation and dissolution are controlled by the equilibrium constant K_{eq} ; thus, c_j^{eq} , the ionic concentration in the equilibrium state for the

j th ionic species can be determined by equation (3.8). For an explicit description of the simulation results hereafter, after the transport process, the ionic concentration is named as a predictor (concentration), denoting by c_j^p . After the chemical reaction of salt precipitation and dissolution, the ionic concentration is named as indicator (concentration), denoting by c_j^{eq} .

According to the law of chemical reaction, when the product of predictors for ionic species is larger than the product of indicators, precipitation appears; when the product of predictors for ionic species is smaller than that of indicators, dissolution appears. Moreover, when the product of predictors ionic concentration is equal to the product of equilibrium concentration, no chemical reaction occurs, and the pore solution is in the equilibrium state:

$$\left\{ \begin{array}{l} \prod_{j=1}^{N_x} (c_j^p)^{a_{ij}} > \prod_{j=1}^{N_x} (c_j^{eq})^{a_{ij}} \text{ , precipitation} \\ \prod_{j=1}^{N_x} (c_j^p)^{a_{ij}} < \prod_{j=1}^{N_x} (c_j^{eq})^{a_{ij}} \text{ , dissolution} \\ \prod_{j=1}^{N_x} (c_j^p)^{a_{ij}} = \prod_{j=1}^{N_x} (c_j^{eq})^{a_{ij}} \text{ , equilibrium} \end{array} \right. \quad (3.31)$$

In this section, we investigate a very common salt (NaCl) that exists in porous materials. By adding or removing ions during the wetting and drying process in the representative porous volume, we simulate several situations of salt precipitation and dissolution. Here are several different parameters that can be controlled in order to estimate the regimes of pore solution:

- Water flux term, Q_w [$\text{kg}/\text{m}^3 \cdot \text{s}$], significantly affects the water saturation degree. When $Q_w < 0$, water is dried out, and water saturation degree decreases; when $Q_w > 0$, water is rewetted, water saturation degree increases.
- Ionic flux term, Q_c [$\text{mol}/\text{m}^3 \cdot \text{s}$], determines ions supply in pore solution. When $Q_c < 0$, ions are removed from the pore solution; when $Q_c > 0$, ions are added into the pore solution.
- S_{lim}^1 and S_{lim}^2 , the upper and low limit of water saturation degree for the pore solution during drying and wetting cycles.

The initialization of parameters in the proposed hygro-chemical transport model is summarised in Table 3.2, which are indirectly estimated by the experimental tests or taken from other reports.

Table 3. 2 Initialization of parameters.

Parameter	Physical definition	Value used in analysis
C_j^0	Initial concentration of ions [mol/m^3]	0.1629 (calculated by equation (3.8))
C_{salt}^0	Initial concentration of salt [mol/m^3]	0
ϕ_0	Initial porosity	0.2
S_l^0	Initial water saturation degree	See in different cases
K_{eq}	Equilibrium constant	37.68 (in reference [125])

Q_w	Water flux term [$\text{kg}/\text{m}^3 \cdot \text{s}$]	See in different cases
Q_c	Ionic diffusion term [$\text{mol}/\text{m}^3 \cdot \text{s}$]	See in different cases

3.4.1 One single drying or wetting process

In this section, we work on five simple cases for a single hydro-chemical process. The schematic can be found in figure 3.12. The corresponding initialization of parameters can be found in Table 3.3.

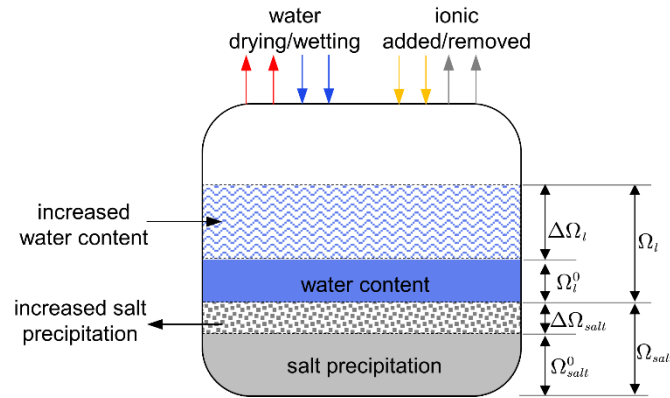


Figure 3. 12 Schematic for hydro-chemical transport in pore volume subjected to single water drying or wetting process.

Table 3. 3 Initialization parameters for one single hydro-chemical transport under five different cases.

Parameter	Water	Ions	C_j^0	C_{salt}^0	Q_w	Q_c	S_l
Case one	drying	-	0.1629	0	-1	0	0.9→0.1
Case two	wetting	-	10^{-8}	1	1	0	0.1→0.9
Case three	-	add	0.1629	0	0	10^{-6}	0.4
Case four	drying	add	0.1	0	-1	10^{-6}	0.9→0.1
		remove	0.1	0	-1	-10^{-6}	0.9→0.1
Case five	wetting	add	0.1	0	1	10^{-6}	0.1→0.9
		remove	0.1	0	1	-10^{-6}	0.1→0.9

1. Case one-precipitation.

This case deals with one single drying process without adding or removing ions. As is shown in figure 3.13 (a), the water saturation degree decreases from 0.9 to 0.1 during the drying process, and the porosity slightly decreases (from 0.2 to 0.1993, see in figure 3.13 (b)), indicating that salt precipitation appears during the drying process. Meanwhile, as water is removed from the porous material, the ionic concentration increases (see in figure 3.13 (c)). Consequently, as shown in figure 3.13 (d), the mass of Na^+ and Cl^- decreases while the mass of salt increases. However, the total mass of components is constant because of mass conservation theory (no ions are added in pore solution).

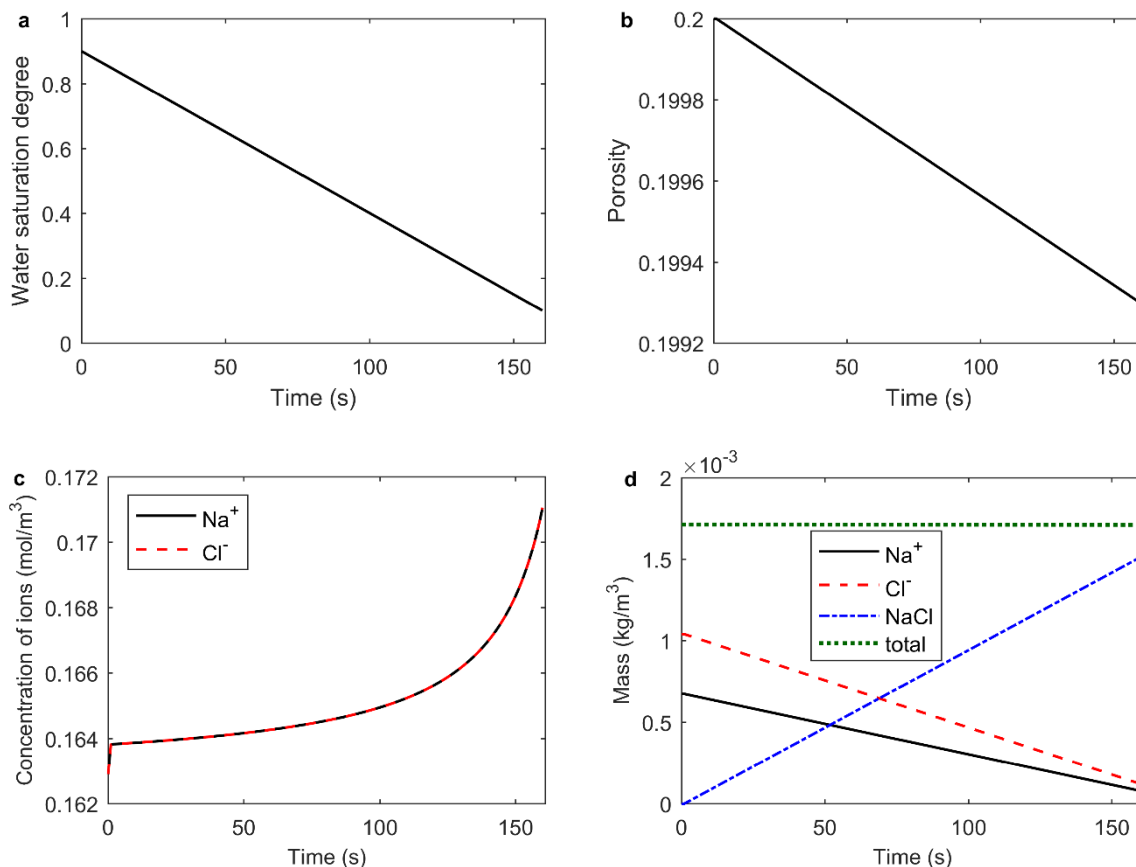


Figure 3. 13 Case one-precipitation with no ions added in the system.

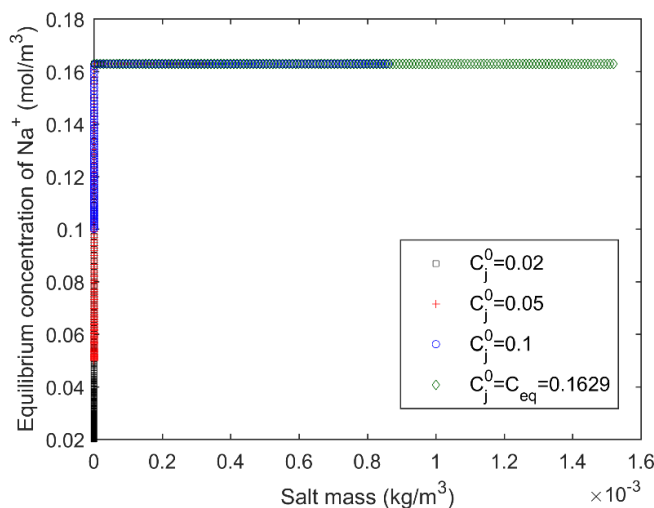


Figure 3. 14 Equilibrium concentration and salt mass in different initial cases of ionic concentration.

Figure 3. 14 investigates the relation between ionic indicator (concentration after chemical reaction) and salt mass by considering four different cases for the initial ionic concentration based on case one (during the water drying process). It can be observed that when the ionic concentration is smaller than the equilibrium constant, no salt is generated. However, as the ionic concentration increases to equilibrium concentration (0.1629 mol/m³), salt starts to precipitate, and it reveals that the larger the initial ionic concentration, the more significant the

quantity of salt precipitation.

2. Case two-dissolution.

This case investigates the water wetting process, and no ions are added and removed. In the initial stage, there is precipitated salt with the amount of $0.0012 \text{ kg/m}^3 \cdot \text{s}$ in the system. As water is added to the system at the rate of $1 \text{ kg/m}^3 \cdot \text{s}$, precipitated salt started dissolving in the pore solution. The initialization for parameters is summarised in Table 3.3.

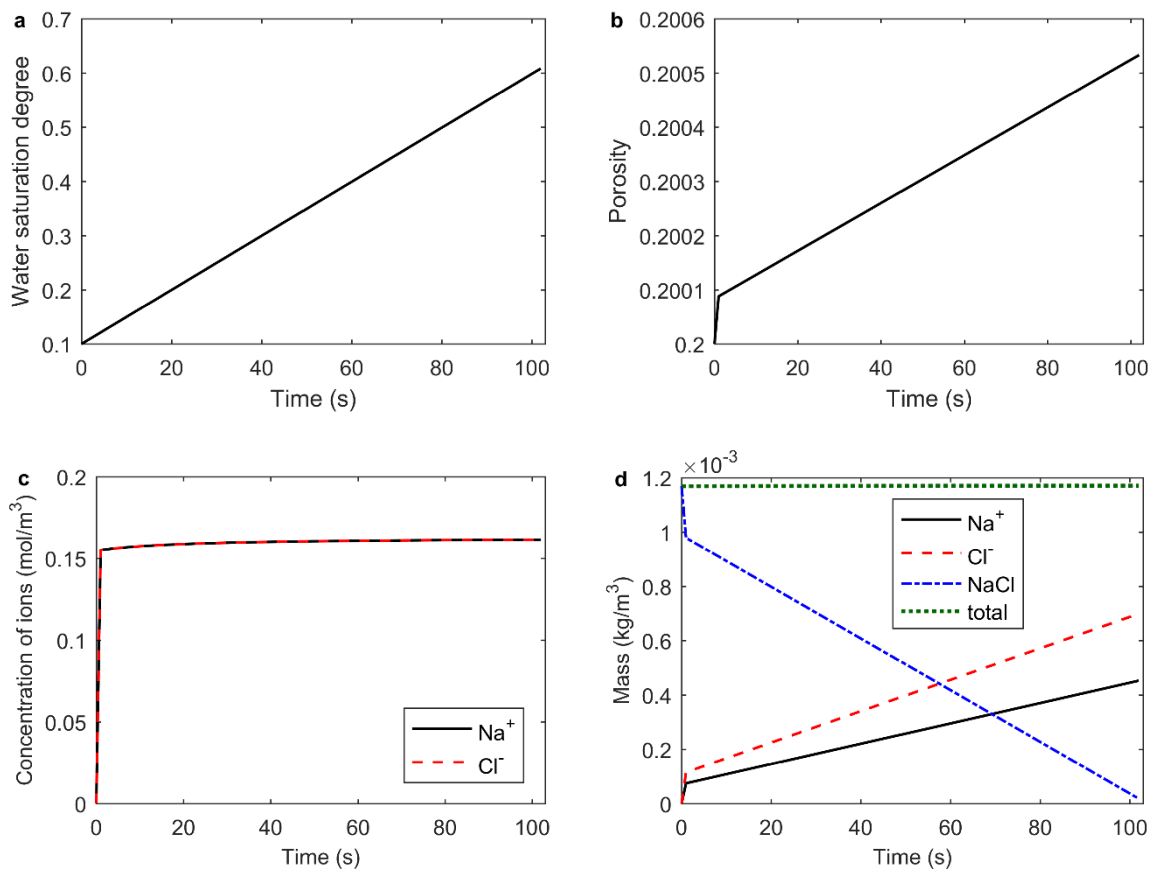


Figure 3. 15 Case two-dissolution with no ions added in the system.

It can be observed in figure 3.15a and b that during the process of water saturation degree increasing from 0.1 to 0.6, the porosity increases, which suggests that salt dissolves during wetting. Ionic concentration slightly increases (see figure 3.15c) because the water saturation degree increases and salt dissolves. Consequently, the ionic mass increases while the salt mass decreases (see figure 3.15d). Salt keeps dissolving until the chemical reaction consumes all the salt, and the time duration for this process is observed as 100s.

3. Case three-add ions, water content is constant.

This case deals with one single process: water content is constant (with the water saturation degree of 0.4); meanwhile, ions are added to the pore solution. As a result, salt precipitates, and the water saturation degree increases because the porous volume is decreasing.

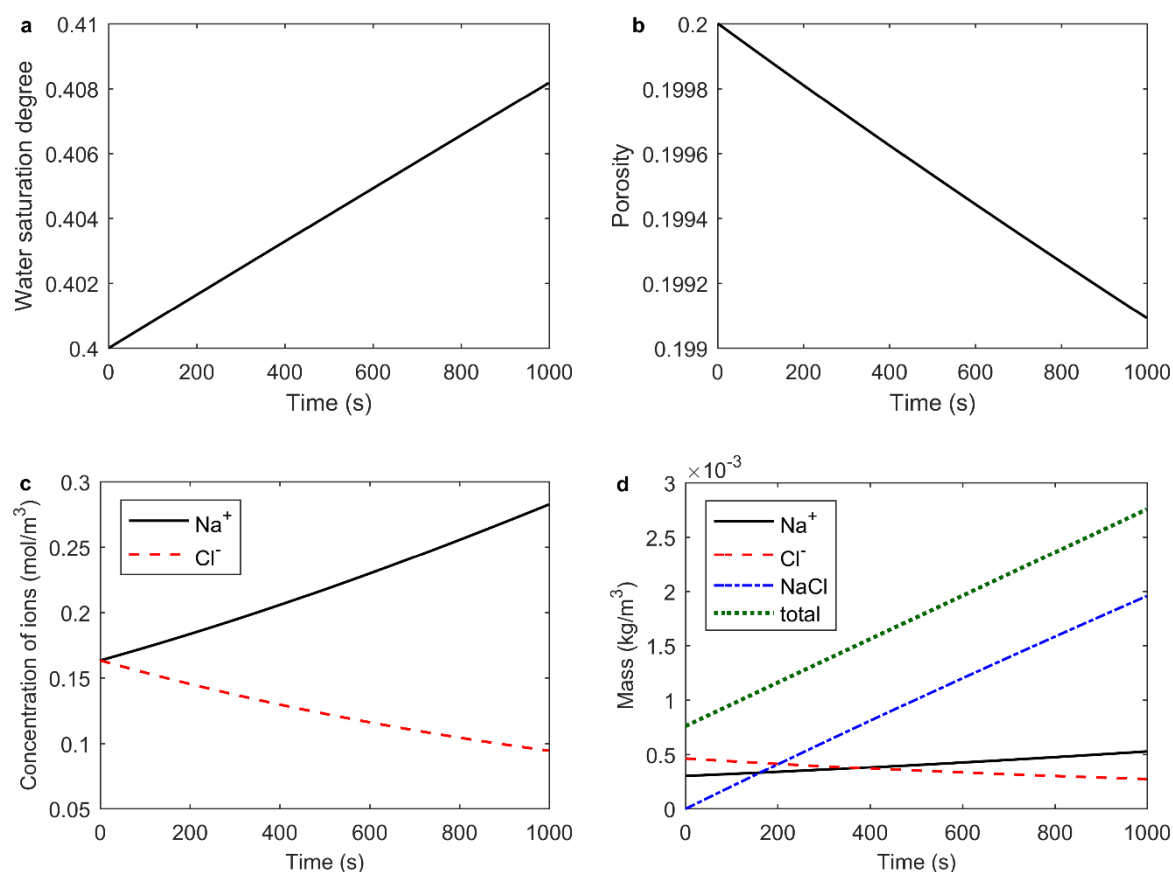


Figure 3.16 Case three- keep water content constant and add ions in the system.

It can be observed in Figure 3.16a that the water saturation degree increases, because salt precipitation occupies spaces in pore volume. Moreover, it can be observed that the concentration of Na⁺ is increasing while the concentration of Cl⁻ is decreasing. However, the product of concentration for two ionic species (predictors) is larger than the product of equilibrium concentration (indicators) so that precipitation continues generating to restore the equilibrium state of the pore solution. Meanwhile, the salt mass increases, as shown in Figure 3.16d. Thus, this case exhibits that even though the water content keeps constant, the water saturation degree may increase because the generation of salt precipitation reduces the pore volume.

4. Case four- drying process with adding/removing ions.

This case studies the drying process by adding or removing the ions in the pore solution. It can be observed from figure 3.17 that when the water saturation degree decreases from 0.9 to 0.1 (see figure 3.17a), porosity decreases in both adding and removing processes (see figure 3.17b). When adding ions in the system, the initial ionic concentration gently increases to the equilibrium concentration, during which no chemical reaction occurred, and the porosity keeps as 0.2. As the water content keeps decreasing, the concentration of Na⁺ increases and Cl⁻ decreases. Once the product of concentration for these two ionic species is larger than that of equilibrium concentration, salt precipitation generates. Thus, porosity starts to decrease. The same phenomenon can be observed in the process of removing ions from the system. A very interesting difference between adding and removing ions is that when removing the ions from

the system, the concentration of Cl^- increases while the concentration of Na^+ decreases, as shown in figure 3.17c).

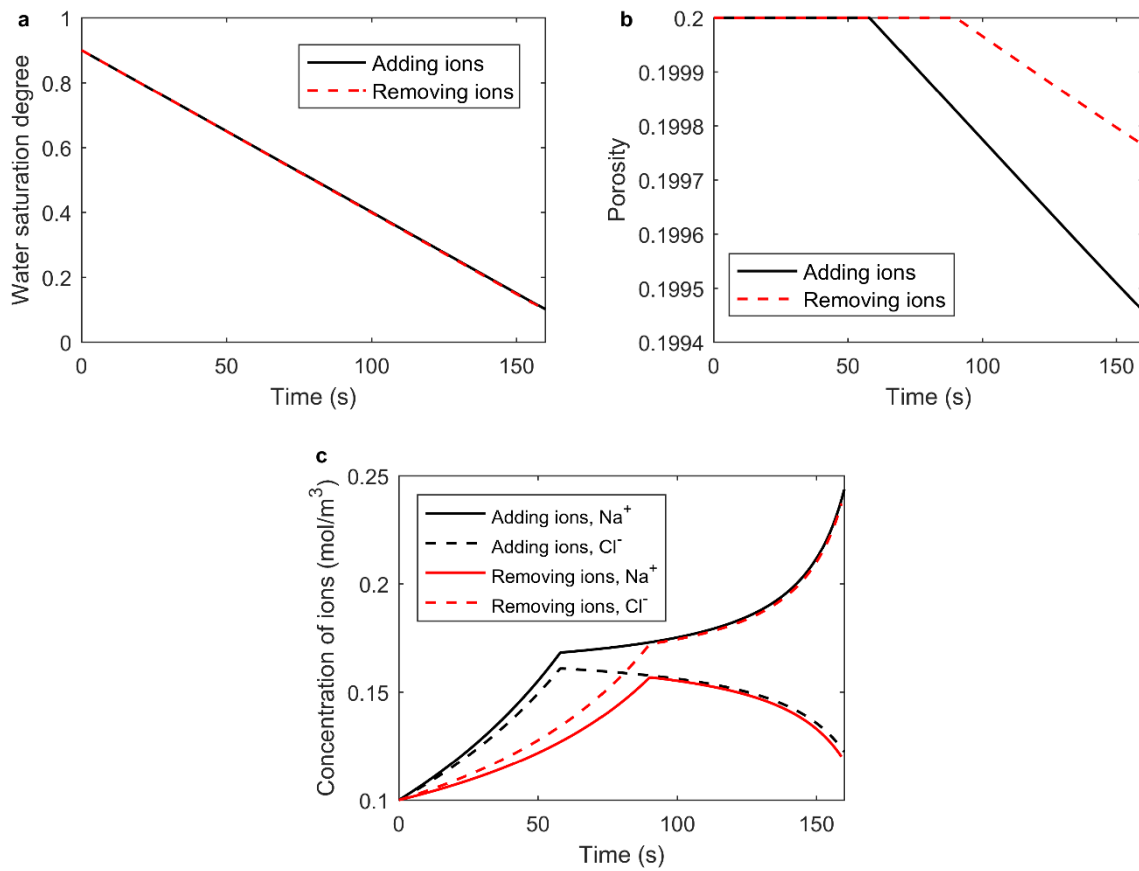


Figure 3. 17 Case four - Water drying with adding or removing ions in the pore solution.

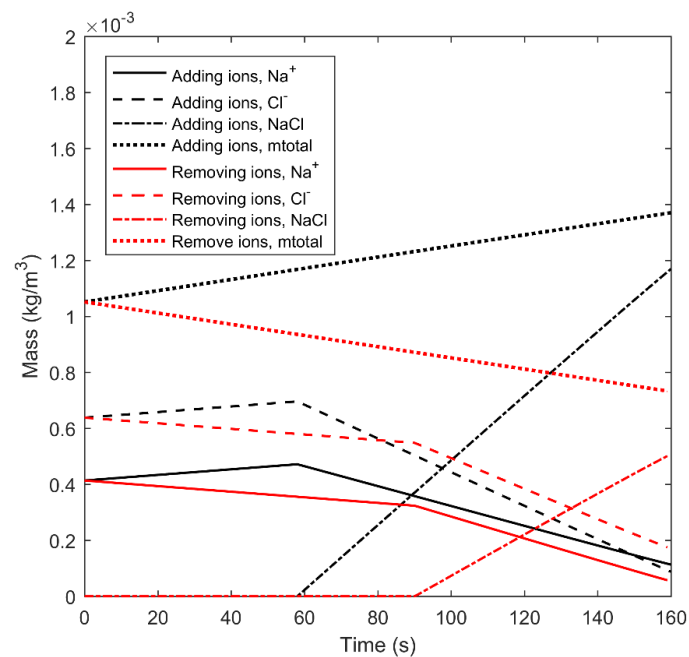


Figure 3. 18 Mass of each components during drying process.

Figure 3.18 shows that adding or removing ions during the drying process may lead to salt precipitation because of ionic concentration increase. However, it is very interesting to be found that the total mass increases during adding ions case while the total mass decreases during the removing ions process, which is consistent with the mass conservation theory.

5. Case five- wetting process with adding and removing ions.

Contrary to case four, during the wetting process, even though the ions are added in this system, the ionic concentrations of Na^+ and Cl^- keep decreasing because of the increment of water saturation degree, as shown in figure 3.19. As a result, the product of ionic concentration is smaller than the product of equilibrium concentration; and no precipitated salt is generated in the initial state. Thus, no chemical reaction occurs in this process. It can be concluded that when there is no salt precipitation in the initial state, the chemical reaction will not occur during the wetting process despite adding or removing ions in the pore solution.

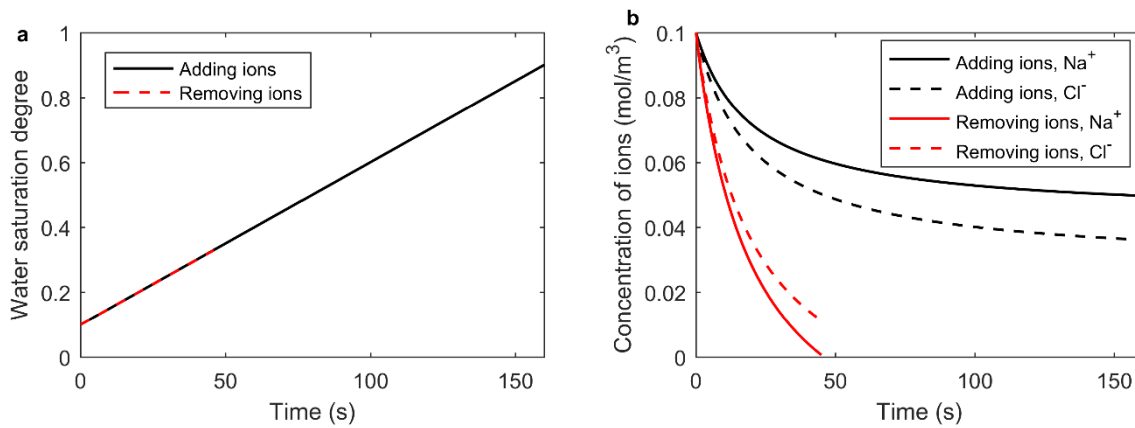


Figure 3. 19 Case five- Water wetting with adding or removing ions in the pore solution.

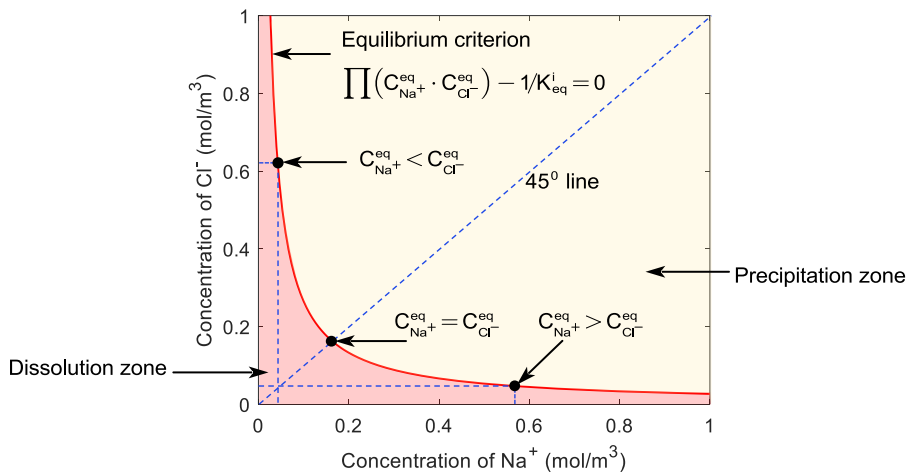


Figure 3. 20 Relation between ionic concentration (predictor) and equilibrium concentration (indictor).

Figure 3.20 presents the schematic of the equilibrium criterion that controls the salt precipitation and dissolution process based on the law of mass action. It can be found when the ionic concentration (predictor) is on the equilibrium criterion, the pore solution is in the

equilibrium state, and no chemical reaction occurs, when the ionic concentration (predictor) is on the left zone of the equilibrium curve, salt dissolution occurs. On the other hand, when the ionic concentration (predictor) is on the right zone, salt precipitation occurs. A conclusion can also be obtained based on the computational results by five cases above ; if no ions are added in the system, the equilibrium concentration for Na^+ and Cl^- (predictor) should be identical; the concentration is on the 45° line. On the contrary, when ions are added to the system, concentration distributes above (on the left side of) the 45° line (concentration of Na^+ is larger than that of Cl^-), while when ions are removed from the system, concentration distributes below (on the right side of) the 45° line (concentration of Cl^- is larger than that of Na^+).

3.4.2 Drying and wetting cycles under different Q_c

The section carries on the pore filling process by salt precipitation, during which ions are added or removed in pore solution periodically. The water saturation degree is controlled in the fixed range within $[S_{lim}^1, S_{lim}^2]$ by water supply Q_w , as presented in figure 3.21 and 3.22.

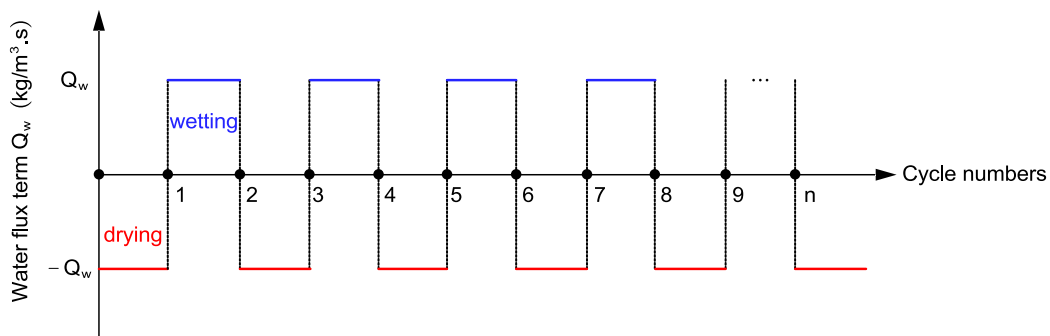


Figure 3. 21 Water flux term during wetting and drying process.

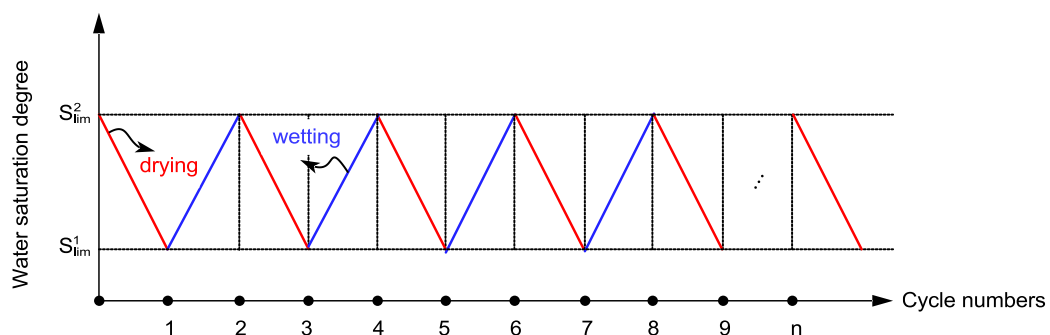


Figure 3. 22 Water saturation degree during wetting and drying process.

3.4.2.1 Water saturation degree ranges in $[0.1, 0.9]$, add ions with different Q_c

In this case, water is cyclically supplied or removed from the porous material with the quantity of Q_w . Correspondingly, water saturation degree periodically varies in the range of $[0.1, 0.9]$. In this way, the pore material undergoes cyclic drying and wetting. Meanwhile, ions (Na^+ and

Cl^-) are continuously added into the pore solution with the constant Q_c (see figure 3.23). As already stated above, salt precipitation will be generated and pore space will be filled in this case.

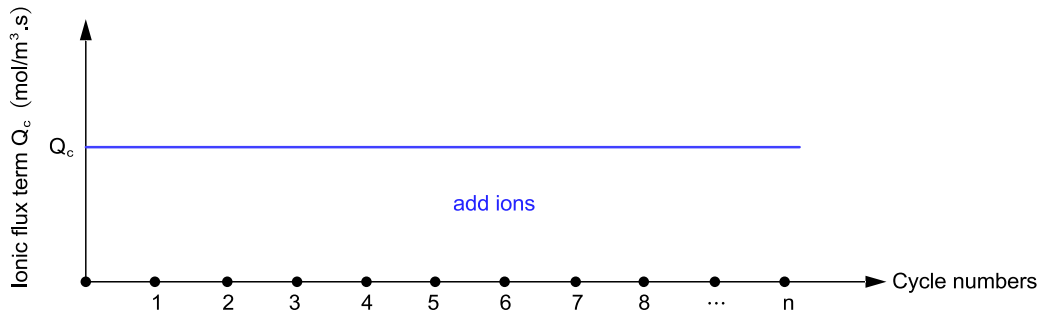


Figure 3. 23 Ionic flux term during wetting and drying process.

Figure 3.24 presents the profile of time duration under different Q_c (with a quantity of 10^{-5} , 10^{-6} and 10^{-7} mol/m³.s) during the pore filling process. In the initial stage of pore filling, the porosity is valued at 0.2, it takes 160s for one time of drying or wetting process regardless of the different ionic flux term. With the cycle numbers increasing, the time duration needs for one drying or wetting process decreases; as is observed, time duration decreases from 160s to 2s when the pores are gradually filled. This phenomenon can be explained by the reason that the quantity of water supply determines the time duration for one single process. Although the water flux term keeps constant during the whole process, the pore volume decreases because of salt precipitation. Therefore, it takes a shorter and shorter time to complete one single drying or wetting process.

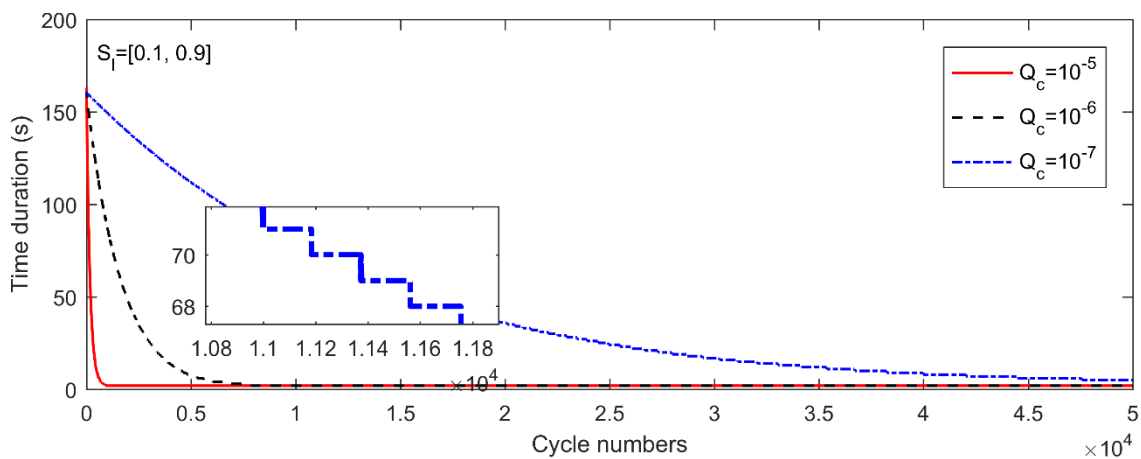


Figure 3. 24 Time duration under drying-wetting cycles with different Q_c .

Figure 3.25 shows the evolution of porosity when adding ions during drying and wetting cycles. The larger the quantity of ionic flux term, the faster the porosity decreases to zero. It is observed from computation results that after 912, and 7866, and 70438 cycle numbers of drying and wetting, the cases for adding ions with a quantity of 10^{-5} , 10^{-6} and 10^{-7} mol/m³.s induces the filled pore volume with the identical quantity of salt mass (the salt mass relative to the porous material is 426.6 kg/m³). Furthermore, the porosity profiles (jagged curve in a small window) highlights that during the drying process, salt precipitates and the porosity decreases, while during the wetting process, salt dissolves, and porosity slightly increases.

However, as the ions are added to the porous materials during drying and wetting cycles, the whole porosity remains reduced on the full-time scale. It reveals that pore volume is inclined to be filled rather than be emptied when adding ions into pore solution during drying and wetting cycles.

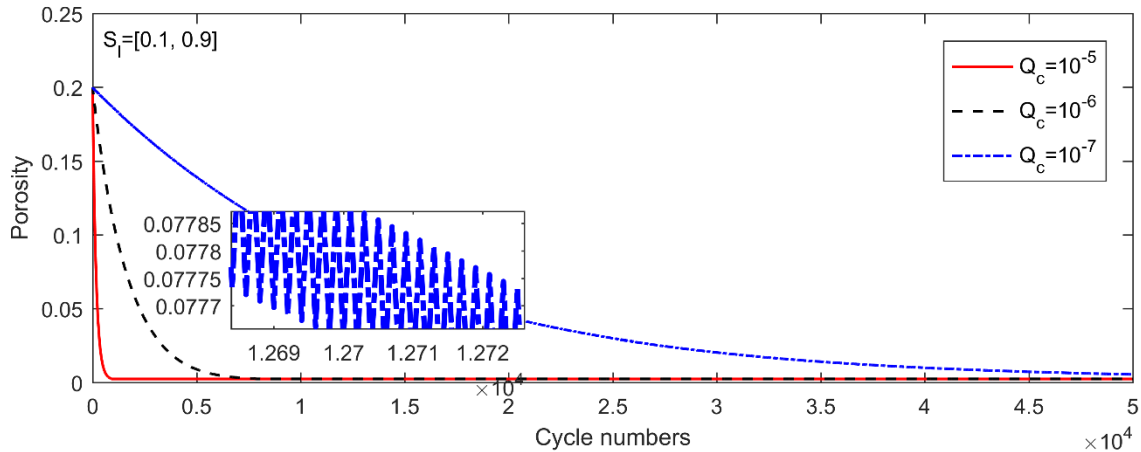


Figure 3. 25 Pore filling process under drying-wetting cycles with different Q_c .

Contrary to the porosity, the cumulative mass of salt increases with the decreased porosity when porous materials are subjected to drying and wetting cycles, as shown in figure 3.26. Repeating the drying and wetting cycles until the salt fills pore volume with the mass quantity of 426.6 kg/m^3 relative to the porous material. The salt precipitation is originated from two main causes: the ionic flux term from the external environment causing the increase of the ionic concentration in the pore solution; the drying of the porous material also increases the ionic concentration in the pore solution. Consequently, both two processes induce the salt precipitation reaction. Meanwhile, it can be observed from the jagged curve in blue that the salt mass increases after the drying process and decreases after the wetting process, which is in contradiction with the porosity evolution.

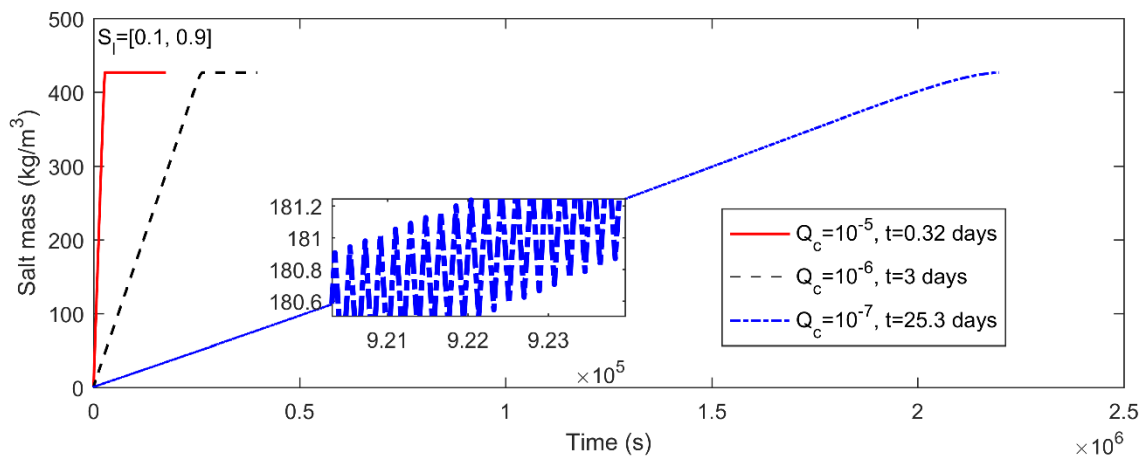


Figure 3. 26 Salt mass under drying-wetting cycles with different Q_c .

It can be observed in figure 3.27 that when Q_c is significant, for instance, $Q_c = 10^{-5} \text{ mol/m}^3 \cdot \text{s}$, ionic concentrations distribute widely, and the concentrations of Na^+ and concentration of Cl^- are significantly different (see figure 3.27a). Moreover, the concentration of Na^+ is much larger than the concentration of Cl^- during the process of adding ions. On the contrary, when Q_c is

small, such as $Q_c = 10^{-7} \text{ mol/m}^3 \cdot \text{s}$, the distribution range of ionic concentrations becomes narrow, and the concentrations for Na^+ and Cl^- are approaching the 45° line (see figure 3.27d). It can also be observed that after wetting process, the ionic concentrations (predictors) distribute on the left side of the equilibrium criterion curve; after drying process, the ionic concentrations (predictors) distribute on the right side of the equilibrium criterion curve. Moreover, after chemical reactions, the equilibrium concentrations (indicators) for both Na^+ and Cl^- are on the criterion curve. Thus, it reveals that the ionic concentration for drying and wetting cycles also obeys the law of mass action, and the evolution of ionic concentration is consistent with equation (3.31).

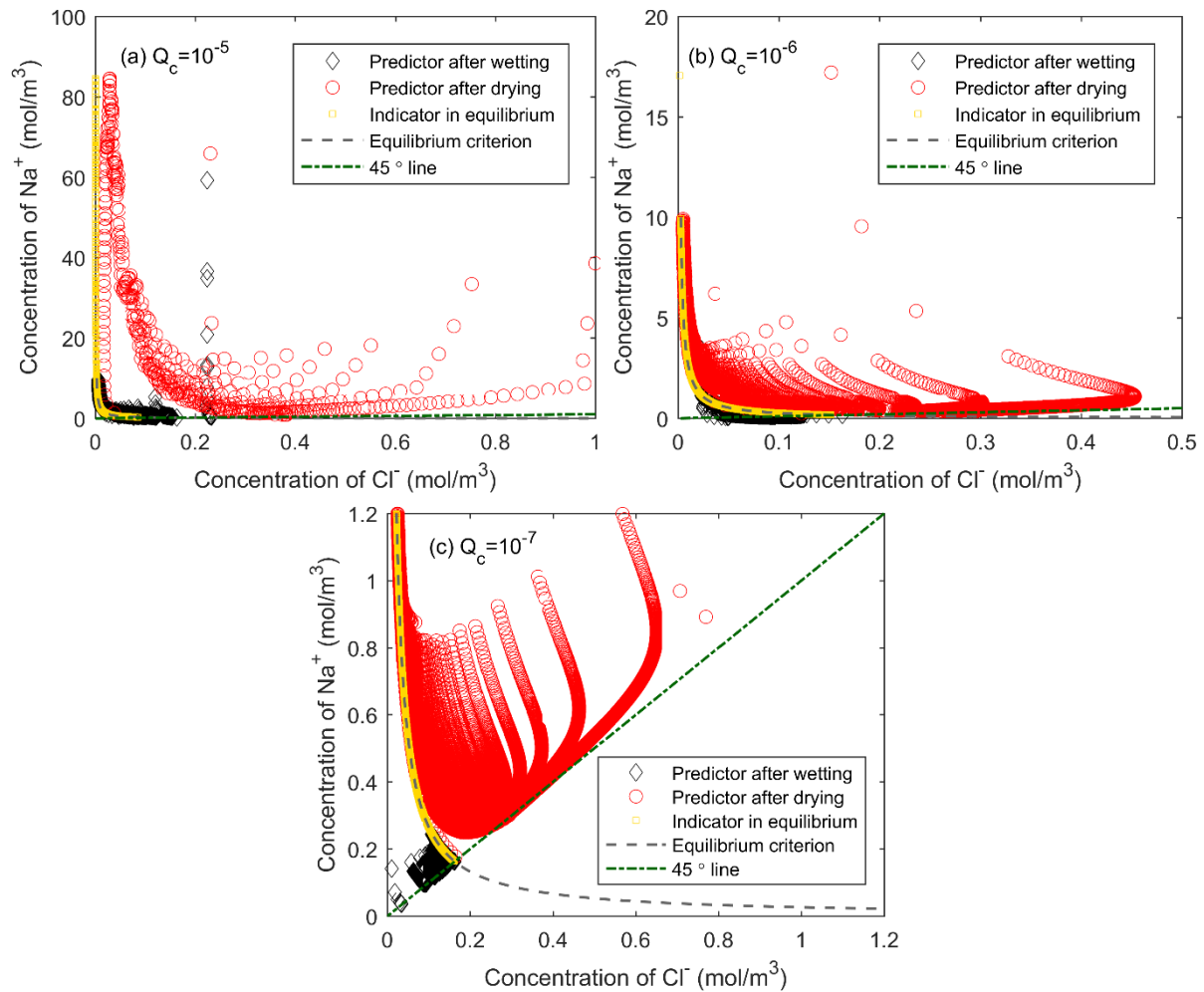


Figure 3. 27 Relation between concentration of Na^+ and concentration of Cl^- under drying-wetting cycles with different Q_c .

3.4.2.2 Water saturation degree ranges in [0.1, 0.9], add/remove ions with different Q_c

Porous materials in reality do not always undergo the case of gaining ions in the pore solution. In fact, ions may also leave from the solution during the drying and wetting cycles; thus, in this case, we investigate the situation that ions are firstly added during the k th times of cycles, and then ions are removed during the $2k$ th times of cycles, as showed in figure 3.28.

Figure 3.29 shows such a case that ions are added in pore solution during the first 100 cycle

numbers with the quantity of $10^{-7} \text{ mol/m}^3 \cdot \text{s}$. After that, ions are removed from the pore solution with the quantity of 5×10^{-8} or $1 \times 10^{-8} \text{ mol/m}^3 \cdot \text{s}$ during the second 100 cycle numbers, respectively. Repeating this process until the pore volume is filled. It reveals that removing ions from pore solution slows down the pore filling process; the larger the quantity of removing ions, the longer the porosity decreases from 0.2 to zero.

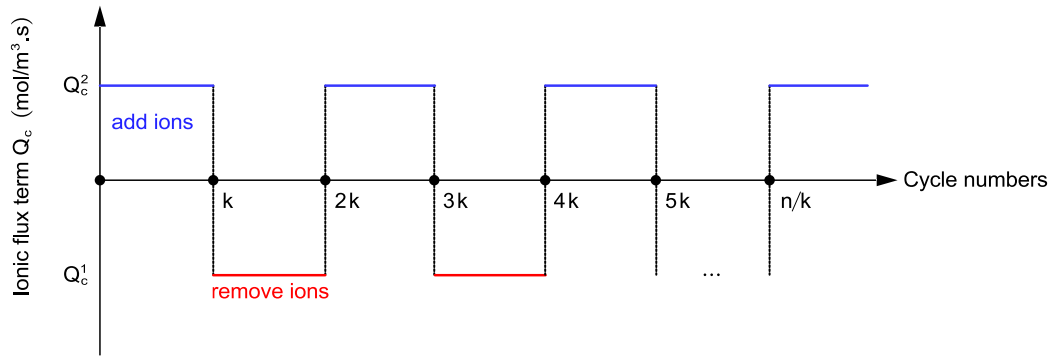
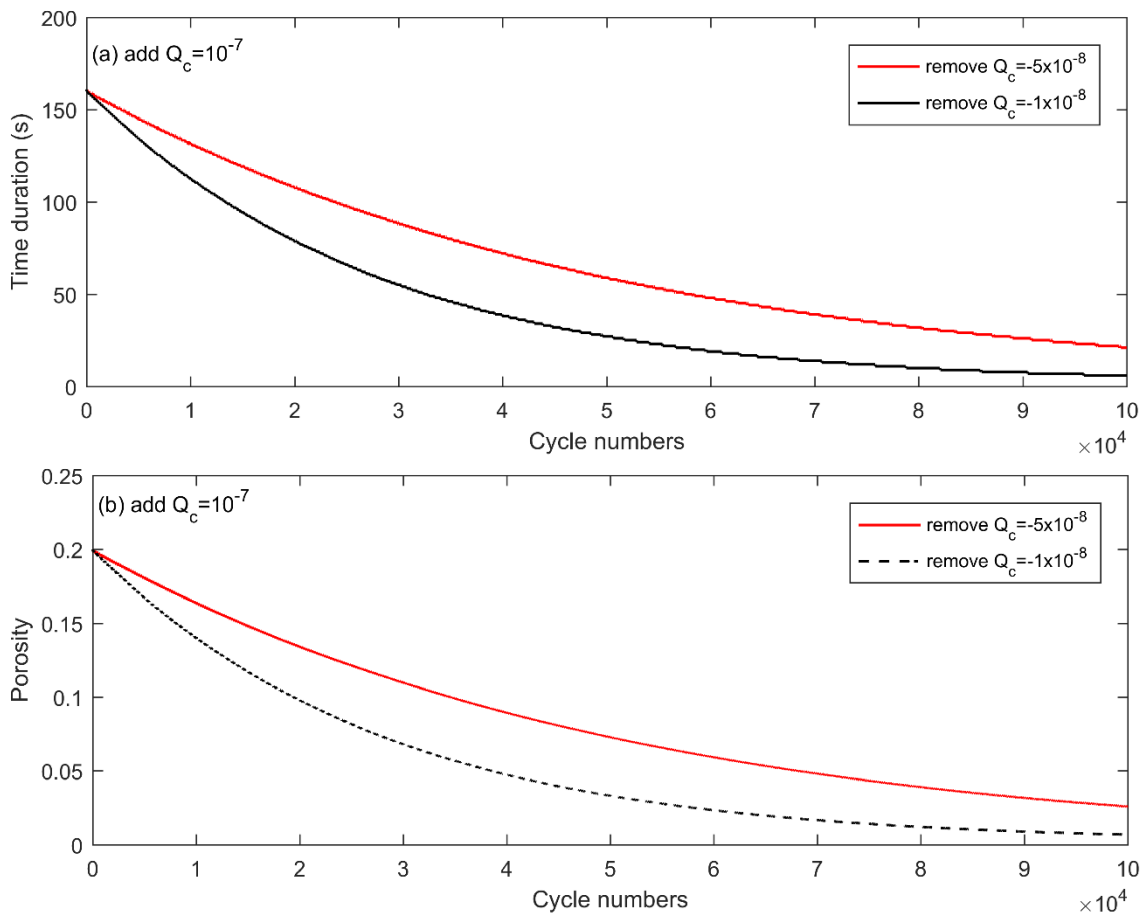


Figure 3. 28 Adding or removing ions during wetting and drying process and k is the time step for adding and removing ions.



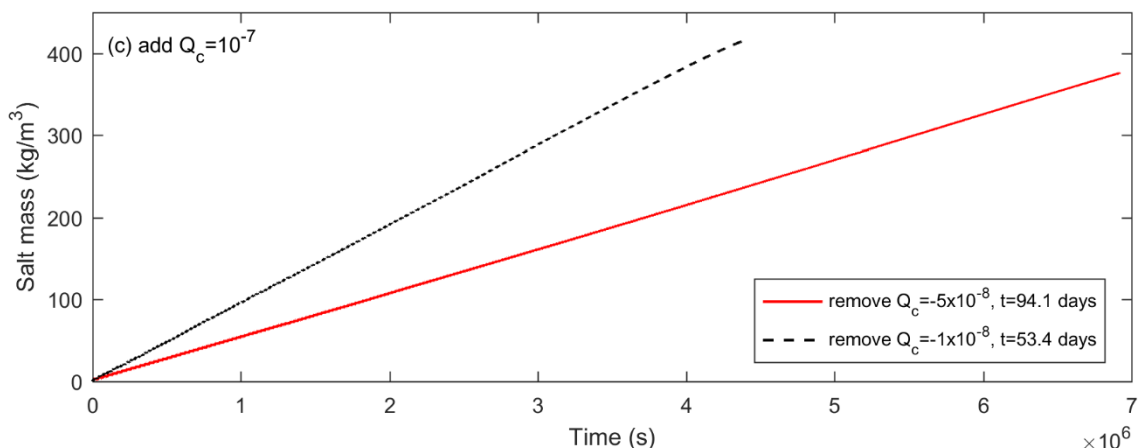


Figure 3. 29 Adding and removing ions during drying and wetting cycles, the time step k was 100.

Figure 3.39b presents that the porosity keeps decreasing although ions are periodically added and removed in pore solution. The pore volume is inclined to be fully filled after 10^5 cycle numbers of drying and wetting. The significant difference is that removing ions with the quantity of $5 \times 10^{-8} \text{ mol/m}^3 \cdot \text{s}$ requires more cycle numbers in filling pores (that is, decreasing the porosity from 0.2 to 0) than the case of periodically (at intervals of 100 cycle numbers) removing ions with the quantity of $10^{-8} \text{ mol/m}^3 \cdot \text{s}$.

The salt mass (in figure 3.29c), which is determined by salt precipitation, is also affected by adding and removing ions. The salt mass exhibits apparent fluctuation: adding ions into pore solution induces salt precipitation and removing ions from the pore solution causes salt dissolution. However, as the quantity of added ions is larger than the removed ions, the cumulative salt mass increases after several cycles.

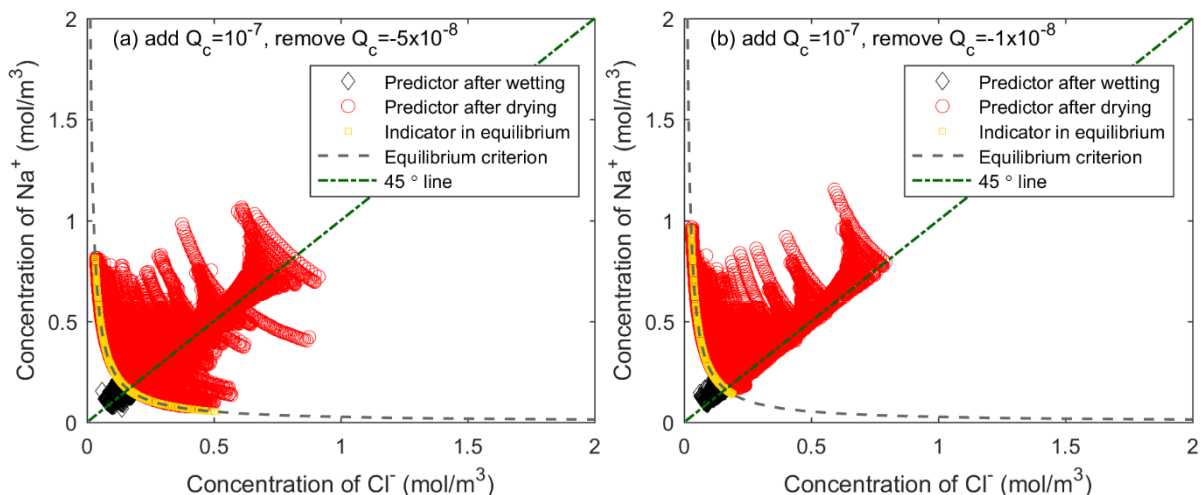


Figure 3. 30 Relation between concentration of Na^+ and concentration of Cl^- under drying-wetting cycles with the case of adding ions with $10^{-7} \text{ mol/m}^3 \cdot \text{s}$, meanwhile, removing ions with (a) $-5 \times 10^{-8} \text{ mol/m}^3 \cdot \text{s}$ and (b) $-10^{-8} \text{ mol/m}^3 \cdot \text{s}$.

It can be observed in figure 3.30 when removing ions from the pore solution, the distribution of ionic concentration may cross the 45° line because removing ions from the pore solution induces the concentration of Cl^- being larger than the concentration of Na^+ . A comparison between figure 3.33a and b suggests that this tendency becomes apparent when the quantity

of removing ions is significant.

3.4.3 Drying and wetting cycles under varying intervals of water saturation degree

Most porous materials experience various intervals of water saturation degree during the drying and wetting cycles. For instance, the building structures in the marine environment are exposed to continuous drying and wetting by tidal and splash action [132]. Different parts of the structures may be exposed to a varied intervals of water saturation degree due to drying and wetting during the same tidal cycles. Therefore, it is crucial to investigate the influence of various intervals of water saturation degree on hygro-chemical transport when porous materials are subject to cyclic drying and wetting.

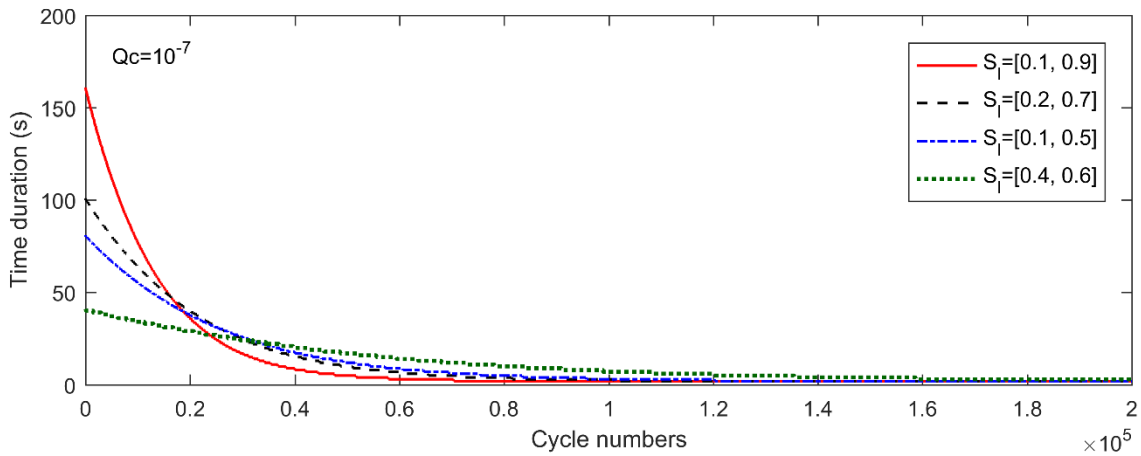


Figure 3.31 Time duration under drying and wetting cycles with constant ionic flux term (adding ions) while different intervals of water saturation degree.

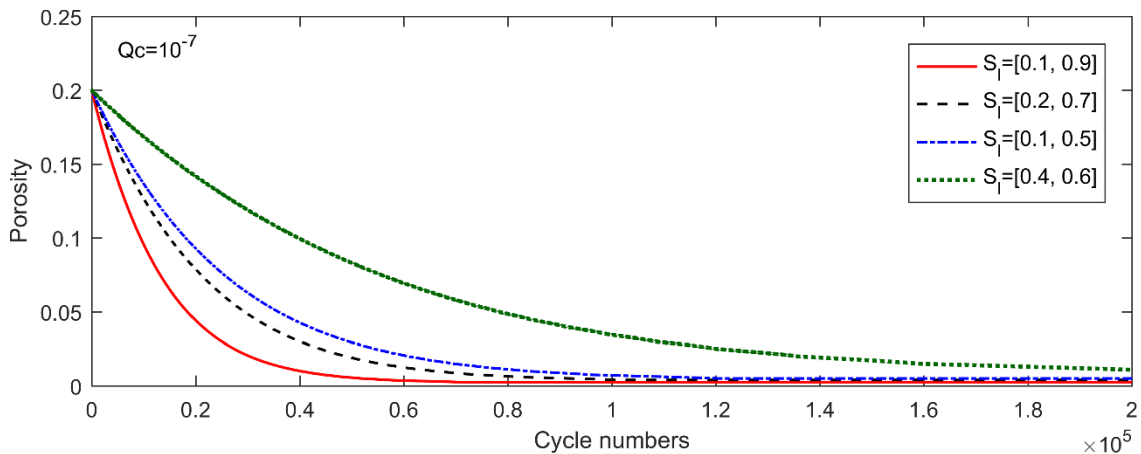


Figure 3.32 Porosity under drying and wetting cycles with constant ionic flux term (adding ions) while different intervals of water saturation degree.

It is observed in figure 3.31 that the water flux is valued at $Q_c = 10^{-7} \text{ mol/m}^3 \cdot \text{s}$ while the limitation of water saturation degree S_{lim}^1 and S_{lim}^2 varies. When the water saturation degree is in a wide range, such as $[0.1, 0.9]$, the initial time duration for single drying or wetting

process is large with the value of 160s. Moreover, the initial time duration for the single drying and wetting process is 100s, 80s, and 40s when the water saturation degree is in the intervals of [0.2, 0.7], [0.1, 0.5] and [0.4, 0.6], respectively. The results suggest that water saturation degree affects the time duration during the single drying and wetting process; the smaller the interval of water saturation degree, the shorter the time duration for one single drying and wetting process. Moreover, it should be noted that the accumulation of time durations for single transport is the exposure time required for the porous materials to be filled (by precipitated salt) after undergoing numerous drying and wetting cycles.

Figure 3.32 shows the porosity evolution under various intervals of water saturation degree due to cyclic drying and wetting. It can be observed that after undergoing the same number of cycles, the porosity decreases more significantly for the case of water saturation degree in [0.1, 0.9] than that of the water saturation degree in [0.4, 0.6]. It may be ascribed that when the porous materials are subjected to the wide range of water saturation degree, the salt precipitation is significant, which spends fewer cycle numbers for the pore volume filled. It should be noted that natural porous material in common exposure environments is exposed to less extreme moisture ranges, shorter time duration for single drying and wetting process, and less decreased porosity to those imposed in this research. Therefore, actual pore volume is likely to be less filled than the simulated results in this research.

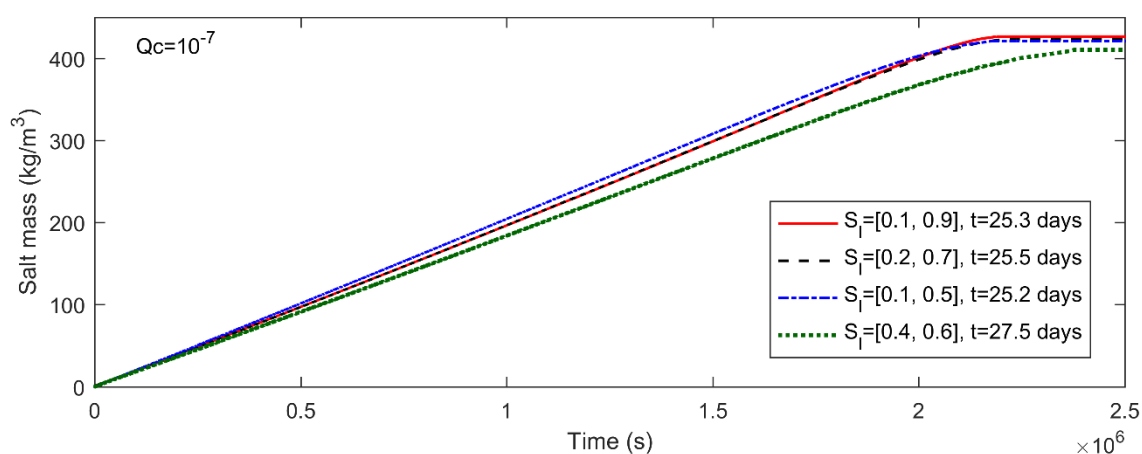


Figure 3.33 Cumulative salt mass under drying and wetting cycles with constant ionic flux term (adding ions) while different intervals of water saturation degree.

The cumulative salt mass under different intervals of water saturation degree is presented in figure 3.33. It can be observed that after a period of drying and wetting cycles, the porosity is completely filled with the same quantity of precipitated salt. The small interval of water saturation degree demands a more significant number of cycles to generate the same quantity of salt mass requires for filling all the pores. For instance, porous materials subjected to water saturation degree within the range of [0.4, 0.6] require 205510 numbers of cycles to generates the same amount of salt. In contrast, the case with a water saturation degree in the range of [0.1, 0.9] needs 70438 cycles. Although the cycle numbers are increased for the porous material that experiences a small interval of water saturation degree, it takes less time for one single drying or wetting process, as mentioned in figure 3.31. Therefore, the cumulative time required to fill the pore volume is almost the same for porous materials that undergo different intervals of water content. This result indicates that varying intervals of water content do not

induce significant differences in the time required to fill all the pores by salt precipitation when porous materials exposed to drying and wetting cycles.

It can be observed in figure 3.34 that when water saturation degree varies in extreme conditions, the concentration deviates significantly from the equilibrium state (see figure 3.34a), a large amount of salt generates during single drying or wetting process. On the other hand, when the water saturation degree varies in a narrow range (see figure 3.34d), the ionic concentration is approaching the equilibrium concentration, and the chemical reaction is not fierce in one single drying or wetting process. Thus, it requires more cycle numbers for the porous materials with a narrow range of water saturation degree to generate the same quantity of precipitated salt when compared with that of a wide range of water saturation degree.

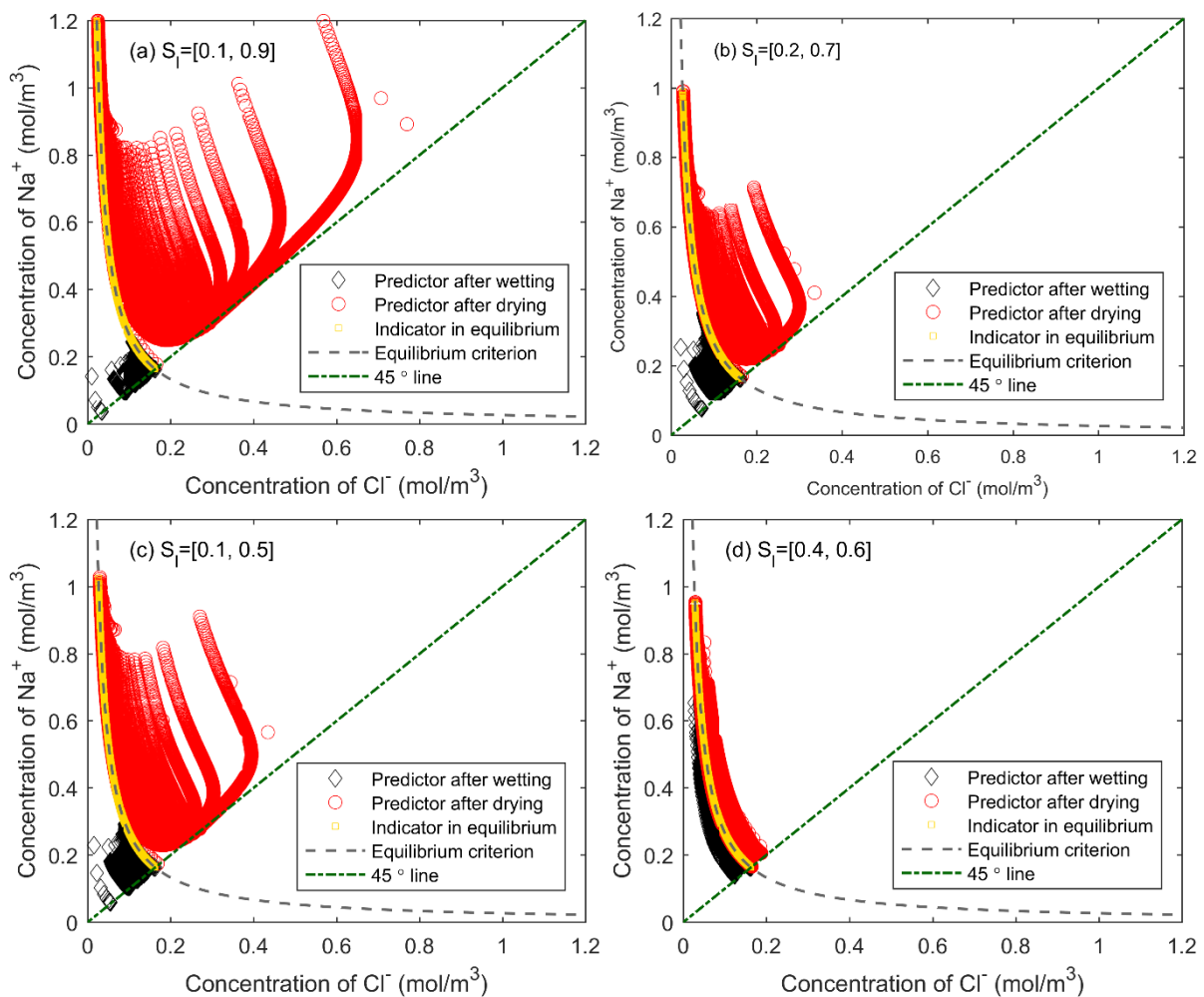


Figure 3. 34 Relation between concentration of Na^+ and concentration of Cl^- under drying-wetting cycles with the case of adding ions with $10^{-7} \text{ mol/m}^3 \cdot \text{s}$ while changing intervals of water saturation degree.

Figure 3.35 shows that ionic flux term $\text{Log}Q_c$ and cycle number $\text{Log}N$ obey exactly the linear relationship, as expressed in equation (3.32), and fitting parameters are summarised in Table 3.4. It can be found that the simulated results are fitting well with the predicted curve with very high correlation coefficients. Based on equation (3.32), one can predict the cycle numbers to fill the pore volume by taking different values of Q_c . Meanwhile, it indicates that the interval of water saturation degree significantly affects the cycle numbers; the smaller the

interval of water saturation degree, the more cycle numbers required to fill the pore volume.

$$\text{Log}N = \alpha + \beta \cdot \text{Log}Q_c \tag{3.32}$$

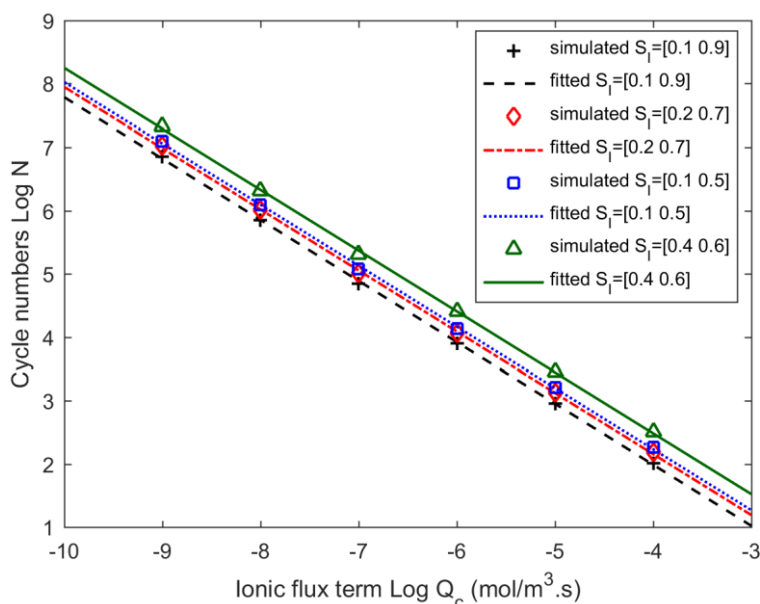


Figure 3. 35 Prediction between $\text{Log}Q_c$ and cycles numbers $\text{Log}N$ under different intervals of water saturation degree.

Table 3. 4 Fitting results for relation between Q_c and cycle numbers N .

Water saturation degree	α	β	R^2
[0.1, 0.9]	-1.8757	-0.9662	1
[0.2, 0.7]	-1.7022	-0.9650	1
[0.1, 0.5]	-1.6251	-0.9649	1
[0.4, 0.6]	-1.3583	-0.9608	1

Figure 3.36 gives prediction curves between ionic flux term and exposure time for filling pores (with porosity decreased from 0.2 to 0) under different intervals of water saturation degree. The relation between $\text{Log}Q_c$ and $\text{Log}t$ presents the linear relationship (Q_c and t follows exactly the power equation) with the good correlation coefficients that compromises at one. The fitting function is expressed in equation (3.33), and the fitting parameters are summarised in Table 3.5. It can be found that the simulated results are fitting well with the predicted curve. Moreover, the fitting curves under different intervals of water saturation degree are almost overlapped, revealing that varying the interval of water saturation degrees do not affect the cumulative time required for filling the pores. With this relation, one can predict the exposure time to fill the pore volume by taking different values of Q_c . For instance, if the ionic flux term is valued at $10^{-9} \text{mol/m}^3 \cdot \text{s}$, and the predicted time is 4.85 years for the porosity decreased from 0.2 to 0 when porous materials are subjected to the water saturation degree with the range of [0.1, 0.9]. Meanwhile, the predicted time is about 4.97 years for the case with the water saturation degree varied in the range of [0.4, 0.6]. The prediction results are consistent with

our modelling results; that is, varying intervals of water saturation degree induces no significant impacts on exposure time required to fill pore volume when porous materials are subjected to the same ionic flux term.

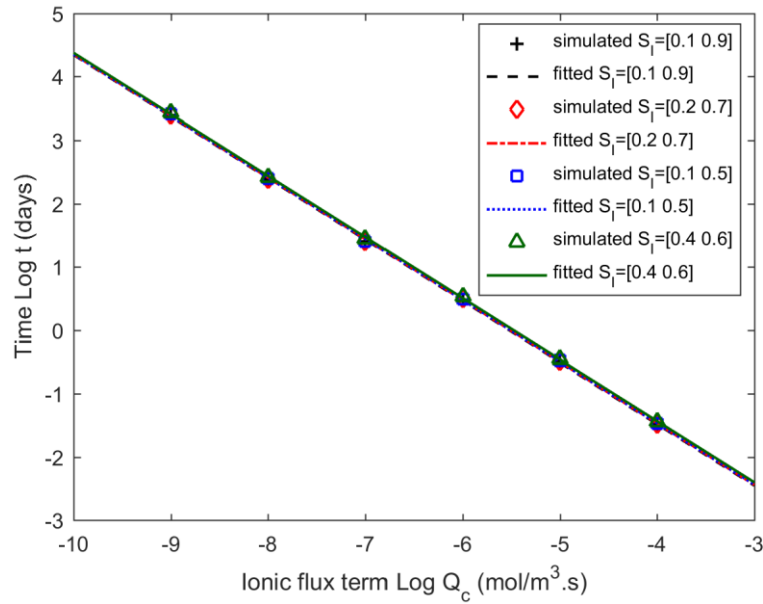


Figure 3. 36 Prediction between $\text{Log}Q_c$ and cumulative time $\text{Log}t$ under different intervals of water saturation degree.

$$\text{Log}t = a + b \cdot \text{Log}Q_c \quad (3.33)$$

Table 3. 5 Fitting results for relation between Q_c and time t .

Water saturation degree	a	b	R ²
[0.1, 0.9]	-5.3648	-0.9709	1
[0.2, 0.7]	-5.3505	-0.9702	1
[0.1, 0.5]	-5.3459	-0.9699	1
[0.4, 0.6]	-5.3036	-0.9680	1

3.5 Conclusions

In this section, a local-like model is developed to deal with water-ionic transport coupling with salt precipitation and dissolution when porous materials are subjected to drying and wetting cycles. The proposed model consists of transport equations according to the mass balance theory and the chemical reactions based on the law of mass action. Operator-splitting method is used to solve the hydro-chemical equations. By adopting this model, the transport process in porous material under drying and wetting cycles are investigated, and the following conclusions can be drawn:

For the single drying or wetting process, even if no additional ions are added or removed in the saline solution, salt precipitates when the porous material is dried out; salt dissolves when

the porous material is rewetted. For the case that ions are added into the pore solution while keeping water content constant, salt precipitates out when the ionic concentration is over the equilibrium concentration. Consequently, water saturation degree increases due to the reduction of the pore volume. For the case that both water and ions simultaneously transport in the pore solution, precipitation or dissolution appears conditionally when the product of ionic concentrations deviates from the product of equilibrium concentrations.

When porous material is subjected to drying and wetting cycles, it is observed that the water flux term Q_w is the main factor to determine the time duration for the transport process. The larger the value of the water flux term, the faster the water saturation degree decreases or increases to limitation. Moreover, it is observed that when keeping continuously adding ions into pore solution during cyclic exposure, water drying induces a more significant reduction of porosity (pore filling) compared to water wetting. Because of this, the pore volume is inclined to be filled rather than emptied when porous materials are subjected to drying and wetting cycles.

As salt precipitation partially originated by ions transport from the external environment, the ionic flux term Q_c significantly affects salt generation. A significant ionic flux term induces a considerable amount of salt precipitation. Consequently, the pore volume can be filled after experiencing a short time of drying and wetting cycles. For instance, it takes about 27 and 246 days to fill the pore volume by adding ions into the pore solution with the rate of 10^{-7} and 10^{-8} mol/m³.s, respectively, when porous materials are subjected to cyclic drying and wetting varying within the water saturation degree of [0.1, 0.9].

Furthermore, the simulation results for adding and removing ions periodically (by a constant time step, for instance, 100 steps) suggest that when the quantity of added ions is more significant than removed ions from pore solution, salt precipitation is inclined to be generated. Subsequently, pores are filled after a period of drying and wetting exposure.

The effects of varying intervals of water saturation degree on salt precipitation are investigated. When porous materials are exposed to an extreme interval of water saturation degree, the concentrations of Na⁺ and Cl⁻ deviates significantly from equilibrium concentration. Thus a large amount of salt precipitation is generated for a single time of the drying or wetting process, which reduces the cycle numbers required to fill the pore volume. However, an extensive range of water saturation degrees requires a longer time for single drying and wetting cycles. Thus the exposure time (accumulation of time duration for every single time of drying or wetting process) is not changed. It suggests that the interval of water saturation degree does not affect the exposure time required to fill pore volume when porous materials are subjected to drying and wetting cycles with the same ionic flux term.

It is important to emphasize that the deteriorations associated with drying and wetting cycles are extremely time-consuming due to the slow process of water and ions intrusion. For instance, porous materials may experience a long time for drying by decreasing the water saturation degree from 0.9 to 0.1, not merely spending 160s as is computed in our modelling simulations. Thus, more sensible (small quantity) water and ionic flux terms should be considered for a more realistic transport process in further investigation.

Adopting the proposed model can evaluate how long the pore volume is filled by salt precipitation when porous materials are subjected to cyclic drying and wetting. This model provides a pore-scale view of the transport process incorporating the chemical reactions, which can be used for numerous applications in computing deterioration-related problem.

Appendix 3A. Iterative schema for local chemical equilibrium

Precipitation and dissolution of solid-phase are the chemical reactions that can be described by a set of nonlinear algebraic equations under local equilibrium condition:

$$K_{eq}^i \prod_{j=1}^{N_s} \left(c_j^0 - \prod_{k=1}^{M_p} a_{kj} \Delta c_{s-l,k} \right)^{a_{ij}} - 1 = 0 \quad (3A.1)$$

Then the criterion of chemical equilibrium based on the law of mass action is implemented to discriminate the salt precipitation or dissolution, as is show in equation (3.7).

$$f_i = K_{eq}^i \prod_{j=1}^{N_s} (c_j^0)^{a_{ij}} - 1 \quad (3A.2)$$

Note that equation (3.6) is a set of non-linear equations, which can be solved by the Newton-Rapson method. The initial concentration c_j^0 in equation (3.6) is inputs and the increased concentration of the precipitated species $\Delta c_{s-l,k}$ is the essence to figure out, which are lumped into a vector of unknowns, $\mathbf{X}_i (i = 1, 2, \dots, M_p)$. As we have M_p equations and M_p unknowns, then the unknowns can be updated as follows:

$$\mathbf{X}_i^{n+1} = \mathbf{X}_i^n + \Delta \mathbf{X}_i^n \quad (n = 0, 1, 2, \dots) \quad (3A.3)$$

where n is the iteration number and $\Delta \mathbf{X}_i^n$ is the increment of unknowns denoted as

$$\Delta \mathbf{X}_i^n = J^{-1}(\mathbf{X}_i^n) f(\mathbf{X}_i^n) \quad (3A.4)$$

where J is the Jacobian matrix and $f(\mathbf{X}_i^n)$ is the vector of residuals. The iteration will repeat until convergence is attained. In this algorithm, the convergence criterion is that the L2-norm of $\Delta \mathbf{X}_i^n$ satisfied a specified tolerance, which is expressed as

$$\|\Delta \mathbf{X}_i^n\| \leq err \quad (3A.5)$$

Except for the Newton-Raphson method, the modified Newton-Raphson method and Boyden method are also adopted to solve equation (3.6) in order to determine the most appropriate one that is the least time-consuming. Figure 3.2 presents us the schema of the chemical box realized by MATLAB code. In this chemical box, we first give the inputs such as initial ionic concentration, initial salt concentration, the equilibrium constant, and the essential information for the chemical equations. Then the criterion of chemical equilibrium based on the law of mass action is implemented to discriminate the salt precipitation or dissolution, as shown in equation (3.7). After that, the three Newton-Raphson methods are integrated to solve the nonlinear algebraic equations. Meanwhile, the integration process makes it possible to switch from one method to another in the case of non-convergence of the current method. Finally, we get the computational results of incremental concentration for precipitated species and ionic concentration (in equilibrium state) after chemical reactions. This chemical box can deal with several reactions simultaneously, which are governed by the criterion of chemical equilibrium, *i.e.*, the law of mass action.

Appendix 3B. Solution procedure of transport equations

In the proposed local-like transport model, the water flux term and ionic flux term are time-dependent only, which can be regarded as constant inputs. The evaporation term is supposed to be zero, and the water flux term is shown in equation (3.26):

$$Q_w = \text{div}(m_w v_{w-l}) + \text{div}(m_w v_{l-s}) = \text{cte} \quad \text{and} \quad \dot{m}_{vap} = 0 \quad (3B.6)$$

Thus, the water conservation equation can be simplified as:

$$\frac{\partial m_w}{\partial t} + Q_w = 0 \quad (3B.7)$$

Substituting equation (3.23) into equation (3.27) can obtain:

$$\frac{\partial}{\partial t}(\rho_w \phi S_l (1 - \sum_{j=1}^{N_s} c_j \omega_j)) + Q_w = 0 \quad (3B.8)$$

which can be extended as:

$$\rho_w \frac{\partial(\phi S_l)}{\partial t} - \rho_w \left(\sum_{j=1}^{N_s} \frac{\partial(c_j \phi S_l)}{\partial t} \omega_j \right) + Q_w = 0 \quad (3B.9)$$

Let us denote that $B(t) = \phi S_l$ and $B_0 = \phi_0 S_l^0$, then equation (3B.9) can be expressed as:

$$\rho_w \frac{\partial(B)}{\partial t} - \rho_w \sum_{j=1}^{N_s} \left(\frac{\partial(c_j B)}{\partial t} \omega_j \right) + Q_w = 0 \quad (3B.10)$$

Meanwhile, in our local-like model, the precipitation salt at the initial state ($t=0$) was also assumed as zero, the ionic flux term are considered as constant and denoting by Q_c :

$$Q_c = \text{div}(m_j v_{j-l}) + \text{div}(m_j v_{l-s}) \quad (3B.11)$$

Therefore, the mass balance of the dissolved ions can be expressed as:

$$\frac{\partial m_j}{\partial t} + Q_c = -\dot{m}_{i-j} \quad (3B.12)$$

By substituting equation (3.22) into equation (3.29), we have:

$$\frac{\partial(c_j B)}{\partial t} + \frac{Q_c}{M_j} = 0 \quad (3B.13)$$

Thus, equation (3B.13) can be solved by given an expression for function $c_j(t)B(t)$, which is expressed as:

$$c_j B = -\frac{Q_c}{M_j} t + c_j^0 B_0 \quad (3B.14)$$

By substituting equation (3B.14) into equation (3B.10), we have:

$$\rho_w \frac{\partial(B)}{\partial t} + \rho_w \sum_{j=1}^{N_s} \left(\frac{Q_c}{M_j} \omega_j \right) + Q_w = 0 \quad (3B.15)$$

Solving equation (3B.15) can obtain:

$$B = -\left(\sum_{j=1}^{N_s} \frac{Q_c \omega_j}{M_j} + \frac{Q_w}{\rho_w} \right) t + B_0 \quad (3B.16)$$

Thus, the ionic concentration for the j th species after adding or removing water and ions (quantified by water flux term Q_w and ionic flux term Q_c) was expressed as:

$$c_j = \frac{-\frac{Q_c}{M_j} t + c_j^0 B_0}{-\left(\sum_{j=1}^{N_s} \frac{Q_c \omega_j}{M_j} + \frac{Q_w}{\rho_w} \right) t + B_0} \quad (3B.17)$$

The water saturation degree after water and ionic transport can be read as:

$$S_l = \frac{B}{\phi} \quad (3B.18)$$

It should be noted in equation (3B.18) the porosity is determined by salt precipitation and dissolution reaction, which can be calculated according to equation (3.17) (after salt precipitation or dissolution). Moreover, when the time $t > 0$, chemical reaction occurred, and \dot{m}_{i-j} is not zero, the corresponding variation of ionic mass relative to precipitated or dissolved salt should be taken into account in (3.29).

Chapter 4

Modelling of Water Sorption Isotherm and Permeability Based on the Probabilistic Approach of Pore Structure Evolution

4.1 Introduction

Moisture in porous material plays a vital role in the degradation of porous materials. Moisture provides a carrier and path for aggressive chemical species in a porous material, leading to degradations due to relevant physical and chemical processes such as salt precipitation and dissolution [1,4]. Success in modelling moisture distribution and its relevant coefficients is of utmost importance for assessing the durability of porous materials. To a large degree, moisture-related coefficients alter with the moisture distribution in porous material [3]. However, it is difficult to precisely evaluate the moisture-related coefficient by experimental measurements or connect it with the pore size distribution. Therefore, numerical modelling method on the basis of pore size distribution is essential to illustrate the mechanisms of water-dependent behaviour in a porous material, further estimate their service life, and improve their quality. Water sorption isotherm is such an essential material characterization that can evaluate the pore size distribution as well as connect the water content in porous materials with the external environmental conditions.

Water sorption isotherm in porous materials describes the relationship between relative humidity (RH) and equilibrium water content, which is very important in describing the water-dependent activities [49], such as water-vapour transitions in porous materials. Additionally, the derived properties from the water sorption isotherms are essential in modelling some durability-related processes such as drying, shrinkage, leaching, acid and sulphate attacks, freeze-thaw attacks, and carbonation-induced corrosion [133]. The relative humidity (RH) is a decisive parameter having clear relation with capillary pressure. Based on the determined water sorption isotherm, it is possible to further derive the capillary interface (waterfront) in a porous material. By doing this, a representation of the water content against relative humidity is build up. As suggested in previous reports [49], relative humidity closely relates to the

moisture transport in porous materials. When the RH is small, water is mainly distributed in small pores [6], which dominate the bottle-neck effects while making a slight contribution to moisture transport. When the RH is large, water appears in large pores, such as larger gel pores and capillary pores, significantly affecting water front and moisture transport movement. Therefore, a modelling approach for the description of water sorption isotherm should be the first step in order to gain a good estimation for the water-related processes in porous materials.

Many models for water sorption isotherm of porous materials have been developed in the last decades, such as Brunauer-Skalny-Bodor (BSB) model, Brunauer-Emmett-Teller (BET) model, and dynamic vapour sorption (DVP) method [49,133]. In this chapter, the water sorption isotherm of the porous materials is modelled based on the proposed probabilistic pore size distribution model. This model is developed with an assumption of cylindrical pores in a partially saturated state. Firstly, the water front in the porous network is determined by adopting the equilibrium relations between liquid water and the gaseous phase. After that, the water saturation degree under arbitrary relative humidity in porous materials is derived according to our porous network model.

In addition to interpreting the relationship between relative humidity and water content in porous materials under an isothermal condition, water sorption isotherm can also derive transport properties such as permeability and diffusivity of porous materials at different saturation levels [134]. In this chapter, the permeability of porous material is investigated based on the water sorption isotherm and the proposed probabilistic pore size distribution model.

Permeability is a significant indication in describing the moisture transport in porous materials. Many experiential measurements can be adopted to test permeability. For instance, the inputs method, in which the depth of water penetration is measured, and the output method, in which a steady-state outflow of fluid through a porous material is recorded [135]. In addition, the water permeability method is also an available measurement to obtain the permeability in porous material by saturating the specimen using a high-pressure triaxial cell [136]. However, such direct measurements of permeability are complex in some cases. As has been illustrated by Ait-Mokhtar et al. [95] in experimental research, a good measurement of permeability requires perfect saturation of the materials, which is difficult to obtain. Moreover, the high pressure during measurement may damage the pore structure by the load-induced cracking in porous materials when the specimen has a very low permeability. Therefore, the numerical modelling for permeability of porous materials should be a good choice when the experimental measurement is impossible.

It is commonly used to relate permeability in porous materials to its porosity, for instance, the Darcy-Poiseuille model, the Archie model, the Katz Thompson model, and the Carman-Kozeny model [42]. However, porous materials with the same average pore size and porosity but different porous populations can have very different permeability. Regardless, these models themselves have limitations; for instance, the Katz Thompson model works better for the porous system with the interconnected capillary pores than the system in which the gel pores dominate the transport [137]. Unfortunately, the prediction models that consider the pore size distribution and pore morphology are inadequate. Holly et al. [47] have stressed that

opened and connected pores strongly influence permeability while the relation between pore size distribution and permeability remained unclear. Thus, it is crucial to evaluate the permeability by considering the pore size distribution and more morphological details about pores.

As to the complex and heterogeneous pore shapes in a porous material, probabilistic pore size distribution is a valuable tool for the description of pore size distribution. Ait-Mokhtar et al. [95,138] proposed an analytic model to describe the permeability with the connection of porosity based on the statistical pore size distribution. The pore sizes, measured by MIP, were described as a lognormal distribution. The water permeability was interpreted according to Darcy's law and Hagne-Poisuille law. By investigating the permeability for three mortars and the granite, it was observed that permeability was affected dramatically by the porosity. Amiri et al. [89] developed a modelling approach for predicting permeability, which considered more factors by introducing a tri-dimensional cubic pore network, including porosity, tortuosity, critical pore radius, and constrictivity. This work introduced polymodal distributions and explored the possibility of applying this model to all shapes of pore size distribution. The simulated results revealed that the constrictively factor determined by the number of modes for pore size distribution dominated the permeability. This chapter aims to develop an analytical model for permeability based on the probabilistic pore size distribution model to explore how porosity and pore size distributions affect the permeability in the porous material.

With this motivation, this chapter consists of two main contents. Firstly, the analytical model for water sorption isotherm is developed based on the proposed probabilistic pore size distribution model. By adopting this analytical model, each relative humidity value can correspond to the pore size determined by the capillary pressure according to the Young-Laplace equation and Kelvin's equation. With the determination of the critical pore size for the water front, the external relative humidity is linked with the water front in the porous material. Thus, the water saturation degree under the given relative humidity can be derived by adopting the probabilistic network model. The second part first clarifies intrinsic permeability, liquid water permeability, gas permeability, relative liquid permeability, and relative gas permeability in porous materials. After that, numerical models for each permeability are presented by a network model of its microstructure. Effects of modified porosity and pore size distribution are investigated by introducing two different cases of water front derived from the water sorption isotherm under given relative humidity. The first case is that porous material is subjected to constant relative humidity with the permanent water front. In order to investigate the effects of porosity change on permeability, the analytical model for permeability is developed based on the successive transformations of pore size distribution regarding two different transformation models for pore sizes with the constant water front. The second case is the varying relative humidity and moved water front in the probabilistic porous network by developing an analytical model for permeability based on the single transformation of pore size distribution regarding two different transformation models of pore size modification due to salt precipitation and dissolution. Finally, the permeability model is validated by comparing with experimental data provided in [89].

4.2 Modelling of water sorption isotherm based on the probabilistic porous network

During the deterioration process associated with water in porous materials, water mainly exists as water and vapour phase due to the wetting and drying influences. When the porous material is wetted, water adsorption appears in porous spaces, and the water saturation degree increases. Meanwhile, chemical staffs dissolve in water solution. When the porous material is dried, water desorption appears, and liquid water transfers into water vapour. Consequently, the water saturation degree decreases, and chemical staffs in water solution generates solid phases [5]. In this way, porous materials are affected by the water-related activities in terms of porous structures (porosity and pore size distribution) and transport properties. It can be found that water adsorption and desorption are strongly related to the characterization of water content in porous materials, which plays vital roles for developing a reliable models to evaluate the water-dependent activities and even predict durability issues for porous materials.

Water sorption isotherm in porous materials is the relationship between relative humidity and equilibrium water content under an isothermal condition, which is important in describing the moisture transition (between liquid and vapour) and transport properties (such as permeability and diffusivity) in porous materials [49]. The sorption isotherm can be divided into desorption and adsorption isotherm. Figure 4.1 shows a schematic for the water sorption isotherm. It can be observed that the desorption curve is always on the above of the adsorption curve, which is also known for the hysteresis effects [139].

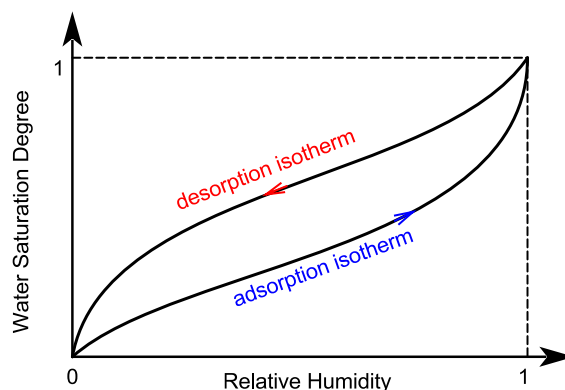


Figure 4. 1 Water sorption isotherm of porous materials.

As previously mentioned, the cyclic variations of relative humidity strongly affect the capillary front (i.e., waterfront) in natural environment. The capillary front dominates the water saturation degree and the location of salt precipitation and dissolution in the proposed model. Salt precipitation and dissolution mainly affect pores in proximity to the waterfront. Thus, modifications of pore size may predominantly restrict to a certain pore population with sizes close to the radius of the capillary meniscus. Consequently, these pores may suffer from the risk of fission if the precipitated volume in the confined space is larger than the pore volume. Thus, one may conclude that the description of water-related activities mainly depends on the evolution of liquid water in porous materials. Therefore, the modelling approach for the water

sorption isotherm concerning relative humidity and water saturation degree is necessary for moisture transport.

In this part, the water sorption isotherm is modelled according to the following steps, as shown in figure 4.2. In the first step, the varying relative humidity of the environment is introduced in the system. In the second step, the capillary pressure is estimated from the varying relative humidity by adopting the equilibrium relation between water and gas phases. In the third step, the critical pore size for the water front is determined according to the Young-Laplace equation. In the last step, the water saturation degree is simulated according to the probabilistic pore network, and the effects of salt precipitation and dissolution are introduced by considering the varying porosity.

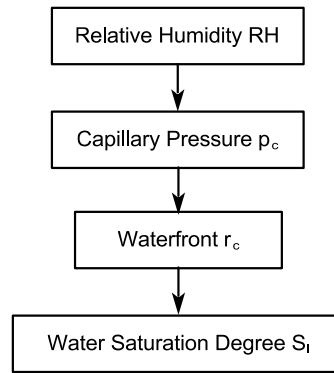


Figure 4. 2 Flowchart for determining the water saturation degree based on water sorption isotherm in porous materials.

4.2.1 Relation for relative humidity and capillary pressure

The difference between the liquid water pressure p_l and the gas pressure p_g ($p_g = p_v + p_a$, and p_v is the pressure of water vapor and p_a is the pressure of the dry air) is called the capillary pressure p_c , which is the function of water saturation degree S_l [140,141]:

$$p_c(S_l) = p_g - p_l \quad (4.1)$$

Capillary pressure is the bridge connecting the relative humidity and the waterfront. In order to find out the relation between the capillary pressure and water saturation degree, we will first study the relation between the relative humidity and capillary pressure. The equilibrium relation between the relative humidity and capillary pressure can be expressed through Kelvin's equation [132,133]:

$$p_c = - \frac{\rho_w RT}{M_w} (\ln RH) \quad (4.2)$$

where M_w is the molar mass of water (kg/mol), ρ_w is the water density (kg/m³), R is the perfect gas constant (J/K/mol), and T is the temperature (K).

Equation (4.2) considers the capillary pressure of pure water. However, the porous solution

in natural conditions often contains dissolved ions. Thus, the effects of ions should also be considered for the equation (4.2) by introducing the parameter a_w [66]:

$$p_c = - \frac{\rho_w RT}{M_w} (\ln RH - \ln a_w) \quad (4.3)$$

where a_w is the water activity which is calculated according to a two-parameter analytical function proposed by Lin et al., [142,143]:

$$\ln a_w = - \hat{m}_T M_w [1 - A_\phi (\sum_j x_j z_j^2 \frac{\sqrt{I}}{1 + b_j \sqrt{I}}) + \frac{\alpha I^\alpha}{(\alpha + 1)T} (\sum_j x_j z_j^2 S_j)] \quad (4.4)$$

where I is the ionic strength that is given in equation (4.5), and A_ϕ is the Debye–Huckel constant that is calculated as $0.39 \text{ kg}^{1/2}/\text{mol}^{1/2}$. Other parameters can be found in Table 4.1.

$$I = \frac{1}{2} \sum_j \hat{m}_j z_j^2 \quad (4.5)$$

where \hat{m}_j is the molality of the j th ionic species (mol/kg); z_j is the valence number of the j th ionic species.

It should be noted that in equation (4.4), the quantity of ions is described as molality, while in our hygro-transport model proposed in chapter 3, the ionic concentration is described as molarity. Thus, the molar concentration (molarity) of the j th ionic species c_j (mol/L) should be converted into molality \hat{m}_j (mol/kg) according to the relation as follows:

$$\hat{m}_j = \frac{c_j}{\rho_l - \left(c_{salt} M_{salt} + \sum_j c_j M_j \right)} \quad (4.6)$$

where ρ_l (kg/L) is the density of the salt solution, c_{salt} (mol/L) is the concentration of salt, M_j (kg/mol) is the molar mass of the j th ionic species and M_{salt} (kg/mol) is the molar mass of the salt.

The relation between the density of NaCl solution (ρ_l) and its concentration c_{salt} (mol/L) is given as [144]:

$$\rho_l = 0.0377 c_{salt} + 1.0001 \quad (4.7)$$

With equation (4.3) and (4.4), one can deduce the capillary pressure of the saline solution in porous materials when subjected to the varying relative humidity.

Table 4.1 gives the parameters used for computing the water activity a_w in equation (4.4)

Table 4. 1 Parameters for computing a_w . [142,143]

Parameters	Values
Molar mass of water, M_w (kg/mol)	1.8×10^{-3}
Molar concentration of water, c_w (mol/L)	55.5
Approaching parameter of ion, b_j	4.352 (Na ⁺); 1.827 (Cl ⁻)
Solvation parameter of ion, S_j	26.448 (Na ⁺); 19.245 (Cl ⁻)
Molar mass of the j th ionic species, $M_j \times 10^{-3}$ (kg/mol)	22.98 (Na ⁺); 35.43 (Cl ⁻)
Molar mass of NaCl, M_{salt} (kg/mol)	58.43
Constant, α	1.29
Temperature, T (K)	293
Molar gas constant, R (J/k/mol)	8.314
Molality of the j th ionic species, \hat{m}_j (mol/kg)	See in different cases
Molar concentration of the j th ionic species, c_j (mol/L)	See in different cases
Molar concentration of salt solution, c_{salt} (mol/L)	1
Sum of molality of ionic species, \hat{m}_T (mol/kg)	$\hat{m}_T = \sum_j \hat{m}_j$
Mole fraction of j th ionic species, x_j	\hat{m}_j / \hat{m}_T
Absolute charge number of ion, z_j	1 (Na ⁺); -1 (Cl ⁻)

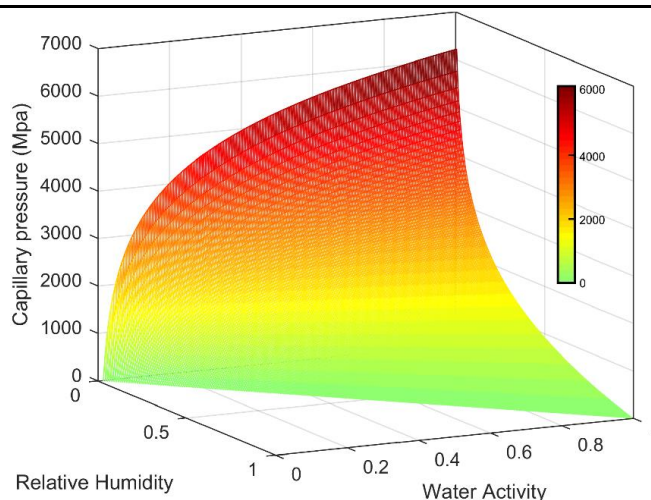


Figure 4. 3 Effects of water activity and relative humidity on the capillary pressure.

Figure 4.3 shows the effects of ions on the liquid/vapour equilibrium by considering the chemical activity a_w of liquid water in NaCl solution. The water activity is a parameter indicating how far the pore solution deviates from the ideal solution, which has a value ranging from 0 to 1. For the very dilute solution with a small ionic concentration, the water activity does not deviate too much from 1, and the effect of ionic concentration on the capillary pressure can be neglected [66]. For a concentrated solution with higher ionic concentration, water activity is expressed as a function of ionic strength of the solution and chemical activities of ions, as has been present in equation (4.4). It can be observed that with the increase of relative humidity, the capillary pressure decrease, and with the increased ionic concentration

(or with the decreased water activity), the capillary pressure decreases.

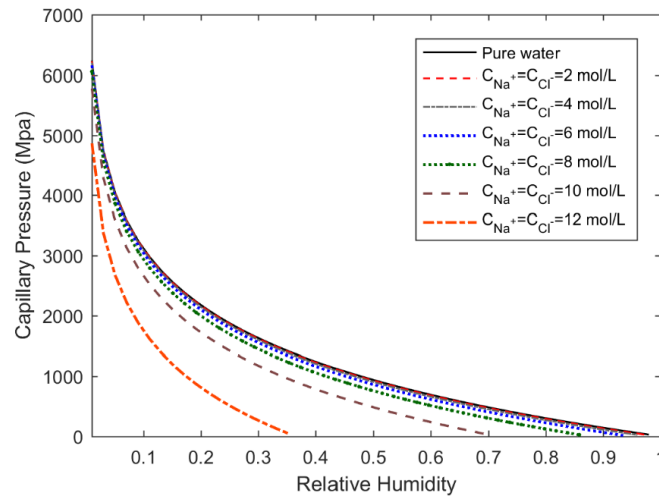


Figure 4. 4 Capillary pressure versus relative humidity under a given NaCl concentration.

It can be found in figure 4.4 that the presence of ions in pore solution has a great influence on capillary pressure. As the increment of ionic concentration, the water activity deviates more and more significantly from the ideal solution (with $a_w = 1$), and the capillary pressure decreases for porous materials subjected to the same relative humidity. It may be attributed to the reason that the presence of ions increases the van der Waals force between the molecules of saline solution. As a result, the liquid pressure increases while the capillary pressure decreases according to equation (4.3).

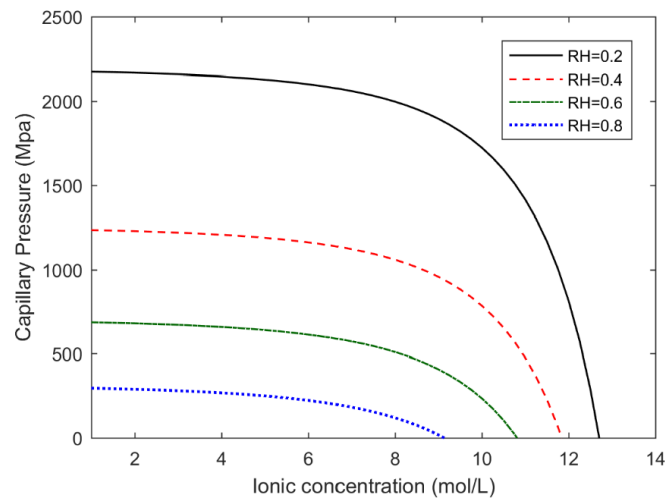


Figure 4. 5 Effects of NaCl concentration on the capillary pressure under a given relative humidity.

Figure 4.5 investigates the relation between capillary pressure and varying ionic concentration under different configurations of relative humidity. For a given relative humidity, as the increment of ionic concentration, the capillary pressure decreases. This decrease can be divided into two stages: firstly, when the ionic concentration increases from zero to a certain value c_{j0} , the capillary pressure slightly decreases; secondly, after the concentration increasing larger than c_{j0} , the capillary decreases significantly. For instance, when the ionic concentration increases from 0mol/L to 8mol/L under the relative humidity of 0.2, the capillary pressure decrease slowly from 1240MPa to 1060MPa; when the ionic concentration keeps

increasing to 11.75mol/L, the capillary pressure decreases to 67MPa.

4.2.2 Relation for capillary pressure and waterfront

Porous materials in natural conditions are generally partially saturated; that is, part of pores in porous material are filled with water and while others are filled with gaseous phase (consists of water vapour and drying air). The liquid water and the gaseous phase are in equilibrium, forming a liquid meniscus under the isothermal conditions, as shown in figure 4.6.

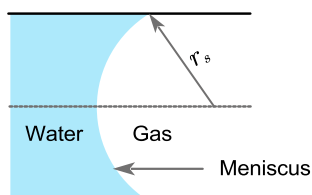


Figure 4. 6 Interface equilibrium in a pore with the radius of r_s .

According to the Young-Laplace equation, the radius r_s for the meniscus that separates liquid from gaseous phases can be derived as [140]:

$$r_s = \frac{2 \cdot \gamma \cdot \cos \theta}{p_c} \quad (4.8)$$

where γ is the surface tension of the liquid, and θ is the contact angle of liquid and the porous material, which can be regarded as 0. It can be found that capillary pressure p_c is inversely proportional to the radius r_s . In small pores, higher capillary pressure p_c is required to move the capillary interface from water-side to gas-side. In larger pores, p_c is small, and the capillary interface can easily move in pore radius.

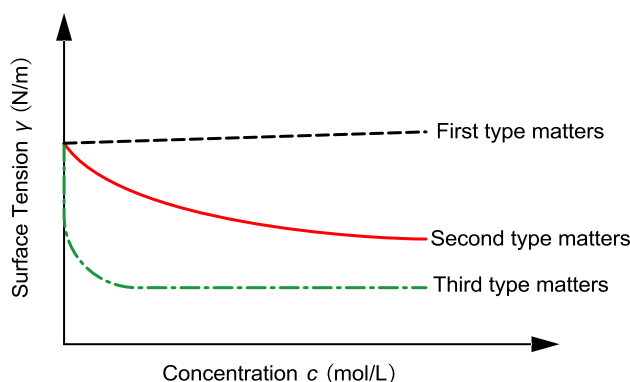


Figure 4. 7 Relation between the surface tension of solutions and its concentration [145].

Surface tension γ is an important factor in the phenomenon of capillarity, which measures the force acting at a boundary between two phases, such as water and gaseous. It is an effect of capillary action that occurs when liquids are discharged and come into contact with materials that contain pore system [146]. Several factors affect the surface tension, except for intrinsic properties of porous materials and temperature, the concentration of the solution also influences the surface tension. However, for the first type solution such as NaCl, the surface tension is slightly affected by the concentration of solution, as is presented in figure 4.7.

Therefore, the surface tension is considered to be constant with the value of 0.07275 N/m in this research [96].

When porous materials are exposed to the environment with the dynamic relative humidity, small changes in relative humidity will cause a corresponding alteration in the capillary interface. If we assume the pores in porous materials are cylindrical in shape, thus, the relationship between capillary interface and the relative humidity can be obtained according to the Young-Laplace equation and Kelvin's equation [42]:

$$r_c = C \cdot r_s = - \frac{2C \cdot \gamma \cdot \cos\theta \cdot M_w}{\rho_w RT} \cdot \frac{1}{\ln RH - \ln a_w} \quad (4.9)$$

where r_c is the critical pore size in which waterfront (capillary interface) locates in our probabilistic model. It should be noted that meniscus radius r_s obtained from the Young-Laplace equation should be converted into the critical pore radius r_c in our probabilistic porous network by introducing a parameter C, which is the calibrated parameter that makes sure the critical pore radius of capillary interface can cover the whole range of pores. According to the research of Koichi [42], the parameter C varies in different porous materials, which can be obtained after comparisons of capillary interface radii by the analytical model with experiments results.

With the relation in equation (4.9), one can calculate the critical pore radius of porous materials under varying relative humidity. In order to validate this analytical model, we introduce the experimental results of pore size distribution on three kinds of mortar cement (CEM I 52.5, CEM II 32.5, CEM II 32.5+Accelerator) and one masonry cement. The pore size distributions were measured by the MIP method, and results can be found in the report by Amiri et al. [89].

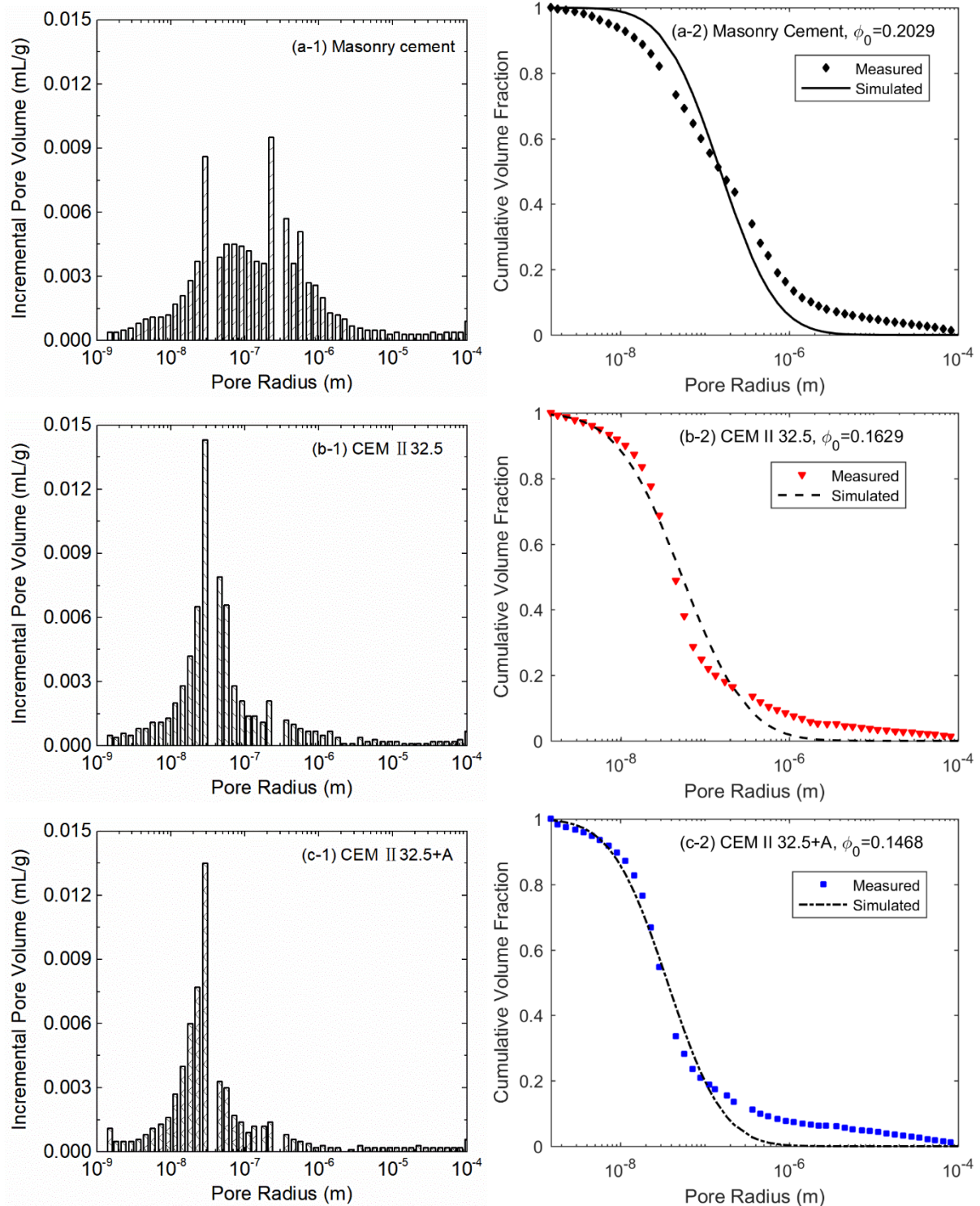
Figure 4.8 shows the incremental pore volume versus the pore radius (on the left side) for four different material), and the cumulative volume fraction versus the pore radius and the corresponding simulated results by the lognormal distribution function (on the right side). The properties and the simulated parameters of materials are summarised in Table 4.2.

Table 4. 2 Tested properties and fitted values for parameters of the lognormal distribution models for the pore size distribution of four kinds of mortars.

Matrix properties	Masonry cement	CEM II 32.5	CEM II 32.5a	CEM I 52.5
Porosity ϕ_0	0.2029	0.1626	0.1468	0.1242
Cumulative Pore Volume V_p (mL/g)	0.0971	0.0720	0.0634	0.0543
Maximum Radius ($\times 10^{-6}$ m)	160.2297	164.7190	164.4630	163.9534
Minimum Radius ($\times 10^{-6}$ m)	0.0015	0.0015	0.0015	0.0015
Simulated σ_r	1.2	1.4	1.2	1.4
Simulated μ_r	-15.694	-16.736	-17.136	-17.151

It can be found from figure 4.8 the simulated cumulative distribution curves with the 95%

confidence level fit well with the measured results of the pore size distribution. Moreover, it can also be observed that for masonry cement with the largest porosity (0.2029), the majority of pore size distributes evenly in the intervals of $[1 \times 10^{-9} \text{m}, 1 \times 10^{-6} \text{m}]$. While for cement mortars, such as CEMI 52.5 with the smallest porosity (0.1242), the range of the pore size is relatively narrow compared with masonry cement, and most pore sizes locate in the range of $[1 \times 10^{-9} \text{m}, 1 \times 10^{-7} \text{m}]$. In all, the results show that the probabilistic model for pore size distribution has the ability to cover the majority of pore sizes obtained from experiments.



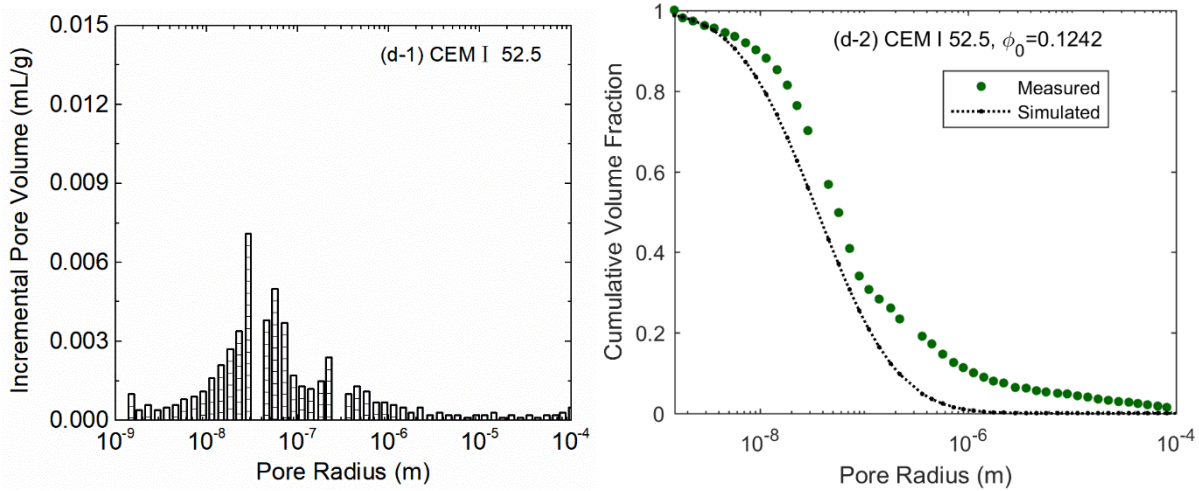


Figure 4. 8 Measured and simulated pore size distribution for four different materials: Incremental pore volume distribution (on the left side) and experimental and simulated cumulative volume fraction (on the right side).

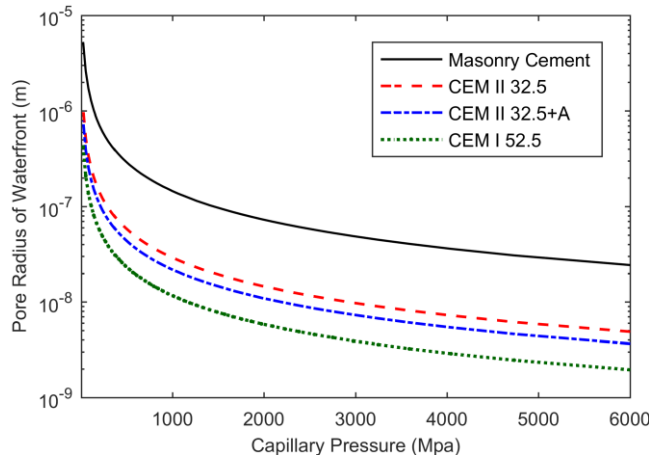


Figure 4. 9 Determination for the location of the waterfront based on capillary pressure.

When the relative humidity varies from zero to one, the capillary pressure decreases from 6232MPa to 27.6MPa. Accordingly, the capillary interface moves from small pores to large pores, as shown in figure 4.9. The capillary pressure is inversely proportional to the pore radius. The larger the capillary pressure, the smaller the capillary interface it can determine. Moreover, it is observed that under the same relative humidity, the critical pore radius for capillary interface decreases with gradually decreased porosity (with the value of 0.2029, 0.16, 0.14, and 0.12 for masonry cement, CEM II 32.5, CEM II 32.5+A and CEM I 52.5, respectively). It reveals that the waterfront has a close relationship with the porosity; large porosity determines large critical pore size for the waterfront.

Figure 4.10 presents the critical pore radius for the waterfront in four different porous materials. It can also be observed that for masonry cement with the largest porosity (0.2029), the critical pore radius varies in a range of $[2.33 \times 10^{-8} \text{m}, 5.27 \times 10^{-6} \text{m}]$, which is one order of magnitude larger than the that of CEM I 52.5 with the smallest porosity (0.1242), and critical pore radius ranges within $[3.5 \times 10^{-9} \text{m}, 7.9 \times 10^{-7} \text{m}]$. It can be found that as the relative humidity increases, adsorbed water gradually fills large pores, and the waterfront moves from gel pores to capillary pores. Finally, the range of the critical pore radius can cover almost the whole range of the

pore sizes in porous materials. By integrating the pore volume fraction function with the varying pore radius of waterfront, one can estimate the water saturation degree in porous materials under dynamic relative humidity.

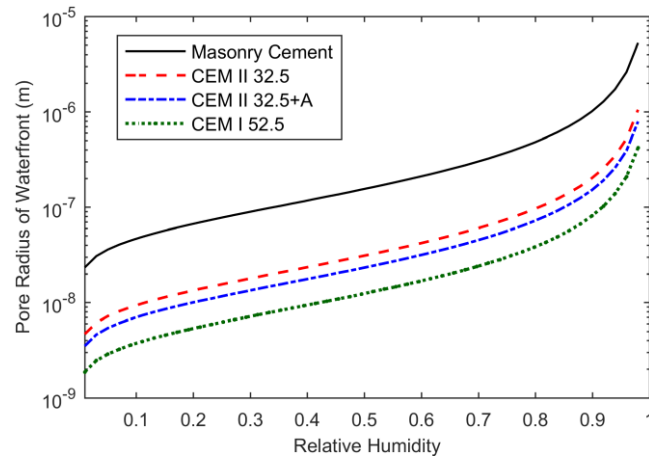


Figure 4. 10 Waterfront with varying relative humidity.

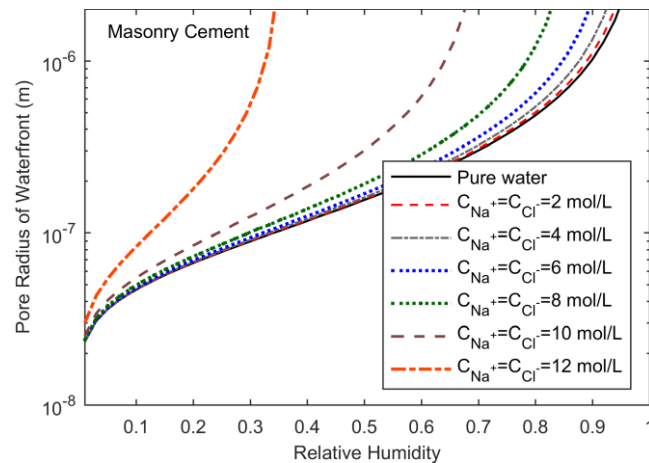


Figure 4. 11 Relation between the relative humidity and the waterfront under different solutions.

Figure 4.11 shows that the concentration of the pore solution affects the pore radius of the waterfront by influencing the capillary pressure. Under a given relative humidity, the pore solution with the higher ionic concentration induces a larger pore radius of waterfront. It indicates that the pore solution with a high ionic concentration leads to a larger water saturation degree than the dilute pore solution under the same relative humidity for the same material. It is because that the concentrated pore solution has a higher liquid pressure, and the capillary pressure becomes small under the constant gas pressure. Thus, water is more readily moving from the liquid phase towards the gas phase. Consequently, the waterfront can easily exist in larger pores with the concentrated solution compared to dilute solution or pure water.

4.2.3 Water saturation degree based on the probabilistic porous network

As mentioned previously, the varying relative humidity induces the movement of the

waterfront. Once the waterfront under the given relative humidity is obtained, the water saturation degree can be derived by adopting the probabilistic porous network proposed in Chapter 2.

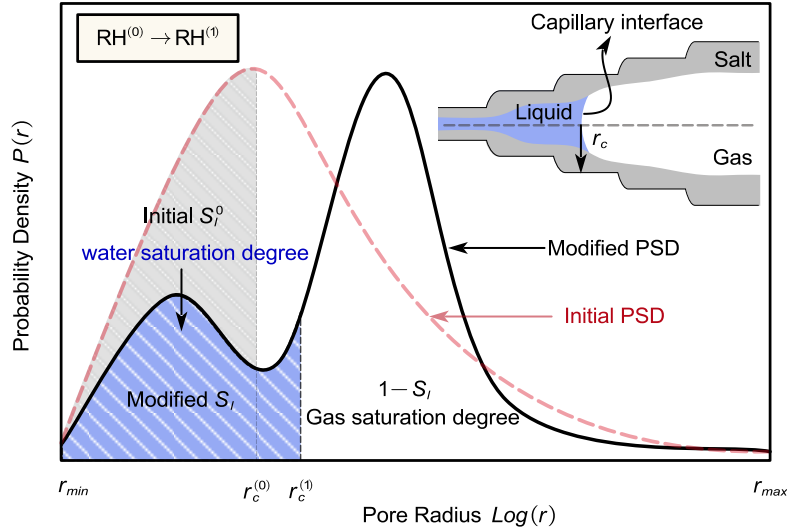


Figure 4. 12 Water saturation degree obtained from the pore size distribution.

The initial pore size distribution before salt precipitation and dissolution obeys the lognormal probability density function [43,44,46–48]. As shown in figure 4.6, after salt precipitation and dissolution, the pore solution is in the equilibrium state. The pores with a radius smaller than r_c are saturated with saline solution. The rest of the pores are filled with gaseous phases (consist of water vapour and dry air). Even though there would be a thin film of water adsorbing on the walls of large pores, it can be disregarded compared to the large radius of the pore size. Therefore, the water saturation degree S_l can be obtained by integrating the pore volume with sizes smaller than the capillary pore radius r_c over the pore size distribution function.

According to figure 4.12, the water saturation degree for initial pore size distribution with the porosity of ϕ_0 can be expressed as [6]:

$$S_l^0 = \int_0^{r_c} P_0(r_0) dr = \frac{1}{2} \operatorname{erfc} \left(- \frac{\ln(r_0) - \mu_r}{\sqrt{2} \sigma_r} \right) \quad (4.10)$$

The water saturation degree for modified pore size distribution with the porosity of ϕ_1 can also be obtained by adopting the modified pore size distribution models proposed in Chapter 2. As mentioned in Chapter 2, we have two probabilistic methods to interpret the modified pore size distribution and three transformation models to depict relationships between pore radius before and after modification. Due to the limited space of this dissertation, only method two and non-linear transformation models (monotonic and non-monotonic transformation) will be adopted hereafter in describing the pore size distribution in this Chapter.

Thus, the water saturation degree after the porosity varying from ϕ_0 to ϕ_1 is given by:

$$S_i = \frac{\phi_0}{\phi_1} \int_0^{r_z} \frac{f(r_0)}{r_0} P_0(r_0) dr_0 \quad (4.11)$$

With the analytical models for water saturation degree, two situations will be considered in the following:

- water saturation degree under constant relative humidity based on the successive transformations of pore size distribution with the constant waterfront;
- water saturation degree under varying relative humidity based on the single transformation of pore size distribution with the varying waterfront. Detailed information for the analytical models of water saturation degree is illustrated in Appendix 4A. In this case, the waterfront varies with the relative humidity.

Figure 4.13 shows the profile of water saturation degree under varying relative humidity for four different materials before pore size modifications. It can be observed that for different materials, the water saturation degree varies from 0 to 1 when the waterfront moves from small pores to large pores due to varying relative humidity. It indicates that the analytical models for water sorption isotherm can well depict the evolution of moisture content in the given porous materials.

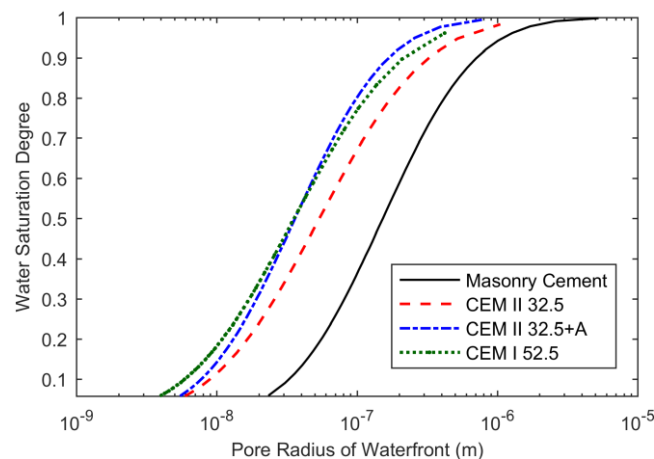


Figure 4. 13 Determining the water saturation degree with the waterfront based on the probabilistic model.

Figure 4.14 shows the water sorption isotherm for different porous materials. By adopting the proposed analytical model, one can obtain the water saturation degree within porous material under a given relative humidity. It can be observed that masonry cement with the largest porosity has a water sorption isotherm curve above CEM I 52.5 with the smallest porosity. This gap between different materials is small when they are completely dried or saturated. Moreover, under a given relative humidity (location of waterfront), CEM I 52.5 always shows the weakest contribution of liquid water. It is natural to link the phenomenon with the microstructure (porosity and pore size distribution) of porous materials. When the relative humidity is around 0.6, the difference of the isotherm between the masonry cement and CEM I 52.5 is the largest. However, in natural conditions, the isotherm curve for water adsorption differs from the isotherm curve for water desorption in reality due to the hysteresis effect [139]. It should be noted that in our model, the hysteresis behaviour is not considered. A more

comprehensive distribution of water content needs to be further developed in our probabilistic model for drying and wetting processes, respectively, to describe hysteresis effects in porous materials.

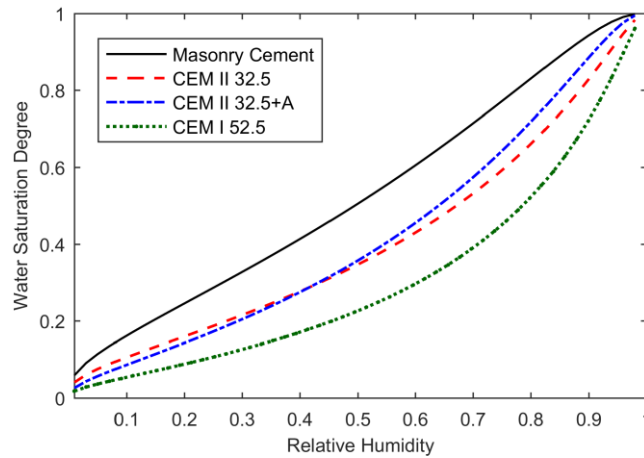


Figure 4. 14 Modelling of the water sorption isotherm in four porous materials.

Figure 4.15 presents the effects of saline solution on the water sorption isotherm. The porous material contains concentrated pore solution can be easily saturated at a lower range of relative humidity. In contrast, it requires a higher relative humidity range to fully saturate the porous material that contains dilute solution. For instance, when the porous material contains a solution with an ionic concentration of 8 mol/L, it can be saturated when the relative humidity is reaching 85%. While when the porous material contains the pore solution with the ionic concentration of 12 mol/L, it requires the relative humidity to increase from 0 to 35% to saturate the porous material. However, it should be noted that in reality, the pore solution is not such concentrated. As investigated in chapter 3, the concentration of ionic species referring to salt precipitation and dissolution is in the unit of mol/m³, which is considerably smaller than the concentration in figure 4.15. Thus, the effects of salt concentration should not be so significant as presented in figure 4.15.

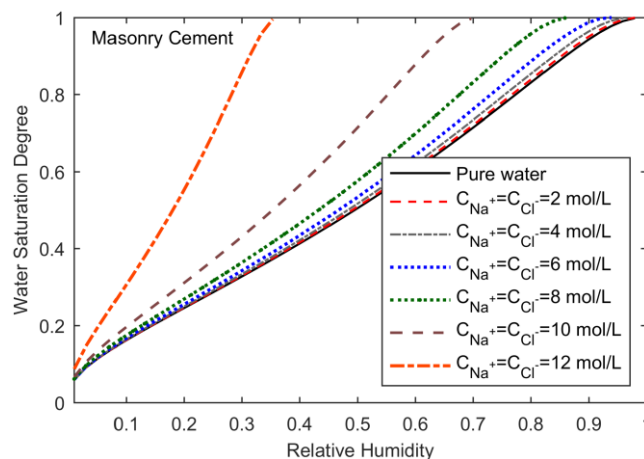


Figure 4. 15 Influence of the ionic concentration on the modelled water sorption isotherm for masonry cement.

Based on the water sorption isotherm, Van Genuchten proposed a fitting relation between the capillary pressure p_c and water saturation degree S_l [74]:

$$p_c = a(S_l^{-b} - 1)^{1-1/b} \quad (4.12)$$

where a and b are fitting parameters dependent on the microstructure of the porous materials. Such a fitting expression is also investigated in our research, and the fitted parameters can be found in Table 4.3.

Table 4. 3 Fitting results for relation between the capillary pressure p_c and the water saturation degree S_l .

Materials	a	b	R ²
Masonry Cement	692.88	1.7986	0.989
CEM II 32.5	442.03	1.844	0.989
CEM II 32.5+A	542.69	1.687	0.987
CEM I 52.5	349.1	1.7294	0.989

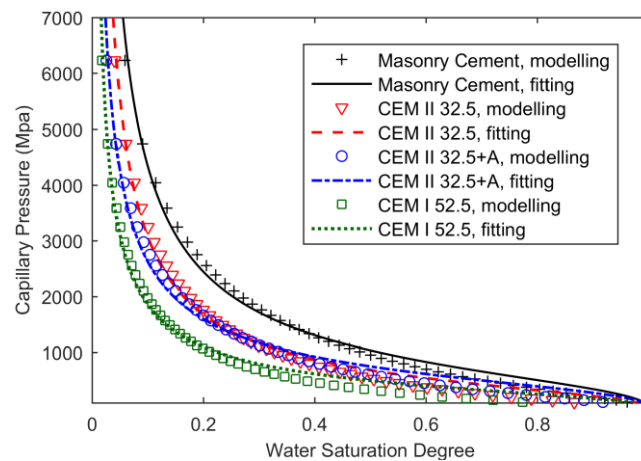


Figure 4. 16 Water saturation degree versus capillary pressure for different materials.

Figure 4.16 presents the relations between the capillary pressure p_c and the water saturation degree S_l for different materials. With these relations, one can estimate the water saturation degree in the porous material under the given capillary pressure.

4.3 Modelling of permeability based on the probabilistic porous network

Based on the water sorption isotherm, the interaction between external relative humidity for the environment and water content in porous materials has been built up. In this section, the permeability will be investigated based on the water sorption isotherm and the pore size distribution model.

Intrinsic permeability is one of the most crucial indications for porous materials when estimating the transport process. Several experimental methods can be adopted to measure the intrinsic permeability, among which water is the most commonly used fluids. However, the

disadvantages of this method are apparent: the intruded water may dissolve the chemical staffs such as the salt or the hydrated cement in porous materials, which induces the modification of pore structure. In addition, it is quite difficult to saturate all the pores when the specimen has low permeability [137]. Moreover, a good measurement of permeability requires perfect water saturation of the materials, which is generally difficult to attain [138]. Furthermore, when measuring the porous material with low intrinsic permeability, the pressure needs to generate the fluid movement is too large that may exceed the compression strength of the material. As a result, the porous material may have a risk of being damaged under such high pressure. Therefore, analytical model should be a good choice when the direct measurement for permeability is difficult.

This section aims to develop an analytical model to describe the permeability of porous materials by adopting the probabilistic model for pore size distribution (characterised as method two in Chapter 2). Furthermore, by introducing the non-linear transformation models of pore radius (monotonic and non-monotonic transformation models), the effects of modified porosity induced by pore filling or pore emptying on permeability are also explored in this section. Moreover, the modelling results for permeability are compared with the experimental measurements on four different cement pastes.

Based on the assumption that the pores are cylindrical, the flux term of the fluid (liquid or gas) is given according to Darcy's law [141]:

$$J_{\pi-s} = -K_0^\pi \frac{\rho_\pi k_{r\pi}}{\mu_\pi} \nabla p_\pi \quad (4.13)$$

where $J_{\pi-s}$ is the mass flux term of liquid water ($\pi = l$) and gas mixture ($\pi = g$) with relative to the solid phase of porous materials, K_0^π is the intrinsic permeability of porous material that is measured by using the fluid π , $k_{r\pi}$ is the relative permeability of phase π , μ_π is the dynamic viscosity of the phase π , and p_π is the pressure of phase π .

Intrinsic permeability in theory is denoted as K_0 , which is the inherent property of material regardless of fluids used in measurement. From the experimental point of view, the intrinsic permeability could be approached when the porous material is fully saturated with the fluid π , and then it can be converted to the intrinsic permeability by considering the density and viscosity of the fluid. Therefore, the intrinsic permeability measured by liquid or gas should be identical with the theoretical permeability with the relation of $K_0 = K_0^l = K_0^g$. However, this relation cannot be realized in experimental measurements. The intrinsic permeability of the same porous material measured by liquid or gas does not present an identical relation. Koichi [42] has proposed that the intrinsic permeability measured by gas is 1~3 orders of magnitude larger than the intrinsic permeability measured by liquid, and the difference can be explained by the reason that pore water viscosity is altered in a time-dependent manner when adopting water to measure the intrinsic permeability. Therefore, an analytical method for intrinsic permeability should be a good choice, which is independent of the fluids inside.

As mentioned previously that the permeability is highly dependent on the pore structure; thus, the intrinsic permeability K_0 can be obtained based on the probabilistic models of pore size distribution [42]:

$$K_0 = \frac{\phi^2}{50} \left(\int_0^{\infty} r dV \right)^2 \quad (4.14)$$

where dV is the pore size distribution based on the proposed probability density function. This relation gives an interpretation for the role of pore structure plays in the overall transport of fluids in porous materials.

For the porous material with the arbitrary moisture content in the unsaturated state, water fills pores with the radius from 0 to r_c , and r_c is the capillary interface that separates the liquid water from the gas. Thus, the liquid permeability can be decided as:

$$K_l = \frac{\phi^2}{50} \left(\int_0^{r_c} r dV \right)^2 \quad (4.15)$$

It can be found that for the unsaturated porous material, only the saturated pores with the radius smaller than r_c contribute to the liquid transport.

Meanwhile, gas exists in the pores with the radius larger than r_c , and the corresponding permeability for the gas phase can be given as:

$$K_g = \frac{\phi^2}{50} \left(\int_{r_c}^{\infty} r dV \right)^2 \quad (4.16)$$

On the basis of intrinsic permeability, liquid permeability, and gas permeability, the relative permeability of phase π is introduced, which denotes the contribution of the partially saturated fluid relative to overall pore space.

The relative permeability of liquid can be expressed as:

$$k_{rl} = \frac{K_l}{K_0} \quad (4.17)$$

and the relative permeability for the gas is given as:

$$k_{rg} = \frac{K_g}{K_0} \quad (4.18)$$

When porous materials are completely saturated with liquid, the liquid permeability K_l is identical to the intrinsic permeability K_0 , and the relative permeability of liquid k_{rl} should be equal to 1. On the other hand, when the porous material is completely dried (and the porous space is saturated with gas), the gas permeability K_g is identical with the intrinsic permeability K_0 , and the relative permeability of gas k_{rg} should be equal to 1. Thus, the relative permeability $k_{r\pi}$ varies within the range of $[0, 1]$ according to the water saturation degree (which is determined by relative humidity).

Next, the permeability will be implemented by considering two cases of relative humidity: the constant relative humidity with the constant pore radius of waterfront r_c ; the varied relative humidity with the altering pore radius of waterfront r_c .

4.3.1 Permeability under constant RH based on successive transformations of pore sizes

When the porous material is subjected to the open system, the external relative humidity is regarded as constant under the same temperature and gas pressure of the environment, as is shown in figure 4.17. If salt precipitation near the waterfront, the pore space for the liquid phase is occupied by precipitated salt. Consequently, the waterfront should move towards larger pores. A quantity of water evaporates into the atmosphere to keep the waterfront remaining in the initial state. In contrast, if the porous material undergoes salt precipitation, pore volume near the waterfront increases because the precipitated salt dissolves in the pore solution. Consequently, the pore space engaged with the dissolved salt will be filled by the liquid phase. Thus, the waterfront should move back to the small pores. However, a quantity of water condenses in the porous material to maintain the waterfront constant. To be concluded, the waterfront is regarded as permanent when the porous material under constant relative humidity, which can be realised by water evaporation during the salt precipitation process and water condensation during the salt dissolution process.

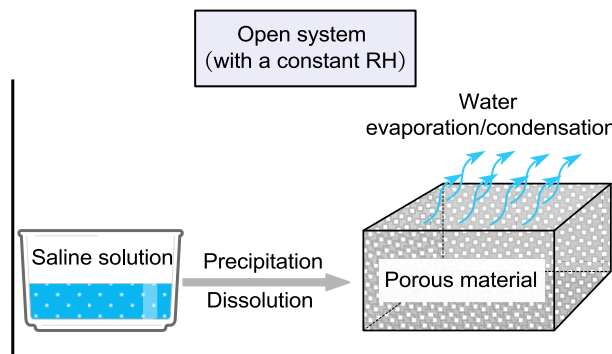


Figure 4. 17 Open system with constant RH (With the given room temperature, the saturated salt solution can control the RH).

Next, the permeability will be implemented under the case of the constant waterfront. Moreover, the effects of porosity on permeability will be investigated by adopting successive transformations of pore size distribution due to salt precipitation and dissolution. The modifications of pore radius are implemented by taking both monotonic and non-monotonic transformation models. The analytical models for permeability under constant waterfront based on successive transformations can be found in Appendix 4B.

Table 4. 4 Parametric initialisations for successive transformations of pore size distribution.

Chemical reaction	RH	s_l^0	r_c (m)	β (m)	ϕ
Salt precipitation	0.3854	0.4	1.1276×10^{-7}	1×10^{-7}	0.20→0.14
Salt dissolution	0.3854	0.4	1.1276×10^{-7}	1×10^{-7}	0.20→0.50

The permeability of masonry cement is investigated by considering a constant relative

humidity yield at 0.3854, and the corresponding water saturation degree is determined as 0.4. The parametric initialisations for successive transformations due to salt precipitation and dissolution are summarised in Table 4.4.

Figure 4.18 shows the pore size distribution due to successive transformations of salt precipitation and dissolution with the constant relative humidity and waterfront. The porosity is supposed to decrease from 0.2 to 0.14 after 20 times of modification due to salt precipitation, and porosity increase from 0.2 to 0.5 after 20 times of modification induced by salt dissolution.

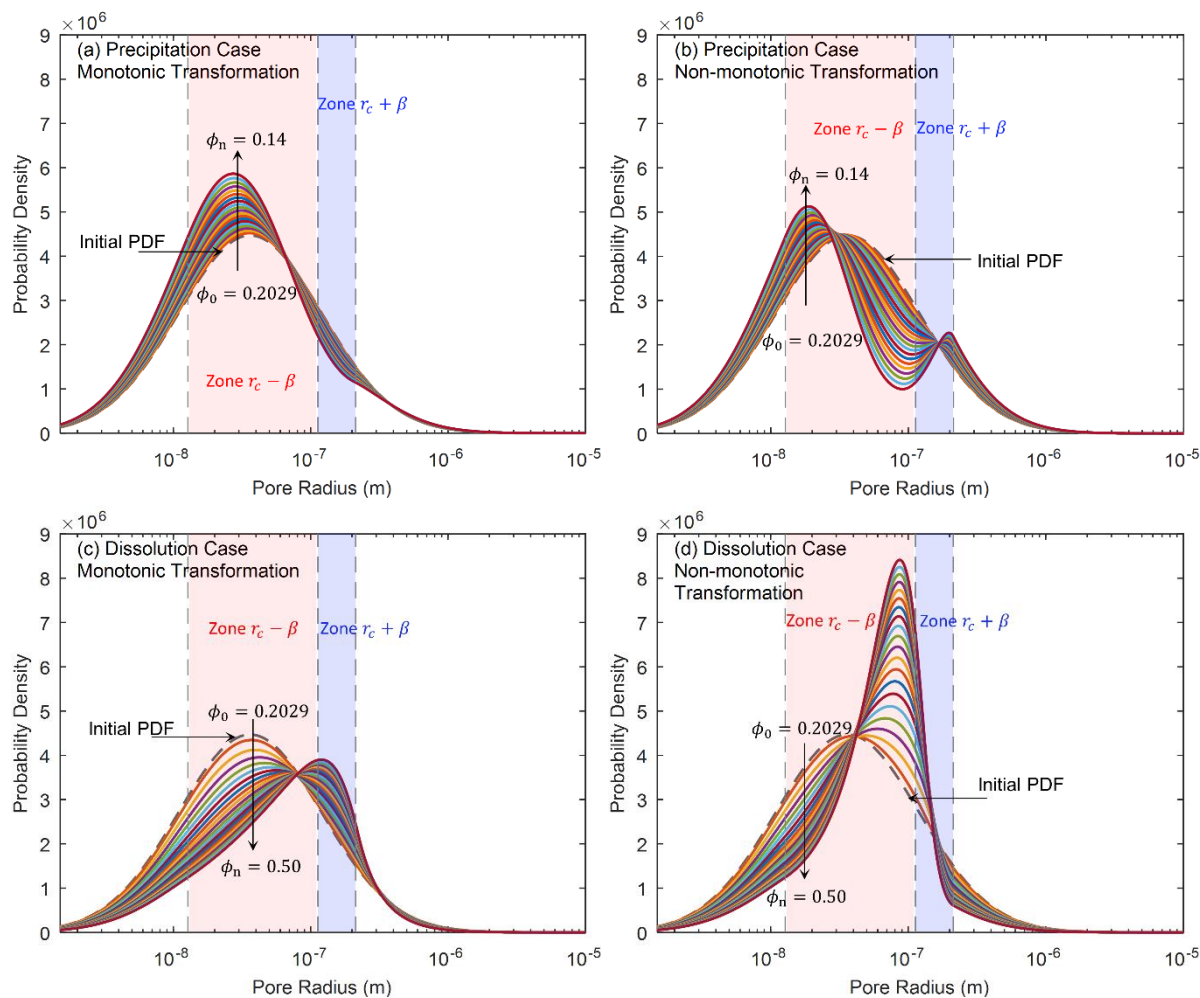


Figure 4. 18 Evolution of pore size distribution with successive transformations due to salt precipitation and dissolution under the constant RH.

It can be observed in figure 4.19 that even though the relative humidity keeps constant, the water saturation degree is altered due to the modification of pore size distribution with the changed porosity. Moreover, with the same porosity, the water saturation degree also presents different values by following two different transformation models of the pore sizes. It reveals that the water saturation degree is determined not only by the waterfront but also by the porosity and pore size distribution.

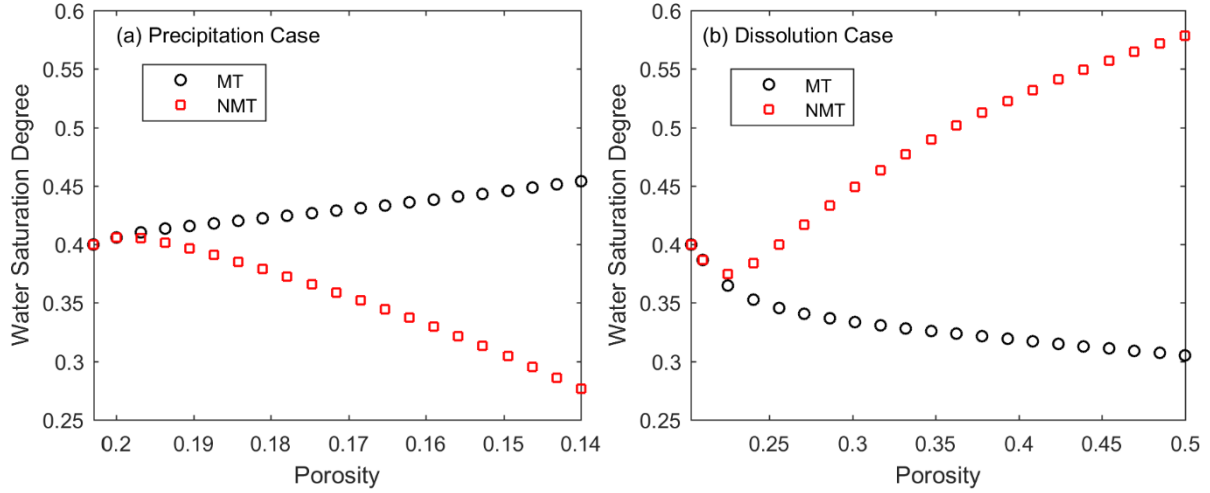


Figure 4.19 Evolution of water saturation degree with successive transformations due to (a) salt precipitation and (b) salt dissolution under the constant relative humidity.

As previously mentioned, the waterfront keeps unchanged with the situation of the constant relative humidity while the water saturation degree increases/decreases due to the modification of the pore structure. Thus, different cases regarding water evaporation or condensation should be considered to keep the waterfront constant.

1. Case one-no water evaporation/condensation.

In this case, no water evaporation or condensation appears, and $\dot{m}_{vap}=0$. It indicates that the liquid volume before ($v_l^0 = S_l^0 \phi_0 V$) and after ($v_l^1 = S_l^1 \phi_1 V$) transformation are in identical relation with $v_l^0 = v_l^1$. By substituting equation (4.10) and (4.11) into this relation, we have:

$$\phi_0 \int_0^{r_c} P_0(u) du = \phi_1 \int_0^{r_c} P_1(u_1) du_1 \quad (4.19)$$

In this case, equation (4.19) should be satisfied for the pore size transformation in order to keep the waterfront constant when no water exchanges between the atmosphere and porous material.

2. Case two-Water evaporation/condensation occurs.

Another case is that water evaporates or condenses in porous material to keep the constant waterfront. The volume of evaporated or condensed water should be the volume of salt precipitation or dissolution on the left side of the water waterfront. Thus, the mass of evaporated/condensed water should be calculated as:

$$\dot{m}_{vap} = \rho_w (\phi_0 - \phi_i) \int_{r_c - \beta}^{r_c} P_i(u_i) du_i \quad (4.20)$$

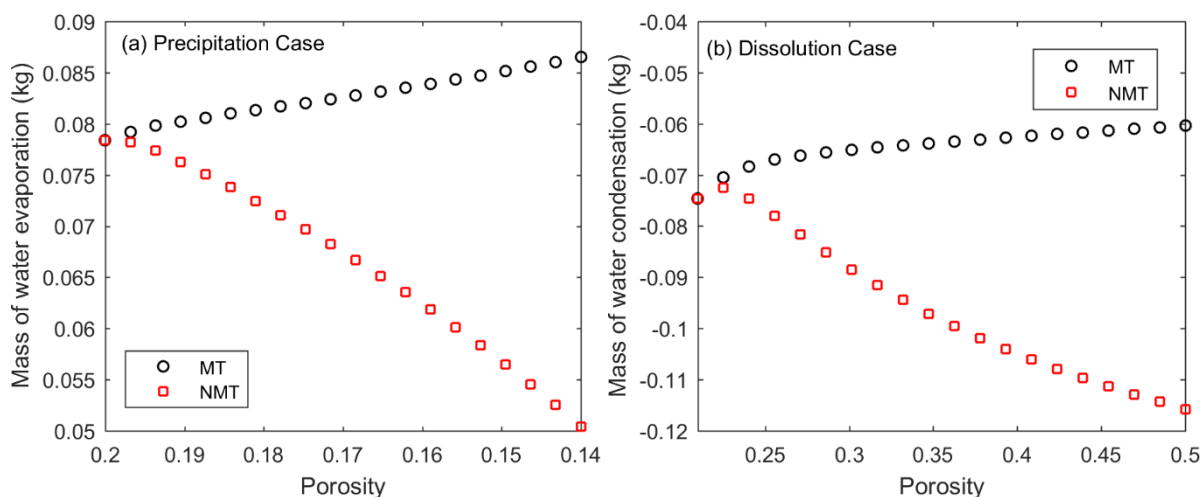


Figure 4.20 Mass of (a) evaporated water under salt precipitation case and (b) condensed water under salt dissolution case due to successive transformations under the constant relative humidity.

MT denotes the monotonic transformation model and NMT denotes the non-monotonic transformation model.

It can be observed in figure 4.20 that during salt precipitation, the water evaporates into the environment, and the mass of evaporated water increases when the modified pore size follows the monotonic transformation model while the mass of evaporated water decreases when the modified pore size follows the non-monotonic transformation model. During the salt dissolution, the water condenses into the porous materials, and the evolution trend for water is inverse with that of the precipitation case.

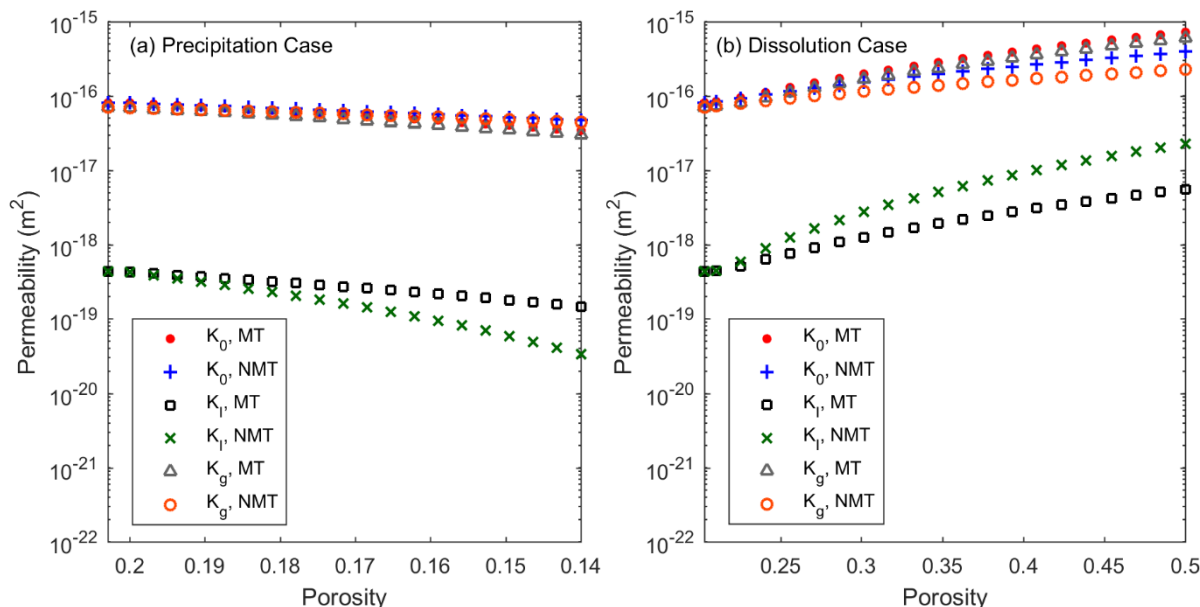


Figure 4.21 Evolution of permeability due to successive transformations induced by (a) salt precipitation and (b) salt dissolution under the constant relative humidity.

Figure 4.21 shows the relation between porosity and permeability in the unsaturated porous material. Firstly, it can be observed that during the salt precipitation process, intrinsic permeability, liquid permeability and gas permeability implemented by both monotonic and non-monotonic transformation are decreasing as the porosity decreases. It can be explained by

the reason that salt precipitation reduces the cross-section of pore space, consequently, permeability decreases. On the other hand, salt dissolution enlarges the pore volume, facilitating the transport of fluids; thus, the permeability is improved. Moreover, it can be found that the liquid permeability is more sensitive to the porosity modification than the intrinsic permeability and gas permeability in both salt precipitation and salt dissolution cases, especially when pore size modification follows the highly localized transformation model (NMT). For instance, when pore materials are subjected to salt precipitation with porosity decreasing from 0.2029 to 0.14, the liquid permeability implemented by non-monotonic transformation model decreases in the range of $[1 \times 10^{-20} \text{m}^2, 1 \times 10^{-18} \text{m}^2]$, while that of intrinsic permeability and gas permeability range within a quite narrow interval of $[2 \times 10^{-17} \text{m}^2, 1 \times 10^{-16} \text{m}^2]$. In all, porosity and pore size distribution make significant contributions to intrinsic permeability, liquid permeability, and gas permeability.

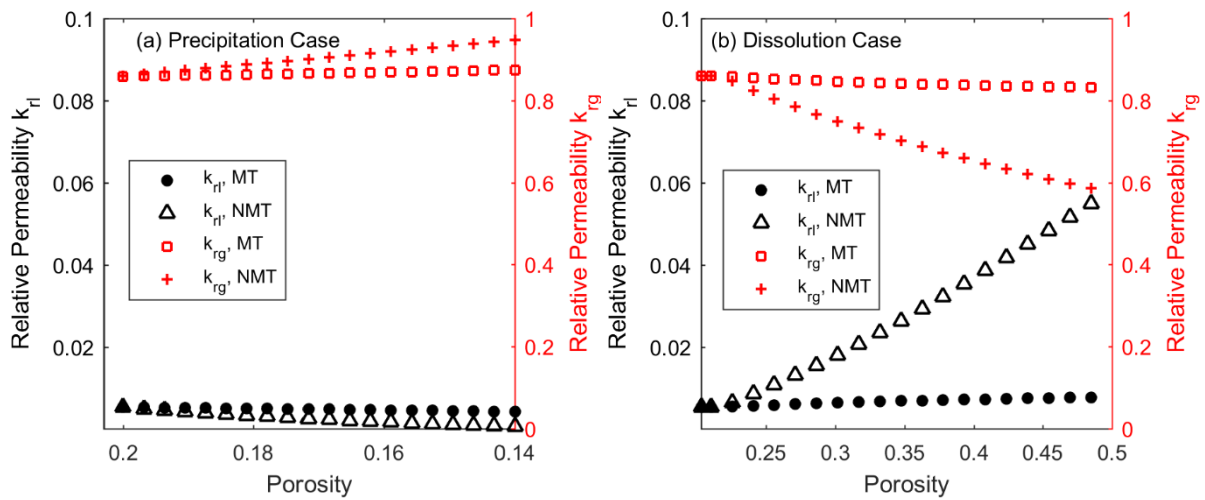


Figure 4.22 Evolution of relative permeability due to successive transformations induced by (a) salt precipitation and (b) salt dissolution under the constant relative humidity.

Finally, the influences of porosity on the relative permeability k_{rg} and k_{rl} are investigated under the constant relative humidity, as is shown in figure 4.22. It is observed that relative liquid permeability k_{rl} is quite small than the relative gas permeability k_{rg} at a lower relative humidity with the value of 0.3875. Moreover, it can also be found that relative permeability k_{rg} and k_{rl} implemented by monotonic transformation are not sensitive to the porosity modification in both precipitation and dissolution cases. However, the relative permeability k_{rg} and k_{rl} implemented by the non-monotonic case are affected significantly by porosity modification. Meanwhile, this influence is quite considerable when the porosity deviates significantly from the initial one. However, porous materials in natural conditions are generally not in constant relative humidity, and the equilibrium of capillary interface can be easily disturbed with the change of environmental conditions. Thus, it is vital to explore the permeability under unstable relative humidity.

4.3.2 Permeability under varying RH based on single transformation of pore sizes

In this section, a closed system is considered, in which the porous material is confined within a varying relative humidity, as shown in figure 4.23. When the porous material is subjected to vapour of wetting saline solution, salt precipitation/dissolution occurs, which alters the concentration of pore solution. Consequently, the relative humidity is changed. The waterfront moves with the varying relative humidity according to the water sorption isotherm. Therefore, the water saturation degree can be derived based on the determination of the waterfront under the given relative humidity.

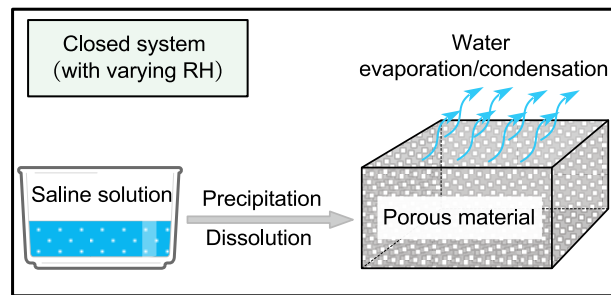


Figure 4. 23 Closed system with varying RH (This system is also the sorption isotherm experiment when the RH keeps constant).

When the porous material undergoes a variation of porosity from ϕ_0 to ϕ_i due to salt precipitation and dissolution, i is the number of transformations. The intrinsic permeability can be obtained as:

$$K_0^{(i)} = \frac{\phi_i^2}{50} \left(\int_0^{\infty} f(r_0, r_c) P_i(r_i) dr_i \right)^2 \quad (4.21)$$

The liquid permeability with varying waterfront is given as follows:

$$K_l^{(i)} = \frac{\phi_i^2}{50} \cdot \left(\int_0^{r_c^{(i)}} f(r_0, r_c) P_i(r_i) dr_i \right)^2 \quad (4.22)$$

The gas permeability with varying waterfront is given as follows:

$$K_g^{(i)} = \frac{\phi_i^2}{50} \cdot \left(\int_{r_c^{(i)}}^{\infty} f(r_0, r_c) P_i(r_i) dr_i \right)^2 \quad (4.23)$$

where $f(r_0, r_c)$ is the transformation function for the relationship between the initial pore radius and the modified pore radius, and detailed information for the permeability models can be found in Appendix 4B.

4.3.2.1 Validation of the analytical model for permeability

In this section, experimental results of the intrinsic permeability for four different materials are compared with the modelling results obtained by our model. The intrinsic permeability, liquid permeability, and gas permeability can be simulated by considering the initial porosity and the varying water saturation degree from 0 to 1. As mentioned previously, the intrinsic permeability K_0 is an inherent property of the porous material and independent of the fluids in it. As presented in figure 4.24a, with the water saturation degree increases, the intrinsic permeability keeps constant and independent of the water saturation degree, while the liquid permeability is increasing and gas permeability decreases. When the porous material is saturated with water, the liquid permeability is identical to the intrinsic permeability. On the contrary, when the porous material is dried out, the gas permeability equals the intrinsic permeability.

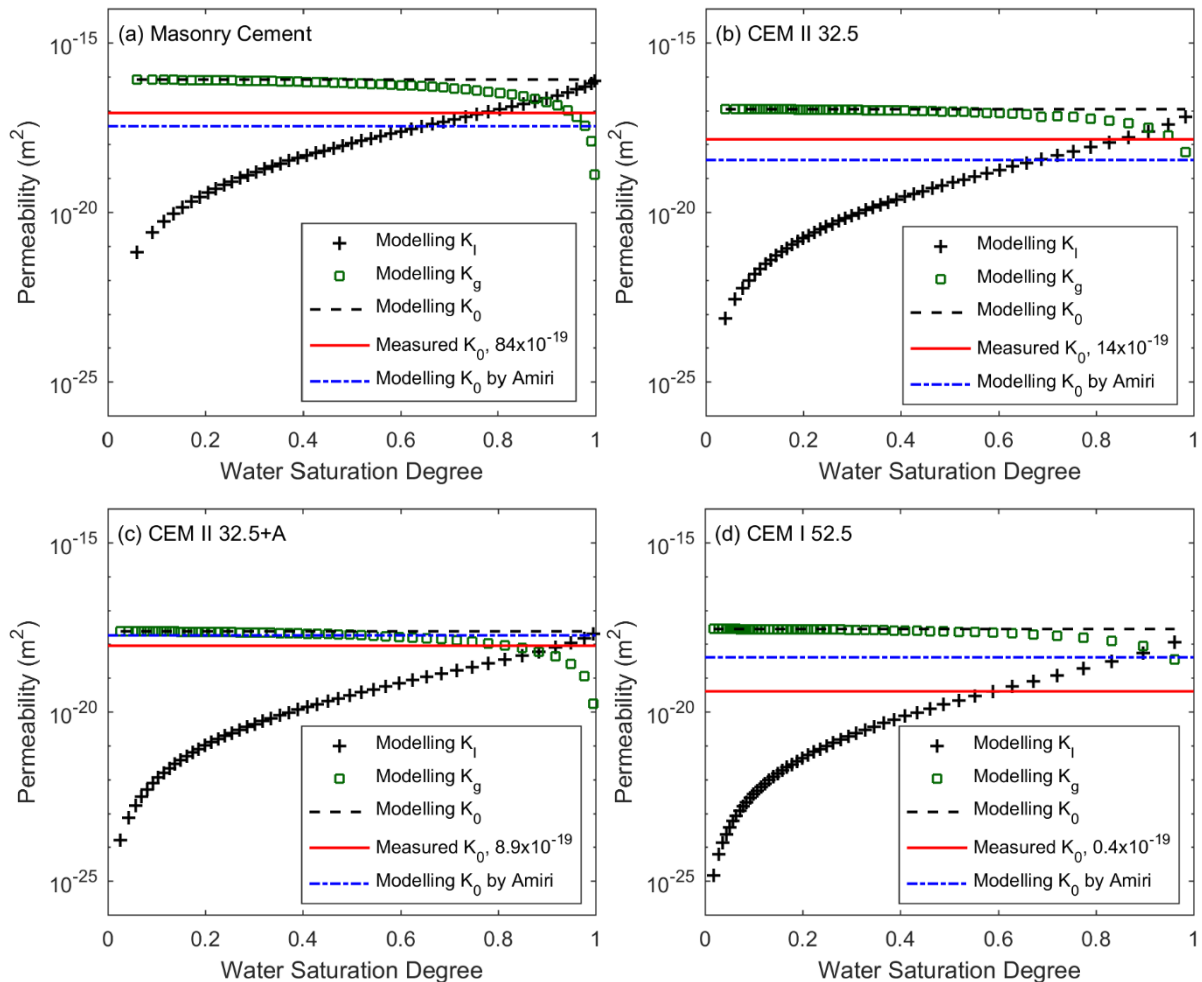


Figure 4. 24 Modelling results for permeability of four different materials.

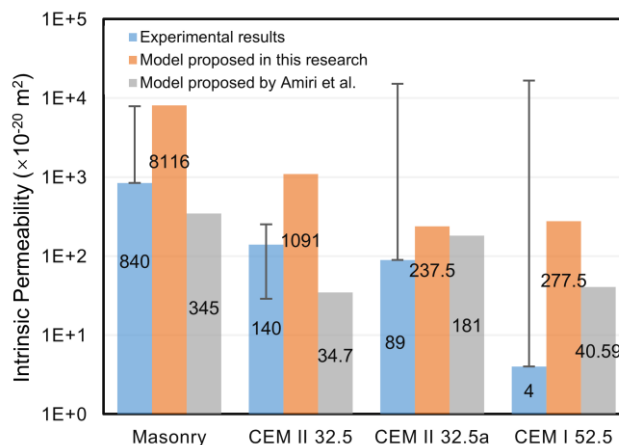


Figure 4. 25 Comparisons of permeability between experimental and modelling results for four different materials.

Moreover, figure 4.25 presents comparisons on modelling and experimental intrinsic permeability obtained by Amiri et al. [89] with our modelling results, which are also summarised in Table 4.5. It can be observed that the results obtained by our proposed model are 1-3 orders of magnitude larger than the tested value; that is, the intrinsic permeability is overestimated by adopting our proposed model, especially for CEM I 52.5, the intrinsic permeability is quite larger (almost three orders of magnitude) than the tested value. The permeability is affected by the porosity, porous shape, and connectivity. In our probabilistic model, pores are considered cylindrical with the uniform channel for pores with the same radius. This assumption overestimates the connectivity (pore throat) of the porous structure. Moreover, the inaccuracy characterisation of pore size distribution with disregarding the tortuosity also induces the difference between experimental results. To be compared, the modelling results implemented by Amiri's analytical model underestimate the intrinsic permeability for masonry cement, CEM II 32.5 and CEM II 32.5+A, and overestimates the intrinsic permeability for CEM I 52.5. The researcher has explained that the discrepancy might be induced by the simplifying assumption that each pore radius has the same length. In all, Amiri's model is more accurate than our proposed model regarding the comparison of intrinsic permeability with experimental results. However, this does not mean that our model is useless. In fact, our model provides a preliminary description of evolved permeability when pore structure and water content (or RH) are altered, which is not mentioned in other reports.

Table 4. 5 Tested and fitted permeability for four kinds of mortars.

Matrix properties	Masonry cement	CEM II 32.5	CEM II 32.5a	CEM I 52.5
Porosity ϕ_0	0.2029	0.1626	0.1468	0.1242
Measured K_0 ($\times 10^{-19}$ m ²)	84	14	8.9	0.4
Simulated K_0 ($\times 10^{-19}$ m ²)	811.6	109.1	23.75	27.75
Simulated K_0 by Amiri ($\times 10^{-19}$ m ²)	34.5	3.47	18.1	4.059

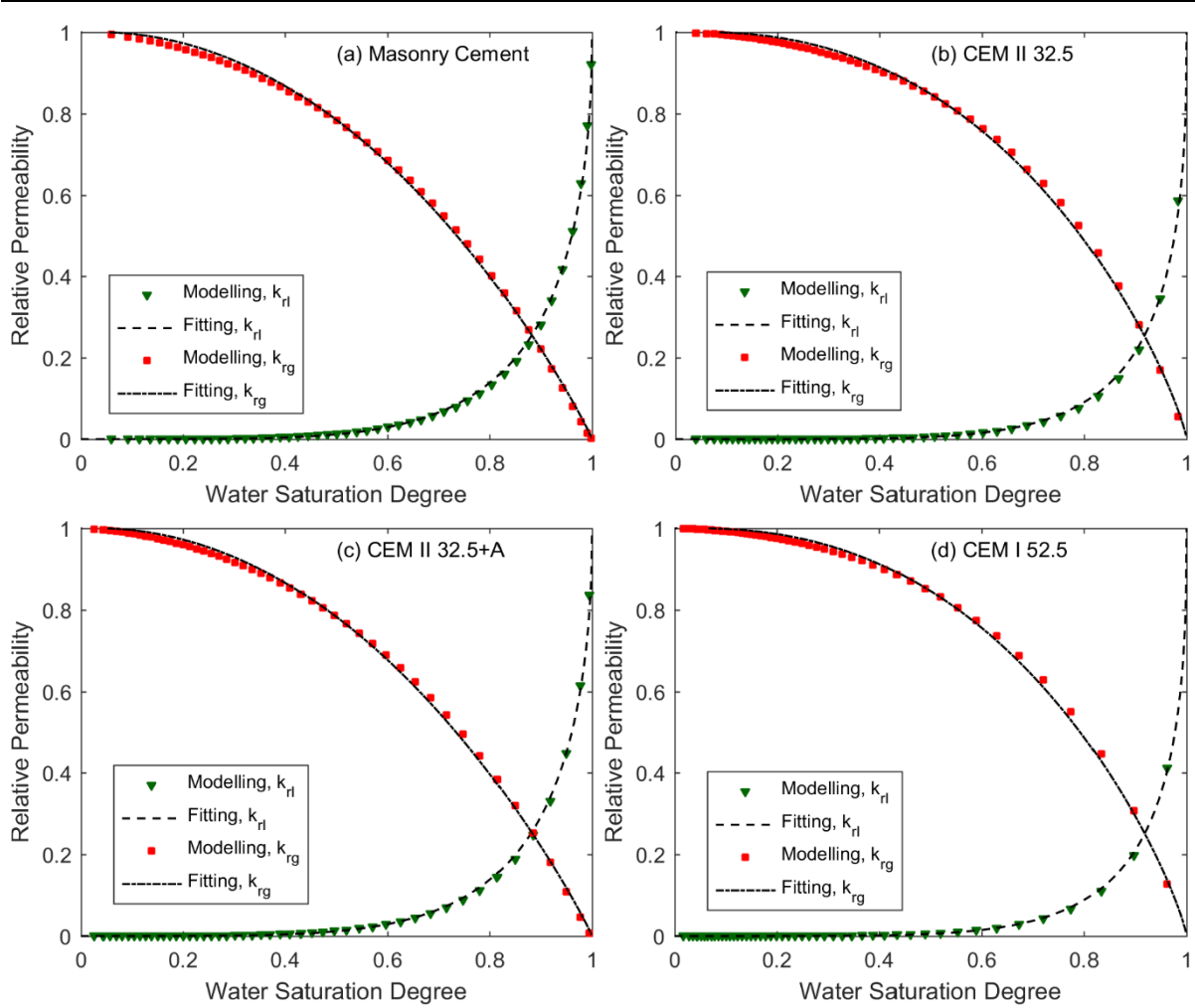


Figure 4. 26 Relative permeability versus water saturation degree for four different materials.

The relative permeability of liquid and gas for the four different materials can be obtained based on the proposed probabilistic model under varying relative humidity, as is presented in figure 4.26. The relation between relative permeability and water saturation degree are fitted according to the analytical expressions proposed by Van Genuchten [140]:

$$k_{rl}(S_l) = \sqrt{S_l} [1 - (1 - S_l^{1/m})^m]^2 \quad (4.24)$$

and

$$k_{rg}(S_l) = (1 - S_l)^p [1 - S_l^{1/m}]^{2m} \quad (4.25)$$

where m and p are fitting parameters which are summarised in Table 4.5. It can be observed that fitting parameter m is in good agreement with range values given by Van Genuchten, which was valued at 0.5 [147]. With expressions (4.24) and (4.25), one can estimate the relative permeability of water and gas under a certain water saturation.

Table 4.5 Fitting parameters for relation between relative permeability and water saturation degree S_l .

Materials	Relative liquid permeability k_{rl}		Relative gas permeability k_{rg}	
	m	R^2	p	R^2

Masonry Cement	0.49437	0.998	-0.050856	0.999
CEM II 32.5	0.42723	0.997	-0.031438	0.998
CEM II 32.5+A	0.49399	0.998	-0.047685	0.999
CEM I 52.5	0.42333	0.999	-0.021819	0.997

4.3.2.2 Evolution of permeability due to salt precipitation and dissolution

As illustrated in Chapter 3 that during the water-ionic transport process, chemical reactions can modify the pore structure by affecting its porosity: porosity decrease after salt precipitation, and porosity increases after salt dissolution. Furthermore, the modified porosity can contribute to the influences of transport properties by increasing or decreasing the section across which allows the fluids (water, ions and gas) to pass through it. Therefore, in this section, we will investigate the influences of porosity on permeability by considering the single and successive modifications of porosity on masonry cement. It should be emphasized that in our analytical model for permeability, the evolution of salt precipitation and dissolution is involved by considering modification of porosity, which is not found in other models as to the author's knowledge.

1. Evolution of permeability under single modification of porosity.

In this case, we investigate the effect of porosity based on the successive evolutions of pore size distribution due to salt precipitation and dissolution by adopting two transformation models.

Figure 4.27 shows that the water saturation degree increases as the waterfront gradually moves to large pores (due to the increased relative humidity) in both the precipitation and dissolution processes. The larger pore radius of the capillary interface, the more significant the water saturation degree. Meanwhile, the modified water saturation degree derived by monotonic transformation model is larger than the initial one during salt precipitation and is smaller than the initial one during salt dissolution. While for non-monotonic transformation model during the salt precipitation case, when the waterfront locates in small pores, the modified water saturation degree is smaller than the initial one. When the waterfront locates in the pore with a size larger than $1.5 \times 10^{-7} \text{m}$, the modified water saturation degree becomes larger than the initial one. On the contrary, during the salt dissolution process, the modified water saturation degree implemented by non-monotonic transformation model is larger than the initial one when the waterfront locates in the pores smaller than $1.1 \times 10^{-7} \text{m}$. As the waterfront keeping moving towards large pores, the modified water saturation degree becomes smaller than the initial one.

It reveals that under lower relative humidity, water saturation degree is greater influenced by the different modes of pore size distribution than in larger relative humidity. Meanwhile, under higher relative humidity, the influences of porosity on water saturation degree are larger than that under lower relative humidity.

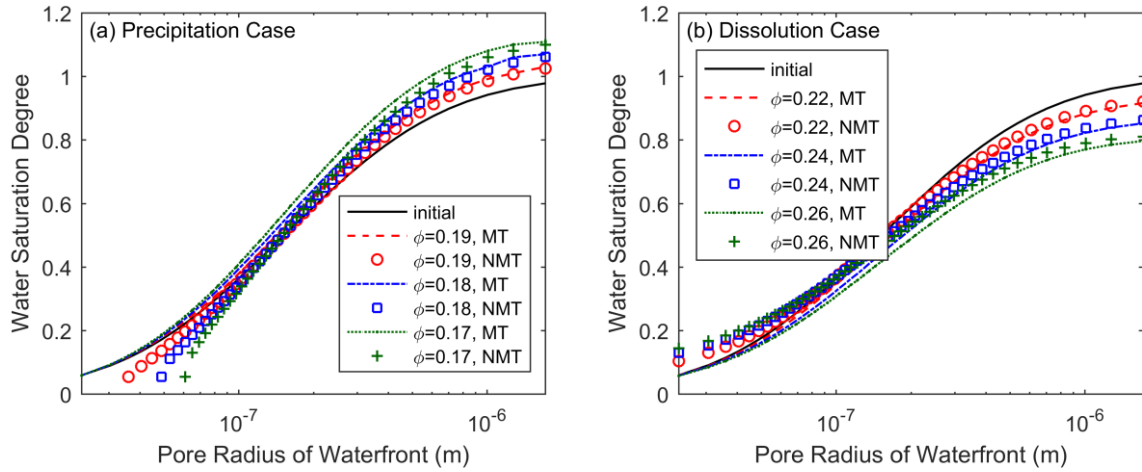


Figure 4. 27 Evolution of water saturation degree with single modification of porosity induced by (a) salt precipitation and (b) salt dissolution under varying relative humidity.

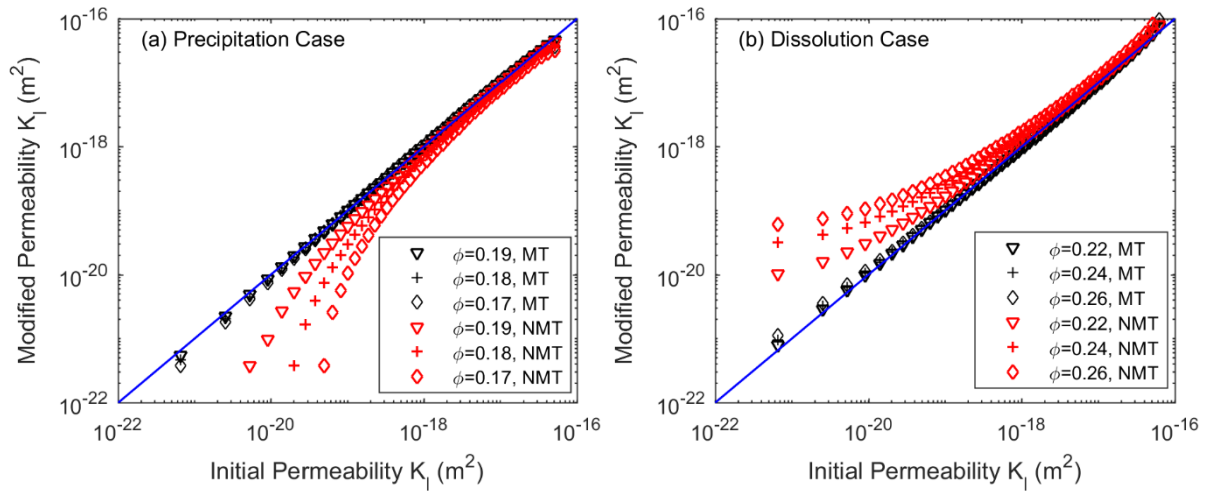


Figure 4. 28 Comparison of liquid permeability with single modification of porosity induced by (a) salt precipitation and (b) salt dissolution under varying relative humidity.

Figure 4.28 shows the comparisons between initial and modified liquid permeability in masonry cement when porosity decreases from 0.20 to 0.19, 0.17 and 0.16 in salt precipitation; and porosity increases from 0.2 to 0.22, 0.24 and 0.26 in salt dissolution. Similar to the water saturation degree, the liquid permeability increases with the waterfront moving towards large pores disregarding the different porosities and transformation models. This phenomenon is concise with the research conducted by Huang et al. [6], that is, large water content improves the connectivity of pore space that facilitates water transport; consequently, the liquid permeability is improved. Furthermore, the porosity also has an unneglectable influence on liquid permeability. The modified liquid permeability is smaller than the initial one after porosity decrease, and the modified liquid permeability is larger than the initial one after porosity increase. This gap is more and more significant as the porosity deviating largely from the initial one. Meanwhile, it can also be found that noticeable differences exist in liquid permeability that are implemented by different transformation models. Liquid permeability implemented by non-monotonic transformation is more sensitive to porosity modification than that by monotonic transformation model.

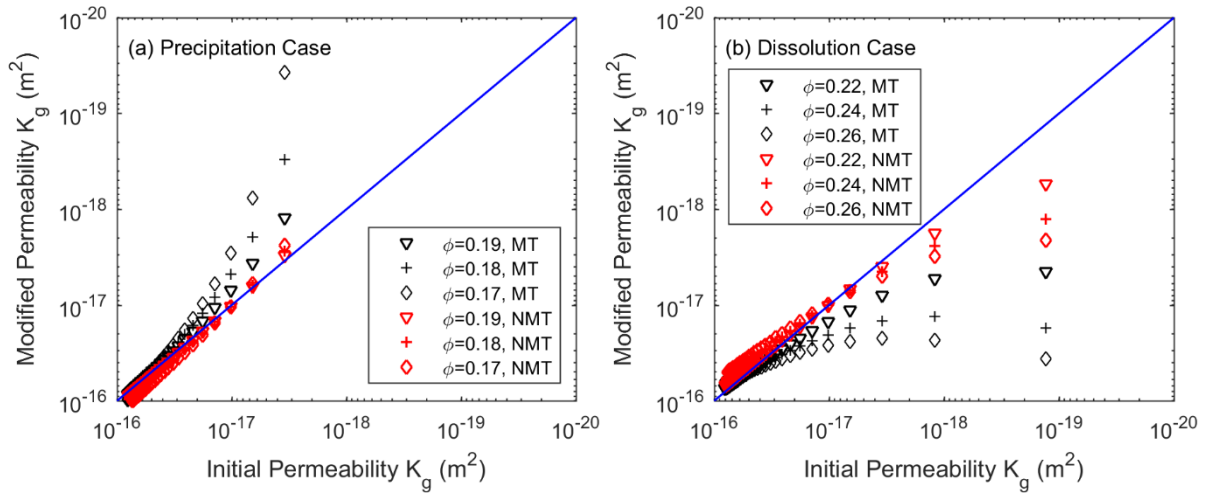


Figure 4. 29 Comparison of gas permeability with single modification of porosity induced by (a) salt precipitation and (b) salt dissolution under varying relative humidity.

On the contrary, as the water saturation degree increases, the gas permeability decreases in salt precipitation and salt dissolution cases (figure 4.29). When the porous material is subjected to salt precipitation or dissolution with a lower water saturation degree, the porosity modification makes more significant influences on gas permeability implemented by non-monotonic transformation model than that by monotonic transformation model. When the porous material is in a larger water saturation degree, the porosity modification affects much on the gas permeability implemented by monotonic transformation model rather than that by non-monotonic transformation model. In summary, it may be said that the liquid and gas permeability is affected not only by the water saturation degree but also by the modification of porosity and the corresponding pore size distributions.

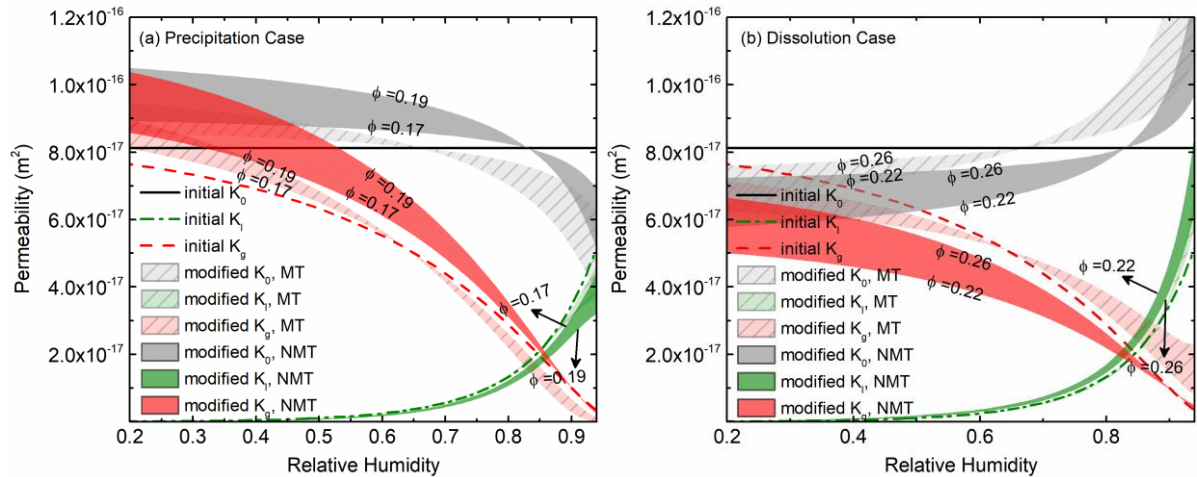


Figure 4. 30 Evolution intrinsic permeability K_0 , liquid permeability K_l and gas permeability K_g with single modification of porosity induced by (a) salt precipitation and (b) salt dissolution under varying relative humidity.

It can be observed from figure 4.30 that the intrinsic permeability decreases when salt precipitation appears; the intrinsic permeability increases when salt dissolution appears. Moreover, when the water saturation degree is small, the varied porosity makes a greater contribution to the gas permeability than that to liquid permeability. On the contrary, when the

porous materials are gradually saturated with water, the modified porosity greatly influences the liquid permeability rather than the gas permeability.

In addition, it can also be seen that under lower relative humidity, which also corresponds to a lower water saturation degree, the gas movement dominates a large part of pore space, the gas permeability is noticeable. As a result, the liquid water movement may be inactive for low values of external relative humidity. While for high relative humidity, liquid water movements play a prominent role and liquid permeability is significant. It can also be observed that when the relative humidity is lower, the gap between gas permeability and liquid permeability is larger than in higher relative humidity, and this phenomenon is especially significant for the salt precipitation case.

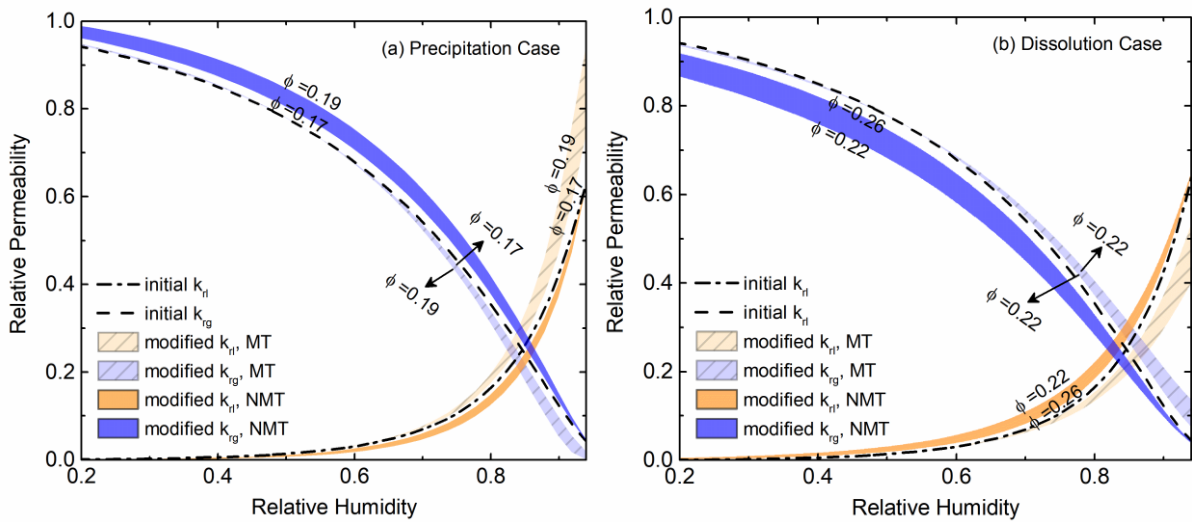


Figure 4.31 Evolution of relative liquid permeability k_{rl} and relative gas permeability k_{rg} with single modification of porosity induced by (a) salt precipitation and (b) salt dissolution under varying relative humidity.

The relative permeability for liquid and gas is also affected by the evolution of porosity. For both salt precipitation and dissolution case, the relative permeability for liquid increases from 0 to 1 while the relative permeability for gas decreases from 1 to 0, as shown in figure 4.31.

In conclusion, the modelling results reveal that varied porosity and the corresponding pore size distribution affect the intrinsic permeability, gas permeability, and liquid permeability. Moreover, the water and liquid permeability are also influenced by the water saturation degree (or the RH). Therefore, for the materials in natural conditions with a water-unsaturated state and unstable relative humidity, our modelling approach may be a good choice in evaluating the evolution of permeability due to varying RH and porosities.

2. Evolution of permeability under successive modifications of porosity.

In this case, we investigate the evolution of permeability under successive modifications of porosity for masonry cement when subjected to salt precipitation and dissolution. When salt precipitation occurs, the porosity decreases from 0.2029 to 0.155 by 50 successive steps of transformation. When salt dissolution appears, the porosity increases from 0.2029 to 0.30 by 50 successive steps of transformation. Meanwhile, the pore radius of waterfront varies in the

range of $[2.33 \times 10^{-8} \text{m}, 1.72 \times 10^{-6} \text{m}]$. The evolution of pore size distribution is presented in figure 4.32.

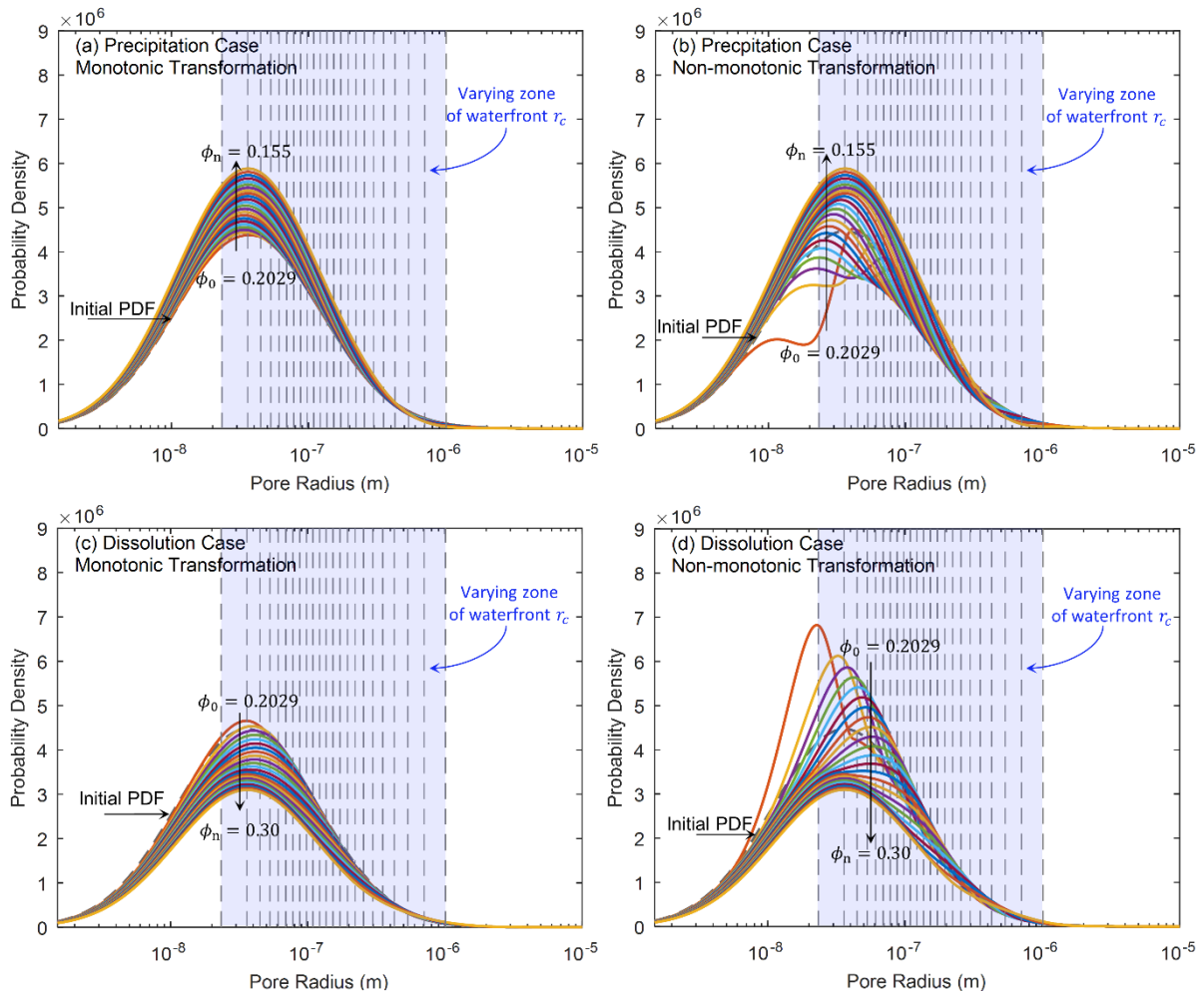


Figure 4. 32 Evolution of pore size distribution with successive modifications of porosity induced by salt precipitation and salt dissolution under varying relative humidity.

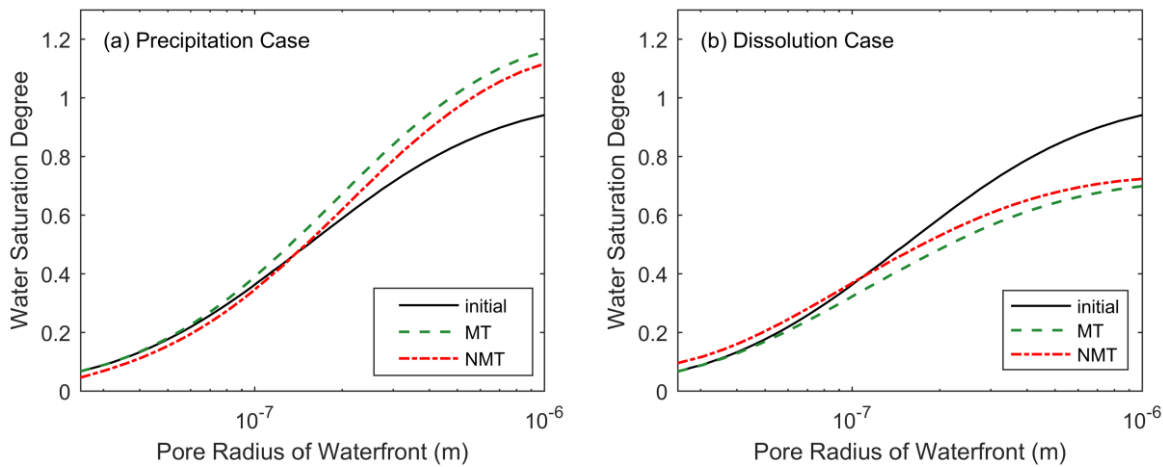


Figure 4. 33 Evolution of water saturation degree with successive modifications of porosity induced by (a) salt precipitation and (b) salt dissolution under varying relative humidity.

It can be found in figure 4.33 that during the salt precipitation process, the modified water

saturation degree becomes higher than the initial one; the deviation is more and more significant as the porosity decreases. On the contrary, the modified water saturation degree becomes lower than the initial one as the salt dissolution appears. This phenomenon can be explained that based on the definition of water saturation degree, salt precipitation reduces the pore volume, and thus the water saturation degree increases as the relative humidity increases. While the salt dissolution enlarges the pore volume, consequently, the modified water saturation degree decreases.

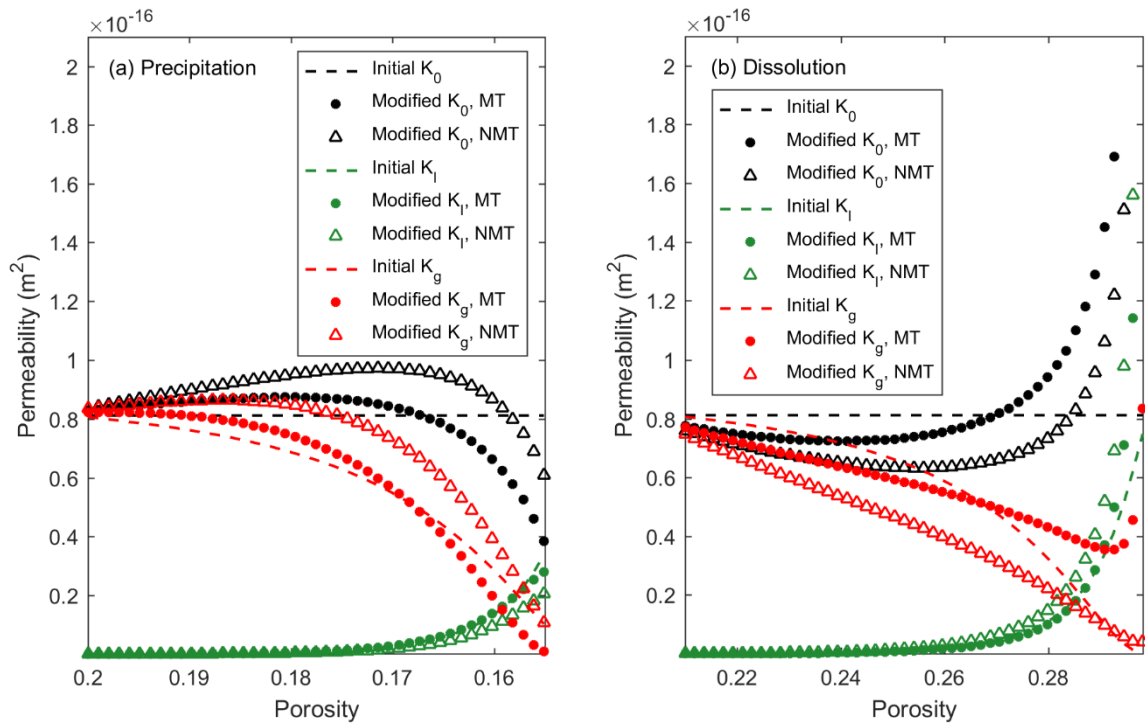


Figure 4.34 Evolution of intrinsic permeability K_0 , liquid permeability K_l and gas permeability K_g with successive modifications of porosity induced by (a) salt precipitation and (b) salt dissolution under varying relative humidity.

Under successive modifications of porosity, the intrinsic permeability is affected significantly by salt precipitation and dissolution. It can be observed in figure 4.34a that the intrinsic permeability increases then decreases both for monotonic and non-monotonic transformation. At the same time, the liquid permeability increases, and gas permeability decreases for both two transformation models when the porosity decreases from 0.2 to 0.155. The results implemented by non-monotonic transformation deviate more noticeably from the initial one when compared with that by monotonic transformation model. During the salt dissolution process (figure 4.34b), the porosity increases from 0.2 to 0.30. The intrinsic permeability implemented by both two transformation models increases and is more significant than the initial one when the porosity increases to 0.3. Meanwhile, the liquid permeability increases more and more significantly as the porosity keeps increasing. It is worth noting that when the porosity is compromised at around 0.3, the gas permeability trends to increase for both monotonic and non-monotonic transformation models, which is not observed when adopting the single transformation of pore sizes.

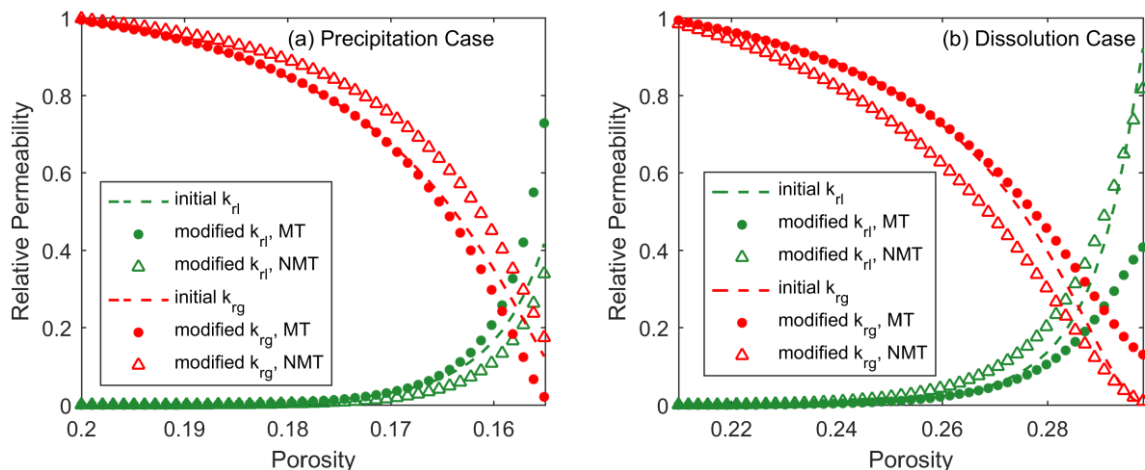


Figure 4.35 Evolution of relative liquid permeability k_{rl} and relative gas permeability k_{rg} with successive modifications of porosity induced by (a) salt precipitation and (b) salt dissolution under varying relative humidity.

Figure 4.35 shows the evolution of relative permeability for liquid and gas under successive modifications of porosity. In both salt precipitation and dissolution cases, the relative liquid permeability increases while the relative gas permeability decreases with the increased relative humidity. Under the salt precipitation case, the relative liquid permeability implemented by monotonic transformation is more significant than that by non-monotonic transformation. In contrast, the relative liquid permeability implemented by non-monotonic transformation is more significant than monotonic transformation when subjected to salt dissolution. This situation is inverse for the relative gas permeability. It reveals that in addition to the effects of modified porosity, the water saturation degree and the transformation models of pore size distribution greatly affect the relative permeability of both liquid and gas.

4.4 Conclusions

This chapter investigates the water sorption isotherm and permeability in porous materials. The significant finding in this chapter is that it is possible to describe the water related properties in porous materials as a function of overall porosity and waterfront (or capillary interface) incorporated into statistical (or the so-called probabilistic) pore size distribution model. Following conclusions can be drawn according to the modelling results:

First, the capillary pressure is deduced according to the equilibrium relation between capillary pressure and relative humidity through Kelvin's equation. Meanwhile, the effects of ionic and salt concentration are investigated by introducing the water activity parameter. It is found that the presence of ions in pore solution plays a significant role in capillary pressure: the capillary pressure becomes lower as the ionic concentration increasing at a given relative humidity.

Second, the capillary pressure is adopted as a connection between the external relative humidity and moisture content in porous materials. The waterfront (or the so-called capillary interface) for the probabilistic porous network is solved based on the Young-Laplace equation. With this relation, the evolution for waterfront under the varying relative humidity are

investigated for four different porous materials. It is revealed that the capillary pressure is inversely proportional to the pore radius. Higher capillary pressure required when determining the waterfront in small pores. Moreover, it is indicated that the waterfront is also affected by the overall porosity of the porous material; large porosity induces a large critical pore radius for the waterfront. In all, by adopting the proposed models, the pore radius of waterfront can be deduced, which can cover the whole range of the pore sizes for the porous material.

Third, by adopting the proposed probabilistic pore size distribution model, the water saturation degree is simulated based on the varying waterfront. The water sorption isotherm is also obtained, which is the reflection of the physical microstructural through its interaction with moisture. It is observed that the porous material with a small porosity shows a weak distribution of liquid water under a given relative humidity. Moreover, the effects of ionic concentration on water sorption isotherm are also investigated. The results find that the porous material with a high concentrated pore solution is easily saturated under a lower relative humidity range. However, it should be noted that the water saturation degree obtained in this chapter is simply the summation of the condensed pore volumes and does not include any contribution of the water sorption hysteresis. For further research, the author intends to develop analytical models for water saturation degree under drying and wetting processes, respectively.

Fourth, analytical models for description the intrinsic permeability K_0 , liquid permeability K_l , gas permeability K_g and relative permeability for liquid k_{rl} and gas k_{rg} are developed based on the statistical distribution model of pore structure, which makes it possible for a direct exploitation of permeability with the evolution of pore size distribution. The permeability under the constant waterfront (with a given relative humidity) is proposed. Moreover, the evolutions of permeability due to salt precipitation and dissolution are also estimated, gaining further insight into how the evolution of pore size distribution affects permeability.

Finally, permeability under varying relative humidity is estimated based on the single transformation of pore size distribution with the moving waterfront. It is found that for low values of external relative humidity, which also corresponds to a lower water saturation degree, the gas movement dominates a large part of pore space, the gas permeability is noticeable. While for higher relative humidity, liquid water movement plays a prominent role and liquid permeability is significant. Moreover, it can also be observed that when the external relative humidity is lower, the gap between gas permeability and liquid permeability is more significant than higher relative humidity. Additionally, when salt precipitation occurs, decreased porosity diminishes the intrinsic permeability, and the difference between gas permeability and liquid permeability becomes smaller. When salt dissolution appears, the increased porosity improves the intrinsic permeability, and the gap between liquid permeability and gas permeability increases as the porosity increases. To be concluded, the proposed modelling approach reveals that the intrinsic permeability is affected only by the porosity and its pore size distribution; the alteration of external relative humidity does not make contributions to it. In comparison, the liquid and gas permeability is influenced not only by pore structure but also relative humidity. Most importantly, materials in natural conditions often exist in a water-unsaturated state and are subjected to the environment with aggressive

chemical staffs, and the water content is generally not stable. Thus our modelling approach may be a good choice in evaluating permeability evolution due to varying water saturation degrees and porosities.

However, it should be emphasized that the modelling approach in evaluating the permeability of porous materials in this research is highly simplified that lacks the consideration of tortuosity of pore structure; consequently, it overestimates the permeability of porous material. Thus, more morphological parameters of pore structure should be considered in further research in order to give a more realistic estimation of permeability.

Appendix 4A. Determination of water saturation degree based on the probabilistic pore size distribution model

Based on the proposed probabilistic porous network in Chapter 2, water saturates pores smaller than r_c , thus the water saturation degree is the integration of the pore volume fraction within the range from zero up to capillary front r_c .

- ❖ **Water saturation degree after successive transformations of pore size distribution with constant relative humidity.** When pore size distribution subjected to successive modifications of salt precipitation and dissolution, the waterfront r_c and opening zone β are assumed to be constant, while the porosity undergoes a decrease or increase with $\phi_0 \rightarrow \phi_1 \rightarrow \dots \rightarrow \phi_i \rightarrow \phi_{n+1}$ by n times of transformation.

Therefore, the water saturation degree after successive transformation model should be considered by adopting monotonic transformation model and non-monotonic transformation model, respectively.

- By adopting monotonic transformation model, the water saturation degree is given as follows:

$$MT: S_i^{(n+1)} = \frac{\phi_0}{\phi_{n+1}} \left[\int_0^{r_c-\beta} P_0(r_n) dr_n + \int_{r_c-\beta}^{r_c} \frac{\prod_{i=0}^n (r_n + \varepsilon_i \cdot H(r_n, r_c))}{(r_n)^{n+1}} P_0(r_n) dr_n \right] \quad (4A.1)$$

- By adopting non-monotonic transformation model, the water saturation degree can be deduced as:

$$NMT: S_i^{(n+1)} = \frac{\phi_0}{\phi_{n+1}} \left[\int_0^{r_c-\beta} P_0(r_n) dr_n + \int_{r_c-\beta}^{r_c} \frac{\prod_{i=0}^n (r_n + \varepsilon_i \cdot G(r_n, r_c))}{(r_n)^{n+1}} P_0(r_n) dr_n \right] \quad (4A.2)$$

- ❖ **Water saturation degree after single transformation of pore size distribution with varying relative humidity.** When pore size distribution subjected to single modification of salt precipitation and dissolution with the porosity undergoes transformation from ϕ_0 to ϕ_i , the waterfront r_c and opening zone β are assumed to be changed due to the varying relative humidity.

Before working on the water saturation degree, the transformation model with the varying waterfront r_c and opening zone β can be described as follows:

The S-shape function $S_{MT}^{(i)}$ for monotonic transformation model is expressed as:

$$S_{MT}^{(i)} = \begin{cases} 0 & r_c^{(i)} \leq r_0 \leq r_c^{(i)} - \beta^{(i)} \\ H^{(i)}(r_0, r_c) = \frac{3}{4} \left(\frac{r_0 - r_c^{(i)}}{\beta^{(i)}} - \frac{(r_0 - r_c^{(i)})^3}{3(\beta^{(i)})^3} \right) + \frac{1}{2} & r_c^{(i)} - \beta^{(i)} < r_0 \leq r_c^{(i)} + \beta^{(i)} \\ 1 & r_c^{(i)} + \beta^{(i)} < r_0 < \infty \end{cases} \quad (4A.3)$$

The symmetric S-shape function S_{NMT} for non-monotonic transformation model is given by:

$$S_{NMT}^{(i)} = \begin{cases} 0 & 0 \leq r_0 \leq r_c^{(i)} - \beta^{(i)} \\ G^{(i)}(r_0, r_c) = \frac{3}{4} \left(\frac{2r_0 + \beta^{(i)} - 2r_c^{(i)}}{\beta^{(i)}} - \frac{(2r_0 + \beta^{(i)} - 2r_c^{(i)})^3}{3(\beta^{(i)})^3} \right) + \frac{1}{2} & r_c^{(i)} - \beta^{(i)} < r_0 \leq r_c^{(i)} \\ K^{(i)}(r_0, r_c) = -\frac{3}{4} \left(\frac{2r_0 - \beta^{(i)} - 2r_c^{(i)}}{\beta^{(i)}} - \frac{(2r_0 - \beta^{(i)} - 2r_c^{(i)})^3}{3(\beta^{(i)})^3} \right) + \frac{1}{2} & r_c^{(i)} < r_0 \leq r_c^{(i)} + \beta^{(i)} \\ 0 & r_c^{(i)} + \beta^{(i)} < r_0 < \infty \end{cases} \quad (4A.4)$$

Therefore, the water saturation degree after single transformation of pore size distribution with varying waterfront and opening zone should be considered by adopting monotonic transformation model and non-monotonic transformation model, respectively.

- By adopting monotonic transformation model, the water saturation degree modification can be given as:

$$MT: S_l^{(i)} = \frac{\phi_0}{\phi_i} \left[\int_0^{r_c^{(i)} - \beta^{(i)}} P_0(r_0) dr_0 + \int_{r_c^{(i)} - \beta^{(i)}}^{r_c^{(i)}} \frac{(r_0 + \varepsilon_i \cdot H^{(i)}(r_0, r_c))}{r_0} P_0(r_0) dr_0 \right] \quad (4A.5)$$

- By adopting non-monotonic transformation model, we have:

$$NMT: S_l^{(i)} = \frac{\phi_0}{\phi_i} \left[\int_0^{r_c^{(i)} - \beta^{(i)}} P_0(r_0) dr_0 + \int_{r_c^{(i)} - \beta^{(i)}}^{r_c^{(i)}} \frac{(r_0 + \varepsilon_i \cdot G^{(i)}(r_0, r_c))}{r_0} P_0(r_0) dr_0 \right] \quad (4A.6)$$

Appendix 4B. Permeability based on the probabilistic pore size distribution model

- ❖ **Permeability after successive transformations of pore size distribution with constant relative humidity.** When pore size distribution subjected to successive modifications of salt precipitation and dissolution, the waterfront r_c and opening zone β are assumed to be constant, while the porosity undergoes a decrease or increase with $\phi_0 \rightarrow \phi_1 \rightarrow \dots \rightarrow \phi_i \rightarrow \phi_{n+1}$ by n times of transformation.

- By adopting monotonic transformation model, the intrinsic permeability for the porous material is given as follows:

$$MT: K_0^{(n+1)} = \frac{\phi_{n+1}^2}{50} \cdot \frac{\phi_0^2}{\phi_{n+1}^2} \left[\int_0^{r_c - \beta} r_n P_0(r_n) dr_n + \int_{r_c - \beta}^{r_c + \beta} (r_n + \varepsilon_i \cdot H(r_n, r_c)) \frac{\prod_{i=0}^n (r_n + \varepsilon_i \cdot H(r_n, r_c))}{(r_n)^{n+1}} P_0(r_n) dr_n + \int_{r_c + \beta}^{\infty} (r_n + \varepsilon_i) \frac{\prod_{i=0}^n (r_n + \varepsilon_i)}{(r_n)^{n+1}} P_0(r_n) dr_n \right]^2 \quad (4B.7)$$

The liquid permeability for the porous material is given as follows:

$$MT: K_l^{(n+1)} = \frac{\phi_{n+1}^2}{50} \cdot \frac{\phi_0^2}{\phi_{n+1}^2} \left[\int_0^{r_c - \beta} r_n P_0(r_n) dr_n + \int_{r_c - \beta}^{r_c} (r_n + \varepsilon_i \cdot H(r_n, r_c)) \frac{\prod_{i=0}^n (r_n + \varepsilon_i \cdot H(r_n, r_c))}{(r_n)^{n+1}} P_0(r_n) dr_n \right]^2 \quad (4B.8)$$

The gas permeability for the porous material is given as follows:

$$MT: K_g^{(n+1)} = \frac{\phi_{n+1}^2}{50} \cdot \frac{\phi_0^2}{\phi_{n+1}^2} \left[\int_{r_c}^{r_c + \beta} (r_n + \varepsilon_i \cdot H(r_n, r_c)) \frac{\prod_{i=0}^n (r_n + \varepsilon_i \cdot H(r_n, r_c))}{(r_n)^{n+1}} P_0(r_n) dr_n + \int_{r_c + \beta}^{\infty} r_n P_0(r_n) dr_n \right]^2 \quad (4B.9)$$

- By adopting non-monotonic transformation model, the intrinsic permeability for the porous material is given as follows:

$$NMT: K_0^{(n+1)} = \frac{\phi_{n+1}^2}{50} \cdot \frac{\phi_0^2}{\phi_{n+1}^2} \left[\begin{aligned} & \int_0^{r_c - \beta} r_n P_0(r_n) dr_n \\ & + \int_{r_c - \beta}^{r_c} (r_n + \varepsilon_i \cdot G(r_n, r_c)) \frac{\prod_{i=0}^n (r_n + \varepsilon_i \cdot G(r_n, r_c))}{(r_n)^{n+1}} P_0(r_n) dr_n \\ & + \int_{r_c}^{\infty} (r_n + \varepsilon_i \cdot K(r_n, r_c)) \frac{\prod_{i=0}^n (r_n + \varepsilon_i \cdot K(r_n, r_c))}{(r_n)^{n+1}} P_0(r_n) dr_n \\ & + \int_{r_c + \beta}^{\infty} r_n P_0(r_n) dr_n \end{aligned} \right]^2 \quad (4B.10)$$

The liquid permeability for the porous material is given as follows:

$$NMT: K_l^{(n+1)} = \frac{\phi_{n+1}^2}{50} \cdot \frac{\phi_0^2}{\phi_{n+1}^2} \left[\begin{aligned} & \int_0^{r_c - \beta} r_n P_0(r_n) dr_n \\ & + \int_{r_c - \beta}^{r_c} (r_n + \varepsilon_i \cdot G(r_n, r_c)) \frac{\prod_{i=0}^n (r_n + \varepsilon_i \cdot G(r_n, r_c))}{(r_n)^{n+1}} P_0(r_n) dr_n \end{aligned} \right]^2 \quad (4B.11)$$

The gas permeability for the porous material is given as follows:

$$NMT: K_g^{(n+1)} = \frac{\phi_{n+1}^2}{50} \cdot \frac{\phi_0^2}{\phi_{n+1}^2} \left[\begin{aligned} & \int_{r_c}^{r_c + \beta} (r_n + \varepsilon_i \cdot K(r_n, r_c)) \frac{\prod_{i=0}^n (r_n + \varepsilon_i \cdot K(r_n, r_c))}{(r_n)^{n+1}} P_0(r_n) dr_n \\ & + \int_{r_c + \beta}^{\infty} r_n P_0(r_n, r_c) dr_n \end{aligned} \right]^2 \quad (4B.12)$$

- ❖ **Permeability after single transformation of pore size distribution with varying relative humidity.** When pore size distribution subjected to single modification of salt precipitation and dissolution with the porosity undergoes transformation from ϕ_0 to ϕ_i , the waterfront r_c and opening zone β are assumed to be changed due to the varying relative humidity.

- By adopting monotonic transformation model, the intrinsic permeability for the porous material is given as follows:

$$MT: K_0^{(i)} = \frac{\phi_i^2}{50} \cdot \frac{\phi_0^2}{\phi_i^2} \left[\int_0^{r_c^{(i)} - \beta^{(i)}} r_0 P_0(r_0) dr_0 + \int_{r_c^{(i)} - \beta^{(i)}}^{r_c^{(i)} + \beta^{(i)}} \frac{(r_0 + \varepsilon_i \cdot H^{(i)}(r_0, r_c))^2}{r_0} P_0(r_0) dr_0 + \int_{r_c^{(i)} + \beta^{(i)}}^{\infty} \frac{(r_0 + \varepsilon_i)^2}{r_0} P_0(r_0) dr_0 \right]^2 \quad (4B.13)$$

The liquid permeability for the porous material is given as follows:

$$MT: K_l^{(i)} = \frac{\phi_i^2}{50} \cdot \frac{\phi_0^2}{\phi_i^2} \left[\int_0^{r_c^{(i)} - \beta^{(i)}} r_0 P_0(r_0) dr_0 + \int_{r_c^{(i)} - \beta^{(i)}}^{r_c^{(i)}} \frac{(r_0 + \varepsilon_i \cdot H^{(i)}(r_0, r_c))^2}{r_0} P_0(r_0) dr_0 \right]^2 \quad (4B.14)$$

The gas permeability for the porous material is given as follows:

$$MT: K_g^{(i)} = \frac{\phi_i^2}{50} \cdot \frac{\phi_0^2}{\phi_i^2} \left[\int_{r_c^{(i)} - \beta^{(i)}}^{r_c^{(i)} + \beta^{(i)}} \frac{(r_0 + \varepsilon_i \cdot H^{(i)}(r_0, r_c))^2}{r_0} P_0(r_0) dr_0 + \int_{r_c^{(i)} + \beta^{(i)}}^{\infty} \frac{(r_0 + \varepsilon_i)^2}{r_0} P_0(r_0) dr_0 \right]^2 \quad (4B.15)$$

- By adopting non-monotonic transformation model, the intrinsic permeability for the porous material is given as follows:

$$NMT: K_0^{(i)} = \frac{\phi_i^2}{50} \cdot \frac{\phi_0^2}{\phi_i^2} \left[\int_0^{r_c^{(i)} - \beta^{(i)}} r_0 P_0(r_0) dr_0 + \int_{r_c^{(i)} - \beta^{(i)}}^{r_c^{(i)}} \frac{(r_0 + \varepsilon_i \cdot G^{(i)}(r_0, r_c))^2}{r_0} P_0(r_0) dr_0 + \int_{r_c^{(i)}}^{r_c^{(i)} + \beta^{(i)}} \frac{(r_0 + \varepsilon_i \cdot K^{(i)}(r_0, r_c))^2}{r_0} P_0(r_0) dr_0 + \int_{r_c^{(i)} + \beta^{(i)}}^{\infty} r_0 P_0(r_0) dr_0 \right]^2 \quad (4B.16)$$

The liquid permeability for the porous material is given as follows:

$$NMT: K_l^{(i)} = \frac{\phi_i^2}{50} \cdot \frac{\phi_0^2}{\phi_i^2} \left[\int_0^{r_c^{(i)} - \beta^{(i)}} r_0 P_0(r_0) dr_0 + \int_{r_c^{(i)} - \beta^{(i)}}^{r_c^{(i)}} \frac{(r_0 + \varepsilon_i \cdot G^{(i)}(r_0, r_c))^2}{r_0} P_0(r_0) dr_0 \right]^2 \quad (4B.17)$$

The gas permeability for the porous material is given as follows:

$$NMT: K_g^{(i)} = \frac{\phi_i^2}{50} \cdot \frac{\phi_0^2}{\phi_i^2} \left[\int_{r_c^{(i)}}^{r_c^{(i)} + \beta^{(i)}} \frac{(r_0 + \varepsilon_i \cdot K^{(i)}(r_0, r_c))^2}{r_0} P_0(r_0) dr_0 + \int_{r_c^{(i)} + \beta^{(i)}}^{\infty} r_0 P_0(r_0) dr_0 \right]^2 \quad (4B.18)$$

Chapter 5

Conclusions and Perspectives

5.1 Conclusions

This dissertation mainly developed modelling approaches for the evolution of pore size distribution due to salt precipitation and dissolution in porous materials. Moreover, moisture transports involving chemical species and chemical reactions concerning salt precipitation and dissolution were proposed to investigate the pore filling and emptying processes when porous materials were subjected to cyclic drying and wetting. Based on the probabilistic representation for the evolution for pore size distribution, the transport properties were evaluated by introducing the water sorption isotherm to characterise the location of the capillary interface (waterfront). The major conclusions in general were outlined as follows:

Chapter 2 dealt with the water-dependent evolution of pore size distribution induced by salt precipitation and dissolution. Two probabilistic methods were established regarding the probability density functions for initial and modified pore-size distributions. Three transformation models were constructed to interpret the relation between the initial pore radius and modified pore radius during salt precipitation and dissolution. Linear transformation model describes an overall modification of pore sizes, which was far from reality; Monotonic and non-monotonic transformation models allowed estimation on water-dependent modifications of pore sizes. The former permitted the diffused modifications to all unsaturated pores. Non-monotonic transformation model restricted the highly localized modifications to pores at proximity to the waterfront, which induced bimodal pore size distribution and a higher filling/emptying ratio than monotonic transformation model. In all, the proposed probabilistic model provided a reasonable interpretation of physical parameters and water-dependent evolution of pore size distribution.

In chapter 3, a local-like model was developed to describe the hygro-chemical transport process in porous materials involving salt precipitation and dissolution when subjected to drying and wetting cycles. The proposed model consisted of transport equations according to the mass balance theory and the chemical reactions based on the law of mass action. Operator-splitting method was used to solve the hygro-chemical equations. Adopting the proposed model could evaluate how long the pore volume was filled by salt precipitation under cyclic drying and wetting. This model could provide a pore-scale view of the transport process coupling with chemical reactions, which could be used for numerous applications, such as

mechanisms of salt precipitation and dissolution, the evolution of water saturation degree and porosity, the estimation of ionic concentration, or even the assessment of pore structures.

In chapter 4, an analytical permeability model based on probabilistic pore network was proposed for evaluating the intrinsic permeability K_0 , liquid permeability K_l , gas permeability K_g and relative permeability for liquid k_{rl} and gas k_{rg} in porous materials. It was found that samples with higher porosity were more permeable. Meanwhile, pore size distribution and critical pore size were crucial factors that determine permeability in addition to porosity. Even though modelling results obtained by our model were higher than the measured permeability, it could be a preliminary tool for permeability evaluation when experimental measurements were difficult. Moreover, the proposed permeability model could also be used in evaluating the influences of modified porosity on permeability when porous materials were subjected to salt precipitation and dissolution.

5.2 Perspectives

5.2.1 Development of compound-lognormal pore size distribution

Porous materials have a wide range of pore sizes, including gel pores, smaller capillary pores, large capillary pores, and entrapped air voids. Many authors [6,43,46,47] have suggested that various types of pore sizes play different roles in physical and mechanical properties of porous materials. For instance, shrinkage and creep properties are strongly related to gel pores; capillary pores determine the water condensation, water saturation degree, and transport properties, while air voids significantly affect the strength of porous materials [14,17]. Our model adopted single lognormal distribution of pore sizes to investigate the transport properties in porous materials, which mainly dealt with the pore size distribution of capillary pores. The effects of gel pores and large air voids on transport properties remain unclear. Therefore, a compound lognormal distribution model should be more suitable for further analysis of pore size distribution contains very small pores and very large pores.

A compound-lognormal distribution of pore sizes before salt precipitation and dissolution can be expressed as follows:

$$P_0(r_0) = \sum_{k=1}^n \left[\frac{\alpha_k}{\sigma_{r,k} \sqrt{2\pi} r_0} \exp - \frac{(\ln(r_0) - \mu_{r,k})^2}{2\sigma_{r,k}^2} \right] \quad (5.1)$$

where α_k is the weighing factors of the k th lognormal distribution and $\sum \alpha_k = 1$, $\mu_{r,k}$ is location parameter and $\sigma_{r,k}$ is shape parameter in the k th lognormal distribution.

This model can represent a more extensive range of pore sizes. For instance, $k=1, 2, 3$ denoting gel pores, small capillary pores, and large capillary pores, $\alpha_k = 0.2, 0.6, 0.2$ presenting the proportions of each type of pore size shown in figure 5.1. By adopting this compound model, it is possible to investigate:

- a combination graphical model that represent the modified pore size distribution after salt

precipitation and dissolution for each category of pore sizes by adopting the compound-lognormal distribution.

- a further development for the contribution of each category of pore sizes makes on the transport properties, such as permeability, diffusivity;

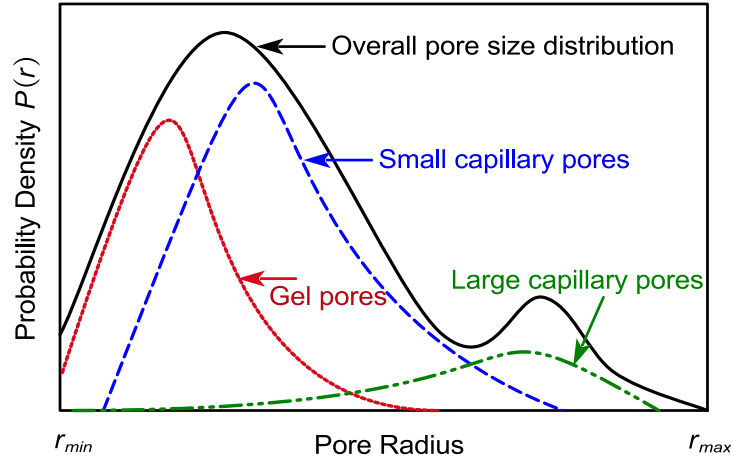


Figure 5. 1 Schematic for compound lognormal distribution for gel pores, small capillary pores and large capillary pores.

5.2.2 Extended description of water saturation degree

Our research considers a simple case of unsaturated porous materials; that waterfront divides the pore space into the saturated part and unsaturated part. However, an adsorbed film of water existed in the unsaturated pores with sizes larger than r_c . An extended profile of water saturation degree can be considered in further research that pore volume is regarded as a saturated part and partially saturated part [42]. The water saturation degree, therefore should be the sum of contributions from filled and partially filled pores, as is given in:

$$S_l = \int_0^{r_c} P(r) dr + S_r \int_{r_c}^{\infty} P(r) dr \quad (5.2)$$

where S_r is the water saturation degree for unsaturated pores, which can be determined as:

$$S_r = 1 - \left(\frac{r - t_a}{r} \right)^2 \quad (5.3)$$

The thickness of adsorbed layer t_a is given by an empirical expression based on the relative humidity:

$$t_a = (3.85 - 1.89 \ln(-RH)) \times 10^{-10} \quad (5.4)$$

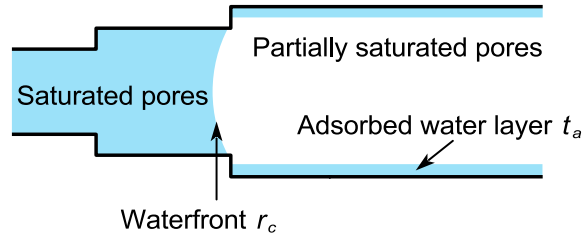


Figure 5. 2 A novel profile of water saturation degree.

5.2.3 Coupling of pore structure evolution and reactive transports

This dissertation proposed a preliminary model to illustrate the evolution of pore structures induced by salt precipitation and dissolution from a geometrical perspective. We also developed a local-like model to describe the reactive transports in porous materials under drying and wetting cycles. However, the interactions (coupling effects) between the pore structure and reactive transport remain unclear. Thus, the author intends to establish a coupling model in further, which couples the evolution of pore structure (pore filling process) with the local-like reactive transport model. This coupling model aims to elucidate how the pore structure evolves with the reactive transports under complicated exposure conditions. The schematic of this model can be found in figure 5.3.

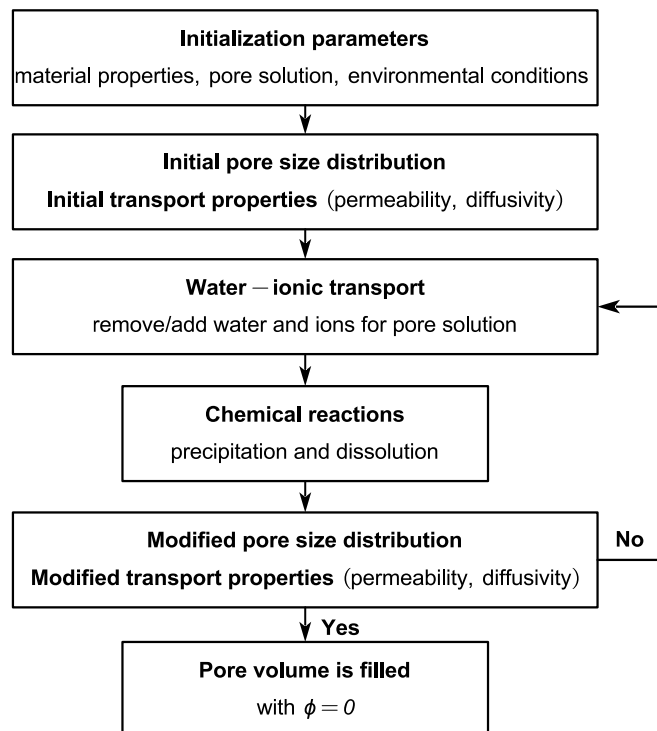


Figure 5. 3 Flowchart for local coupling between pore structure and reactive transport in porous materials.

5.2.4 Extending probabilistic approach to diffusivity based single fluid model

Further research should also be focused on the development of water diffusivity. According to Darcy's law, the water flux term in the liquid phase can be given as:

$$J_l = K' \nabla p_c \quad (5.5)$$

where K' is expressed as $K' = (K_0 k_{rl} \rho_w) / \mu_l$, K_0 is the intrinsic permeability, k_{rl} is the relative liquid permeability, μ_l is the dynamic viscosity of liquid water, which have been described in chapter 4.

The water flux term in gaseous phase can be expressed as [140,141]:

$$J_v = D_v \frac{\rho_v M_w}{\rho_w R T} \nabla p_c \quad (5.6)$$

where D_v is the equivalent diffusion coefficient of water vapour (m^2/s), ρ_v is the water vapour density, ρ_w is the Liquid Water Density (kg/m^3), M_w is the molar mass of water (kg/mol), R is the gas constant ($\text{J}/\text{k}/\text{mol}$), T is the temperature.

Therefore, the transport of water flux term can be given as the sum of the liquid phase and gaseous phase:

$$J_w = J_l + J_v = (K' + D_v \frac{\rho_v M_w}{\rho_w R T}) \nabla p_c = (K' + D_v \frac{\rho_v M_w}{\rho_w R T}) \frac{\partial p_c}{\partial S_l} \nabla S_l \quad (5.7)$$

According to the water conservation and water diffusion equation, we have:

$$\frac{\partial(\rho_w \phi S_l)}{\partial t} = - \text{div}(J_w) \quad (5.8)$$

and

$$\frac{\partial(S_l)}{\partial t} = \text{div}(D(S_l) \nabla S_l) \quad (5.9)$$

Based on equation (5.7), (5.8) and (5.9), we can obtain:

$$D(S_l) = - \frac{1}{\rho_w \phi} (K' + D_v \frac{\rho_v M_w}{\rho_w R T}) \frac{\partial p_c}{\partial S_l} \quad (5.10)$$

As has been presented in Chapter 4 that capillary pressure is the function of water saturation degree. Thus, we have:

$$\frac{\partial p_c}{\partial S_l} = a(1-b)(S_l^{-b}-1)^{-1/b} S_l^{-b-1} \quad (5.11)$$

Finally, the water diffusivity should be expressed as:

$$D(S_l) = -\frac{1}{\rho_w \phi} \left(K' + D_v \frac{\rho_v M_w}{\rho_w R T} \right) (a(1-b)(S_l^{-b}-1)^{-1/b} S_l^{-b-1}) \quad (5.12)$$

With expression(5.12), the water diffusivity can be obtained based on the proposed water permeability model and probabilistic pore size distribution model.

List of symbols

r_0	initial pore radius (m)
$P_0(r_0)$	initial probability density function
r_1	modified pore radius (m)
$P_1(r_1)$	modified probability density function
μ_r	location parameter of lognormal distribution
σ_r	shape parameter of lognormal distribution
ε	erosion parameter for pore radius (m)
r_c	pore radius for waterfront (m)
β	opening zone for waterfront (m)
a_{ij}	stoichiometric coefficient of the j th ionic species in the i th precipitated species (—)
c_j	ionic concentration for the j th ionic species (mol/m ³)
c_j^{eq}	ionic concentration for the j th ionic species in equilibrium state (mol/m ³)
K_{eq}^i	equilibrium constant in the i th precipitated species (—)
K_{con}	conditional equilibrium constant for ideal solution (—)
γ_j	chemical activity coefficient for the j th ionic species (—)
$\Delta c_{s-j,k}$	increased concentration for the i th precipitated species relative to the pore solution (mol/m ³)
Nx	number of ionic species (—)
Mp	number of precipitated species (—)
Ω	total volume of porous material (m ³)
Ω_π	volume for π , π may be dry air (a), vapor water (v), liquid water (w), precipitated salt (salt), solid phase (s), liquid solution (l), the i th precipitated species (i), or the j th ionic species (j) (m ³)
Ω_s^0	volume for the solid skeleton of porous material (m ³)
ϕ	total open porosity (m ³ /m ³)
S_l	degree of saturation for pore solution (m ³ /m ³)
s_α	amount for the α th species in moles relative to porous material, α may be j th ionic species (j), or i th precipitated species (i) (mol/m ³)
n_α	amount for the α th species in moles (mol)

M_α	molar mass for the α th species in moles (kg/mol)
ω_α	molar volume for the α th species in moles (m^3/mol)
m_π	mass for π phase relative to porous material (kg/m^3)
ρ_π	density for π phase (kg/m^3)
Q_w	water flux term relative to porous material ($\text{kg}/\text{m}^3 \cdot \text{s}$)
Q_c	ionic flux term relative to porous material ($\text{mol}/\text{m}^3 \cdot \text{s}$)
K_0	intrinsic permeability in theoretical
K_0^π	intrinsic permeability as measured by phase π in experimental $\pi = l(\text{liquid})$ or $g(\text{gas})$
$k_{r\pi}$	relative permeability of phase π which depends on the saturation degree of phase π
K_l	liquid permeability, which is given by $K_0^l \cdot k_{rl}$
K_g	gas permeability, which is given by $K_0^g \cdot k_{rg}$
K'	conventional permeability of porous materials (apparent permeability) which is given by $\frac{K_0^\pi \cdot k_{r\pi}}{\mu_\pi}$
V	total volume of the porous material, which is regarded as 1×10^{-3} (m^3)
M_w	molar mass of water, which is valued as 1.8×10^{-3} (kg/mol)
R	molar gas constant, which is valued at 8.314 (J/k/mol)
T	temperature, which is valued at 293k
a_w	water activity
I	ionic strength (mol/kg)
A_ϕ	Debye – Hückel constant
c_j	ionic concentration for the j th ionic species (mol/m^3)
\hat{m}_j	molality of the j th ionic species in salt solution (mol/kg) and $\hat{m}_T = \sum_j \hat{m}_j$ (mol/kg)
ρ_j	density of the j th ionic species (kg/m^3) which have a relationship with molar concentration c_j $\rho_j = 37.741 \times 10^3 c_j + 1000.1$
r_c	critical pore radius for the capillary interface (m)
p_c	capillary pressure (MPa)
RH	relative humidity
γ	liquid – gas surface tension, which is valued at 0.07275 (N/m)
θ	contact angle of water and the porous material

List of figures

Figure 1. 1 Schematic of pores [13].	5
Figure 1. 2 Bottle-ink effect.	6
Figure 1. 3 Classification of pore sizes in this research.	8
Figure 1. 4 Fitting results for the size-frequency distribution of sample A3 and D. [41].	12
Figure 1. 5 Schematic for the pore structure altered by calcium leaching.[57]	13
Figure 1. 6 Schematic for salt precipitation inside porous materials (subflorescence) and on the surface of porous materials (efflorescence).	14
Figure 1. 7 Simple Darcy flow through a homogeneous material induced by pressure gradient.	15
Figure 1. 8 Schematic of the methods for solving the reactive transport equations.	21
Figure 1. 9 Schematic for the water sorption isotherm.	26
Figure 2. 1 Classification of pore sizes in cement-based material.	30
Figure 2. 2 Phases of a porous material.	31
Figure 2. 3 Modification of pore radius due to salt precipitation and dissolution. r_0 = initial pore radius, r_1 = modified pore radius after salt precipitation and dissolution, r_c = capillary pore radius at which waterfront is located, $\varepsilon(r_0, r_c)$ = eroded size of pore.	33
Figure 2. 4 Initial and modified pore volume fractions with the consideration of transformation effects.	34
Figure 2. 5 Classical transformation technique of the random variable r_0 .	35
Figure 2. 6 Non-linear transformation models. (a) Monotonic transformation model. (b) Non-monotonic transformation model.	38
Figure 2. 7 Relationship between water saturation degree and pore radius of waterfront.	39
Figure 2. 8 Pore size distribution of masonry cement. (a) Experimental and simulated cumulative volume fraction. (b) Incremental pore volume distribution.	40

Figure 2. 9 Profile for probability density curve of initial pore size distribution fitted by lognormal distribution.	40
Figure 2. 10 Linear transformation model of pore size distribution. (a) Probability density curve. (b) Cumulative volume fraction curve.	41
Figure 2. 11 Relationship between porosity ϕ_{min} and waterfront rc under different opening zone β for monotonic transformation model.	42
Figure 2. 12 Pore size distribution after single occurrence of salt precipitation/dissolution. Precipitation case: porosity decreases from 0.2 to 0.1; Dissolution case: porosity increases from 0.2 to 0.5. MT1 denotes monotonic transformation-method one; NMT1 denotes non-monotonic transformation- method one; MT2 denotes monotonic transformation-method two; NMT2 denotes non-monotonic transformation- method two.	43
Figure 2. 13 Parameter ε against porosity.	45
Figure 2. 14 Pore size distribution after single occurrence of salt precipitation by both method one and method two. The initial porosity of 0.20 decreases to 0.16 which corresponds to increments in water saturation degree from 0.40 to 0.50.	46
Figure 2. 15 Pore size distribution with varied waterfront after successive occurrences of salt precipitation and dissolution, respectively. (j is transformation times and valued at 5 in this implementation. When precipitation occurs, porosity decreases from 0.2 to 0.15; when dissolution occurs, porosity increases from 0.2 to 0.3).	47
Figure 2. 16 Pore size distribution after single occurrence of salt precipitation by method two. The initial porosity of 0.20 decreases to five degrees of porosity (0.19, 0.18, 0.17, 0.16, and 0.15) which corresponds to reductions in water saturation degree from 0.50 to five degrees (0.48, 0.46, 0.44, 0.42, 0.40).	48
Figure 2. 17 Pore size distribution after single occurrence of salt dissolution by method two. The initial porosity of 0.20 increases to five degrees of porosity (0.21, 0.22, 0.23, 0.24, and 0.25) which corresponds to increases in water saturation degree from 0.40 to five degrees (0.42, 0.44, 0.46, 0.48, 0.50).	48
Figure 2. 18 Evolution of pore volume fraction due to salt precipitation and dissolution by	

method two.	49
Figure 2. 19 Filling and emptying ratios after single (a) salt precipitation and (b) salt dissolution by method two.	50
Figure 2. 20 Parameter ε against porosity for successive transformations of (a) salt precipitation and (b) salt dissolution by method two.	51
Figure 2. 21 Effect of single and successive transformations on pore size distribution (a and c) and filling/emptying ratio (b and d) by method two. Gradient colour represents successive modifications in the pore size distribution and filling/emptying ratio. As the colour is getting lighter, the porosity deviates more and more significantly from the initial one.	52
Figure 2. 22 Evolution of water saturation degree due to successive transformations. (a) Water saturation degree varies with decreased porosity during salt precipitation process. (b) Water saturation degree varies with increased porosity during salt dissolution process.	53
Figure 3. 1 SEM image of salt (NaCl) precipitation in the pore space of sand stone after evaporation of water in the pore solution. The micro cracks marked in the red cycles could be due to salt precipitation in the pore space [123].	64
Figure 3. 2 Schematic for chemical box implemented by MATLAB.	68
Figure 3. 3 Schematic for one chemical reaction with two different equilibrium constant.	69
Figure 3. 4 One precipitation reaction under different chemical equilibrium constant.	69
Figure 3. 5 Iterative numbers of each method under different chemical reaction cases.	70
Figure 3. 6 Sodium chloride (NaCl) precipitation and dissolution in pore solution.	71
Figure 3. 7 Concentrations for each compositions after successive (a) salt precipitation and (b) salt dissolution.	71
Figure 3. 8 Drying and wetting cycles with salt precipitation and dissolution.	72
Figure 3. 9 Description of representative porous materials.	73
Figure 3. 10 Hygro-chemical transport within the representative porous volume.	76
Figure 3. 11 Basic framework of two-step method for the proposed hygro-chemical transport model.	77

Figure 3. 12 Schematic for hygro-chemical transport in pore volume subjected to single water drying or wetting process.	79
Figure 3. 13 Case one-precipitation with no ions added in the system.	80
Figure 3. 14 Equilibrium concentration and salt mass in different initial cases of ionic concentration.	80
Figure 3. 15 Case two-dissolution with no ions added in the system.	81
Figure 3. 16 Case three- keep water content constant and add ions in the system.	82
Figure 3. 17 Case four - Water drying with adding or removing ions in the pore solution. ..	83
Figure 3. 18 Mass of each components during drying process.	83
Figure 3. 19 Case five- Water wetting with adding or removing ions in the pore solution. ..	84
Figure 3. 20 Relation between ionic concentration (predictor) and equilibrium concentration (indicator).	84
Figure 3. 21 Water flux term during wetting and drying process.	85
Figure 3. 22 Water saturation degree during wetting and drying process.	85
Figure 3. 23 Ionic flux term during wetting and drying process.	86
Figure 3. 24 Time duration under drying-wetting cycles with different Q_c	86
Figure 3. 25 Pore filling process under drying-wetting cycles with different Q_c	87
Figure 3. 26 Salt mass under drying-wetting cycles with different Q_c	87
Figure 3. 27 Relation between concentration of Na^+ and concentration of Cl^- under drying-wetting cycles with different Q_c	88
Figure 3. 28 Adding or removing ions during wetting and drying process and k is the time step for adding and removing ions.	89
Figure 3. 29 Adding and removing ions during drying and wetting cycles, the time step k was 100.	90
Figure 3. 30 Relation between concentration of Na^+ and concentration of Cl^- under drying-wetting cycles with the case of adding ions with $10^{-7}mol/m^3.s$, meanwhile, removing ions with (a) $-5 \times 10^{-8}mol/m^3.s$ and (b) $-10^{-8}mol/m^3.s$	90
Figure 3. 31 Time duration under drying and wetting cycles with constant ionic flux term (adding ions) while different intervals of water saturation degree.	91

Figure 3. 32 Porosity under drying and wetting cycles with constant ionic flux term (adding ions) while different intervals of water saturation degree.	91
Figure 3. 33 Cumulative salt mass under drying and wetting cycles with constant ionic flux term (adding ions) while different intervals of water saturation degree.	92
Figure 3. 34 Relation between concentration of Na ⁺ and concentration of Cl ⁻ under drying-wetting cycles with the case of adding ions with 10 ⁻⁷ mol/m ³ .s while changing intervals of water saturation degree.	93
Figure 3. 35 Prediction between LogQ _c and cycles numbers LogN under different intervals of water saturation degree.	94
Figure 3. 36 Prediction between LogQ _c and cumulative time Logt under different intervals of water saturation degree.	95
Figure 4. 1 Water sorption isotherm of porous materials.	104
Figure 4. 2 Flowchart for determining the water saturation degree based on water sorption isotherm in porous materials.	105
Figure 4. 3 Effects of water activity and relative humidity on the capillary pressure.	107
Figure 4. 4 Capillary pressure versus relative humidity under a given NaCl concentration.	108
Figure 4. 5 Effects of NaCl concentration on the capillary pressure under a given relative humidity.	108
Figure 4. 6 Interface equilibrium in a pore with the radius of r_s	109
Figure 4. 7 Relation between the surface tension of solutions and its concentration [145].	109
Figure 4. 8 Measured and simulated pore size distribution for four different materials: Incremental pore volume distribution (on the left side) and experimental and simulated cumulative volume fraction (on the right side).	112
Figure 4. 9 Determination for the location of the waterfront based on capillary pressure.	112
Figure 4. 10 Waterfront with varying relative humidity.	113
Figure 4. 11 Relation between the relative humidity and the waterfront under different solutions.	113
Figure 4. 12 Water saturation degree obtained from the pore size distribution.	114
Figure 4. 13 Determining the water saturation degree with the waterfront based on the	

probabilistic model.	115
Figure 4. 14 Modelling of the water sorption isotherm in four porous materials.	116
Figure 4. 15 Influence of the ionic concentration on the modelled water sorption isotherm for masonry cement.	116
Figure 4. 16 Water saturation degree versus capillary pressure for different materials.	117
Figure 4. 17 Open system with constant RH (With the given room temperature, the saturated salt solution can control the RH).	120
Figure 4. 18 Evolution of pore size distribution with successive transformations due to salt precipitation and dissolution under the constant RH.	121
Figure 4. 19 Evolution of water saturation degree with successive transformations due to (a) salt precipitation and (b) salt dissolution under the constant relative humidity.	122
Figure 4. 20 Mass of (a) evaporated water under salt precipitation case and (b) condensed water under salt dissolution case due to successive transformations under the constant relative humidity. MT denotes the monotonic transformation model and NMT denotes the non-monotonic transformation model.	123
Figure 4.21 Evolution of permeability due to successive transformations induced by (a) salt precipitation and (b) salt dissolution under the constant relative humidity.	123
Figure 4. 22 Evolution of relative permeability due to successive transformations induced by (a) salt precipitation and (b) salt dissolution under the constant relative humidity. ..	124
Figure 4. 23 Closed system with varying RH (This system is also the sorption isotherm experiment when the RH keeps constant).	125
Figure 4. 24 Modelling results for permeability of four different materials.	126
Figure 4. 25 Comparisons of permeability between experimental and modelling results for four different materials.	127
Figure 4. 26 Relative permeability versus water saturation degree for four different materials.	128
Figure 4. 27 Evolution of water saturation degree with single modification of porosity induced by (a) salt precipitation and (b) salt dissolution under varying relative humidity.	130

Figure 4. 28 Comparison of liquid permeability with single modification of porosity induced by (a) salt precipitation and (b) salt dissolution under varying relative humidity.	130
Figure 4. 29 Comparison of gas permeability with single modification of porosity induced by (a) salt precipitation and (b) salt dissolution under varying relative humidity.....	131
Figure 4. 30 Evolution intrinsic permeability K_0 , liquid permeability K_l and gas permeability K_g with single modification of porosity induced by (a) salt precipitation and (b) salt dissolution under varying relative humidity.	131
Figure 4. 31 Evolution of relative liquid permeability k_{rl} and relative gas permeability k_{rg} with single modification of porosity induced by (a) salt precipitation and (b) salt dissolution under varying relative humidity.	132
Figure 4. 32 Evolution of pore size distribution with successive modifications of porosity induced by salt precipitation and salt dissolution under varying relative humidity. ..	133
Figure 4. 33 Evolution of water saturation degree with successive modifications of porosity induced by (a) salt precipitation and (b) salt dissolution under varying relative humidity.....	133
Figure 4. 34 Evolution of intrinsic permeability K_0 , liquid permeability K_l and gas permeability K_g with successive modifications of porosity induced by (a) salt precipitation and (b) salt dissolution under varying relative humidity.....	134
Figure 4. 35 Evolution of relative liquid permeability k_{rl} and relative gas permeability k_{rg} with successive modifications of porosity induced by (a) salt precipitation and (b) salt dissolution under varying relative humidity.	135
Figure 5. 1 Schematic for compound lognormal distribution for gel pores, small capillary pores and large capillary pores.	145
Figure 5. 2 A novel profile of water saturation degree.....	146
Figure 5. 3 Flowchart for local coupling between pore structure and reactive transport in porous materials.	146

List of tables

Table 2. 1 Peculiarities for several common methods for PSD measurement.	29
Table 2. 2 Analysed properties of masonry cement and fitting values for parameters of lognormal distribution model.	39
Table 2. 3 Parameters for modified pore size distribution determined by both method one and method two regarding monotonic and non-monotonic transformation models.	44
Table 2. 4 Values of parameters for successive transformations of pore size distribution by method two.	50
Table 3. 1 Classification of chemical reactions in salt solution [76].	65
Table 3. 2 Initialization of parameters.	78
Table 3. 3 Initialization parameters for one single hygro-chemical transport under five different cases.	79
Table 3. 4 Fitting results for relation between Q_c and cycle numbers N	94
Table 3. 5 Fitting results for relation between Q_c and time t	95
Table 4. 1 Parameters for computing a_w . [142,143].	107
Table 4. 2 Tested properties and fitted values for parameters of the lognormal distribution models for the pore size distribution of four kinds of mortars.	110
Table 4. 3 Fitting results for relation between the capillary pressure p_c and the water saturation degree S_l	117
Table 4. 4 Parametric initialisations for successive transformations of pore size distribution.	120
Table 4. 5 Tested and fitted permeability for four kinds of mortars.	127

Bibliography

- [1] M. Koniorczyk, D. Gawin, Modelling of salt crystallization in building materials with microstructure – Poromechanical approach, *Construction and Building Materials*. 36 (2012) 860–873. <https://doi.org/10.1016/j.conbuildmat.2012.06.035>.
- [2] D. Benavente, N. Cueto, J. Martínez-Martínez, M.A. García del Cura, J.C. Cañaveras, The influence of petrophysical properties on the salt weathering of porous building rocks, *Environ Geol*. 52 (2007) 215–224. <https://doi.org/10.1007/s00254-006-0475-y>.
- [3] D. Benavente, M.A.G. del Cura, J. García-Guinea, S. Sánchez-Moral, S. Ordóñez, Role of pore structure in salt crystallisation in unsaturated porous stone, *Journal of Crystal Growth*. 260 (2004) 532–544. <https://doi.org/10.1016/j.jcrysgr.2003.09.004>.
- [4] G. Castellazzi, C. Colla, S. de Miranda, G. Formica, E. Gabrielli, L. Molari, F. Ubertini, A coupled multiphase model for hygrothermal analysis of masonry structures and prediction of stress induced by salt crystallization, *Construction and Building Materials*. 41 (2013) 717–731. <https://doi.org/10.1016/j.conbuildmat.2012.12.045>.
- [5] O. Coussy, Deformation and stress from in-pore drying-induced crystallization of salt, *Journal of the Mechanics and Physics of Solids*. 54 (2006) 1517–1547. <https://doi.org/10.1016/j.jmps.2006.03.002>.
- [6] Q. Huang, Z. Jiang, X. Gu, W. Zhang, B. Guo, Numerical simulation of moisture transport in concrete based on a pore size distribution model, *Cement and Concrete Research*. 67 (2015) 31–43. <https://doi.org/10.1016/j.cemconres.2014.08.003>.
- [7] D. Benavente, M.A. García del Cura, A. Bernabéu, S. Ordóñez, Quantification of salt weathering in porous stones using an experimental continuous partial immersion method, *Engineering Geology*. 59 (2001) 313–325. [https://doi.org/10.1016/S0013-7952\(01\)00020-5](https://doi.org/10.1016/S0013-7952(01)00020-5).
- [8] C. Rodriguez-Navarro, E. Doehne, Salt weathering: influence of evaporation rate, supersaturation and crystallization pattern, *Earth Surface Processes and Landforms*. 24 (1999) 191–209. [https://doi.org/10.1002/\(SICI\)1096-9837\(199903\)24:3<191::AID-ESP942>3.0.CO;2-G](https://doi.org/10.1002/(SICI)1096-9837(199903)24:3<191::AID-ESP942>3.0.CO;2-G).
- [9] B.Y. Lee, K.E. Kurtis, Effect of pore structure on salt crystallization damage of cement-based materials: Consideration of w/b and nanoparticle use, *Cement and Concrete Research*. 98 (2017) 61–70. <https://doi.org/10.1016/j.cemconres.2017.04.002>.
- [10] G.W. Scherer, Stress from crystallization of salt, *Cement and Concrete Research*. 34

-
- (2004) 1613–1624. <https://doi.org/10.1016/j.cemconres.2003.12.034>.
- [11] L. Bertolini, M. Carsana, B. Daniotti, E. Marra, Environmental Factors Affecting Corrosion of Steel Inserts in Ancient Masonry, in: V.P. de Freitas, J.M.P.Q. Delgado (Eds.), *Durability of Building Materials and Components*, Springer, Berlin, Heidelberg, 2013: pp. 229–252. https://doi.org/10.1007/978-3-642-37475-3_9.
- [12] V. Cnudde, A. Cwirzen, B. Masschaele, P.J.S. Jacobs, Porosity and microstructure characterization of building stones and concretes, *Engineering Geology*. 103 (2009) 76–83. <https://doi.org/10.1016/j.enggeo.2008.06.014>.
- [13] R.E. Collins, *Flow of fluids through porous materials*, (1976). <https://www.osti.gov/biblio/7099752> (accessed June 15, 2021).
- [14] S. Maria, Methods for porosity measurement in lime-based mortars, *Construction and Building Materials*. 24 (2010) 2572–2578. <https://doi.org/10.1016/j.conbuildmat.2010.05.019>.
- [15] R. Kumar, B. Bhattacharjee, Porosity, pore size distribution and in situ strength of concrete, *Cement and Concrete Research*. 33 (2003) 155–164. [https://doi.org/10.1016/S0008-8846\(02\)00942-0](https://doi.org/10.1016/S0008-8846(02)00942-0).
- [16] R.L. Day, B.K. Marsh, Measurement of porosity in blended cement pastes, *Cement and Concrete Research*. 18 (1988) 63–73. [https://doi.org/10.1016/0008-8846\(88\)90122-6](https://doi.org/10.1016/0008-8846(88)90122-6).
- [17] K.K. Aligizaki, *Pore Structure of Cement-Based Materials: Testing, Interpretation and Requirements*, CRC Press, 2005.
- [18] G. Ye, K. van Breugel, A.L.A. Fraaij, Numerical and experimental studies of percolation phenomena of hardening cement pastes, in: *Role of Cement Science in Sustainable Development*, Thomas Telford Publishing, 2003: pp. 103–112. <https://doi.org/10.1680/rocsisd.32460.0010>.
- [19] F.A.L. Dullien, *Porous Media: Fluid Transport and Pore Structure*, Academic Press, 2012.
- [20] E.W. Washburn, Note on a Method of Determining the Distribution of Pore Sizes in a Porous Material, *Proc Natl Acad Sci U S A*. 7 (1921) 115–116.
- [21] S. Roels, J. Elsen, J. Carmeliet, H. Hens, Characterisation of pore structure by combining mercury porosimetry and micrography, *Mat. Struct*. 34 (2001) 76–82. <https://doi.org/10.1007/BF02481555>.
- [22] S. Diamond, Mercury porosimetry: An inappropriate method for the measurement of pore size distributions in cement-based materials, *Cement and Concrete Research*. 30 (2000) 1517–1525. [https://doi.org/10.1016/S0008-8846\(00\)00370-7](https://doi.org/10.1016/S0008-8846(00)00370-7).
- [23] K.N. Manahiloh, B. Muhunthan, M. Kayhanian, S.Y. Gebremariam, X-Ray Computed Tomography and Nondestructive Evaluation of Clogging in Porous Concrete Field Samples, *Journal of Materials in Civil Engineering*. 24 (2012) 1103–1109.

-
- [https://doi.org/10.1061/\(ASCE\)MT.1943-5533.0000484](https://doi.org/10.1061/(ASCE)MT.1943-5533.0000484).
- [24] A. Thompson, I. Maskery, R.K. Leach, X-ray computed tomography for additive manufacturing: a review, *Meas. Sci. Technol.* 27 (2016) 072001. <https://doi.org/10.1088/0957-0233/27/7/072001>.
- [25] D.H. Everett, *Manual of Symbols and Terminology for Physicochemical Quantities and Units, Appendix II: Definitions, Terminology and Symbols in Colloid and Surface Chemistry, Pure and Applied Chemistry.* 31 (1972) 577–638. <https://doi.org/10.1351/pac197231040577>.
- [26] S. Mindess, J.F. Young, *Concrete*, Prentice-Hall, Englewood Cliffs, N.J., 1981.
- [27] H.M. Jennings, Colloid model of C–S–H and implications to the problem of creep and shrinkage, *Mat. Struct.* 37 (2004) 59–70. <https://doi.org/10.1007/BF02481627>.
- [28] F. Gong, D. Zhang, E. Sicat, T. Ueda, Empirical Estimation of Pore Size Distribution in Cement, Mortar, and Concrete, *Journal of Materials in Civil Engineering.* 26 (2014) 04014023. [https://doi.org/10.1061/\(ASCE\)MT.1943-5533.0000945](https://doi.org/10.1061/(ASCE)MT.1943-5533.0000945).
- [29] B.F. Roberts, A procedure for estimating pore volume and area distributions from sorption isotherms, *Journal of Colloid and Interface Science.* 23 (1967) 266–273. [https://doi.org/10.1016/0021-9797\(67\)90111-7](https://doi.org/10.1016/0021-9797(67)90111-7).
- [30] S. Diamond, A critical comparison of mercury porosimetry and capillary condensation pore size distributions of portland cement pastes, *Cement and Concrete Research.* 1 (1971) 531–545. [https://doi.org/10.1016/0008-8846\(71\)90058-5](https://doi.org/10.1016/0008-8846(71)90058-5).
- [31] A.B. Abell, K.L. Willis, D.A. Lange, Mercury Intrusion Porosimetry and Image Analysis of Cement-Based Materials, *Journal of Colloid and Interface Science.* 211 (1999) 39–44. <https://doi.org/10.1006/jcis.1998.5986>.
- [32] D.N. Winslow, THE PORE SIZE DISTRIBUTION OF PORTLAND CEMENT PASTE, (1968). <https://trid.trb.org/view/99079> (accessed October 25, 2019).
- [33] C. Gallé, Effect of drying on cement-based materials pore structure as identified by mercury intrusion porosimetry: A comparative study between oven-, vacuum-, and freeze-drying, *Cement and Concrete Research.* 31 (2001) 1467–1477. [https://doi.org/10.1016/S0008-8846\(01\)00594-4](https://doi.org/10.1016/S0008-8846(01)00594-4).
- [34] A.C.A. Muller, K.L. Scrivener, A reassessment of mercury intrusion porosimetry by comparison with ¹H NMR relaxometry, *Cement and Concrete Research.* 100 (2017) 350–360. <https://doi.org/10.1016/j.cemconres.2017.05.024>.
- [35] A.C.A. Muller, K.L. Scrivener, A.M. Gajewicz, P.J. McDonald, Use of bench-top NMR to measure the density, composition and desorption isotherm of C–S–H in cement paste, *Microporous and Mesoporous Materials.* 178 (2013) 99–103. <https://doi.org/10.1016/j.micromeso.2013.01.032>.
- [36] J. Greener, H. Peemoeller, C. Choi, R. Holly, E.J. Reardon, C.M. Hansson, M.M. Pintang,

-
- Monitoring of Hydration of White Cement Paste with Proton NMR Spin–Spin Relaxation, *Journal of the American Ceramic Society*. 83 (2000) 623–627. <https://doi.org/10.1111/j.1151-2916.2000.tb01242.x>.
- [37] Y. Yao, D. Liu, Comparison of low-field NMR and mercury intrusion porosimetry in characterizing pore size distributions of coals, *Fuel*. 95 (2012) 152–158. <https://doi.org/10.1016/j.fuel.2011.12.039>.
- [38] E. Gallucci, K. Scrivener, A. Groso, M. Stampanoni, G. Margaritondo, 3D Experimental Investigation of the Microstructure of Cement Paste Using Synchrotron X-Ray Microtomography (μ CT), *Cement and Concrete Research*. 37 (2007) 360–368. <https://doi.org/10.1016/j.cemconres.2006.10.012>.
- [39] M.A.B. Pomentilla, T. Sugiyama, T. Hitomi, N. Takeda, Characterizing the 3D Pore Structure of Hardened Cement Paste with Synchrotron Microtomography, *Journal of Advanced Concrete Technology*. 6 (2008) 273–286. <https://doi.org/10.3151/jact.6.273>.
- [40] M. Cabeza, M. Keddam, X.R. Nóvoa, I. Sánchez, H. Takenouti, Impedance spectroscopy to characterize the pore structure during the hardening process of Portland cement paste, *Electrochimica Acta*. 51 (2006) 1831–1841. <https://doi.org/10.1016/j.electacta.2005.02.125>.
- [41] T. Hatch, S.P. Choate, Statistical description of the size properties of non uniform particulate substances, *Journal of the Franklin Institute*. 207 (1929) 369–387. [https://doi.org/10.1016/S0016-0032\(29\)91451-4](https://doi.org/10.1016/S0016-0032(29)91451-4).
- [42] K. Maekawa, *Multi-Scale Modeling of Structural Concrete*, CRC Press, London, 2014. <https://doi.org/10.1201/9781482288599>.
- [43] D. Hou, D. Li, P. Hua, J. Jiang, G. Zhang, Statistical modelling of compressive strength controlled by porosity and pore size distribution for cementitious materials, *Cement and Concrete Composites*. 96 (2019) 11–20. <https://doi.org/10.1016/j.cemconcomp.2018.10.012>.
- [44] S. Diamond, W.L. Dolch, Generalized log-normal distribution of pore sizes in hydrated cement paste, *Journal of Colloid and Interface Science*. 38 (1972) 234–244. [https://doi.org/10.1016/0021-9797\(72\)90239-1](https://doi.org/10.1016/0021-9797(72)90239-1).
- [45] D. Shi, W. Ma, P.W. Brown, Lognormal Simulation of Pore Evolution During Cement and Mortar Hardening, *MRS Proc.* 176 (1989) 143. <https://doi.org/10.1557/PROC-176-143>.
- [46] D. Shi, P.W. Brown, W. Ma, Lognormal Simulation of Pore Size Distributions in Cementitious Materials, *Journal of the American Ceramic Society*. 74 (1991) 1861–1867. <https://doi.org/10.1111/j.1151-2916.1991.tb07800.x>.
- [47] J. Holly, D. Hampton, M.D.A. Thomas, Modelling relationships between permeability and cement paste pore microstructures, *Cement and Concrete Research*. 23 (1993) 1317–1330. [https://doi.org/10.1016/0008-8846\(93\)90069-L](https://doi.org/10.1016/0008-8846(93)90069-L).

-
- [48] X. Chen, S. Wu, Influence of water-to-cement ratio and curing period on pore structure of cement mortar, *Construction and Building Materials*. 38 (2013) 804–812. <https://doi.org/10.1016/j.conbuildmat.2012.09.058>.
- [49] Z. Jiang, Y. Xi, X. Gu, Q. Huang, W. Zhang, Modelling of water vapour sorption hysteresis of cement-based materials based on pore size distribution, *Cement and Concrete Research*. 115 (2019) 8–19. <https://doi.org/10.1016/j.cemconres.2018.09.015>.
- [50] A.L. Zydney, P. Aimar, M. Meireles, J.M. Pimbley, G. Belfort, Use of the log-normal probability density function to analyze membrane pore size distributions: functional forms and discrepancies, *Journal of Membrane Science*. 91 (1994) 293–298. [https://doi.org/10.1016/0376-7388\(94\)80090-1](https://doi.org/10.1016/0376-7388(94)80090-1).
- [51] C.-F. Chang, J.-W. Chen, The experimental investigation of concrete carbonation depth, *Cement and Concrete Research*. 36 (2006) 1760–1767. <https://doi.org/10.1016/j.cemconres.2004.07.025>.
- [52] H.-W. Song, S.-J. Kwon, Permeability characteristics of carbonated concrete considering capillary pore structure, *Cement and Concrete Research*. 37 (2007) 909–915. <https://doi.org/10.1016/j.cemconres.2007.03.011>.
- [53] V.P. Dimri, R.P. Srivastava, N. Vedanti, *Fractal Models in Exploration Geophysics: Applications to Hydrocarbon Reservoirs*, Elsevier, 2012.
- [54] Y.S. Choi, E.I. Yang, Effect of calcium leaching on the pore structure, strength, and chloride penetration resistance in concrete specimens, *Nuclear Engineering and Design*. 259 (2013) 126–136. <https://doi.org/10.1016/j.nucengdes.2013.02.049>.
- [55] L. Fang, D. Deng, Q. Yuan, Calcium Leaching of Cement Asphalt Paste and Its Effects on Dynamic Mechanical Properties, *Journal of Materials in Civil Engineering*. 30 (2018) 04018127. [https://doi.org/10.1061/\(ASCE\)MT.1943-5533.0002309](https://doi.org/10.1061/(ASCE)MT.1943-5533.0002309).
- [56] H. Hilsdorf, J. Kropp, *Performance Criteria for Concrete Durability*, CRC Press, 1995.
- [57] L. Liu, X. Wang, J. Zhou, H. Chu, D. Shen, H. Chen, S. Qin, Investigation of pore structure and mechanical property of cement paste subjected to the coupled action of freezing/thawing and calcium leaching, *Cement and Concrete Research*. 109 (2018) 133–146. <https://doi.org/10.1016/j.cemconres.2018.04.015>.
- [58] Á. Török, B. Szemerey-Kiss, Freeze-thaw durability of repair mortars and porous limestone: compatibility issues, *Progress in Earth and Planetary Science*. 6 (2019) 42. <https://doi.org/10.1186/s40645-019-0282-1>.
- [59] Z. Yang, W.J. Weiss, J. Olek, Water Transport in Concrete Damaged by Tensile Loading and Freeze–Thaw Cycling, *Journal of Materials in Civil Engineering*. 18 (2006) 424–434. [https://doi.org/10.1061/\(ASCE\)0899-1561\(2006\)18:3\(424\)](https://doi.org/10.1061/(ASCE)0899-1561(2006)18:3(424)).
- [60] M. Koniorczyk, Modelling the phase change of salt dissolved in pore water – Equilibrium and non-equilibrium approach, *Construction and Building Materials*. 24

-
- (2010) 1119–1128. <https://doi.org/10.1016/j.conbuildmat.2009.12.031>.
- [61] M. Prat, Evaporation from a Porous Medium in the Presence of Salt Crystallization, in: L. Mercury, N. Tas, M. Zilberbrand (Eds.), *Transport and Reactivity of Solutions in Confined Hydrosystems*, Springer Netherlands, Dordrecht, 2014: pp. 223–229. https://doi.org/10.1007/978-94-007-7534-3_19.
- [62] N. Sghaier, S. Geoffroy, M. Prat, H. Eloukabi, S. Ben Nasrallah, Evaporation-driven growth of large crystallized salt structures in a porous medium, *Phys. Rev. E*. 90 (2014) 042402. <https://doi.org/10.1103/PhysRevE.90.042402>.
- [63] S. Veran-Tissoires, M. Marcoux, M. Prat, Salt crystallisation at the surface of a heterogeneous porous medium, *EPL*. 98 (2012) 34005. <https://doi.org/10.1209/0295-5075/98/34005>.
- [64] Z. Pavlík, L. Fiala, J. Maděra, M. Pavlíková, R. Černý, Computational modelling of coupled water and salt transport in porous materials using diffusion–advection model, *Journal of the Franklin Institute*. 348 (2011) 1574–1587. <https://doi.org/10.1016/j.jfranklin.2010.06.014>.
- [65] M. Koniorczyk, D. Gawin, Numerical Modeling of Salt Transport and Precipitation in Non-Isothermal Partially Saturated Porous Media Considering Kinetics of Salt Phase Changes, *Transp Porous Med.* 87 (2011) 57–76. <https://doi.org/10.1007/s11242-010-9668-7>.
- [66] V. Baroghel-Bouny, M. Thiéry, X. Wang, Modelling of isothermal coupled moisture–ion transport in cementitious materials, *Cement and Concrete Research*. 41 (2011) 828–841. <https://doi.org/10.1016/j.cemconres.2011.04.001>.
- [67] Z. Zhang, M. Thiery, V. Baroghel-Bouny, Investigation of moisture transport properties of cementitious materials, *Cement and Concrete Research*. 89 (2016) 257–268. <https://doi.org/10.1016/j.cemconres.2016.08.013>.
- [68] E. Samson, J. Marchand, Modeling the effect of temperature on ionic transport in cementitious materials, *Cement and Concrete Research*. 37 (2007) 455–468. <https://doi.org/10.1016/j.cemconres.2006.11.008>.
- [69] N.R. Buenfeld, G.K. Glass, A.M. Hassanein, J.-Z. Zhang, Chloride Transport in Concrete Subjected to Electric Field, *Journal of Materials in Civil Engineering*. 10 (1998) 220–228. [https://doi.org/10.1061/\(ASCE\)0899-1561\(1998\)10:4\(220\)](https://doi.org/10.1061/(ASCE)0899-1561(1998)10:4(220)).
- [70] J. Crank, *The Mathematics of Diffusion*, Clarendon Press, 1979.
- [71] E. Samson, J. Marchand, K.A. Snyder, Calculation of ionic diffusion coefficients on the basis of migration test results, *Mat. Struct.* 36 (2003) 156–165. <https://doi.org/10.1007/BF02479554>.
- [72] V. Baroghel-Bouny, Water vapour sorption experiments on hardened cementitious materials: Part I: Essential tool for analysis of hygral behaviour and its relation to pore

-
- structure, *Cement and Concrete Research*. 37 (2007) 414–437. <https://doi.org/10.1016/j.cemconres.2006.11.019>.
- [73] T. Ishida, K. Maekawa, T. Kishi, Enhanced modeling of moisture equilibrium and transport in cementitious materials under arbitrary temperature and relative humidity history, *Cement and Concrete Research*. 37 (2007) 565–578. <https://doi.org/10.1016/j.cemconres.2006.11.015>.
- [74] T.Q. Nguyen, J. Petković, P. Dangla, V. Baroghel-Bouny, Modelling of coupled ion and moisture transport in porous building materials, *Construction and Building Materials*. 22 (2008) 2185–2195. <https://doi.org/10.1016/j.conbuildmat.2007.08.013>.
- [75] E. Samson, J. Marchand, Numerical Solution of the Extended Nernst–Planck Model, *Journal of Colloid and Interface Science*. 215 (1999) 1–8. <https://doi.org/10.1006/jcis.1999.6145>.
- [76] J. Rubin, Transport of reacting solutes in porous media: Relation between mathematical nature of problem formulation and chemical nature of reactions, *Water Resources Research*. 19 (1983) 1231–1252. <https://doi.org/10.1029/WR019i005p01231>.
- [77] G.T. Yeh, V.S. Tripathi, A critical evaluation of recent developments in hydrogeochemical transport models of reactive multichemical components, *Water Resources Research*. 25 (1989) 93–108. <https://doi.org/10.1029/WR025i001p00093>.
- [78] D.J. Kirkner, H. Reeves, Multicomponent mass transport with homogeneous and heterogeneous chemical reactions: Effect of the chemistry on the choice of numerical algorithm: 1. Theory, *Water Resources Research*. 24 (1988) 1719–1729. <https://doi.org/10.1029/WR024i010p01719>.
- [79] C.W. Miller, L.V. Benson, Simulation of solute transport in a chemically reactive heterogeneous system: Model development and application, *Water Resources Research*. 19 (1983) 381–391. <https://doi.org/10.1029/WR019i002p00381>.
- [80] A.L. Walter, E.O. Frind, D.W. Blowes, C.J. Ptacek, J.W. Molson, Modeling of multicomponent reactive transport in groundwater: 1. Model development and evaluation, *Water Resources Research*. 30 (1994) 3137–3148. <https://doi.org/10.1029/94WR00955>.
- [81] T. Xu, J. Samper, C. Ayora, M. Manzano, E. Custodio, Modeling of non-isothermal multi-component reactive transport in field scale porous media flow systems, *Journal of Hydrology*. 214 (1999) 144–164. [https://doi.org/10.1016/S0022-1694\(98\)00283-2](https://doi.org/10.1016/S0022-1694(98)00283-2).
- [82] J. Carrayrou, R. Mosé, P. Behra, Operator-splitting procedures for reactive transport and comparison of mass balance errors, *Journal of Contaminant Hydrology*. 68 (2004) 239–268. [https://doi.org/10.1016/S0169-7722\(03\)00141-4](https://doi.org/10.1016/S0169-7722(03)00141-4).
- [83] L. Chen, Q. Kang, B.A. Robinson, Y.-L. He, W.-Q. Tao, Pore-scale modeling of multiphase reactive transport with phase transitions and dissolution-precipitation processes in closed systems, *Phys. Rev. E*. 87 (2013) 043306.

-
- <https://doi.org/10.1103/PhysRevE.87.043306>.
- [84] Q. Kang, D. Zhang, S. Chen, Simulation of dissolution and precipitation in porous media, *Journal of Geophysical Research: Solid Earth*. 108 (2003). <https://doi.org/10.1029/2003JB002504>.
- [85] H.E. Reinhardt, *Penetration and Permeability of Concrete: Barriers to organic and contaminating liquids*, CRC Press, 2004.
- [86] Van Breugel, K., Ye, Guang, *Experimental Study and Numerical Simulation of the Development of the Microstructure and Permeability of Cementitious Materials*, 2003. <http://resolver.tudelft.nl/uuid:ed9166f3-dc6e-4c6c-bd06-8d43c6354558>.
- [87] X. Li, Y. Xu, Microstructure-Based Modeling for Water Permeability of Hydrating Cement Paste, *Journal of Advanced Concrete Technology*. 17 (2019) 405–418. <https://doi.org/10.3151/jact.17.405>.
- [88] D. Shi, W. Ma, P.W. Brown, Lognormal Simulation of Pore Evolution During Cement and Mortar Hardening, *MRS Online Proceedings Library Archive*. 176 (1989). <https://doi.org/10.1557/PROC-176-143>.
- [89] O. Amiri, A. Aït-Mokhtar, M. Sarhani, Tri-dimensional modelling of cementitious materials permeability from polymodal pore size distribution obtained by mercury intrusion porosimetry tests, *Advances in Cement Research*. 17 (2005) 39–45. <https://doi.org/10.1680/adcr.2005.17.1.39>.
- [90] D. Manmohan, P.K. Mehta, Influence of Pozzolanic, Slag, and Chemical Admixtures on Pore Size Distribution and Permeability of Hardened Cement Pastes, *CCA*. 3 (1981) 63–67. <https://doi.org/10.1520/CCA10203J>.
- [91] B. Kruczek, Carman–Kozeny Equation, in: E. Drioli, L. Giorno (Eds.), *Encyclopedia of Membranes*, Springer Berlin Heidelberg, Berlin, Heidelberg, 2014: pp. 1–3. https://doi.org/10.1007/978-3-642-40872-4_1995-1.
- [92] P.C. Carman, Fluid flow through granular beds, *Chemical Engineering Research and Design*. 75 (1997) S32–S48. [https://doi.org/10.1016/S0263-8762\(97\)80003-2](https://doi.org/10.1016/S0263-8762(97)80003-2).
- [93] A.J. Katz, A.H. Thompson, Quantitative prediction of permeability in porous rock, *Phys. Rev. B*. 34 (1986) 8179–8181. <https://doi.org/10.1103/PhysRevB.34.8179>.
- [94] R.J. Millington, J.P. Quirk, Permeability of porous solids, *Trans. Faraday Soc.* 57 (1961) 1200–1207. <https://doi.org/10.1039/TF9615701200>.
- [95] A. Aït–Mokhtar, O. Amiri, S. Sammartinot, Analytic modelling and experimental study of the porosity and permeability of a porous medium—application to cement mortars and granitic rock, *Magazine of Concrete Research*. 51 (1999) 391–396. <https://doi.org/10.1680/macr.1999.51.6.391>.
- [96] C. Sun, L. Yuan, X. Zhai, F. Qu, Y. Li, B. Hou, Numerical and experimental study of moisture and chloride transport in unsaturated concrete, *Construction and Building*

-
- Materials. 189 (2018) 1067–1075. <https://doi.org/10.1016/j.conbuildmat.2018.08.158>.
- [97] A. Zolfaghari, H. Dehghanpour, Pore Size Distribution from Water Adsorption Isotherm, in: Society of Petroleum Engineers, 2015. <https://doi.org/10.2118/175155-MS>.
- [98] A. Zolfaghari, H. Dehghanpour, M. Xu, Water sorption behaviour of gas shales: II. Pore size distribution, *International Journal of Coal Geology*. 179 (2017) 187–195. <https://doi.org/10.1016/j.coal.2017.05.009>.
- [99] J. Ahl, Salt diffusion in brick structures Part II The effect of temperature, concentration and salt, *Journal of Materials Science*. 39 (2004) 4247–4254. <https://doi.org/10.1023/B:JMISC.0000033406.40090.b4>.
- [100] C. Gentilini, E. Franzoni, S. Bandini, L. Nobile, Effect of salt crystallisation on the shear behaviour of masonry walls: An experimental study, *Construction and Building Materials*. 37 (2012) 181–189. <https://doi.org/10.1016/j.conbuildmat.2012.07.086>.
- [101] S. Veran-Tissoires, M. Marcoux, M. Prat, Discrete Salt Crystallization at the Surface of a Porous Medium, *Phys. Rev. Lett.* 108 (2012) 054502. <https://doi.org/10.1103/PhysRevLett.108.054502>.
- [102] A. Feraille-Fresnet, P. Tamagny, A. Ehrlicher, J. Sercombe, Thermo-hydro-chemical modelling of a porous medium submitted to high temperature: An application to an axisymmetrical structure, *Mathematical and Computer Modelling*. 37 (2003) 641–650. [https://doi.org/10.1016/S0895-7177\(03\)00058-X](https://doi.org/10.1016/S0895-7177(03)00058-X).
- [103] M. Fenaux, E. Reyes, J.C. Gálvez, A. Moragues, Modelling the transport of chloride and other ions in cement-based materials, *Cement and Concrete Composites*. 97 (2019) 33–42. <https://doi.org/10.1016/j.cemconcomp.2018.12.009>.
- [104] G.W. Scherer, Crystallization in pores, *Cement and Concrete Research*. 29 (1999) 1347–1358. [https://doi.org/10.1016/S0008-8846\(99\)00002-2](https://doi.org/10.1016/S0008-8846(99)00002-2).
- [105] D. Shi, D.N. Winslow, Contact angle and damage during mercury intrusion into cement paste, *Cement and Concrete Research*. 15 (1985) 645–654. [https://doi.org/10.1016/0008-8846\(85\)90064-X](https://doi.org/10.1016/0008-8846(85)90064-X).
- [106] W. Brutsaert, PROBABILITY LAWS FOR PORE-SIZE DISTRIBUTIONS, *Soil Science*. 101 (1966) 85–92.
- [107] K. Maekawa, T. Ishida, T. Kishi, Multi-scale Modeling of Concrete Performance, *Journal of Advanced Concrete Technology*. 1 (2003) 91–126. <https://doi.org/10.3151/jact.1.91>.
- [108] C. Lu, R. Danzer, F.D. Fischer, Fracture statistics of brittle materials: Weibull or normal distribution, *Phys. Rev. E*. 65 (2002) 067102. <https://doi.org/10.1103/PhysRevE.65.067102>.
- [109] J.B. Austin, Methods of representing distribution of particle size, *Ind. Eng. Chem. Anal. Ed.* 11 (1939) 334–339. <https://doi.org/10.1021/ac50134a014>.

-
- [110] Y. Zhang, M. Zhang, Transport properties in unsaturated cement-based materials – A review, *Construction and Building Materials*. 72 (2014) 367–379. <https://doi.org/10.1016/j.conbuildmat.2014.09.037>.
- [111] Y. Yokoyama, T. Yokoi, J. Ihara, The effects of pore size distribution and working techniques on the absorption and water content of concrete floor slab surfaces, *Construction and Building Materials*. 50 (2014) 560–566. <https://doi.org/10.1016/j.conbuildmat.2013.10.013>.
- [112] S. Gupta, H.P. Huinink, M. Prat, L. Pel, K. Kopinga, Paradoxical drying of a fired-clay brick due to salt crystallization, *Chemical Engineering Science*. 109 (2014) 204–211. <https://doi.org/10.1016/j.ces.2014.01.023>.
- [113] M.A. Celia, P.C. Reeves, L.A. Ferrand, Recent advances in pore scale models for multiphase flow in porous media, *Reviews of Geophysics*. 33 (1995) 1049–1057. <https://doi.org/10.1029/95RG00248>.
- [114] H. Dashtian, N. Shokri, M. Sahimi, Pore-network model of evaporation-induced salt precipitation in porous media: The effect of correlations and heterogeneity, *Advances in Water Resources*. 112 (2018) 59–71. <https://doi.org/10.1016/j.advwatres.2017.12.004>.
- [115] K. Schabowicz, Non-Destructive Testing of Materials in Civil Engineering, *Materials*. 12 (2019) 3237. <https://doi.org/10.3390/ma12193237>.
- [116] M. Koniorczyk, P. Konca, Experimental and numerical investigation of sodium sulphate crystallization in porous materials, *Heat and Mass Transfer*. 49 (2013) 437–449. <https://doi.org/10.1007/s00231-012-1093-8>.
- [117] D. Benavente, M.A. García del Cura, R. Fort, S. Ordóñez, Thermodynamic modelling of changes induced by salt pressure crystallisation in porous media of stone, *Journal of Crystal Growth*. 204 (1999) 168–178. [https://doi.org/10.1016/S0022-0248\(99\)00163-3](https://doi.org/10.1016/S0022-0248(99)00163-3).
- [118] M. Zhang, G. Ye, K. van Breugel, Multiscale lattice Boltzmann-finite element modelling of chloride diffusivity in cementitious materials. Part II: Simulation results and validation, *Mechanics Research Communications*. 58 (2014) 64–72. <https://doi.org/10.1016/j.mechrescom.2014.01.001>.
- [119] D. Benavente, M.A. García del Cura, S. Ordóñez, Salt influence on evaporation from porous building rocks, *Construction and Building Materials*. 17 (2003) 113–122. [https://doi.org/10.1016/S0950-0618\(02\)00100-9](https://doi.org/10.1016/S0950-0618(02)00100-9).
- [120] A.T.C. Guimarães, M.A. Climent, G. de Vera, F.J. Vicente, F.T. Rodrigues, C. Andrade, Determination of chloride diffusivity through partially saturated Portland cement concrete by a simplified procedure, *Construction and Building Materials*. 25 (2011) 785–790. <https://doi.org/10.1016/j.conbuildmat.2010.07.005>.
- [121] Z. Zhang, M. Thiery, V. Baroghel-Bouny, Analysis of moisture transport in cementitious materials and modelling of drying–wetting cycles, in: 2012.

-
- [122] Z. Wu, H.S. Wong, N.R. Buenfeld, Transport properties of concrete after drying-wetting regimes to elucidate the effects of moisture content, hysteresis and microcracking, *Cement and Concrete Research*. 98 (2017) 136–154. <https://doi.org/10.1016/j.cemconres.2017.04.006>.
- [123] J. Desarnaud, D. Bonn, N. Shahidzadeh, The Pressure induced by salt crystallization in confinement, *Sci Rep*. 6 (2016) 30856. <https://doi.org/10.1038/srep30856>.
- [124] R. Barbarulo, J. Marchand, K.A. Snyder, S. Prené, Dimensional analysis of ionic transport problems in hydrated cement systems: Part 1. Theoretical considerations, *Cement and Concrete Research*. 30 (2000) 1955–1960. [https://doi.org/10.1016/S0008-8846\(00\)00383-5](https://doi.org/10.1016/S0008-8846(00)00383-5).
- [125] W.L. Lindsay, Chemical equilibria in soils., *Chemical Equilibria in Soils*. (n.d.). <https://www.cabdirect.org/cabdirect/abstract/19811961894> (accessed June 23, 2021).
- [126] L.Y. Li, C.L. Page, Modelling of electrochemical chloride extraction from concrete: Influence of ionic activity coefficients, *Computational Materials Science*. 9 (1998) 303–308. [https://doi.org/10.1016/S0927-0256\(97\)00152-3](https://doi.org/10.1016/S0927-0256(97)00152-3).
- [127] G.-T. Yeh, V.S. Tripathi, A Model for Simulating Transport of Reactive Multispecies Components: Model Development and Demonstration, *Water Resources Research*. 27 (1991) 3075–3094. <https://doi.org/10.1029/91WR02028>.
- [128] J. de Paula, ATKINS' PHYSICAL CHEMISTRY, W. H. Freeman and Company New York, 2006. <http://dspace.fudutsinma.edu.ng/xmlui/handle/123456789/2051> (accessed June 15, 2021).
- [129] H. Akhlaghi Amiri, Numerical Simulation of Low Frequency Electrical Reservoir Heating Method, 2009. <https://doi.org/10.13140/RG.2.2.21471.05286>.
- [130] E. Samson, G. Lemaire, J. Marchand, J.J. Beaudoin, Modeling chemical activity effects in strong ionic solutions, *Computational Materials Science*. 15 (1999) 285–294. [https://doi.org/10.1016/S0927-0256\(99\)00017-8](https://doi.org/10.1016/S0927-0256(99)00017-8).
- [131] G. De Marsily, Quantitative hydrogeology, Academic Press, Inc., Orlando, FL, 1986. <https://www.osti.gov/biblio/6784827> (accessed March 23, 2020).
- [132] P. O'Neill Iqbal, T. Ishida, Modeling of chloride transport coupled with enhanced moisture conductivity in concrete exposed to marine environment, *Cement and Concrete Research*. 39 (2009) 329–339. <https://doi.org/10.1016/j.cemconres.2009.01.001>.
- [133] M. Wu, B. Johannesson, M. Geiker, A study of the water vapor sorption isotherms of hardened cement pastes: Possible pore structure changes at low relative humidity and the impact of temperature on isotherms, *Cement and Concrete Research*. 56 (2014) 97–105. <https://doi.org/10.1016/j.cemconres.2013.11.008>.
- [134] Q. Zeng, D. Zhang, H. Sun, K. Li, Characterizing pore structure of cement blend pastes

-
- using water vapor sorption analysis, *Materials Characterization*. 95 (2014) 72–84. <https://doi.org/10.1016/j.matchar.2014.06.007>.
- [135] S.F. Wong, T.H. Wee, S. Swaddiwudhipong, S.L. Lee, Study of water movement in concrete, *Magazine of Concrete Research*. 53 (2001) 205–220. <https://doi.org/10.1680/macr.2001.53.3.205>.
- [136] G. Ye, P. Lura, K. van Breugel, Modelling of water permeability in cementitious materials, *Mater Struct*. 39 (2006) 877–885. <https://doi.org/10.1617/s11527-006-9138-4>.
- [137] P. Halamickova, R.J. Detwiler, D.P. Bentz, E.J. Garboczi, Water permeability and chloride ion diffusion in portland cement mortars: Relationship to sand content and critical pore diameter, *Cement and Concrete Research*. 25 (1995) 790–802. [https://doi.org/10.1016/0008-8846\(95\)00069-O](https://doi.org/10.1016/0008-8846(95)00069-O).
- [138] A. Ait-Mokhtar, O. Amiri, P. Dumargue, S. Sammartino, A new model to calculate water permeability of cement-based materials from MIP results, *Advances in Cement Research*. 14 (2002) 43–49. <https://doi.org/10.1680/adcr.2002.14.2.43>.
- [139] Z. Zhang, M. Thiery, V. Baroghel-Bouny, Numerical modelling of moisture transfers with hysteresis within cementitious materials: Verification and investigation of the effects of repeated wetting–drying boundary conditions, *Cement and Concrete Research*. 68 (2015) 10–23. <https://doi.org/10.1016/j.cemconres.2014.10.012>.
- [140] F. Meftah, C. Davie, S.D. Pont, A. Millard, Constitutive Parameters, in: A. Millard, P. Pimienta (Eds.), *Modelling of Concrete Behaviour at High Temperature: State-of-the-Art Report of the RILEM Technical Committee 227-HPB*, Springer International Publishing, Cham, 2019: pp. 67–98. https://doi.org/10.1007/978-3-030-11995-9_5.
- [141] F. Meftah, F. Pesavento, C. Davie, S.D. Pont, M. Zeiml, M. Korzen, A. Millard, Advanced Modelling, in: A. Millard, P. Pimienta (Eds.), *Modelling of Concrete Behaviour at High Temperature: State-of-the-Art Report of the RILEM Technical Committee 227-HPB*, Springer International Publishing, Cham, 2019: pp. 27–65. https://doi.org/10.1007/978-3-030-11995-9_4.
- [142] C. Lin, L. Lee, A two-ionic-parameter approach for ion activity coefficients of aqueous electrolyte solutions, *Fluid Phase Equilibria*. 205 (2003) 69–88. [https://doi.org/10.1016/S0378-3812\(02\)00275-3](https://doi.org/10.1016/S0378-3812(02)00275-3).
- [143] H. Lin, L. Lee, Estimations of activity coefficients of constituent ions in aqueous electrolyte solutions with the two-ionic-parameter approach, *Fluid Phase Equilibria*. 237 (2005) 1–8. <https://doi.org/10.1016/j.fluid.2005.08.005>.
- [144] K. Li, C. Li, Modeling Hydroionic Transport in Cement-Based Porous Materials Under Drying-Wetting Actions, *Journal of Applied Mechanics*. 80 (2013). <https://doi.org/10.1115/1.4007907>.
- [145] J.G. Kirkwood, F.P. Buff, *The Statistical Mechanical Theory of Surface Tension*, J.

-
- Chem. Phys. 17 (1949) 338–343. <https://doi.org/10.1063/1.1747248>.
- [146] G.J. Janz, *Thermodynamic Properties of Organic Compounds: Estimation Methods, Principles and Practice*, Elsevier, 2012.
- [147] V. Genuchten, M. Th, A Closed-form Equation for Predicting the Hydraulic Conductivity of Unsaturated Soils¹, *Soil Science Society of America Journal*. (1980). <https://doi.org/10.2136/sssaj1980.03615995004400050002x>.

Résumé en français

L'étude du transport réactif dans les milieux poreux est une problématique majeure qui sous-tend l'analyse de la durabilité des matériaux de construction (béton, pierre, brique...) exposés à des environnements agressifs. Le transport d'espèces chimiques en solution dans le réseau poreux peut donner lieu à des phénomènes de précipitation/dissolution de phases solides au sein de ce réseau poreux qui altèrent ces matériaux.

Les altérations peuvent être de nature à dégrader les propriétés mécaniques dans le temps. La précipitation de phases solides (éventuellement expansives) peut donner lieu à un endommagement par fissuration interne du fait de pressions induites par ces phases solides au niveau des pores, siège de leur précipitation. La dissolution de phases solides peut se manifester par une modification sensible de la morphologie du réseau poreux et de sa connectivité conduisant à une augmentation de sa perméabilité à des agents pathogènes.

D'un point de vue macroscopique, différentes études montrent que l'efflorescence interne due à la précipitation de sels est intimement liée à la localisation du front de dessiccation dans le matériau. Lorsqu'une éprouvette d'un matériau poreux ouvert est plongée partiellement (sur sa partie inférieure) dans une solution saline, l'efflorescence se produit dans la zone tampon séparant la partie saturée en solution (due à la remontée capillaire) de celle (en partie supérieure) qui reste relativement sèche du fait des conditions de dessiccation.

Dans le cadre de ce travail de thèse, ce schéma est également reconduit à l'échelle (plus microscopie) du réseau poreux. A cette échelle, le front hydrique correspond à la localisation du ménisque capillaire (frontière séparant la population de pores saturés en eau de ceux quasi-secs) dont le rayon correspond au pore en deçà duquel les conditions d'équilibre thermodynamique permettent au milieu poreux (de par sa structure porale) de retenir l'eau sous forme liquide pour une humidité relative donnée. Les phénomènes de précipitation/dissolution sont considérés avoir lieu (de façon similaire à l'échelle macroscopique) dans une zone tampon autour du front capillaire.

L'évolution dans le temps de ces altérations dépend de l'incidence des mécanismes de précipitation/dissolution sur l'évolution du réseau poreux qui est le siège et le vecteur du transport réactif. En particulier, l'évolution de la localisation du front capillaire du fait des conditions hygrométriques peut affecter de façon marquée les sites de précipitation/dissolution à l'échelle du réseau poreux, donnant lieu à une transformation hétérogène ou fortement localisée de la structure porale. Ce paradigme rend nécessaire de caractériser, outre l'évolution de la porosité globale, la transformation de la distribution de pores (sous l'effet couplé des conditions hygro-chimiques et des mécanismes de précipitation/dissolution) et son incidence sur les paramètres régissant les mécanismes de transfert.

Une première contribution de ce travail de thèse consiste en une approche probabiliste pour représenter la structure porale et modéliser son évolution due à la précipitation/dissolution de phases solide contrôlée par la présence d'un front capillaire.

Le modèle probabiliste développé se base sur la construction de la fonction densité de probabilité (ici une loi log-normale monomodale est adoptée) qui caractérise la distribution de la taille des pores de la structure porale à l'état initiale du matériau. La schématisation désormais classique d'un réseau poreux de forme cylindrique est adoptée : le pore est caractérisé par son rayon r lequel est considéré comme une variable aléatoire distribuée selon une loi de probabilité.

Il s'agit dans un deuxième temps de proposer une loi de transformation de cette distribution porale et de la relier à l'évolution de la porosité globale. Pour cela différents modèles de transformation de pores sont proposés avec en particulier un focus sur l'étendue des sites de précipitation/dissolution par rapport au voisinage du front capillaire.

Ces modèles de transformation géométrique de la structure porale se ramènent à deux éléments majeurs à élaborer:

- La loi explicitant la transformation géométrique du pore, d'un rayon initial r_0 à rayon altéré r_1 , prenant en compte l'existence d'un front capillaire localisé à un rayon de pore r_c . Ici la forme générique suivante a été adoptée :

$$r_1 = r_0 + \varepsilon(r_0, r_c) \quad (1)$$

où la fonction ε permet de déterminer le taux $\tau = \varepsilon(r_0, r_c)/r_0$ de remplissage/érosion d'un pore par rapport à sa configuration initiale. Il est négatif en cas de précipitation (remplissage) et positif en cas de dissolution (érosion).

- La relation de passage entre les fonctions de densité de probabilité régissant la distribution des tailles de pores avant et après transformation, donnant lieu à une évolution de la porosité totale de sa valeur initiale ϕ_0 à sa valeur modifiée ϕ_1 .

Pour la loi de transformation du rayon de pore, deux façons de prendre en compte l'effet du front capillaire ont été considérées (figure 2.6):

- Dans la première approche, la variation $\varepsilon(r_0, r_c)$ augmente de façon monotone (en valeur absolue) pour les pores localisés dans le voisinage du front capillaire: $r_c - \beta \leq r_0 \leq r_c + \beta$ où 2β est l'étendue de ce voisinage. Pour les pores de rayon au-delà du front capillaire ($r_0 > r_c + \beta$) reste égale à sa valeur maximale (atteinte en $r_c + \beta$) ce qui se traduit néanmoins par un effet relatif de plus en plus faible lorsque le rayon de pore augmente. Il s'agit donc d'un modèle traduisant un mécanisme de précipitation/dissolution relativement diffus dans le réseau poreux.
- La deuxième approche cible un mécanisme de précipitation/dissolution localisé au voisinage du front hydrique. Seuls les pores de rayon $r_c - \beta \leq r_0 \leq r_c + \beta$ sont

transformés en adoptant une variation en cloche (fonction non monotone, centrée sur r_c) de la fonction $\varepsilon(r_0, r_c)$ qui prend des valeurs nulles en dehors de cette intervalle.

Pour la loi de transformation de la loi de probabilité, deux approches sont également considérées quant à la construction de la fonction densité de probabilité $P_1(r_1)$ obtenue après transformation géométrique de la structure porale initiale représentée par la densité de probabilité $P_0(r_0)$:

- Dans la première approche, la transformation géométrique est vue comme un changement de la variable aléatoire. Dans ce cas, une relation classique (en théorie de probabilité de variables continues) existe entre les deux fonctions de densité de probabilité (equation (2.12)-(2.14)). On montre alors que l'exploitation de la relation de changement de variable est équivalente d'un point de vue physique à considérer (cf. equation (2.15)) que le ratio des taux de porosité $d\phi_1/d\phi_0$ ($d\phi_0$ correspondant à une population de pores de rayons compris entre r_0 et $r_0 + dr_0$ se transformant en population de pores de rayons compris entre r_1 et $r_1 + dr_1$ correspondant à $d\phi_1$) est égal au ratio des porosités globales ϕ_1/ϕ_0 . En d'autres termes, la variation macroscopie (correspondant à celle de l'espérance statistique) s'applique également à l'échelle de pore (valeur locale de la variable aléatoire).
- La deuxième approche exploite le schéma de représentation du réseau poreux comme des cylindres de même longueur mais dont le rayon suit une distribution statistique. Dans ce cas, le ratio des taux de porosité $d\phi_1/d\phi_0$ est pris égal au ratio des volumes élémentaires des deux populations de pores (cf. cas précédent) ce qui donne lieu aux relations de passage (equation (2.17)-(2.18)).

Il est à noter que lorsque la variation $\varepsilon(r_0, r_c)$ de rayon de pore n'est pas monotone (cas de la transformation localisée en forme de cloche) alors la fonction densité de probabilité de la configuration transformée présente des asymptotes verticales pour les valeurs des rayons où la fonction $\varepsilon(r_0, r_c)$ atteint des extrema. Ces singularités rendent plus complexe l'implémentation numérique de la première méthode et ont motivé le développement de la deuxième méthode qui permet d'obtenir des fonctions de densité de probabilité qui restent régulières.

Enfin, l'approche est généralisée à une série de transformations successives comme prélude à un couplage avec un modèle de transport réactif donnant lieu à une évolution dans le temps de la porosité. Une relation de récurrence est obtenue pour établir le passage de l'état initial à l'état final en passant par des états intermédiaires. Les paramètres du modèle définissant la fonction $\varepsilon(r_0, r_c)$ peuvent alors être déterminés à partir de la connaissance la porosité initiale et finale. La relation de récurrence permet de remonter le fil des transformations successives

pour établir une relation univoque entre l'état actuel d'un pore et son état initial. La fonction $\varepsilon(r_0, r_c)$ joue alors le rôle d'une fonction hérédité ou mémoire.

Différentes études paramétriques concluent cette première contribution. Elles portent sur une analyse comparative entre les différentes variantes du modèle d'évolution de la structure poreuse et illustrent l'effet de la prise en compte d'un mécanisme de précipitation/dissolution diffus ou localisé au sein du réseau poreux.

La deuxième contribution porte sur la modélisation du transport réactif en milieux poreux partiellement saturés par le couplage d'un modèle chimique de précipitation/dissolution à un modèle de transport de masses (fluides et espèces ioniques). Il s'agit d'un modèle dégénéré (quasi-local) permettant de réaliser des études paramétriques sur l'évolution de la porosité globale sous l'effet des conditions hygro-chimiques.

Le modèle chimique est un modèle classique d'équilibre basé sur la loi d'action de masse régissant des réactions chimiques rapides et réversibles. Ce modèle chimique est similaire au modèle mécanique rigide-plastique : il existe une fonction seuil (contrôlée par la constante d'équilibre) qui régit l'occurrence instantanée de la précipitation/dissolution de phases solides à partir des espèces ioniques présentes dans la solution chimique. Lorsque les concentrations des espèces ioniques augmentent jusqu'à atteindre la valeur seuil (sans pouvoir la dépasser) alors tout apport supplémentaire d'ions donne lieu à une précipitation de phases solide de sorte à préserver l'équilibre. Inversement, lorsque les concentrations des espèces ioniques diminuent par rapport à la valeur d'équilibre, les phases initialement précipitées, sont instantanément dissoutes en quantités suffisantes de sorte à maintenir l'équilibre chimique de la solution.

Bien que le modèle chimique soit classique, sa forte non linéarité a nécessité de faire appel à différents schémas numériques itératifs de résolution de type prédicteur-correcteur. La contribution principale sur ce volet porte donc sur l'implémentation numérique dans l'environnement MATLAB avec trois méthodes de résolutions itératives pouvant se relayer en cas de difficultés de convergence. Plusieurs cas test permettent de valider cette mise en œuvre numérique. Le modèle implémenté est également comparé à un modèle disponible dans le logiciel COMSOL à titre de validation quantitative.

Un point à souligner dans l'implémentation du modèle chimique de précipitation/dissolution est la mise en œuvre d'une stratégie de gestion échelonnée de la masse des phases solides précipitées en vue du couplage avec le modèle de transport. En effet, l'écriture de l'équilibre chimique est habituellement basée sur la concentration de ces phases solides par rapport au volume de la solution chimique, au même titre que sont exprimées les concentrations des espèces ioniques. Cet artéfact de travail rend le modèle de précipitation/dissolution non adapté à l'analyse d'un milieu poreux : la diminution du volume de la solution du fait d'une forte dessiccation ou bien du fait de la réduction du volume de pore par précipitation donne lieu à une augmentation sensible de la concentration des phases solides (exprimée par rapport au

volume de la solution en diminution). La concentration des phases solides devient alors numériquement dominante par rapport à la concentration des espèces ioniques. Il en découle une non-convergence du schéma itératif de résolution. Pour pallier cette pathologie numérique, seule une fraction courante de la masse des phases solides précipitées est considérée, de sorte à maîtriser le contraste entre les différentes concentrations intervenant dans l'équilibre chimique et assurer la stabilité numérique du schéma itératif. La fraction courante sert donc de tampon entre la solution et la masse totale des phases solides précipitées.

Dans un deuxième temps, les équations du modèle de transport des phases fluides ainsi que des espèces ioniques sont dégréées pour aboutir à un modèle de transport réactif quasi-local. Les termes de flux des différentes phases sont remplacés par des apports/retraits massiques directement au point matériel: Q_w pour l'eau et Q_c pour les espèces ionique. Cette approche permet de s'affranchir d'une résolution complète du problème aux limites régissant le transport réactif en milieux poreux. Elle permet néanmoins une première approche d'analyse du comportement local d'un point matériel sous l'effet couplé des conditions hygro-chimiques externes et des mécanismes locaux de précipitation/dissolution. Elle permettra en perspective à ce travail de thèse de disposer d'un modèle de transport réactif fonctionnel pour l'implémentation de l'approche probabiliste de la structure porale précédemment exposée.

Le discrétisation temporelle du modèle quasi-local de transport réactif permet d'établir l'algorithme de résolution pour les variables degré de saturation, porosité et concentrations des espèces ioniques. L'implémentation numérique du modèle est faite dans l'environnement MTALAB. Le couplage avec le modèle local d'équilibre chimique permet d'actualiser les masses précipités/dissoutes des phases solides.

Le volet de la validation du modèle ainsi développé porte sur l'analyse de la robustesse numérique. Des cas tests élémentaires permettent de valider et d'illustrer le fonctionnement du modèle dans le cas de la précipitation ou de la dissolution sous le seul effet d'une réduction, respectivement, d'une augmentation de la saturation en eau de la porosité. Puis, les mécanismes de précipitation et de dissolution sont analysés en prenant également en compte l'apport ou le retrait d'espèces ioniques selon différents scénarii.

Enfin, le modèle de transport réactif est exploité pour mener une étude paramétrique exhaustive sur l'évolution dans le temps de la porosité sous l'effet d'un apport constant d'espèces ionique (pouvant caractériser une valeur moyenne de flux massiques ioniques en conditions réelles) et de cycles de dessiccation/réhumidification du milieu poreux. Différentes valeurs de l'apport massique Q_c et de l'amplitude la variation de la saturation en eau sont considérées. Ces simulations ont permis d'établir une relation empirique pour estimer le temps nécessaire pour remplir, par précipitation de sel NaCl, tout l'espace poreux disponible. Sur ces temps longs, l'amplitude de variation de la saturation en eau ne semble pas un paramètre sensible.

La troisième contribution de cette thèse consiste en l'extension de l'approche probabiliste à l'étude de paramètres majeurs régissant le transport réactif: l'isotherme de sorption/désorption et la perméabilité. L'influence des conditions hygro-chimiques et des mécanismes de précipitation/dissolution sur ces paramètres est analysée à l'aune de données expérimentales disponibles.

Cette partie est un prélude au couplage du modèle de transport réactif à l'approche probabiliste décrivant l'évolution de la structure porale sous l'effet de la précipitation/dissolution. Un premier pas vers la mise en œuvre de ce couplage passe par la prise en compte de l'évolution de la structure porale qui découle du modèle probabiliste dans la caractérisation:

- des mécanismes de sorption/désorption d'eau par la structure porale en évolution, en prenant en compte l'effet de présence d'espèces ioniques en solution sur ces mécanismes. La loi de Kelvin régissant l'équilibre entre les phases liquide et vapeur de l'eau dans un milieu poreux en présence de tension capillaire doit prendre en compte l'activité ionique. Pour une humidité relative donnée, la pression capillaire issue de la loi de Kelvin modifiée est impactée par la présence des ions en solution. La localisation du front capillaire (reliée à la pression capillaire via la relation de Young-Laplace) se trouve également affectée par la présence ionique. Sur la base de cette localisation du front capillaire (donnée par le rayon r_c), le modèle probabiliste permet de déterminer la nouvelle distribution de la structure porale associée à une évolution globale de la porosité. La détermination du rayon capillaire r_c et de la fonction densité de probabilité actuelle permet de déterminer le nouveau degré de saturation associé à l'humidité relative et intégrant la présence ionique. L'isotherme de sorption/désorption est ainsi construite.
- de la perméabilité intrinsèque (purement géométrique), la perméabilité à l'eau et celle au gaz ainsi que la perméabilité relative à l'eau et celle au gaz. Ces paramètres jouent un rôle majeur dans la modélisation du transport de masses (fluides et ioniques) et rendent compte de la connectivité du réseau poreux, de sa tortuosité ainsi que de l'effet la coexistence de deux phases fluides (liquide et gazeux) dans le mécanisme de perméation. Dans ce travail, une relation de la littérature reliant la structure porale à la perméabilité intrinsèque est adoptée pour étendre l'approche à la détermination de la perméabilité intrinsèque et celles à l'eau et au gaz sur la base de la distribution de la structure porale en évolution selon le modèle probabiliste. Ces perméabilités sont déterminées par la donnée de la variation de porosité globale et de celle de la position du front capillaire (correspondant à une humidité relative donnée). L'effet des conditions hydriques lors de la précipitation/dissolution sur ces perméabilités est ainsi pris en compte. Enfin, la détermination de la perméabilité intrinsèques et celles aux fluides permet de déterminer les perméabilités relatives associées et de comparer les évolutions obtenues avec les relations empiriques disponibles dans la littérature.

Il est à noter que dans cette contribution, seule le modèle de transformation de la loi de probabilité basé sur une structure de pores cylindrique est exploité. Comme indiqué

précédemment, la régularité de cette approche (absence d'asymptotes verticales) permet une meilleure stabilité numérique. Cependant, les études paramétriques réalisées montrent une importante sensibilité au choix de la loi de transformation géométrique du pore : l'approche quasi-diffuse versus l'approche localisée au voisinage du front capillaire.

Enfin, ces différentes contributions permettent de mettre en évidence différentes perspectives au travail de thèse et en concluent le mémoire.

AVIS DU JURY SUR LA REPRODUCTION DE LA THESE SOUTENUE

Titre de la thèse:

Probabilistic approach for modelling pore structure and reactive transport in porous media due to precipitation and dissolution of solid phases

Nom Prénom de l'auteur : XIONG QINGXIANG

Membres du jury :

- Madame BELAYACHI-BALAICH Naïma
- Monsieur AIT MOKHTAR Karim
- Monsieur MEFTAH Fekri
- Monsieur BENBOUDJEMA Farid
- Monsieur AMIRI Ouali

Président du jury :

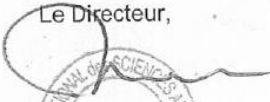
Date de la soutenance : 23 Juillet 2021

Reproduction de la these soutenue

- Thèse pouvant être reproduite en l'état
 Thèse pouvant être reproduite après corrections suggérées

Fait à Rennes, le 23 Juillet 2021

Signature du président de jury

Le Directeur,

Abdellatif MIRAOU


O. AMIRI


Titre : Modélisation probabiliste de l'évolution de la structure porale et du transport réactif dans les milieux poreux dus à la précipitation et à la dissolution de phases solides

Mots clés : Milieux poreux, Précipitation et dissolution, Structure porale, Modélisation probabiliste, Transport réactif, Couplage hygro-chimique.

Résumé : L'étude du transport réactif dans les milieux poreux est une problématique majeure qui sous-tend l'analyse de la durabilité des matériaux de construction exposés à des environnements agressifs. Le transport d'espèces chimiques en solution dans le réseau poreux peut donner lieu à des phénomènes de précipitation/dissolution de phases solides au sein de ce réseau poreux qui altèrent ces matériaux. L'évolution dans le temps de ces altérations dépend de l'incidence des mécanismes de précipitation/dissolution sur l'évolution du réseau poreux qui est le siège et le vecteur du transport réactif. En particulier, l'évolution de la localisation du front capillaire du fait des conditions hygrométriques peut affecter de façon marquée les sites de précipitation/dissolution à l'échelle du réseau poreux, donnant lieu à une transformation hétérogène ou fortement localisée de la structure porale. Ce paradigme rend nécessaire de caractériser, outre l'évolution de la porosité globale, la transformation de la distribution de pores (sous l'effet couplé des conditions hygro-chimiques) et son incidence sur les paramètres régissant les mécanismes de transfert.

Une première contribution de ce travail de thèse consiste en une approche probabiliste pour représenter la structure

porale et modéliser son évolution due à la précipitation/dissolution de phases solide contrôlée par la présence d'un front capillaire. L'évolution de la distribution porale est reliée à celle de la porosité globale. Différents modèles de transformation de pores sont proposés avec en particulier un focus sur l'étendue des sites de précipitation/dissolution par rapport au voisinage du front capillaire. La deuxième contribution porte sur la modélisation du transport réactif en milieux poreux partiellement saturés par le couplage d'un modèle chimique de précipitation/dissolution à un modèle de transport de masses (fluides et espèces ioniques). Il s'agit d'un modèle dégénéré (quasi-local) permettant de réaliser des études paramétriques sur l'évolution de la porosité globale sous l'effet des conditions hygro-chimiques. La troisième contribution de cette thèse consiste en l'extension de l'approche probabiliste à l'étude de paramètres majeurs régissant le transport réactif : l'isotherme de sorption/désorption et la perméabilité. L'influence des conditions hygro-chimiques et des mécanismes de précipitation/dissolution sur ces paramètres est analysée à l'aune de données expérimentales disponibles.

Title : Probabilistic approach for modelling pore structure and reactive transport in porous media due to precipitation and dissolution of solid phases

Keywords : Porous media, Precipitation and dissolution, Pore structure, Probabilistic modelling, Reactive transport, Hygro-chemical coupling.

Abstract : The investigation of reactive transport in porous media is a major problem that underlies the durability analysis of construction materials exposed to aggressive environments. The transport of solutions with chemical species in the porous network may give rise to precipitation/dissolution phenomena of solid phases that may alter these materials. Therefore, the time-dependent alterations are affected by the precipitation/dissolution in the porous network that hosts the reactive transport processes. In particular, the evolution of the capillary front due to the hygrometric conditions affects the pore structure at which the precipitation/dissolution occurs at the pore scale, thus leading to highly localized modifications of the initial pore size distribution. This model makes it necessary, in addition to the characterization of porosity, to address the evolution of the pore size distribution (under the coupled effect of hygro-chemical conditions) and its impact on the transport properties.

For this purpose, this research work proposes, as a first

contribution, a probabilistic approach for representing the pore structure and modelling its evolution due to the precipitation/dissolution of solid phases when controlled by the capillary front. The evolution of the pore structure is related to the modified porosity. Different transformation models are proposed according to the extent of precipitation/dissolution zones concerning the capillary front. The second main contribution is the modelling of reactive transport in partially saturated porous media by coupling a precipitation/dissolution reactive model with a mass transport model for fluids and ionic species. A local-like degenerated model is then developed to investigate the evolution of the overall porosity under different hygro-chemical conditions. The third contribution of this thesis consists of extending the probabilistic approach to study major parameters controlling the reactive transport: sorption/desorption isotherm and permeability. The influences of hygro-chemical conditions and precipitation/dissolution on these parameters are analysed in the light of available experimental data.